Numerical Modelling of High Temperature Phase Change Materials in Latent Heat Thermal Energy Storage Systems for Concentrated Solar Power Plants

by

Soheila Riahi

MSc (Sustainable Energy Technology, TU Delft, The Netherlands)

BSc (Mech. Eng., Sharif University of Technology, Iran)

A thesis submitted for the degree of

Doctor of Philosophy

Barbara Hardy Institute

School of Engineering

University of
South Australia

March 2018

Table of Contents

List of Figures IV
List of Tables V
Declaration VIII
Acknowledgement VIII
List of Publications IX
Nomenclature X
1 Introduction 1
1.1 Background 3
1.1.1 Storage systems 4
1.1.2 CSP applications 5
1.2 Numerical modelling 5
1.3 Design and optimisation 6
1.4 Motivation and Objectives 6
1.5 Structure of thesis 7
2 Literature review 8
2.1 Transport phenomena in melting and solidification 8
2.2 Different configurations of LHTES systems 9
2.2.1 Shell and tubes 9
2.2.2 Flat plate 10
2.3 PCM heat transfer enhancement methods 12
2.3.1 Conduction heat transfer enhancement 12
2.3.2 Convection heat transfer enhancement 14
2.4 Thermodynamic analyses, first and second law 16
2.5 Design and optimisation 18
2.6 Research gaps and opportunities 20
3 Numerical modelling 22
3.1 Computational fluid dynamics 22
3.1.1 Moving boundary 23
3.1.2 Fixed grid 23
3.2 Model setting and validation 24
3.2.1 Two dimensional axisymmetric modelling of inward melting, fixed wall temperature 24
3.2.2 Two dimensional axisymmetric modelling of melting in an annulus 27
3.2.3 Three dimensional modelling of a U-tube element of a two pass prototype at ECN 30
3.3 Investigation of transport phenomena 34
3.3.1 Flow and mass transfer 34
3.3.2 Modes of heat transfer 34
3.3.3 PCM system 35
3.3.4 Numerical calculations 35
3.3.5 Results and discussion 36

3.4 Conclusion 38
4 Thermal performance evaluation and comparison of high temperature PCM systems during charging and discharging 40
4.1 Thermodynamic analysis, first and second law 40
4.2 Shell and Tube system 41
4.3 Plate Fin system 42
4.4 Numerical modelling 44
4.4.1 Geometry and grid 44
4.4.2 Numerical calculations 45
4.4.3 Boundary conditions 45
4.5 Results and discussion 45
4.5.1 Effectiveness 46
4.5.2 Temperature field 47
4.5.3 Mass transfer 49
4.5.4 Phase front evolution 52
4.5.5 Heat transfer 54
4.5.6 Phase Change Duration 55
4.5.7 Entropy Generation 56
4.6 Conclusion 56
5 Impact of Periodic Flow Reversal on the Solidification and Melting Processes in a Latent Heat Shell and Tube Storage System 59
5.1 PCM system 59
5.2 Numerical modelling 59
5.2.1 Geometry and grid 59
5.2.2 Fixed Boundary Condition - FBC 59
5.2.3 Periodic Boundary Condition – PBC 60
5.3 Result and discussion 61
5.3.1 Periodic Boundary Condition at tube-PCM interface 61
5.3.2 Impact on Phase Front 61
5.3.3 Impact on Temperature Field 63
5.3.4 Impact on Mass Transfer 64
5.3.5 Impact on Heat Transfer 64
5.3.6 Impact on Phase Change Time 65
5.4 Conclusions 66
6 Two and three dimensional modelling of high temperature PCM 67
6.1 Two dimensional axisymmetric modelling of an annulus 67
6.1.1 PCM system 67
6.1.2 Numerical calculations 68
6.1.3 Results and discussion 68
6.2 Three dimensional modelling of a U-tube from the UniSA prototype 70
6.2.1 PCM system 70
6.2.2 Numerical calculation 71
6.2.3 Results and discussion 71

6.3 Conclusion 74
7 Design and optimisation procedure of geometrical parameters of a PCM storage system 75
7.1 Design and optimisation procedure using numerical modelling 75
7.1.1 Preliminary design of geometric specification 76
7.1.2 Numerical modelling of a scale model 77
7.1.3 Parametric numerical modelling 79
7.1.4 Design review 79
7.2 Geometrical design and optimisation process case study 80
7.2.1 Preliminary design 80
7.2.2 Scale model study 81
7.2.3 Detailed design, scaling up the model to the prototype scale 81
7.2.4 Sectional numerical modelling 81
7.2.5 Detailed design review 87
7.3 Conclusion 87
8 Conclusion and future research 88
8.1 Conclusion 88
8.2 Future work 90
References 91

List of Figures

***Figure 1.1**: Shares of renewables regional total primary energy supply in 2015 ..... 1*
***Figure 1.2**: Average annual growth rate of world renewables supply from 1990 to 2015 ..... 2*
***Figure 1.3**: Schematic diagram of a concentrated solar power cycle with latent heat energy storage 3*
***Figure 1.4**: Schematic diagram of different alternatives of concentrated solar power cycles with latent heat..... 4*
energy storage: (a) Brayton cycle, (b) Rankine cycle, (c) Combined cycle 4
***FIGURE 2.2.** Schematic drawings: (a) slab-based PCM [17], (b) a module of finned plate system [22] 11*
***FIGURE 2.3.** Schematic drawings: (a) flat plate PCM system [64], (b) fin plate system [32] 11*
***FIGURE 2.4.** Temporal variations versus dimensionless time: (a) dimensionless heat transfer rate from hot 16*
side (Q_h) and cold side (Q_c), (b) melt fraction [106] 16
***FIGURE 2.5.** Schematic drawings: (a) cross section of a shell and tube system, (b) a two-dimensional 19*
sectional model, PCM confined between tubes conveying HTF and referred dimensions 19
***FIGURE 3.1.** Schematic drawings of the numerical model with hot wall at the outer surface. 25*
***FIGURE 3.2.** Temporal evolution of the scalar fields including experimental (exp) and simulated (sim) results: . 26*
***FIGURE 3.3.** Schematic drawings of the annulus geometry a) experimental setup [132], b) symmetrical 27*
numerical model showing locations of temperature monitoring 27
***FIGURE 3.4.** Comparison of the measured and predicted temperature profile with THTF=10°C and Tini=- 4 °C . 28*
***FIGURE 3.5**. Comparison of the measured and predicted total heat transfer rate with THTF=10 °C, Tini= - 4 °C 29*
***FIGURE 3.6.** Schematic drawings:..... 31*
***FIGURE 3.7.** Temperature comparison between model temperature (tm) and thermocouple readings 32*
***FIGURE 3.8.** Temperature comparison between model temperature (tm) and thermocouples (tc) in PCM 32*
***FIGURE 3.9.** Phase fraction in PCM: 32*
***FIGURE 3.10.** Temperature comparison between model temperatures (tm) and thermocouples (tc) in PCM..... 33*
***Figure 3.11**. Schematic drawings: (a) tube bundle carrying HTF in a shell filled with PCM, (b) centre to centre of 36*
two adjacent tubes, (c) numerical model, symmetrical half of the dual-tube element in parallel flow 36
(a) δl =53.2% at 2300s, (b) δl =87.8% at 4450s, (c) δl =97% at 5600s. 36
Conduction and assuming laminar convection: (d) δl =53.2% at 2250s, (e) δl =87.8% at 36
4950s, (f) δl =97% at 6500s. Conduction, and turbulent convection modelling: (g) δl = ... 36
53.2% at 2000s, (h) δl =87.8% at 4200s, (k) δl =97% at 5600s. 36
***Figure 3.13**. Evolution of melt front during the melting process: (a) without convection modelling (wc), ... 37*
(b) including laminar natural convection (cwt), including turbulent natural convection (c&t) 37
***Figure 3.14.** Results comparison: (a) heat flux at the tube surface, without convection modelling (wc),..... 38*
including natural convection (cwt), and turbulent natural convection (c&t), (b) melt fraction,..... 38
wc, cwt, c&t, and cwt coarse grid result (blue dashed line) versus the fine grid (cwt-fg orange 38
dashed line). 38
***FIGURE 4.1.** Schematic drawings of vertical view of the shell and tube systems:..... 42*
***FIGURE 4.2.** Schematic drawings: (a) vertical flat plate LHTES system, (b) side view of the flat plate system 43*
***FIGURE 4.3.** Schematic drawing of the numerical models: (a) fin plate vertical, (b) counter flow vertical, ... 44*
***FIGURE 4.4.** Temporal evolution of effectiveness: (a) melting, (b) solidification..... 46*
***FIGURE 4.5**. Temporal evolution of temperature profile during solidification process: 47*
***FIGURE 4.6.** Temperature evolution in PCM during discharging processes versus: 48*
(a) average temperature, (b) temperature gradient 48
***FIGURE 4.7.** Temporal evolution of temperature profile during melting process: 48*
***FIGURE 4.8.** Temperature evolution in PCM, during charging processes versus:..... 49*
(a) average temperature, (b) temperature gradient 49
***FIGURE 4.9.** Temporal evolution of stream function (kg/s) during solidification process at δs =8.2%,..... 50*
***FIGURE 4.10.** Temporal evolution of stream function during melting process:..... 51*
***FIGURE 4.11.** Temporal evolution of phase front in solidification processes: 53*
(a) FPV b) CFV, c) PFV, d) CFHB, e) PFH..... 53
***FIGURE 4.12.** Temporal evolution of phase front in melting processes:..... 53*
(a) FPV, b) CFV, c) PFV, d) CFHB, e) PFH..... 53
(c)..... 54
***FIGURE 4.14.** Temporal evolution of phase fraction: (a) melting, b) solidification 55*
***FIGURE 4.15.** Entropy generation in PCM during discharging processes versus: 56*

(a) solid fraction, b) temperature gradient 56
FIGURE 4.16. *Entropy generation in PCM during charging processes versus:* 56
(a) melt fraction, b) temperature gradient 56
FIGURE 5.1. *Schematic drawing of the numerical model* 59
FIGURE 5.2. *Periodic flow boundary condition at HTF inlet-outlet:* 60
(a) melting, (b) solidification 60
FIGURE 5.3. *Temporal evolution of temperature profiles at the tube-PCM interface* 61
FIGURE 5.4. *Temporal evolution of solid front during solidification process:* 62
FIGURE 5.5. *Temporal evolution of melt front during melting process:* 62
FIGURE 5.6. *Temporal evolution of temperature profile during solidification process:* 63
FIGURE 5.7. *Temporal evolution of temperature profile during melting process:* 64
FIGURE 5.8. *Temporal evolution of heat flux: (a) melting, (b) solidification* 65
Temporal evolution of energy stored during: (c) charging, (d) discharging 65
FIGURE 5.9. *Temporal evolution of melt fraction:* 66
(a) melting, (b) solidification 66
FIGURE 6.2. *Profiles of the melting process at 8050 seconds and 60% melt fraction:* 68
FIGURE 6.3. *Temporal evolution of scalar fields during the charging process:* 69
FIGURE 6.4. *Temperature profiles of the discharging process:* 69
FIGURE 6.5. *Temporal evolution of scalar fields during the discharging process:* 70
FIGURE 6.6. *Three-dimensional schematic drawings: (a) a complete U-tube geometry, (b) symmetrical* 71
geometry of a quarter of the U-tube and PCM (c) symmetrical grid of the quarter of the U-tube 71
FIGURE 6.7. *Profiles at 1500 seconds and 60% melt fraction: (a) temperature, (b) radial velocity* 72
FIGURE 7.1. *Schematic drawings: (a) cross section of shell and tube, (b) symmetrical model for* ***case 1,*** 82
(c) symmetrical model for ***case 2*** 82
FIGURE 7.2. *Temperature profile comparison during the melting process:* 82
FIGURE 7.3. *Temporal evolution of temperature field during melting process:* 83
FIGURE 7.4. *Temporal evolution of temperature field during solidification process:* 83
FIGURE 7.5. *Temperature profile comparison during solidification process:* 84
FIGURE 7.6. *Temporal evolution of stream function during melting process:* 84
FIGURE 7.7. *Temporal evolution of stream function during solidification process:* 85
Figure 7.8. *Temporal evolution of scalar fields during melting process: (a) heat flux at tube/PCM interface,* 85
Figure 7.9. *Temporal evolution of scalar fields during the solidification process:* 86

List of Tables

Table 3.1: *Thermophysical properties of n-eicosine [40]* ***Table 3.2:*** *Dynamic viscosity of n-eicosine [40]* 24
Table 3.3: *Thermophysical properties of water* ***Table 3.4:*** *Thermophysical properties of HTF [132]* 28
Table 3.7*: thermophysical properties of PCM [135]* ***Table 3.8****: thermophysical properties of air* 35
Table 3.9*: Average (ave) and maximum (max) stream functions:* 37
Table 4.1*: Thermophysical properties of PCM [135]* ***Table 4.2****: Thermophysical properties of air* 41
Table 4.3 – *Mass transfer (kg/s) during solidification process* 51
Table 4.4 – *Mass transfer (kg/s) during melting process* 52

Summary

Energy production and consumption are not balanced and sustainable, resulting in ever increasing and dramatic climate change. Increase in energy prices as a tangible consequence of the unsustainable policies results in less access to affordable energy for the majority of people and lowering industry profitability. This problem and the need for urgent solutions have been recognised by the international community in recent years.

Renewable energy and particularly solar energy can be an important part of the solution. Solar energy being renewable and accessible everywhere around the world, at least for sometimes during a day/year, is the most common shared sustainable source of energy that can enhance the quality of life on earth. The production of low cost electricity from solar thermal energy has been proved as a promising replacement for fossil fuels in conventional power plants. Most renewable energy resources including solar energy are intermittent, non-dispatchable and cannot adapt to fluctuations in demand. However, concentrated solar power (CSP) is capable of producing affordable and continuous electricity on demand with the integration of a thermal energy storage.

The two major alternatives of thermal energy storage are sensible and latent heat storage systems. While sensible heat storage systems have been commercialised during the last decade and proved to be reliable, the potential of latent heat storage providing a reliable system for industrial applications and CSP plants is yet to be proved. The thesis makes a contribution in this area.

While there are intensive research and commercialisation background information in the scope of low temperature phase change materials (PCMs) mainly for air conditioning and refrigeration systems, little knowledge exists in high temperature PCM storage. Recently, there has been more research interest in the scope of medium temperatures PCMs (melting range: 50˚C -300˚C) for industrial application and high temperature PCMs (300˚C – 750˚C) for CSP plants. The focus of this work is on the latter.

For the design and optimisation of such a system, predicting the thermal behaviour of different alternative PCMs in conjunction with different heat transfer fluids (HTFs) in various design configurations is crucial. As the expenses of experiments are high and more complex at high temperatures, numerical modelling provides an alternative virtual laboratory to explore the thermal behaviour of PCM systems. Validated numerical models can be used to understand material behaviour and heat transfer in such a system to predict the thermal performance of different combinations of PCMs/HTFs in different configurations. From the very start of a design procedure to the fine tuning optimisation of a PCM system, the virtual experimental environment provides assistance. Exploring and using this virtual medium for design and optimisation purposes is the main objective of this work.

A numerical model was developed in the platform of ANSYS FLUENT as a commercial code. The model was validated with the low temperature experimental data available from the literature. Dimensional analysis provides a means to interpret and correlate data from low temperature to higher temperature PCMs. Other work from the literature proved that the thermal behaviour of different PCMs with different Prandtl numbers are similar in cases with similar level of natural convection (i.e. same Rayleigh number). The validated model was then used to model other cases for which experimental data were available. To find out the scaled down method from a real application to a prototype scale and further to a model scale, two-dimensional axisymmetric and three-dimensional modelling has been performed for two different configurations. It was found that a two-dimensional axisymmetric model of an annulus where heat transfer fluid passes through the inner tube and PCM is confined in the outer tube is sufficient for representing a parallel flow arrangement. However, this model might have shortcomings for counter flow where the temperature distribution between tubes is not the same everywhere. A three-dimensional U-tube model has been prepared as an element of a two-pass shell and tube experimental setup, the results showed good agreement between the predicted and measured data after allowing for experimental error. The collective results showed that the model set up in the FLUENT platform is reliable for design and optimisation purposes, particularly when there is an understanding of its capabilities and limitations.

Using the validated model, a number of two-dimensional geometries and grids were generated for different configurations of the shell and tube system; namely counter flow and parallel flow in vertical and horizontal orientations. The modelling provided a comprehensive understanding of mass, flow and heat transfer phenomena during the melting and solidification processes including the role of different heat transfer modes; namely conduction and convection. A superior thermal performance has been discovered for the horizontal cases considering the first and second law efficiency of the system while the nature of the convection heat transfer is different for the vertical orientation. Moreover, gaining the knowledge of the rate of heat transfer and duration of storage and release of heat for each configuration enables one to make the right choice for specific applications. Another configuration to be modelled is a rectangular geometry where fin plates surround the PCM in smaller compartments and the heat transfer fluid passes in a channel at the bottom of the system. The analysis demonstrated similar thermal behaviour as the horizontal shell and tube arrangements. Overall, analyses of the results of the numerical studies provided a deep understanding of charging/discharging processes and the potential of each configuration for specific design criteria from upstream and downstream of a CSP plant.

In an attempt to enhance heat transfer in PCM systems and provide a more cost-effective storage system for CSP plants, continuously reversing the direction of the heat transfer fluid for a specific time interval has proved to be effective. A two-dimensional numerical model has been developed using an element of a parallel flow shell and tube. The results showed enhancement of heat transfer during the melting process due to the resonance of natural convection while heat transfer improved during the solidification process due to a higher heat transfer area between solid and liquid particularly after 75% solid fraction. This provides a potential to overcome one of the shortcomings of the latent heat storage systems where heat transfer to the power block slows down at the later stages of a discharge process. This shortcoming has been recognised as redundant PCM, which needs to be added to the capacity of the system. Using the reversing flow method can reduce the redundant PCM, reducing the size and cost of the storage system.

It has been shown in the literature that each combination of PCM/HTF in a particular configuration results in unique flow and thermal characteristics, which needs to be examined. Two different modelling of high temperature PCM in conjunction with sodium as the HTF were performed, using the two-dimensional axisymmetric model for parallel flow and a three-dimensional U-tube model as an element for a counter flow shell and tube system. Results of these numerical studies can be used as a first step in the design and optimisation of a high temperature latent heat storage system.

Using the results and understandings from all of the above studies, a step by step design procedure for a full scale system is proposed. The procedure starts with selection of a configuration that suits the application with an estimation of mass and volume of PCM to provide the required storage capacity. Then a model scale needs to be generated to model the system and obtain its main thermal characteristics, including temperature range, velocity, mass flux and heat transfer rate. Using the results from the numerical modelling and some suggestions from previous parametric studies from the literature (e.g. ratio of tube length to diameter), a detailed design can be developed to acquire the heat transfer area, number of tubes and spacing, length, diameter, and other details. After this step and for further optimisation, alternative numerical modelling such as sectional modelling has been proposed. From the results of this step, the parametric aspects of the system can be revised towards the optimal design, e.g. reduction in heat transfer area and cost savings.

At a time of increasing interest and practical application of solar thermal generation/storage in Australia and around the world, the addition to knowledge in this thesis provides a step forward towards a new era of clean and affordable electricity from solar energy for everyone.

Declaration

This work is performed by myself and does not incorporate any material previously submitted for a degree or diploma in any university. To the best of my knowledge it does not contain any materials previously published or written by another person except where due reference is made in the text; and all substantive contributions by others to the work presented, including jointly authored publications, are clearly acknowledged.

Soheila Riahi



15/03/2018

Acknowledgement

I would like to thank Professor Wasim Saman for his supervision, advice, and guidance. Also, thanks to my co-supervisors, Professor Frank Bruno and Dr. Steven Tay for their supervision and assistance. I appreciate time and constructive remarks provided by Dr Martin Belusko. This work is part of the Australian Solar Thermal Research Initiative (ASTRI) project supported by the Australian Government through the Australian Renewable Energy Agency (ARENA). The Author gratefully acknowledges that the work has been funded by an ASTRI PhD scholarship.

List of Publications

Journal Papers

Soheila Riahi, Wasim Y Saman, Frank Bruno, Martin Belusko, N.H.S. Tay, *Impact of periodic flow reversal of heat transfer fluid on the melting and solidification processes in a latent heat shell and tube storage system.* Applied Energy, 2017. 191: p. 276-286.

Soheila Riahi, Wasim Y Saman, Frank Bruno, Martin Belusko, N.H.S. Tay, *Comparative study of melting and solidification processes in different configurations of shell and tube high temperature latent heat storage system.* Solar Energy, 2017. 150: p. 363-374.

Soheila Riahi, Wasim Y Saman, Frank Bruno, Martin Belusko, N.H.S. Tay, *Performance comparison of latent heat storage systems comprising plate fins with different shell and tube configurations.* Applied Energy, 2018. **212**: p. 1095-1106.

Co-author of a paper:
Raud Ralf, Michael E. Cholette, Soheila Riahi, Frank Bruno, Wasim Saman, Geoffrey Will, Theodore A. Steinberg, *Design optimization method for tube and fin latent heat thermal energy storage systems.* Energy, 2017. 134: p. 585-594.

Conference Papers

Soheila Riahi, Wasim Y Saman, Frank Bruno, N.H.S. Tay, *Numerical modeling of inward and outward melting of high temperature PCM in a vertical cylinder.* AIP Conference Proceedings, 2016. 1734(1): p. 050039.

Soheila Riahi, Wasim Y Saman, Frank Bruno, Martin Belusko, *Thermal Behaviour of High Temperature PCMs under a Periodic Heat Transfer Fluid Flow Reversal.* 2016.

Soheila Riahi, Wasim Y Saman, Frank Bruno, N.H.S. Tay, *Numerical Study Of Melting Process Of A High-temperature Phase Change Material Including Natural Convection And Turbulence.* International Journal of Computational Methods and Experimental Measurements, 2017. **5**(5): p. 723-732.

Soheila Riahi, Wasim Y. Saman, Robert de Boer, Frank Bruno, Simon Smeding, Ivar de Visser, *Numerical Study of a Two Pass Shell and Tube Latent Heat Storage System*. Submitted to SolarPACES2017 for publication in AIP, Aug. 2017.

Patent

An international patent has been registered for the novel method of reversing flow direction, which can enhance the heat exchanger performance. The study is included in chapter 5, and the patent registration number is PCT/AU2017/000145.

Nomenclature

A_{mush}	mushy zone constant
Be	Bejan number, $\Delta P\ L^2/\mu\ \alpha$
C	specific heat, J/kg.K
d, D	Diameter, m
E	Exergy, J/s
Fo	Fourier number, $\alpha t/r^2$ or $\alpha t/z^2$
g	gravitation acceleration, m/s^2
h	heat transfer coefficient, W/m^2 K
H	specific enthalpy [J/kg], or height, m
k	thermal conductivity, W/m K
L	Latent heat of fusion [J/kg], or length, m
m	mass, kg
$\dot{m}$	mass flow rate, kg/s
Nu	Nusselt number, h r/k
P	pressure, Pa
Pr	Pr number, ν/α
q"	heat flux, W/m^2
r	width of enclosure or radius, m
R	Radius, m (e.g. PCM radius in an annulus)
Ra	Rayleigh number, $g\beta z^3(T_h - T_m)/\nu\alpha$
Re	Reynolds number, vD/ν
s	Entropy generation, J/K
S	tube spacing, m
So	source term in momentum equation
Ste	Stefan number, $c_l\ (T_h - T_m)/L$
t	time, s
T	temperature, °C
v	velocity, m/s
w	width, m
W	work, J
$\dot{W}$	power, J/s
wt	weight
X,Y	coordinates
z	height of enclosure, m

Greek symbols

α	thermal diffusivity, m^2 /s
β	thermal expansion coefficient, K^{-1}
δ_T	Thermal boundary layer, m
δl	liquid fraction
δs	solid fraction
ε	effectiveness or small number (0.001)
μ	dynamic viscosity, Pa s
ν	kinematic viscosity, m^2 /s
ρ	density, kg/m^3
σ	Stephan Boltzmann constant 5.67×10^{-8} W/m^2 K^4

Subscripts

b	base of the enclosure
c	cold
ch	charging
d	diameter
dc	discharging
e	environment
h	hot wall or hot HTF
i	inner
in	inlet
l	liquid
m	melt
max	maximum
o	reference or initial or outer
opt	optimal
p	pressure
rev	reversible
z	height

Abbreviations

Δ	difference
∇	gradient
CF	counter flow
PF	parallel flow
CFV	counter flow vertical
CFHB	counter flow horizontal, bottom HTF inlet
CFHT	counter flow horizontal, top HTF inlet
PFV	parallel flow vertical
PFH	parallel flow horizontal
FPV	fin plate vertical
LHTES	latent heat thermal energy storage
SHTES	sensible heat thermal energy storage
NTU	number of transfer unit
GW	Gigawatt, 10^9 Watts
kWh_{th}	kilowatt- hours- thermal

The widely used symbols through this thesis are included in the Nomenclature. Some other symbols and acronyms are defined within the text of particular chapters.

1 Introduction

Global energy production and consumption are not balanced and sustainable, resulting in ever faster dramatic climate change. Increased energy prices as a tangible consequence of the unsustainable policies have resulted in less access to affordable energy for the majority of people, lowering the standard of living, profitability of industry development. Apart from energy prices, there are other consequences from global warming and climate change; melting icebergs resulting in sea level rises endangers livelihood particularly in the coastal areas. On land, unprecedented extreme weather patterns and droughts affect agriculture and food production leading to higher prices for more people [1]. Expanding the poverty around the world and mass migration are other consequences. Combined all together, these problems might lead to higher geopolitical tensions.

Renewable energy and particularly solar energy can be an important part of the solution to mitigate climate change. Transition, however, from the conventional fossil fuel framework to renewable resources and adapting and/or building new infrastructure is not an easy task. It needs an overhaul, a new mindset and willingness among policy makers and educating people to support the right policies even if it is painful in the short term. On the other hand, renewable energy needs to be continuing technological advance and become more financially viable in comparison to conventional energy resources. For this to happen requires more research to steer the progress in the developing and implementing renewable energy technologies. More investment allocation for research in this area requires the understanding and willingness of the policy makers. This problem and the need for urgent attention has been recognised by the international community in recent years. In a study by Elliston et al. [2], comparing three different options of the so-called low-emission fossil fuel electricity generation against a 100% renewables concludes that integration of available renewable technologies is a cost effective and reliable policy. Providing a worldwide insight, the authors report on the existence of national targets in many countries including Ireland, Japan, Australia, and many European countries to provide 80-100% of end-user energy consumption from renewable resources by 2050. Tracking clean energy progress [3], a report by the International Energy Agency (IEA) provides an overview of the progress and targets aimed by its 29 member countries, and beyond. The IEA reports an unprecedented 6% global growth in clean electricity generation in 2016, resulting in renewables contributing 24% of total power generation. Figure1 provided in the report shows regional progress, forecast and targets in clean electricity production.

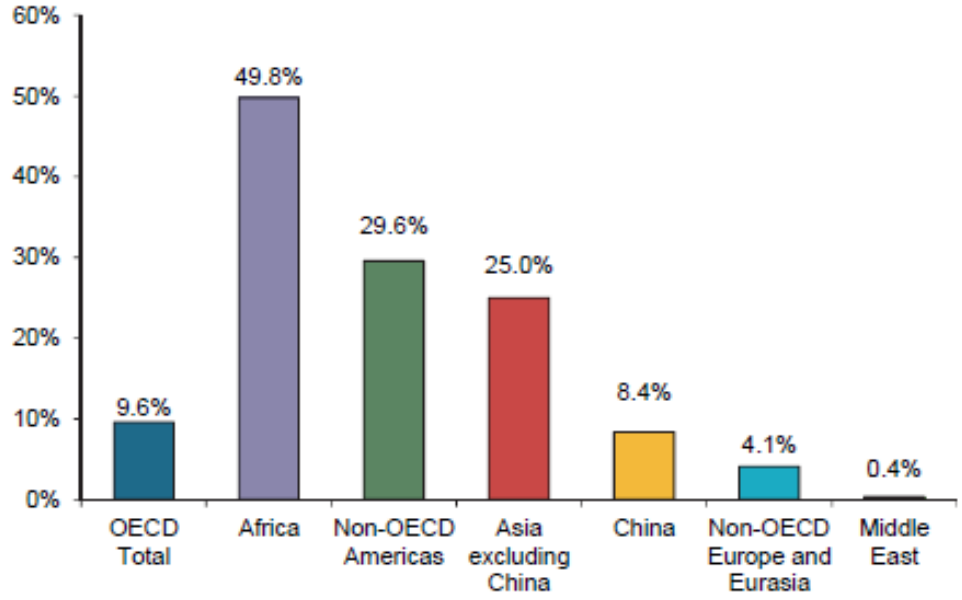


Figure 1.1: Shares of renewables regional total primary energy supply in 2015

Solar energy being accessible everywhere around the world, at least for sometimes during a day/year, is the most common shared sustainable source of energy that can enhance the cloudy perspective of life on earth. The production of low cost electricity from solar thermal energy has been proven as a promising replacement for fossil fuels in conventional power plants. Renewable energy resources including solar energy are intermittent and are not reliable for continuous generation of electricity and adaption to fluctuations in demand. However, a grid using

different renewable resources and supported by sustainable thermal and electrical storage systems is capable of producing affordable and dispatchable electricity on demand. IEA statistics [4] tracking the progress in deployment of renewables shows a higher share for the PV sector compared to solar thermal (45.5% vs 11.4%) (Fig. 1.2), mainly due to progress and cost reductions of both PV panels and Li-ion batteries. This progress has been driven by supporting policies, a better appreciation of the value of storage by regulators and technological advancement. This trend suggests that progress in solar thermal storage technologies and cost reduction can boost electricity generation from solar thermal. While the electrical storage media such as batteries provide a convenient solution at the smaller scale installations like PV where electricity is the output of the solar cells, thermal energy storage systems including sensible and latent heat offer the solution for larger scale electricity generation including CSP where the thermal energy is the output of the solar field. On the other hand, it is important to mention the growing concern about the management of batteries' hazardous waste at the end of life, particularly the Li-ion type due to the growing demand in electronic devices and vehicles [5].

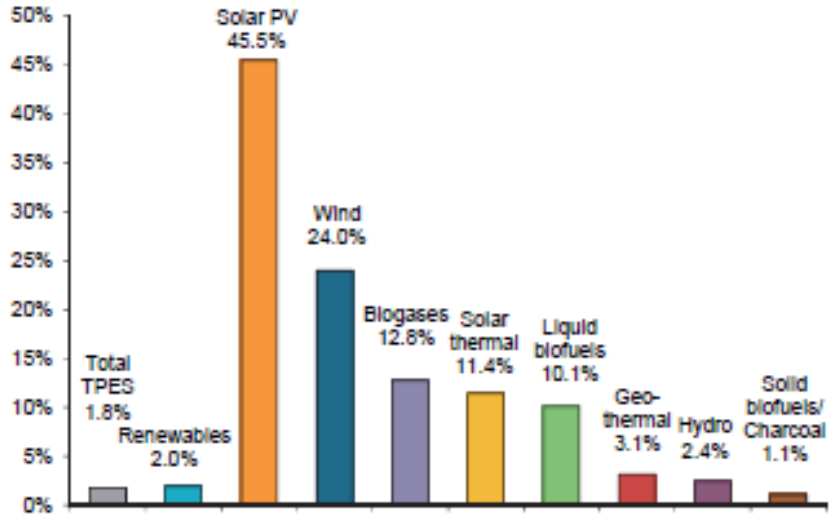


Figure 1.2: Average annual growth rate of world renewables supply from 1990 to 2015

In Australia, a study by Wolfarm et al. [6] shows that electricity generation is the largest CO_2 producer, about 35% of the national emissions. However, the latest annual report by the Australian Energy Market Operator [7] shows that the Australian energy landscape is shifting towards clean electricity. For instance, electricity generation by solar energy increased from 0 to 265 MW since 2008 and it is predicted to rise to 11043 MW by 2020. The corresponding figures for electricity generation from wind are 7235, 10130 and 10678 MW. The Market Operator acting as an advisory body to policy makers, suggested that Australia having quality resources and technical knowhow can lead the transition to renewables. Wolfarm et al. [6] supports the same suggestion as their life-cycle assessment of different scenarios of energy supply mix indicated the feasibility of renewable energy penetration for a considerable decarbonisation of the power generation industry and as a necessary step for climate change mitigation. Another study by Riesz et al. [8] shows that the potential capacity of clean electricity in Australia is 500 times more than demand forecast by the national electricity market (e.g. 24024 GW vs 50 GW). Half of the potential is through concentrated solar power (CSP) with thermal storage, geothermal and biomass, which are considered as dispatchable and adaptable to the conventional grid. Their study proves the technical feasibility of the commercially available CSP with storage to provide 100% of the Australian electricity demand, immediately. Currently, due to the high cost of this approach, an economically viable alternative is a mix of renewables including wind and PV. A conclusion from this result is that the advancement in CSP with thermal storage and cost reductions will make 100% clean electricity from solar thermal a technical and economical viable option to meet the Australian market demand and climate change mitigation targets.

In USA, a study by Jacobson et al. [9] investigated the validity of the main criticism of the large-scale integration of renewables, namely wind, water, and solar being intermittent and unreliable. Simulation of different scenarios showed that including different types of storage of heat, cold, and electricity can provide a stable and reliable grid with 100% renewables without any need for fossil fuels, nuclear power or stationary batteries. The authors suggested that results cover many conditions, which means integration of low-cost 100% renewables (wind, water, solar) can be a worldwide solution for sustainable electricity generation. In a comprehensive study by Caldes and Lechon [10], based on CSP implementation in Spain, socio-economic and environmental impacts of CSP plants

were investigated. The study concluded the dramatic reduction of global warming emissions and remarkable benefits of CSP deployment regarding the national economy and employment.

Clearly, despite the damning evidence on the serious threat of anthropogenic climate change [1], there are two main schools of thought regarding future energy supply options. The first stream, which is now a small minority, denying climate change and its significance, and standing behind the conventional fossil fuel framed system, supporting proposition of low emission electricity generation from clean coal. On the other hand, the second stream believes in global warming and its severe impact on the livelihood on earth, trying to find innovative methods to replace fossil fuels with sustainable energy technologies. Most business leaders understand the dynamic change of the world, the shortcomings of the fossil fuel based economy and inevitable transition to the renewable energy era. They wish to be part of the new era simply for businesses surviving and to do so they accompany the second stream. In Australia, John Hewson, a former Liberal leader and economist once warning that climate change can lead to another recession through which the value of many assets fall, is Solastor chairman, backing solar thermal energy for electricity generation. He spearheaded a plan to fund a 1 MW demo CSP plant in Port Augusta in 2016. It is good to note that the second stream is now gaining momentum.
It is also clear now that energy storage is one of the main challenges to make electricity from renewable resources reliable, secure and cost effective. Solar energy as a sustainable replacement for fossil fuels in conventional power plants can also be stored as thermal energy and backup the cycle during the nights, cloudy days and peak demand periods.

1.1 Background

In a concentrated solar power (CSP) plant (Fig. 1.3), there are two main blocks; a solar field where a collection of mirrors concentrates the solar radiation onto a receiver, transferring the thermal energy to a heat transfer fluid (HTF). The second major block is the electricity generation comprising one or more turbines and generators. Ancillary systems including piping, pumps and heat exchangers connect the two blocks, transferring fluids and energy between them. Through this cycle as shown in Fig. 1.3, HTF from the first block delivers thermal energy directly to a turbine or indirectly through another heat exchanger to the turbine. The outlet cold fluid from the turbine passing through a heat exchanger then enters back to the solar field to heat up and close the cycle.

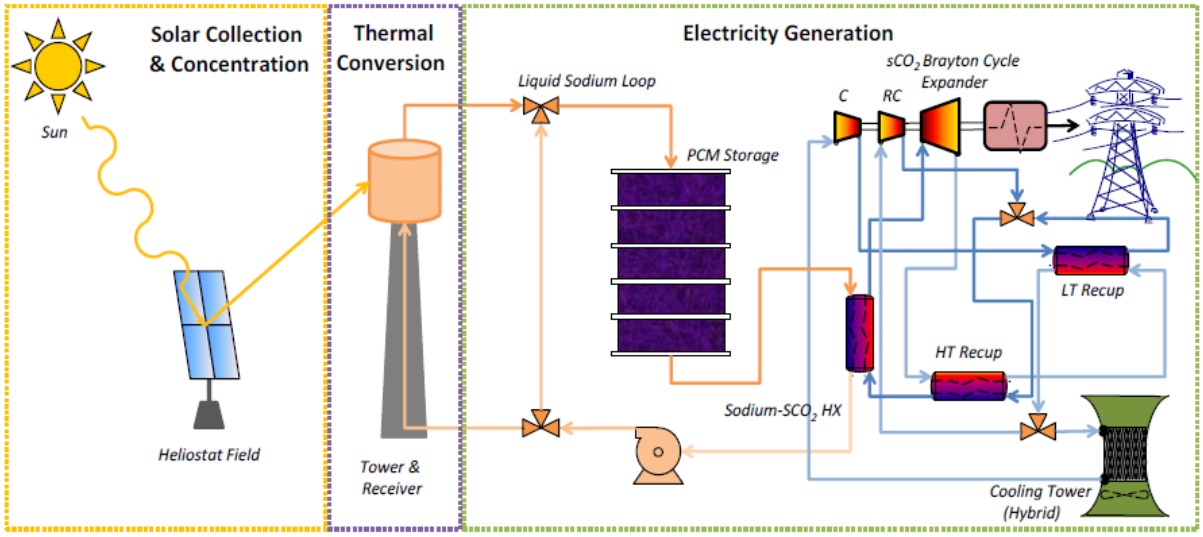


Figure 1.3: Schematic diagram of a concentrated solar power cycle with latent heat energy storage

There are two types of thermodynamic cycles used in conventional power plants, namely Rankine cycle (Fig. 1.4b), and Brayton cycle (Fig. 1.4a). In a Rankine cycle, a fossil fuel fired steam boiler generates steam (e.g. including preheater, evaporator and superheater), recycling the condensed water coming from the condenser. In a CSP plant, the fossil fuel is replaced by the solar thermal energy, providing steam directly to a turbine (DSG) [11] or indirectly through another heat exchanger. While phase change occurs from gas to liquid and vice versa in a Rankine cycle, with the Brayton cycle it is a single-phase process. The medium for heat transfer through the Brayton cycle is a gas, e.g. air in the conventional Brayton cycle working with a gas turbine or supercritical CO_2 (sCO_2) in a new CSP version of the cycle proposed by Turchi et al. [12] to provide higher efficiency. In this cycle, pressure differences convey the gas through the cycle for exchanging heat with different components or heat exchangers. A gas as the driving medium in a Brayton cycle makes it possible to respond rapidly to load

fluctuations and work at higher temperatures (800°C – 1100°C). Using both cycles (Brayton plus Rankine) in series results in a combined cycle, which has been used in conventional power plants to improve the overall efficiency of the cycle from around 35% to more than 50%. For the same purpose, a combined cycle (Fig. 1.4c) can be a favoured choice for the CSP plants [13], for which high working temperatures and pressures through the cycle are expected.

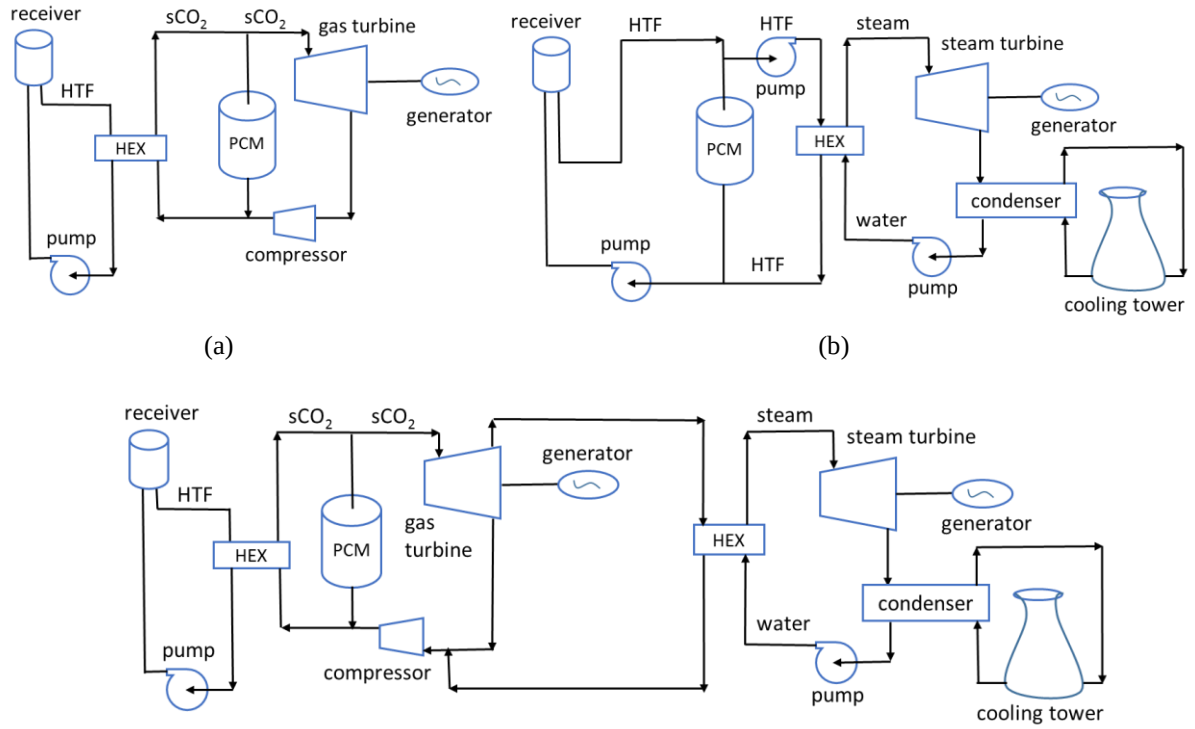


Figure 1.4: Schematic diagram of different alternatives of concentrated solar power cycles with latent heat energy storage: (a) Brayton cycle, (b) Rankine cycle, (c) Combined cycle

When direct solar heat is not available, the electricity generation cycle (single or combined) needs backup heat. The integration of a thermal storage system is a viable solution. During the day when the demand is not high and the system operates at partial load, storage of the solar thermal energy in a suitable medium provides that viable solution. Apart from thermochemical heat storage where heat storage and release occur through reversible endo/exothermic chemical reactions, the two other options are sensible and latent heat storage systems.

1.1.1 Storage systems

A sensible heat thermal energy storage (SHTES) system involves a single-phase process, relying on the heat capacity (MC_p, J/K) of the medium and temperature difference (ΔT, K). SHTES systems have been commercialised during the last decade and it has been reported that they are reliable. They have been integrated in different CSP plants in different countries, as reported by Kuravi et al.[14]. Here, the HTF and the storage medium are the same, providing thermodynamic advantages (e.g. same inlet and outlet temperature of HTF), but also can be disadvantageous in some cases regarding the transportation through pumping system. Decomposition of the available molten salts at temperatures higher than 550 ºC limits their application [15]. Moreover, preventing the molten salt from freezing in the piping system, particularly in cold climates, require trace heating which adds to the cost of system.

On the other hand, latent heat thermal energy storage (LHTES) systems rely on the latent heat of fusion of the storage medium (MH, J), undergoing a nearly isothermal process of phase change from solid to liquid to store heat or liquid to solid to release heat. Thermal storage systems based on the heat capacity of the storage medium and temperature difference (SHTES) results in low energy density and a larger size system. A numerical study by Wang et al. [16], comparing thermal performance and energy density of SHTES with LHTES showed that the latter exhibit much higher energy density leading to smaller system and cost savings. While one kg of sodium nitrate stores 182 kJ latent heat energy through an isothermal phase change process in a LHTES, the same thermal

energy can be stored in the same amount of material within 105 K temperature difference in a SHTES. Charging and discharging heat through an isothermal process makes the LHTES a good match with an isothermal secondary system such as water evaporation for steam production (Fig. 1.4b).

The heat of fusion of material combined with the melting temperature are among the important thermophysical properties of a PCM suitable for a specific application, as well as the specific heat capacity and thermal conductivity. In a phase change process, thermal energy transfers from liquid to solid along a narrow region where phase fraction is between zero and one. The temporal evolution and the shape (e.g. one or two-dimensional) of the interface area or phase front depends on the transport phenomena which are the result of the thermophysical properties of the PCM and the configuration of the system. Therefore, understanding the thermal behaviour of a PCM in a LHTES system relates to the temporal evolution of the phase front, its impact and interaction with the transport phenomena involved in a phase change process. A better understanding provides more controllability to exploit the optimal capability of the system.

In contemplating the use of PCM for high temperature energy storage, there is an intensive research and commercialisation background in the scope of low temperature PCMs, mainly for air conditioning and refrigeration applications [17-20]. Recently, there has been more research interest in the scope of medium temperatures PCMs (melting range: 50˚C-300˚C) [21, 22] for industrial applications (e.g. waste heat recovery) and high temperatures (300˚C–750˚C) [11, 23-25] for CSP plants. Moreover, improved thermal performance of concentrated solar thermal energy systems has been the focus of research programs to reduce the cost of electricity generation, such as the Sunshot initiative in USA [26] and the Australian Solar Thermal Research Initiative in Australia (ASTRI). To achieve higher performances for CSP plant, a higher temperature receiver and HTF are proposed (e.g. for combined cycle purposes by Segal [13] or review by Ho and Iverson [27]) which require the adaptation of a LHTES system. This requires research on high temperature PCMs, and HTF in innovative configurations and further heat transfer enhancement methods. At the LHTES level, low thermal conductivity of the potential molten salts and eutectic PCMs is an issue [28] for which different methods, mainly by extended heat transfer area using fins/mesh/nanoparticles, or encapsulation have been proposed in the literature [29-31]. However, those methods add complexity, reducing the volume fraction of PCM, and energy storage density, resulting in higher cost of the system. More research work is required to find innovative solutions to exploit the inherent potential of the system for improving heat transfer rate and thermal performance.

1.1.2 CSP applications

One of the main applications of a high temperature LHTES system is the integration between the solar field and the power block in a CSP plant. This system should be capable of storing adequate thermal energy when excess direct solar energy is available and provide adequate heat transfer to the power block when direct thermal energy from the solar field does not meet the energy demand. This makes the electricity generation cycle continuous and cost effective. Apart from being integrated in the electricity generation cycle as a heat storage medium, a LHTES system might be used for fast heat storage to protect a receiver from exceeding its high temperature limits and thermal stresses as proposed by Verdier et al [32]. High temperature differences (e.g., $\Delta T>50°C$) are expected in using a LHTES system, particularly for protection purposes. In another application, a LHTES can be used as an auxiliary source of energy during peak energy demand periods in a CSP plant where a higher rate of energy release might be necessary. For these applications, the first priority in the design criteria is the high rate of heat transfer to the HTF either for heat storage or heat release. Thermal energy storage must be able to meet both objectives of storing sufficient amounts of energy in the available time and delivering adequate heat transfer during extraction to a HTF with a specific outlet temperature. These are the essential factors in designing a LHTES, however, the system should be optimised for the highest PCM volume fraction leading to the highest energy density and lowest cost.

1.2 Numerical modelling

As the expenses of laboratory experiments, prototype manufacturing and testing, and pilot plants are high particularly in the high temperature area, numerical modelling provides an alternative virtual laboratory to explore the performance of different LHTES options. While numerical modelling can be used to explore thermal performance of a component such as LHTES, software such as TRNSYS [33] are available to simulate the whole cycle. A Sandia report prepared by Ho [34] provides information about the available software and codes for the analysis of CSP technologies. A combination of the simulations at the component and the cycle level provides insight into the performance of the whole cycle with different components, e.g. with or without a TES.

For the design and optimisation of a LHTES system, predicting the thermal behaviour of different alternative PCMs and HTFs in different configurations is crucial. A validated numerical model can be used to examine mass, flow and heat transfer in such a system to predict the thermal performance of different combinations of PCMs/HTFs in different configurations. Apart from in-house codes developed for specific purposes, there are commercial codes such as FLUENT[35] and COMSOL[36] available for the general computation of fluid dynamics. Moreover, there are open platforms such as OpenFoam where some models are provided but one can access the source to update those models for a specific purpose or develop a model and integrate with some others. Through this thesis, ANSYS DESIGN MODELLER [37] and FLUENT [35] are used to explore different combinations of PCM/HTF in different configurations, providing knowledge of the thermal performance of different LHTES systems. The results assist in the selection, design and optimisation of a system for a specific application and design criteria.

1.3 Design and optimisation

Design criteria for a LHTES system to be integrated in a CSP plant is determined by the upstream (solar field) and downstream (power block) conditions including the inlet/outlet temperatures and working pressure of the HTF. The main property of the PCM that needs to be matched with those conditions is the melting temperature of the PCM. The storage capacity and operating time of the system depends on the demand and the cycle specifications.

To design an optimum LHTES system, a thermodynamic analysis can assist. From the first law perspective, the system should provide the highest efficiency in both melting (charging) and solidification (discharging) processes. Latent heat effectiveness (ε) is a figure used to assess the efficiency of the system in the storage of the provided heat or releasing the stored heat. Ideally, the highest performance of the system ($\varepsilon = 1$) occurs when the outlet temperature of the HTF equals the melting temperature of the PCM ($T_{out} = T_m$) for both charging and discharging processes. However, there are limitations such as the available temperature of HTF in a charging process while in a discharging process, it is crucial to provide the required rate of heat transfer at the necessary temperature. Furthermore, considering the second law, an optimum design should minimise entropy generation and recover the highest exergy or the highest useful work/power [38]. In addition to the first and second law analyses at the LHTES component level, integrating an optimal LHTES requires a thermodynamic analysis of the whole cycle including the storage system during the charging and discharging processes [39].

1.4 Motivation and Objectives

Accelerating the transformation to the new clean energy era is the motivation for this research work. Working towards the target of 100% renewable energy from wind, water and solar is attractive as the environmental and socio-economic shortcomings of the fossil fuel based economy are obvious. Clean energy from the sun can be a major part of that target if our research effort makes it possible. This research work aims to be a part of making progress in this direction.

Considering the need for a more cost-effective thermal storage system for a CSP plant and making it competitive with the conventional systems, this work aims to provide tools and assistance in the design and optimisation of a LHTES system. As higher efficiencies are expected for future CSP plants, which require high temperature LHTES systems, the focus of this work is to explore different configurations in the high temperature range (> 300°C). Due to the complexity and high expenses of experiments, this work aims to take advantage of the virtual platform provided by numerical modelling through commercial code ANSYS FLUENT [35]. Developing a validated model provides a means to examine the thermal performance of different LHTES systems with the aim of finding innovative configurations that serve the high temperature cases. The provision of optimal LHTES systems will facilitate improving the performance of the whole cycle.

To overcome the low thermal conductivity of the alternative molten salt and eutectic PCMs, this work aims to find and propose methods and/or configurations to exploit the role of natural convection in the heat transfer process to facilitate optimal performance from the first law perspective and highest exergy recovery. The proposed research aims to fill the gap in developing a design method with numerical modelling involved, assisting in detailed design and further fine-tuning. Moreover, the literature review showed that there are parametric studies ignoring natural convection or involving natural convection in a single-phase process. This work attempts to address the situation, using numerical modelling in detailed design and in parametric studies of the phase change process including natural convection. Narrowing down all the learnings, this work aims to propose a step by step

design and optimisation process with the assistance of numerical modelling from the selection of an initial configuration to the detailed design and finally for the optimisation purposes.

1.5 Structure of thesis

This thesis continues with chapter two, providing a thorough literature review in the related field and insight into the available knowledge. Further subdivisions of chapter two provide literature review in the areas of transport phenomena in phase change processes, thermal performance of different configurations of LHTES system, proposed enhancement methods, thermodynamic analysis, and a closing section to explore the studies in the area of design and optimisation. At the end of chapter two, the identified gaps in the knowledge and the aim of this work towards filling those gaps are highlighted.

Chapter three includes the development of the model and validation with the available experimental data for low temperature PCMs. The model is used for two two-dimensional axisymmetric studies and a three dimensional modelling where the predicted results are compared against experimental data. Furthermore, the validated model is used for two-dimensional investigations of the transport phenomena including flow, mass and heat transfer and their role in defining the thermal characteristics of PCM in each configuration.

The validated model provided a means for two-dimensional studies of different configurations of LHTES systems, included in chapter four. Comparison of the thermal performance of different configurations of PCM systems in chapter four provides valuable knowledge to select a suitable configuration for different applications with different priorities in design criteria. Through this chapter, the results comparison and analyses of the thermal performance of counter and parallel flow shell and tube systems in horizontal and vertical orientations are presented. Moreover, through numerical modelling, the thermal performance of a fin plate rectangular configuration is compared with the shell and tube systems. The fin plate system is explored to relax the constraints regarding the HTF and PCM material selection particularly for high temperature/pressure systems. Providing separate zones for the HTF and PCM is one of the advantages of the system. The results of the numerical study of the system and thermal performance advantages are discussed.

Through chapter five, a novel method namely reversal flow method (RFM) is introduced which has been found to enhance thermal performance of the charging and discharging processes. This is a major contribution and achievement through this work. The results of a two-dimensional model are presented to show the evolution of temperature profiles, phase front, and the heat transfer in time in the PCM domain during charging and discharging processes.

The chapters above provide the knowledge of two and three-dimensional modelling and the extent that a scaled down model can represent a real design and/or prototype. However, there is a need to use the modelling for design and optimisation of high temperature PCMs. Chapter six starts with two-dimensional axisymmetric modelling of an annulus as an element of a parallel flow with a high temperature PCM (modelling at low temperature level is presented in chapter 3). Furthermore, results of a three-dimensional model of a U-tube system for high temperature PCM are presented to achieve a more accurate representation of counter flow configurations. The three-dimensional model mimics a U-tube element from the counter flow shell and tube experimental set up at UniSA. Collectively, these studies provide more insight into different scaled down approaches from a real scale to a model, small enough to take less time and computing resources with accurate results for the engineering applications. Results of the three-dimensional numerical investigations provide valuable knowledge for the design and optimisation of a LHTES system.

Using all the knowledge gained through the research program presented in the previous chapters, a step by step procedure for the design and optimisation is proposed in the first section of chapter seven. The method starts with selection of a configuration, an estimation of the required bulk mass/volume of the PCM using the knowledge from the modelling studies through this work and the previous parametric studies from the literature. Then each step is elaborated in more detail, showing the role of numerical modelling for a detailed design and further tuning and optimisation. Moreover, in the second section of chapter seven, the proposed procedure is employed for the design and optimisation of a case study system to provide 100 kWh_{th} thermal energy for one hour. Results and analysis of the sectional modelling for a parametric study and optimisation of system are presented. Finally, chapter eight provides conclusions, summary of the findings from the thesis and suggestion for future work.

2 Literature review

Previous literature in the area of LHTES systems is vast and provides a background about different configurations, and their thermal performances to some extent. However, design and optimisation of a LHTES systems for high temperature applications such as CSP plants requires more deep and detail understanding of transport phenomena, first and second law assessments, and a comparison of their capability/adaptability for different design criteria. The design parameters including the material selection, high temperature/pressure and cost effectiveness require intense research work to provide innovative solutions. Ultimately, the prospective results of the research effort in this area provide practical and cost effective thermal energy storage from solar energy to generate affordable and reliable electricity.
In this chapter, a thorough literature review of the pool of knowledge in the scope of LHTES systems and related subjects shows the gaps that need to be fulfilled with new knowledge. Finding the research gaps in different scopes related to the design and optimisation of a LHTES system, they are mentioned briefly at the end of each section. Then a summary of the gaps accompanied by the research opportunities and intended work to fill the gaps is provided at the end of this chapter.

2.1 Transport phenomena in melting and solidification

There have been significant analytical, experimental and numerical investigations in the field of melting and solidification to provide an understanding of thermal behaviour of PCM. The ultimate goal of all investigations is to gain knowledge on the optimum design of a LHTES system for different applications.
A comprehensive experimental and numerical study of the melting in a cylindrical enclosure by Jones et al. [40], provided a useful benchmark which could be used as a baseline for other numerical works, e.g. [41]. The experimental set up included a polycarbonate cylinder filled with paraffin wax and subjected to a fixed temperature at the outer surface by a water bath, and isolated at the top. The bottom was subjected to a fixed temperature lower than the wax melting temperature. Results showed the four distinct regimes during the melting process which had already been realised through analytical and numerical work by Jany and Bejan [42]. The four regimes are namely conduction dominant, mixed conduction and convection, convection dominant and "shrinking solid" for fluids with Pr>1 in rectangular enclosures heated from a side.
In another experimental and numerical investigation, Sharifi et al. [43] studied the outward melting in a cylindrical enclosure. The experimental data for the cases of 5° and 10° tilt angles with 0°, 45°, 90° and 135°azimuth angles showed that output profiles such as temperature field and melting front shapes are not symmetrical as they were with both angles zero. Using wax (n-octadecane) with a melting temperature of 28 °C, the authors aimed to validate the experimental results for the base case with an already validated model to suggest that the measured data for the tilted and rotated cases can be used as benchmarks for the validation of 3D models. Through an experimental and numerical study, Amin et al. [44] proposed an effective thermal conductivity for water as PCM encapsulated in a sphere. The numerical model accounted for the melting process of ice with different temperature differences, ignoring the effect of natural convection. They correlated results with the experimental measurements at different temperature differences, proposing an effective thermal conductivity as a function of Rayleigh (Ra) number.
Basal and Ünal [45] developed a computational code to study a triple concentric-tube LHTES, ignoring natural convection. Results showed that melting duration does not change with the mass flow rate of the HTF, however it decreases exponentially as the temperature of the HTF rises. The inclusion of natural convection might change the results of the study.

Apart from the studies where natural convection was included or ignored, limited research has investigated the natural convection impact on the mass transfer, heat transfer area (melt front in a melting process), temperature gradient in space and time for the melting process of a high temperature PCM. In an attempt to investigate the impact of natural convection on the melting front evolution, Assis et al. studied the melting process of wax in spheres with different diameter and fixed outer temperature, experimentally and numerically (using Fluent) [46, 47]. Volumetric expansion of liquid PCM, close contact melting and sinking of solid were included in their study. Using Fluent, Shmueli et al. [48] numerically studied the melting process of wax in a cylindrical enclosure with fixed outer temperature. The investigation included the natural convection and volumetric expansion of the liquid PCM to provide more understanding of the heat transfer mechanism and melting front evolution. In a recent numerical analysis using Fluent, Fornarelli et al. [49] demonstrated the impact of natural convection on the melting front evolution, mass flux and melting time in an element of a LHTES unit with parallel flow arrangement.
In a numerical study by Wang et al. [50], the alternate charge-discharge of a molten salt PCM (Na NO3) contained in a rectangular cavity was investigated. They used a step temperature change in time at one side with adiabatic condition at all other boundaries. The results revealed completely different characteristics during charging and discharging. Due to the minor role of natural convection the average heat transfer rate is lower and decreases

smoothly during the solidification process. The heat transfer rate in melting stages follows a more complex path compared to the solidification process. The phase change front is rather vertical in discharging, presenting a conduction dominant process. On the other hand, in charging cases it develops in a 2-D manner and is horizontally faster at the top compared to the bottom of the enclosure consistent with a natural convection dominant process [42]. Considering a LHTES application in CSP, a system with balanced thermal response during charging and discharging provides higher performance. The study introduced three approaches to resolve the inherent imbalance of such a system, however, the practical approach is to improve the heat transfer rate.

There are limited investigations on the impact of turbulence on the melting process in a LHTES system and the importance of this phenomenon in high temperature PCM systems. In a two dimensional numerical study, Markatos and Periclbous [51] developed a model to capture the changes in temperature and velocity fields while flow changes from laminar to turbulent in an enclosed cavity, i.e., from $Ra=10^3$ to 10^{16}. Results of the study revealed a higher Nusselt number (Nu) and heat transfer rate for higher Ra for which correlation between Nu and Ra were proposed. In numerical and analytical work, Lakeh *et al* [52] studied the impact of turbulent natural convection in a supercritical TES in a vertical tube with fixed outer temperature. Comparing different aspect ratios of the system, they found that the charging time is significantly shorter due to the heat transfer enhancement of turbulence.

2.2 Different configurations of LHTES systems

2.2.1 Shell and tubes

PCMs have high volumetric energy densities, however due to the low thermal conductivity of most candidate materials, the design of thermally responsive configurations of LHTES systems is required. A promising configuration for PCM thermal storage systems is the shell and tube arrangement where the heat transfer fluid flows through tubes surrounded by the PCM. Tube based LHTES systems are fundamentally tubes bundled in a shell, however limited research has investigated the characteristics of different flow arrangements with different boundary conditions to serve the specific design criteria. Limited research has been conducted regarding heat transfer between a parallel tube bundle and high temperature PCMs, with a specific focus on the boundary condition imposed on the PCM. In most cases the tube to PCM boundary condition was taken to be a fixed temperature or a fixed heat flux, and was generally considered as a single tube [40, 41, 43, 48, 53]. Nevertheless, in most real applications, the HTF flows via several tubes and depending on the tube and PCM arrangement, different boundary conditions occur at the tube-PCM interface. To achieve a suitable design at reasonable cost, an understanding of the performance of different configurations is necessary.
The possible configurations are counter flow, parallel flow, staggered, serpentine and other new arrangements (e.g. different sizes of tubes) that were proposed based on constructal law by Bejan [54, 55]. The concept of counter and parallel flow in the context of a LHTES unit is different from the definition used for conventional shell and tube heat exchangers. Here, counter flow refers to when the HTF in two adjacent tubes (immersed in PCM) is flowing in the opposite direction whereas parallel flow refers to when the HTF in all tubes immersed in PCM is flowing in the same direction (Fig. 2.1). The same concept has been used in previous literature by Cao et al. [56].

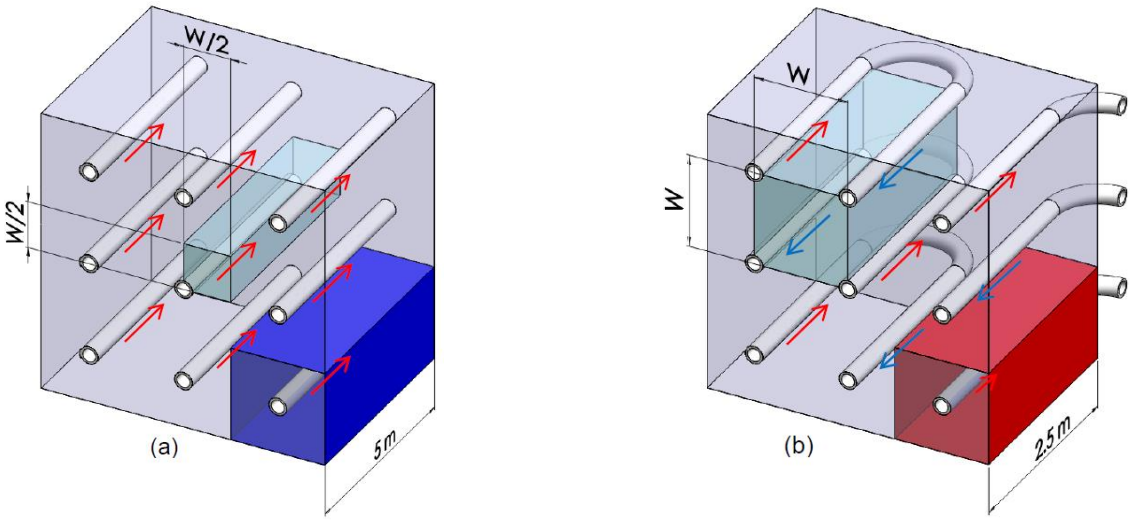


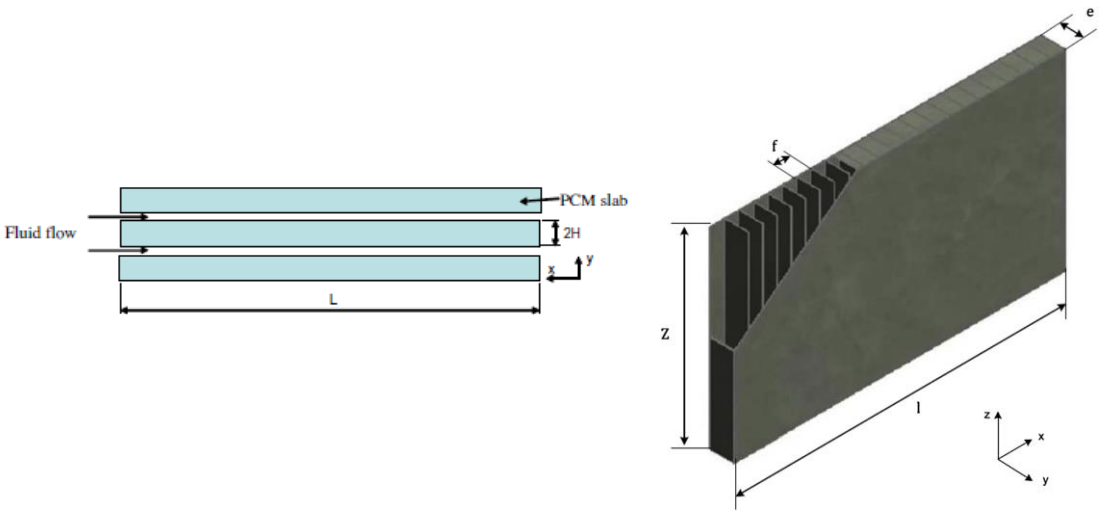
FIGURE 2.1. Schematic drawings of tube bundle in PCM: (a) parallel flow, (b) counter flow [23]

Kurnia et al. [57], numerically studied different configurations of U-tube in PCM. Examples include a U-tube with inline and staggered fin, and a form of serpentine. They investigated the impact of different types of fins on natural convection and the heat transfer rate. In a recent two parts study, Belusko et al. [23, 24] numerically investigated an effective tube-in-tank system as LHTES for CSP plants. In the first study, the impact of different tube and flow arrangements (e.g. single pass parallel flow, one and 2-D counter flow) on the PCM boundary conditions and discharging effectiveness were assessed. The main conclusion from the first study [23] is that different arrangements of HTF flow in the tube bundle influences the evolution of the phase front and the heat transfer area during a steady phase change process. Results of the second study [24] showed that for cases of a latent heat dominant system, the counter flow arrangement delivers a higher effectiveness while for the cases of a sensible heat dominant storage system, parallel flow was the better choice. However, this study ignored natural convection.

Through an analytical and numerical research, Lorente et al. [53] studied the evolution of vertical and horizontal melting fronts, temperature field and heat storage during a melting process in a vertical cylinder with a fixed heated bar in the centre. In another analytical and numerical study, Lorente et al. [58] found an optimal configuration of two concentric helices at fixed temperature immerged in a cylindrical tank of PCM. Using constructal law and numerical calculations, for a fixed period of heat storage (8 hours) and 95% volume fraction of PCM, the authors proposed parameters such as helices diameter and pitch to deliver a more uniform melting rate with increased global performance. The scale-analysis also showed the optimal energy storage can be delivered through uniform melting or least temperature gradient in space and time. This means using less material, leading to a more cost-effective LHTES unit.
The impact of the direction of HTF on the phase change front evolution was investigated experimentally and numerically by Longeon et al. [59]. The comparison of HTF inlet from the top and bottom of an element of a parallel tube bundle immersed in PCM, (i.e. an annular system), showed a thermocline profile along the inner tube (i.e., the boundary condition at tube/PCM interface) for the top HTF injection in melting cases. A uniform temperature profile was reported for the bottom injection due to the mixing effect of natural convection. The phase change front in discharging cases was insensitive to the injection side of HTF, presumably due to the minor role of natural convection.
Laing et al. [60] developed a new LHTES system for direct steam generation (DSG) through experimental investigation. The parallel flow configuration, including longitudinal fins, imposed the saturated steam temperature for the boundary condition of the PCM. The authors proposed optimal types of fins and the HTF (saturated water) recirculation system to overcome the increasing of thermal resistance between the tube and phase change front, particularly in a discharge process. In another study for the DSG purposes, Pirasaci and Goswami [61] numerically studied the effect of different parameters (e.g., length of tube, distances between tube, tube diameter) on the performance of an element in a parallel flow LHTES. Garcia et al. [11] experimentally and numerically investigated a finned tube LHTES at pilot scale for use in a DSG cycle. Results showed satisfactory performance to meet the plant requirement.
There is no comparative study on the phase front evolution during a phase change process of a high temperature PCM in a shell and tube heat exchanger in different configurations, namely counter and parallel flow, and in different orientations, namely vertical and horizontal. The impact of the phase front evolution on the temperature and velocity profile, heat transfer, phase change time and effectiveness of the system are very important to understand for the design and optimisation of a high temperature PCM to be used in a CSP plant.

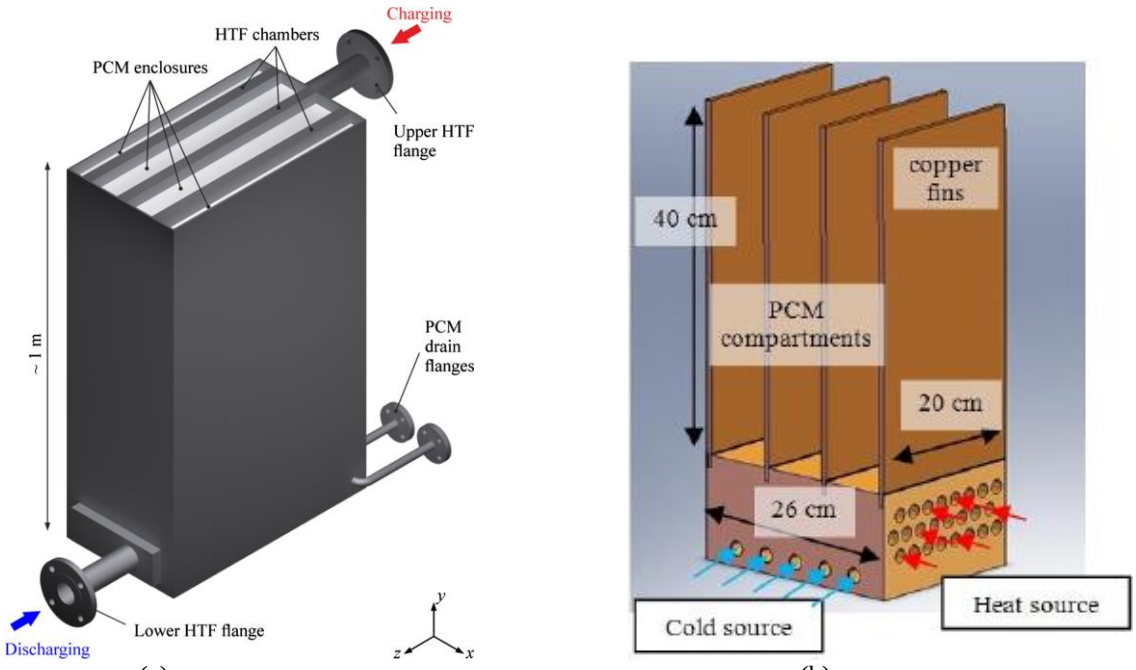
2.2.2 Flat plate

Using a rectangular geometry, PCM can occupy rectangular enclosures while HTF flows through narrow rectangular passages between the PCM containers. Depending on the plate orientation or HTF flow direction, a system can be considered as horizontal or vertical. Furthermore, in this configuration, there have been efforts to model slab-based systems where thin slabs of PCM (e.g. 25 mm) with narrow gaps (e.g. 5 mm) for HTF (Fig. 2.2a) is introduced for the highest heat transfer [17]. Belusko et al. [17] provided a literature review and proposed an effectiveness-NTU method to characterise slab-based PCM systems. The authors using air and water as HTFs within different slab and gap thicknesses provided an analytic solution to determine the transition thresholds from 1-D to 2-D phase front where the 1-D solutions are no longer valid. In a numerical study, Amin et al. [62] proposed an analytic solution for energy storage effectiveness that can be used for the optimisation of a slab-based PCM design. Through a parametric study, the impact of different sizes of gaps (0.005-0.75 m), different mass flow rates of HTF and slab thickness (0.2 -0.01 m) of PCM on the energy storage were studied.
From the results of an experimental and numerical study, Campos-Celador et al. [22] proposed an analytical method and a simplified numerical model for the design and optimisation of a modular finned plate LHTES system for cogeneration applications. HTF flows in narrow channels (at a few mm scale) between the modules (Fig. 2.2b). As a result of a comprehensive numerical study, de Gracia et al. [63] proposed a correlation for the calculation of



(a) (b)

FIGURE 2.2. Schematic drawings: (a) slab-based PCM [17], (b) a module of finned plate system [22]



(a) (b)

FIGURE 2.3. Schematic drawings: (a) flat plate PCM system [64], (b) fin plate system [32]

heat transfer coefficient of a LHTES comprising flat plate PCMs and air flow between the plates. Using an effective heat capacity method, the authors developed a numerical model and through a parametric study found the correlation of convective heat transfer coefficient.

The performance of a pilot scale (7.5 kWh) new flat plate LHTES system (PCM melting temperature equal to 219.5 °C) was experimentally investigated by Johnson et al. [64]. The PCM was contained in vertical rectangular enclosures (4.2x101 cm cross section) while HTF flows through vertical passages through PCM (Fig. 2.3a). The authors found that the proposed LHTES being open at the top facilitates the PCM filling and inclusion of different material and types of structures (plates/fins) inside the tank to optimise the heat exchange performance for different applications. The charging and discharging processes within the same experimental setup [64] was numerically studied by Vogel et al. [65]. Using FLUENT [35], they found that including the effect of natural convection results in better agreement between the predicted and the experimental data.

In another configuration from the plate heat exchanger category, plates are included in a rectangular enclosure filled with PCM and connected to the channels or tube bundle alongside or at the base of the enclosure (Fig. 2.3b). HTF passes through the channels or tubes, conducting heat to the PCM through the plates. This configuration might be considered horizontal or vertical depending on the plate orientation. Using COMSOL [36] and a numerical model developed by Calvet et al. [29], Verdier et al. [32] studied a vertical flat plate LHTES prototype attached to a receiver for the protection against high thermal stresses in a hybrid solar-gas turbine power plant. In this LHTES unit, PCM (Li_2CO_3 with a melting point of 723 °C) is contained in a tank divided into rectangular sections by copper vertical plates. At the bottom, the tank is attached to an electrical heater/tube bundle as the heat source/sink. They found that it takes 4 hours to fully charge and 2.5 hours to discharge the system with 200 K temperature difference between the HTF and PCM.
Soares et al. [66] experimentally studied a vertical stack of rectangular cavities filled with a bulk PCM. Cavities made from aluminium plates, conducting heat from/to a heat source/sink attached to one side of the LHTES unit to air as the HTF flowing at the other side of the LHTES unit to mimic e.g. a brick wall. The authors provided benchmark data for validation of numerical models to support the optimum design of rectangular LHTES systems for applications in the building industry or other applications.
In two numerical investigations, Shatikian et al. [67, 68] studied a rectangular LHTES system where plates immersed in PCM were used as the heat transfer interface and constant temperature [67] or constant heat flux [68] was applied as the boundary condition at the base of the system. A parametric study revealed the impact of PCM, plate thickness and different temperatures or heat fluxes at the base on the performance of the system. From the results of both studies, the authors proposed correlations for Nusselt number and melt fraction.
In another numerical study by Saha et al. [69], considering the same rectangular LHTES with thin plates immersed in PCM, constant heat flux at the base of the system was imposed. The authors proposed different correlations for Nusselt number and melt fraction for three different aspect ratios; namely shallow, square and tall enclosures.
In experimental and numerical studies by Hosseinizadeh et al. [70], using the same rectangular LHTES system as above with constant heat flux at the base, the impact of the number, height and thickness of thin plates on the thermal performance of the system was evaluated. Results from 2-D and 3-D numerical modelling, using FLUENT [35] showed good agreement with the experimental data.

There have been investigations of different categories of shell and tube, rectangular and fin plate rectangular systems for LHTES in isolation, however limited knowledge is available in comparing their performance.
In an early attempt by Wei et al. [71], cases of slab and tube capsules in a tank were numerically and parametrically compared in regards to thermal performance and rapid heat release. In the slab in tank configuration, PCM was confined in thin slabs (2 mm) and HTF flowed through multi-pass tubes between the slabs. In the shell and tube system, PCM is contained in the shell and the HTF flows through the tubes. The numerical model was validated with an experimental study of a conventional plate heat exchanger as LHTES with the same PCM and HTF as used for the numerical cases. Results showed a high impact of slab thickness or tube diameter and void fraction in cases with a low heat transfer coefficient. Comparing the latter two cases, for a void fraction of 0.25, the heat release is faster for the plate configuration for thicker PCM slabs or larger tube diameters, e.g. d>4 mm.
Medrano et al. [72] experimentally evaluated five commercial types of LHTES systems; shell and tube, flat plate and compact heat exchangers. The results showed a better performance with the shell and tube system when fins or graphite matrix were included in the PCM. Regarding the other two configurations, the compact type was promising while the commercial flat plate type performance was considered inadequate.

2.3 PCM heat transfer enhancement methods

2.3.1 Conduction heat transfer enhancement

2.3.1.1 Fins, metal foam, nano-particles and encapsulation

There has been considerable research proposing various methods to enhance the heat transfer in LHTES systems. This has been summarised comprehensively by Liu et al [73] and recently reviewed by Liu et al [74]. The traditional approach in designing effective LHTES systems has been through enhancing the heat transfer in the PCM using fins, foams or encapsulated PCM [29, 45, 57, 75, 76] . However, these techniques increase cost.
Through a numerical investigation, Liu et al. [75] studied the heat transfer enhancement effect of including metal foam in an element of a horizontal shell and tube LHTES system. An example was using PCM/foam in the outer tube and HTF in the inner tube of an annulus. Introducing an effective thermal conductivity for the PCM and metal foam, the evolution of melting front, temperature and velocity fields were explored.
From the results of a numerical study, Gue and Zhang [77] proposed the integration of aluminium foil in high temperature PCM as an effective solution to enhance the heat transfer in a LHTES system. Using ANSYS Fluent, Liu et al. [75] studied the impact of metal foam in an element of shell and tube latent heat thermal storage while constant heat flux was used at the tube side. The melting process in the porous medium, considering pure conduction heat transfer showed enhanced heat transfer due to the high thermal conductivity of the metal foam.

In the experimental and numerical work by Zheng et al. [78], the performance of a LHTES system including encapsulated sodium nitrate in a cylindrical shell was examined at pilot scale. Results showed high energy storage density, about 211 kJ/kg of the capsule weight (from which 95% stored in PCM) while about 42% of the heat storage resulted from the latent heat transfer. Other examples with encapsulated PCM are an experimental study using low temperature PCM (wax) by Ettouney et al. [79] and a numerical study using high temperature PCM ($Na\ NO_3$) in cylindrical and spherical capsules by Elmozughi et al. [30]. In a recent experimental examination, a geopolymer encapsulation was proposed by Jacob et al. [80] to cope with the corrosive nature of high temperature eutectic salts as PCM. The stability and performance of the system proved to be acceptable.
The impact of nano-particles of Al_2O_3 in the melting of wax as PCM was investigated in an experimental work by Ho and Gao [81]. The LHTES system was a cavity filled with PCM and the side walls were kept at different hot and cold temperatures. For a 10% (wt) of Al_2O_3, the results showed more than 60% reduction in the convection heat transfer rate which outweighed the benefit from the enhancement of conduction heat transfer. Adding nano-particles of graphite to a macro-encapsulated PCM (i.e. capsule diameter of 5 cm) was experimentally and numerically investigated by Calvet et al. [29], using COMSOL. For a 13% (wt) graphite load, the authors reported 35% - 58% reduction in charging and discharging time without any reduction in the thermal storage.
Shell and tube heat exchangers have been investigated as a promising LHTES alternative, both from the effectiveness and manufacturing and maintenance point of view. Most of the research in this area has explored the impact of extension of heat transfer surface by fins, or other methods. For instance, in a numerical study by Sciacovelli et al. [82] and an experimental study by Rathod and Banerjee [31] longitudinal fins were proposed to be a good compromise for low thermal conductivity PCMs to enhance heat transfer rate. Moreover, in a numerical study, Tay et al. [83] examined the impact of pinned and finned tubes on the thermal performance of a PCM in tank system compared with a bare tube in the PCM.
Extending the tube surface carrying the HTF has also been a subject of interest. In a numerical attempt Basal and Ünal [45] suggested a triple concentric system in which PCM is filled in the middle and HTF flows through the inner and outer tubes. Aiming for a higher surface-to-volume ratio and therefore higher heat transfer performance, Languri et al. [84] proposed a configuration of six corrugated copper plates which contains PCM in square enclosures and are attached at a 60 degree angle to the pipe with the HTF. Comparing the results of their study with another study, the authors reported faster response (°C/s) during the sensible heat storage, e.g. nine times faster compared to a multi-tube arrangement. However, the amount of heat source in the two compared arrangements were not the same.
All of the above methods to extend heat transfer area reduce the PCM volume fraction which results in less energy storage density, add complexity and cost of the system. Other techniques have been proposed such as cascade PCMs, hybrid PCMs, heat pipes and thermosiphons as well as methods to enhance natural convection in the liquid zone.

2.3.1.2 Cascade PCMs

In a numerical study, Li et al. [85] investigated the melting process of three PCMs with different melting temperatures confined in a shell along a tube with air as the HTF. Through a parametric analysis while ignoring natural convection, the authors proposed an optimised design of a LHTES to be used in a CSP plant. In another numerical study using Fluent, Wang et al. [86] proposed a multi-PCM system in conjunction with a zigzag passage for air as the HTF to extend the heat transfer surface between the HTF and PCM. Liu et al. [25] recently studied a three-PCM system integration in a sCO_2–Brayton cycle. Using the analytic method ε-NTU [17] and CFD modelling, the results of the study showed higher effectiveness for the extraction of sensible heat for the cascade system.
Li et al [87] provided an exergy analysis of a loop including a system of solar collector-receiver and a LHTES system comprising of two PCMs during a charging process. Results of the study showed exergy efficiency improvement about 19%-53.8% compared with a single PCM system. The authors proposed a range of melting temperatures of 1000-1150 K and 750-900 K for the PCM1, 2 for the CSP application. Xu et al. [88], provided a similar study with a system of three PCMs (1, 2 and 3). Considering two different pipe lines passing through the cascade system with different HTF, they studied the charging and discharging inlet temperatures of HTFs, the NTU of each pipe line in conjunction with the optimal melting temperature for each PCM to achieve the highest exergy efficiency. Overall, results show that increasing the inlet temperature of HTFs improves the exergy efficiency of the whole cycle. For CSP plants, a range of 800-1200 K and 350-400 K were suggested for charging and discharging inlet temperature of HTFs. Higher NTUs enhances the exergy efficiency of the system up to a figure of 5, while a range of NTU= 4-5 for PCMs 1, 2, 3 is suggested for the CSP applications.

2.3.1.2 Hybrid sensible –PCMs

A packed bed of rocks as a sensible heat storage medium in direct contact with air as HTF for high temperature air-based cycles has been the subject of interest for instance by Hänchen et al. [89] and Zanganeh et al. [90], and using α-alumina beads as a TES medium and compressed air as the HTF by Andersson et al. [91]. To achieve a

higher performance, a hybrid system of packed bed and encapsulated $AlSi_{12}$ as the PCM has been proposed by Zanganeh et al. [92]. The proposed system adds a layer of (9 cm) encapsulated PCM at the top of a column (diameter=40 cm, height= 127 cm) of rocks with mean diameter of 3 cm to stabilise the outlet air temperatures at 575 °C and higher. The experimental and numerical investigation showed that the air outlet temperature can be stabilised at the melting temperature of PCM.

Applying a new hybrid SHTES-LHTES concept, Zauner et al. [93] experimentally and numerically investigated a shell and tube system where high density polyethylene confined in tubes as the PCM and thermal oil passes through the shell and acts as the HTF as well as sensible heat storage medium. The techno-economic assessment showed the feasibility of the system to respond to peak load in a district heating system or where waste heat is available for instance in aluminium casting where high temperature heat is released through the cooling and solidification of aluminium. Moreover, the authors mentioned the flexibility of the system to deliver different ratio of SHTE/LHTE by different sizes of tube diameter and/or number of tube; e.g. fewer tubes or smaller diameter for higher rate of sensible heat.

2.3.1.3 Heat pipes and thermosiphons

A numerical investigation by Nithyanandam and Pitchumani [94], studied the impact of embedded thermosiphons on the thermal behaviour of PCM in a LHTES system. Using Fluent, modelling of the charging and discharging processes was performed to find the optimal arrangements of tubes and heat pipes with improved effectiveness. In another experimental and numerical effort, Malan et al. [95] proposed the integration of both heat pipe and metal fins as a solution to enhance the performance of LHTES systems. In a numerical study by Almsater et al. [96] using a MATLAB code from Shabgrad et al. [97] and Fluent [35], the benefits of including finned heat pipes in a LHTES compared with the bare heat pipes were investigated. The results of the study showed that adding four axial fins to the heat pipes increase thermal storage and heat delivery during the first 3 hours by 106% and 79% in melting and solidification processes, respectively. Moreover, considering the combined effect of evaporation and condensation in the heat pipes showed threefold and fourfold enhancement of thermal performance of the system during charging and discharging, respectively. From the results of the parametric analysis, the authors suggested that in between the length, HTF mass flow rate and tube outer diameter, evaporator and condenser length, vapour core diameter (in the heat pipe), and fin height, the most influential parameter is the evaporator length.

Recently, Naghavi et al. [98] published a comprehensive review of experimental and computational investigation in the field of hybrid systems of heat pipes and LHTES systems, HP- LHTES. The authors concluded that, the hybrid system enhances the shortcomings of individual systems; the overheating problem with the heat pipes and low thermal conductivity of PCMs. A higher thermal efficiency has been reported for both low and high temperature storage system using solar thermal energy, however a full techno-economic assessment is necessary for a particular application due to complexity of the hybrid system. The proposed computational methods in the related literature were one or two-dimensional where natural convection effect was not considered. The authors suggested that three-dimensional impact and natural convection effects should be considered in future work.

2.3.2 Convection heat transfer enhancement

The literature in the scope of impact of different configurations and orientations on the convection heat transfer is reviewed in section 2.2, covering different LHTES configurations and orientations. Here, two specific methods proposed recently to enhance natural convection and performance of a LHTES system are reviewed.

2.3.2.1 Dynamic melting

In a numerical study, Tay et al. [99] investigated the effect of dynamic melting (e.g. recirculating the melted PCM) on the melting front evolution and heat transfer rate for the cases of the parallel and counter flow arrangement in an element of a tube bundle in PCM. They found an enhancement of heat transfer between 15-80% and a decrease in phase change time for the cases where the flow rate of the recirculating liquid PCM is equal or greater than that of the HTF. This was related to the mixing effect of PCM on changing the melting front from one to two-dimensional leading to a shorter time for the melting process. The authors reported a higher rate of heat transfer for the case of counter flow; however, for the cases of higher flow rates of liquid PCM, the performance of parallel and counter flow arrangements was the same.

2.3.2.2 Resonance

Collectively, all above studies advance the understanding of the heat transfer characteristics of the phase boundary and potentials to enhance heat transfer with or without additional material. However, they apply either a fixed HTF inlet boundary condition or a wall at fixed temperature/ heat flux. A periodic flow boundary condition applied to the inlet represents a novel approach to enhancing heat transfer using the existing design of a tube

bundle. The impact of pulsed flow of the HTF on temperature boundary condition at the tube wall will impact the phase boundary. The initial inspiration for the research presented in this thesis on periodic boundary condition was the need to improve the heat transfer performance in PCM storage systems. The literature shows that limited studies have been conducted with PCMs considering periodic boundary conditions and its impact on the melting and solidification processes in a PCM system. However, the impact of a periodic boundary condition on natural convection in single phase fluids has been well studied.

Finding correlations between the frequency of periodic boundary condition and resonance of natural convection has been a major subject of research. Lage and Bejan [100] numerically and theoretically studied the resonance of natural convection in a square cavity with periodic heat flux imposed on one side, a fixed cold temperature on the other side and insulation on the top and bottom. A steady oscillatory regime was reported after transient fluctuating heat transfer in all cases. Numerical results revealed the resonance of natural convection to a specified frequency of pulsating heat flux, i.e. highest amplitude of oscillatory heat transfer. For three different cases with Pr= 0.01, 0.7 and 7, the resonance of heat transfer was reported at Ra= 10^9, 10^8, 10^7, respectively. From scale analysis, the authors suggested a correlation between the resonance frequency, Ra and Pr.

In another investigation, Antohe and Lage [101], theoretically and numerically studied the impact of amplitude of a pulsating heat flux on free convection heat transfer in the same enclosure as the previous study [100]. Results showed that the amplitude of the periodic heat flux boundary condition affects the amplitude of oscillatory heat transfer but has no impact on the resonance frequency of convection heat transfer. For the same case as previous studies [100, 101], Antohe and Lage [102] numerically studied the effect of Pr (e.g. Pr=0.01, 0.7, 7) on the resonance of natural convection. The results revealed the highest amplitude of oscillatory natural convection heat transfer for Pr~1 and the damping effect of higher or lower Pr in two other cases while other parameters, including Ra were kept the same. This was expected as in the cases of high viscosity (high Pr) or very low viscosity (low Pr and high thermal diffusivity), natural convection is not the prevalent mode of heat transfer.

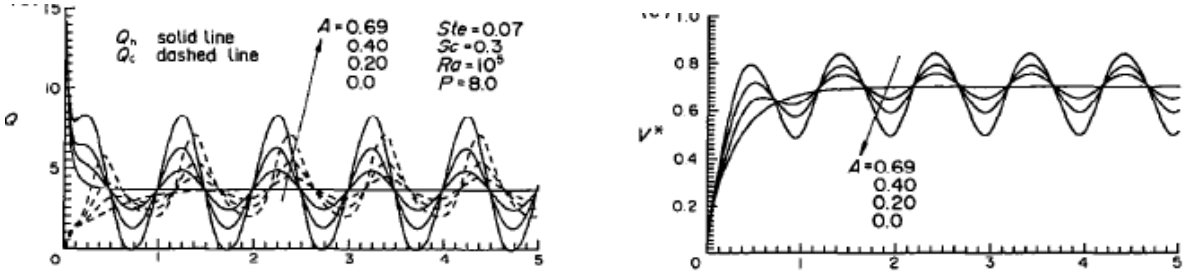
The authors of the above three studies [100-102] did not explicitly discuss the effect of pulsating heat flux on the mean heat transfer rate, however, in an experimental investigation, Antohe and Lage [103] investigated the mean heat transfer rate correlation with the period of pulsating heat source and Ra in the same geometry filled with water. They found that at moderate frequency of a pulsating heat source, the time-mean heat transfer coefficient increased by about 20% compared to steady heating with the same time-mean heat flux whereas a very high frequency decreased the heat transfer rate.

Kwak et al. [104] numerically studied a case of sinusoidal varying temperature imposed on the side wall of a square cavity with a cold temperature at the other wall while the top and bottom were insulated. The impact of the different amplitude and frequency of the periodic boundary on the mean heat transfer and the amplitude of oscillatory convection heat transfer were investigated for the case with Pr= 0.7 and Ra=10^7. Results showed that for a smaller amplitude of periodic heat source, the amplitude of oscillatory heat transfer is linearly dependent while for the larger imposed amplitude a nonlinear correlation was recognized. Interestingly, for lower implemented amplitude of heat source, no gain in time-mean heat transfer rate is delivered while for higher amplitudes at a moderate frequency, heat transfer increased nonlinearly. The authors found that time-mean heat transfer can be maximised at a moderate frequency in a band close to the resonance frequency.

Roslan et al. [105] numerically investigated the thermal behaviour of a fluid in a cavity under the impact of a sinusoidal heated cylinder in the centre while the sides were kept at a fixed cold temperature. Considering the frequency of sinusoidal heating temperature and radius of the cylinder, improvement of heat transfer was realised within a range of frequency and amplitude of oscillating temperature and radius of the cylinder.

In the previous studies in the scope of periodic heat source boundary conditions, the impact on natural convection and response to different oscillatory heat source frequencies and amplitudes with different Pr, Ra and Ste numbers were considered. Summarising the results of the literature reviewed in this field, control or enhancement of natural convection is possible by implementing an oscillatory heat source boundary condition at a specific amplitude and frequency close to the resonance frequency. Obviously, this is possible in cases where natural convection is a dominant or a major heat transfer mode; Pr~1 and high Ra.

Limited research has applied a periodic boundary condition to phase change processes. Ho and Chu [106] numerically studied melting of tin (Pr=0.0157) in a vertical enclosure with sinusoidal hot temperature at one side, fixed cold temperature at the other side, and adiabatic boundary conditions elsewhere. They studied the impact of subcooling (cold temperature), Ra, frequency and amplitude of the periodic boundary condition at the hot wall on the melting process with natural convection. Despite the amplification of the heat transfer rate, the steady mean values of the heat transfer rate and melt fraction did not change (Fig. 2.4).



(a) (b)

FIGURE 2.4. Temporal variations versus dimensionless time: (a) dimensionless heat transfer rate from hot side (Q_h) and cold side (Q_c), (b) melt fraction [106]

In another study [107], Ho and Chu studied the ice periodic melting in the same case as the first study. To investigate the density inversion phenomenon of water at about 4 ºC, they studied two cases of Ste=0.051 and 0.101 related to the average temperature at the hot wall equal to 4ºC and 8ºC, respectively. Results of the steady oscillatory regime showed the mean value of heat transfer and the melting rate increased with the higher amplitude of pulsating temperature imposed on the hot wall for Ste=0.101 while the opposite occurs for the case of Ste=0.051, due to different flow evolution in the region between the phase front and hot wall. For higher frequencies, the mean value of melting rate decreased while the mean value of heat transfer was almost constant. In a numerical analyses, Krishnan et al. [108], studied the impact of a pulsed heat source on the evolution of the melting front of a PCM with and without metal foam in a rectangular container. Including the influence of Ra, Ste and the frequency of the pulsed temperature (above and below the melting temperature of PCM), the study showed a profound impact on the PCM melting process for a pulse period > $Ra^{-0.25}$/Ste.

In all the previous studies in the scope of periodic boundary condition, the amount of heat provided to the system was changed periodically, so that a fixed temperature or heat flux was not applied to the system. However, in many real applications, periodically changing the amount of heat exposed to a system is not practical.

2.4 Thermodynamic analyses, first and second law

The investigation of different configurations of LHTES systems to understand the heat transfer between the solid and liquid at the phase front provides the required knowledge to determine the optimum design from the first law analysis and highest effectiveness for each application. In all the studies above, the performance of different configurations of LHTES systems from the heat transfer and heat storage perspectives (e.g. first law analysis) were assessed. While the above mentioned studies cover the first law analysis at the component level, the whole system including the solar field and power block can be studied from the same perspective.

For a full picture, comparative analyses of the entropy generation of different arrangements should also be included. There has been some research effort in the scope of entropy generation analyses, providing insight in its calculation and/or minimisation [109-113]. The second law analysis can be conducted at the level of the whole cycle (e.g. from the receiver to the LHTES system and to the power generation cycle) or at the component level, e.g. LHTES system only. At the component level, and in addition to the heat transfer analysis, designing an optimal LHTES requires a thermodynamic analysis of the whole cycle of charging and discharging [39]. In this approach, both first and second-law analyses should be covered. The irreversibilities due to the heat and mass transport and viscous dissipation affect the performance of LHTES systems just like many other thermal systems. In cases of laminar flow, irreversibility generation due to viscous dissipation is negligible in comparison to the heat transfer [111]. Entropy, a thermodynamic property quantifies such irreversibility and provides a means for the second-law analysis of the system to realise the limits and also enhancement opportunities [109]. In a study by Segal [13], considering three subsystems as the solar field, receiver, and a power block based on a gas turbine, efficiency depends on three interdependent factors; concentration ratio of solar field, average temperature of the receiver and pressure ratio of the gas turbine. Increasing the concentration ratio decreases the efficiency of the solar field while increasing the efficiency of the receiver. Increasing the average temperature of the receiver while decreasing the receiver efficiency results in a higher efficiency of the power block. Thus, there is a need to find an optimal receiver temperature in conjunction with the optimal pressure ratio of the gas turbine (for a single Brayton cycle or a combined cycle) for the highest concentration ratio at the solar field. The analytical study showed that a range of 1200-1300 K to be the optimum receiver temperature. The result of a recent study by Ho et al. [27], showed the same trend that for each concentration ratio, thermal efficiency of the receiver decreases as its temperature increases. Integrating TES to this cycle adds more complexity; finding the optimal compromise conditions at each component level and the whole cycle. There has been some research efforts to find the impact of the receiver temperature as the HTF inlet temperature during charging, melting temperature of PCM, the

number of transfer unit (NTU) of TES, and other parameters on the optimal configuration. The more relevant studies are discussed in the following.

In a numerical study, Wang et al. [16] compared the thermal performance and energy density aspects of the SHTES and LHTES systems. Results showed that LHTES systems provide a much higher energy density, leading to a smaller size for the same storage capacity compared with a SHTES system. However, the focus of this study is the comparison of the exergy destruction aspects of the systems.

In an early attempt, Bejan [38] studied thermodynamic aspects of designing a sensible heat storage system. Using a simple liquid pool heated by a hot gas flow (which is released to the environment afterwards), a number of irreversibility unit (N_I) was introduced as the ratio of destroyed useful work to the maximum available work. The main contributions to N_I being; pressure drop through the pipe carrying the hot gas and the heat transfer due to finite temperature difference between two fluids. The two aspects of optimisations were proposed to be; an optimum storage time beyond which the rate of charging decreases, and an optimum NTU beyond which useful work destruction increases due to higher pressure drop. However, for all NTU and temperature differences between the hot gas and environment, the optimum design can be achieved for a dimensionless time = mc_pt/MC ~1, where mc_p is the mass flow rate and specific heat of the hot gas, MC is the heat capacity of the liquid bath, and t is the charging time.

Using a simple model where a hot gas comes in contact with a solid and exits the system to the atmosphere, De Lucia and Bejan studied the thermodynamics and entropy generation in melting [114] and in the whole cycle of melting and solidification [39]. The focus of both studies was to find an optimum melting temperature for the PCM to minimise entropy generation. The result of the first study [114] showed the geometric average of the hot fluid and environment temperatures as the optimum melting temperature ($(T_h T_e)^{1/2}$. Moreover, considering a melting process through a pure conduction process, the results showed entropy generation increases with time (different from sensible heat storage, reaching a minimum), decreasing smoothly with a higher temperature heat source and sharply by the higher number of heat transfer unit (NTU). During a convection dominant process, entropy generation is independent of the time with the same dependency to the heat source temperature and NTU. However, an interesting result was that with a large enough NTU, about 50% of the thermal energy can be stored in the PCM.

Results of the second study[39], showed that the proposed optimum melting temperature [114] is correct when Ste→0 and it is smaller in other cases of melting. During the solidification stage, entropy generation increases smoothly with time while it decreases with higher NTU and melting temperature of PCM. Overall, the higher melting temperature and NTU with lower time of phase change process result in lower total entropy generation.

Comparing energy and exergy aspects of sensible and latent heat storage, Bjurstörm and Carlsson [115] provided a parametric analysis. They found little difference between the energy and exergy efficiencies of the two storage systems. The results did not show higher energy or exergy efficiency for the LHTES while the benefit of higher energy density provides a smaller system. An economic evaluation was not included in the study.

Considering the growth of interest in latent heat storage in recent years and research in this area, Jegadheeswaran et al. [112] provided a comprehensive review of the related literature. Through this work, the major correlations for the calculation of energy and exergy efficiencies of a CSP cycle including a LHTES system were collected from previous studies. The collective conclusion states that, for the HTF, higher Re (higher velocity) with lower temperature difference between HTF inlet temperature and melting temperature of PCM result in lower entropy generation in both processes. However, this result is not conclusive as the higher pumping power for a higher Re was not included in those studies. While a geometric average of the HTF inlet temperature and environment has been suggested as an optimum melting temperature in some investigations, an arithmetic mean of the temperatures is a better estimate regarding the whole cycle of charging and discharging. Exergy loss increases exponentially with NTU while it rises linearly with the pressure drop.

Guelpa et al. [111] investigated the performance of a LHTES system on the basis of the first and second law of thermodynamics. Using an annulus, PCM filled the outer pipe with HTF flowing through the inner pipe (with and without fins), they studied the time evolution and spatial distribution of entropy. Using FLUENT [35], modelling the solidification process of a type of wax, results showed that using fins to improve heat transfer rate generates higher irreversibility but due to a higher rate of exergy release, the entropy generation reduces by about 5%. The authors suggested that the study of the local entropy distribution might assist in geometry and fin arrangement improvement, i.e. towards a more uniform entropy generation to achieve lower solidification time. For instance, a case with double the number of fins and half thickness of each fin (fixed total volume of fins) resulted in a 16% reduction in solidification time without impact on entropy generation. Furthermore, non-uniform distribution of fins (lower fin spacing towards the top of unit) along the pipe length resulted in reduced entropy generation without any effect on the rate of energy release and solidification time.

Shabgard et al. [113] provided a thorough first and second law analysis of a typical LHTES for CSP application, studying ten variables and operating parameters involved in the designing of a LHTES. Assuming a 1-D heat transfer, they developed a mathematical model for the charging/discharging cycle while considering two practical constraints: (i) equal stored and recovered thermal energy, and (ii) 24 hours as the total time of charge-discharge

cycle. The analysis resulted in eight independent and two dependent variables. Using the model to optimise the stored energy in the LHTES and the exergy recovery during the discharge process, results showed that a higher HTF inlet temperature achieves higher optimal energy stored and exergy recovery during discharge. Moreover, for the range of non-dimensional charging inlet temperature of HTF (T_{nch} =T_{ch} /T_e) equal to 1.5, 2, 3, 4; while the discharging non-dimensional temperature (T_{nd} =$T_{dc,}$/T_e) is equal to 1, the optimal storage achieved by non-dimensional melting temperature ($T_{nm,opt}$ =T_m/T_e) equal to 1.35, 1.8, 2.55, 3.45, respectively. However, for the maximum exergy recovery with the same range of T_{ch}, results showed T_{dc} should be in the range of 1.27, 1.55, 2, 2.4 in conjunction with the $T_{nm,opt}$ being equivalent to 1.4, 1.85, 2.85, 3.7, respectively. This result proposes a higher optimal melting temperature to achieve higher exergy recovery compared to the geometric and arithmetic means of the environment and HTF inlet temperature. For instance in case of T_{ch} = 923 K, T_{dc} =750 K and T_e=288 K, results in $T_{m,opt}$=806 K compared to the geometric mean; $(T_{ch}\,T_e)^{1/2}$=515 K and arithmetic mean; $(T_{ch}+T_e)/2$ = 605.5 K. Moreover, results of the study showed that a ten-fold increase in the PCM surface area resulted in a six times higher exergy recovery.

All of the above studies considered first and/or second law analyses of a thermal storage system as a component working in different cycles including for solar thermal power generation. However, there have been research efforts in the scope of thermodynamic and thermo-economic investigations of cycles with integrated thermal energy storage. Rezaie et al. [116] studied the energy and exergy characteristics of a seasonal sensible heat storage (water, 12000 m^3) integrated in a district heating system. In between the charging and discharging stages, a storing stage was considered as the mixing process of the high and low temperatures in the large tank destroys part of the available exergy. Using the collected data for a typical year (2006), and assuming uniform temperature throughout the tank, the results showed 54% and 25% as energy and exergy efficiency for the charging stage. Moreover, 86% and 50% were the energy and exergy efficiencies for the discharging stage and 60% and 12% for the whole cycle of charging, storing and discharging. The results of the analytical study were in good agreement with the collected data from the operating district heating system.

Providing a holistic exergy analyses, Mafuz et al. [117] studied a parabolic trough pilot plant in Iran. Oil as the HTF generates steam for the turbine. Using four different PCMs with different melting temperature and latent heat of fusion, they compared the performance of the cycle with and without a PCM storage system. With the HTF inlet temperature equal to 265 °C, results showed 9.25% exergy efficiency of the collector-receiver without a heat storage system while about 21% enhancement of the cycle efficiency for a PCM with melting temperature equal to 250 °C, and about 17% for a PCM with 191 °C melting point.

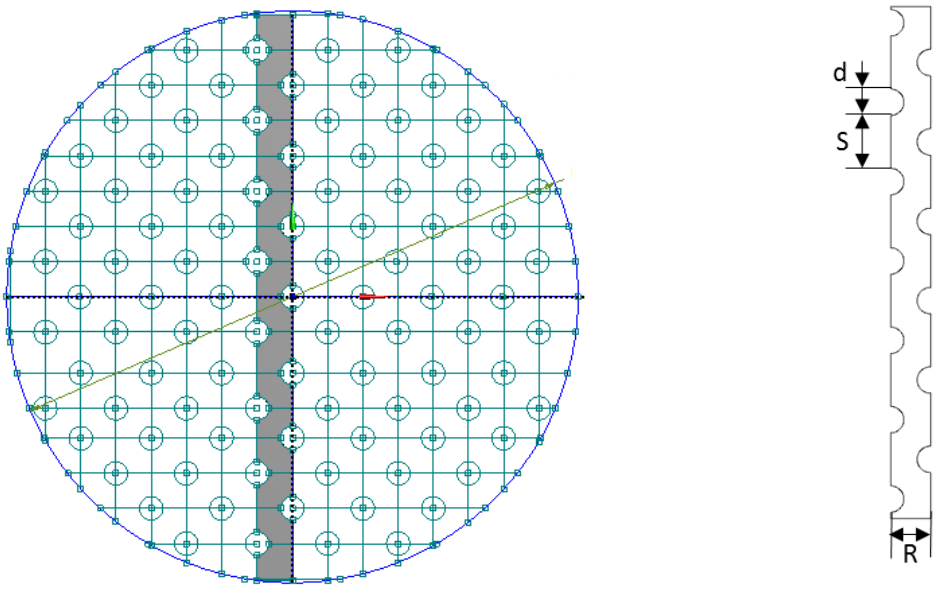
The literature in the area of exergy analysis of a CSP cycle including a TES lacks a comparison between SHES and LHTES systems in conjunction with the alternative HTFs (e.g. supercritical CO2 (sCO2) and liquid sodium) and PCMs (e.g. high temperature molten salt and aluminium). A team including the author of this thesis has studied such a comparison (work included in a journal paper currently under review), including the losses due to the receiver and pumping components while comparing different cycle capability to recover exergy against the maximum theoretical efficiency of the Carnot cycle.

2.5 Design and optimisation

In the scope of geometrical aspects of a LHTES system, a range for effective length of tubes (e.g. in a parallel configuration), the ratio of the tube length to diameter, and the spacing have been proposed in the literature [118-120]. This includes non-dimensional length, L/d = 10 - 80, and radius R/r = 1.3 - 4, where L is one pipe length, r and d are the outer radius and diameter of a pipe, respectively. R equals half the centre to centre distance of the two adjacent pipes, representing the PCM radius and relates to S as the spacing between two closest pipes; 2R= S+d (Fig. 2.5).

In an earlier numerical modelling and parametric analysis by Neagu and Bejan [121], the authors proposed the optimised distribution of high thermal conductivity material (in the form of 2-D plates and 3-D pins with fixed volume fraction, Ø) to achieve the highest heat flow through a low thermal conductivity fluid flow. Conduction heat transfer was considered in a vertical orientation while plates/pins are heated from the sides. The authors proposed correlations for the optimisation of the thickness/diameter, height and distances between plates/pins for the particular range; $Ø_{plate/pin}$ = 0.01-1, $k_{plate/pin}/k_{fluid}$ = 10^2-10^4. Overall, the results showed that in the specific studied cases, the pin inserts presented less global resistance compared with the plate inserts. The authors suggested that the simple optimisation results from their study can be used for a preliminary design of such a system. Regarding pins with cylindrical shape, the proposed graphs can be used for an estimate of pipe spacing in a shell and tube case.

Recently, in an analytical and numerical study by Wang et al. [120], a parameter was proposed to assess the performance of a LHTES system comparing the heat storage and pumping power, namely energy efficiency ratio. Through the parametric analysis, the authors suggested that a laminar flow of HTF provided higher energy efficiency ratio. This is to be expected as a lower velocity results in lower pressure drop and lower pumping power, however a higher Re provided a higher rate of heat transfer at the cost of higher pumping power. Using an effective thermal conductivity (considering the impact of natural convection in PCM with a 1-D phase front), the



(a) (b)

FIGURE 2.5. Schematic drawings: (a) cross section of a shell and tube system, (b) a two-dimensional sectional model, PCM confined between tubes conveying HTF and referred dimensions

results showed that energy efficiency ratio decreased as the L/r ratio increased from 50 to 300, and R/r increased from 1.3 to 5. On the other hand, the heat transfer rate increased with the higher L/r ratio and decreased with thehigher R/r ratio, (e.g. high sensitivity to the tube outer diameter). A higher inlet temperature of HTF enhances the heat transfer rate (e.g. shorter duration of melting process), however it has a minor impact on the energy efficiency ratio.

Developing a heat transfer model and validating it with other numerical and theoretical models from the literature, Tehrani et al. [119] performed a wide range of parametric investigations. An element of a shell and tube LHTES system (an annulus with HTF in the inner tube and PCM confined in the shell) was selected for the study, considering conduction heat transfer and 1-D phase front. Aiming for a high temperature thermal storage system, T_h=565 ˚C and T_c=286 ˚C, the required volume for a sensible heat storage and four different types of PCM were proposed for alternate heat storage/release of 111 GJ (30.8 MWh_{th}) during 10 hrs. Comparing the size of the storage medium for the sensible and latent heat systems, up to 70% reduction was found using PCM. Considering the R/r = 1.3 – 3, the results showed the best performance with the highest stored energy occurring at the lowest ratio, 1.3, however, increasing the non-dimensional length, L/d from10-100 provided the higher amount of stored/ released heat for all PCMs regardless of L and R/r. For smaller R/r, increasing L/d is more effective to optimise the system while in general the study suggests lower R/r and higher L/d to enhance the thermal performance of a LHTES unit. Aiming for the highest heat storage/release capacity with the minimum heat transfer area, and a laminar flow of HTF, the authors suggested 36 -63 m^2 of heat transfer area per GJ for four different PCMs, being 45 m^2 for the molten salt with L/d = 60, R/r = 1.3 and L=5 m. To calculate the number of pipes, dividing the volume of the system by the volume of one element (annulus), the authors proposed a correction factor for each type of PCM, being 0.8 for the molten salt. Nonetheless, the generalisation of the qualitative results of the study is valid for a laminar flow at the HTF side.

Overall, assuming conduction heat transfer as the dominant mode and/or 1-D phase front, the results of those studies provide a first estimate and are more accurate for a design process based on the discharging process through which those assumptions are valid. However, regarding the melting process as the design and optimisation basis when ΔT_{ch} (20-50 ˚C) < ΔT_{dc} (100-200 ˚C), convection heat transfer needs to be considered. Limited studies can be found in the scope of optimisation of spacing between heat transfer elements (e.g. tubes) in the presence of natural convection. Regarding an optimal architecture for an array of heat transfer surfaces such as plates/fins/pins or tubes distributed in a fluid, Bejan and Lorente [122] proposed an analytic method to find the intersection point of large and small spacing asymptotes as a tradeoff between flow and thermal resistances. For the optimal spacing between parallel plates (S_{opt}) confined in a fixed volume (fixed L, W, H), they proposed correlations to achieve the highest heat transfer density, balancing fluid flow resistance and heat flow resistance. Bejan et al. [123] by experimental, analytical and numerical studies, and Bejan and Lorente [122] by an analytical study, proposed correlations for the optimal spacing between tubes in a horizontal staggered arrangement of pipes confined in a fixed volume (fixed L, W, H) for the highest heat transfer density to/from the tube bundle in a cross flow. From the results of the studies, dimensionless groups and/or correlations were proposed for the optimal

spacing, and maximum thermal conductance. In those correlations, two Ra numbers are accounted for, Ra_H as the global order of natural convection while Ra_d presents the impact of tube diameter on the local boundary layer which is important in a horizontal orientation of the tubes. The authors provided a derivation for the total number of tubes in the staggered tube arrangement for a preliminary design.
While natural convection is involved in the above optimisation studies, phase change process is not considered. In the above optimisation studies either a phase change process with conduction heat transfer with 1-D phase front were assumed [118-120] or natural convection without phase change was included [123]. The main lesson from those studies is that relatively closer spacing (e.g. the lower limit of R/r = 1.35- 4, [118]) provides higher conduction heat transfer while relatively wider spacing between heat transfer elements (tubes, plates, pins or fins) provides higher rate of natural convection heat transfer.
In two numerical studies, Esapour et al. [124, 125] investigated the melting process in a shell with diameter equal to 9.5 cm filled with wax as PCM while considering four cases with 1, 2, 3, 4 tubes carrying water as HTF. The amount of PCM and total mass flow rate of HTF were considered the same in all cases. Results of the first study showed more tubes increasing heat transfer area and reducing melting time. The same effect was achieved with higher temperature of the HTF. Through the second study, different arrangements of the tubes inside the PCM were explored. For instance, the longest melting time when all four tubes were located at the upper half of the shell and in the case where tubes are located at the bottom half, the melting time is the shortest. While these studies provide some general insight into the melting process, however they are not helpful in the optimisation process where narrow ranges of tube spacing/sizes need to be examined.

Designing a LHTES, the system should be capable of storing the required thermal energy in the PCM during the available time (upstream criteria) and delivering sufficient heat transfer rate to HTF during the required time (downstream criteria). Considering those design criteria in high temperature cases for CSP application, the temperature difference between HTF and melting temperature of PCM is expected to be low (e.g. <50 K) during charging in comparison to a higher temperature difference available for the discharging process (e.g. >150 K). These conditions require design of a LHTES system constrained by the melting process and adjusting it to the discharging criteria.
From the optimisation point of view, the objective is to find an optimal system with the highest thermal conductance and lowest flow resistances (e.g. both in HTF and PCM zones), considering conduction, natural convection, and phase change phenomena. This requires a compromise between highest effectiveness (first law efficiency) and lowest entropy generation or highest exergy recovery (second law performance). Moreover, a higher volume fraction of PCM is desirable, leading to a higher storage density, smallest size and least cost of the system.

2.6 Research gaps and opportunities

The above thorough literature review shows the significant research effort in the area of LHTES and related fields. Providing a cost effective thermal storage system mainly for CSP application is a very important and urgent matter from different aspects as explained in chapter one. Concluding from the literature review, there is no reliable and thorough method for the design and optimisation of a LHTES system particularly for high temperatures/pressures that are in demand for high efficiency power cycles Here, a summary of the research gaps, opportunities and research work necessary to fill the gaps through this thesis follows.
There has been limited investigation on the impact of turbulence in the melted PCM during the melting process (section 2.1). Considering the importance of natural convection and turbulence in the charging process of heat storage systems, numerical investigations can provide insight into the effect of natural convection and turbulence on the temperature and velocity fields, heat transfer area and rate, and duration of the phase change process.

As mentioned in section 2.2.1 there is a lack of comparative study on the phase front evolution during a phase change process of a high temperature PCM in a shell and tube heat exchanger in different configurations.
The impact of the tube-PCM boundary condition on the phase front evolution, temperature and velocity profiles, heat transfer rate, phase change time and effectiveness of different configurations should be investigated.

From the literature review in section 2.2.2 limited knowledge was found on the thermal performance comparison of different shell and tubes and plate/rectangular configurations as LHTES systems. Considering the broad applications of LHTES systems, particularly for CSP plants, there is a research opportunity to find the potential and capabilities of different configurations for different applications of LHTES.

The methods mentioned to increase heat transfer area (section 2.3.1.1) results in reducing the PCM volume fraction leading to lower thermal storage density, higher complexity and cost of the system. There is a need for solutions that exploit the inherent potential of PCMs to improve heat transfer and other aspects of thermal

performance such as less entropy production. Techniques that can enhance natural convection need to be examined. A search for methods to enhance natural convection is part of this thesis, included in chapter 5.
The literature review detailed in section 2.3.2.2 showed that implementing periodic boundary conditions to enhance natural convection in a single or double phase system with a fixed temperature or heat flux can add new knowledge in this scope. This thesis aims to use the periodic boundary condition concept to tube bundles, advancing the knowledge into heat transfer enhancements through manipulating the boundary conditions.

The last section of the literature review (2.5) revealed that there is a research opportunity in the scope of designing and optimisation of PCM system to propose a procedure including the numerical modelling in different steps.

Summarising the literature reviewed, the following gaps require research investigations:

- ***There is a need for a validated numerical model to explore the thermal performance of high temperature PCMs (300 ℃-850 ℃).***
- ***To achieve the required accuracy from numerical modelling with less computational time, a suitable scale down approach needs to be found leading to an appropriate two and three dimensional model scale.***
- ***Impact of natural convection and turbulence on the temperature and velocity fields, heat transfer area and rate, and duration of the phase change process should be examined.***
- ***Thermal performance of different configurations of shell and tube LHTES systems including parallel and counter flow in horizontal and vertical orientations should be examined to suggest suitable ones for different applications with different requirements.***
- ***Thermal performance of fin plate rectangular LHTES systems as an innovative configuration for high efficiency CSP cycles (requiring high operating temperature/pressure) needs to be investigated.***
- ***To exploit inherent potential of LHTES systems, the impact of a periodic boundary condition at the tube/PCM interface needs to be studied in systems with constant heat source/sink.***
- ***There is a need for a design and optimisation procedure including the role of numerical modelling. There is a gap in the related literature of design and optimisation, accounting for both the phenomena of natural convection and phase change with the highest volume fraction of the PCM.***

3 Numerical modelling

In general, experimental investigations are time consuming and expensive to run in comparison to numerical modelling. Experimental investigations involving high temperature material or hazardous conditions are even more difficult to implement. In the field of PCMs, there have been experimental studies of materials with melting temperature up to 50°C for different types of geometries such as a square cavity [126], a sphere [46], and a cylinder [40]. Recently, there have been efforts to study PCMs with a higher melting/fusion temperature, such as a flat plate LHTES experimental setup with working temperature up to 300°C which was designed and operated by DLR [64]. Vogel et al. [65] used the experimental results from [64] in validating a numerical study (using FLUENT) of melting and solidification of a mixture of potassium nitrate (KNO3) and sodium nitrate (NaNO3) with a melting temperature of 219.5°C.

Experimental studies provide a real and practical insight in each field, however, using a validated numerical model by experimental data provides an opportunity to explore many more cases as well as undertake parametric studies. The knowledge gained in conjunction with dimensional analysis can be used for the design and optimisation of a system for a specific application. In the case of LHTES systems including charging by melting PCM and discharging by solidifying PCM, the thermal performance of different combinations of PCM/HTF in different configurations such as shell and tubes and plate heat exchangers can be explored by validated numerical models. The melting process involving conduction, natural and forced convection is more complicated compared with the solidification process which is mainly dominated by conduction in the PCM domain and forced convection in the HTF domain. Thus, a comparison of the predicted results for a melting process is sufficient for the validation purpose of a model. In this chapter, a numerical model is set for the melting and solidification processes in two and three dimensional cases and the predicted results are validated with available experimental data. Then, the model is used to understand the transport phenomena including laminar and turbulent convection.

3.1 Computational fluid dynamics

Analysing fluid dynamic problems including transient cases require solving the Navier-Stokes equations. Apart from some simple cases in fluid mechanics, analytical solutions of the Navier-Stokes equations are not available and numerical solutions are the practical choice. Computational fluid dynamics (CFD) provides a virtual laboratory to explore different problems and provide the necessary solutions. The validation of numerical studies generally relies on experimental data, and the lack of data for high temperature PCMs might affect the development and confidence in using reliable numerical models. It has been suggested that differences in Pr do not affect the melting process with natural convection, for cases with $Pr \gg 1$ [127]. This was previously examined numerically by Sparrow et al. [126], who concluded similar thermal behaviour for materials with Pr equal to 7 and 70. Therefore, a model validated with measured data for a moderate-Prandtl number, ~ 50, at low melting temperature [40], can provide a reliable tool for the investigation of a low-Prandtl number PCM, ~ 10, at high melting temperature [127].

Numerical modelling of a phase change process mainly involves flow, mass and heat transfer in the HTF and PCM domains including the latent heat transfer or enthalpy changes across the solid/liquid interface. This may require a different approach in melting compared with a solidification process as the dominant heat transfer mode might be different. For a solidification case, conduction is the main heat transfer mode, resulting in a one dimensional (1-D) heat transfer across the solid/liquid interface that moves parallel to the cold/hot surface. However, in a melting process conduction and convection are both involved where natural convection plays a more important role. A convection dominated process leads to a non-linear process and two-dimensional heat transfer across the solid/liquid interface that moves in parallel and perpendicular to the hot surface. In a LHTES system, apart from the PCM, a heat source/sink is provided by a HTF for which forced convection is the heat transfer mode, leading to a conjugate problem for mathematical modelling. This makes the modelling and prediction of the thermal behaviour of PCM more challenging and demanding in terms of computation time and resources.

For numerical modelling of the phase change problem, the transient Navier-Stokes equations (Eqs. 1, 2, 3) are solved with special treatments to include the latent heat transfer and phase change, and zero velocity in the solid region. The assumptions to simplify the problem are:

i) constant density except in the linear density-temperature relation in the Boussinesq approximation
ii) density difference between solid and liquid is negligible
iii) constant thermophysical properties for PCM and HTF.
iv) the natural convection flow is laminar, incompressible and inviscid
v) internal thermal radiation is negligible.

$$\nabla.\left(\rho\vec{\vartheta}\right) = 0 \tag{1}$$

$$\frac{\partial(\rho\vec{\vartheta})}{\partial t} + \nabla.\left(\rho\vec{\vartheta}\vec{\vartheta}\right) = -\nabla p + \nabla.\left(\mu\nabla\vec{\vartheta}\right) + \rho_o[1-\beta(T-T_o)]g + So \tag{2}$$

$$\frac{\partial(\rho H)}{\partial t} + \nabla.\left(\rho\vec{\vartheta}H\right) = \nabla.(k\nabla T) \tag{3}$$

Where ρ is density, $\vec{\vartheta}$ is velocity vector, t is time, p is pressure, T is temperature, β is thermal expansion coefficient, g is the gravitational acceleration, So is a source/sink term, H is the total enthalpy, and k is thermal conductivity of the material. ρ_o, and T_o refer to a reference state, e.g. density and temperature at the melting point.

Numerical modelling of the phase change processes has been treated with two main approaches in the literature, namely tracking the interface as a moving boundary [128] and a fixed grid [129]. Here, a brief explanation of each approach follows:

3.1.1 Moving boundary

In a front tracking method, resolution of the grid generated for a geometry is not fixed and the grid transforms to a higher resolution at the interface as it moves during the process. The energy equation is solved numerically including the latent heat transfer across the interface. The main assumption in this approach is that a distinct phase front exists between the solid and liquid that is well suited for instance for pure metals or freezing water. This method is less favourable for alloys or mixtures like eutectic salts where there is a mushy zone between the solid and liquid domains [129].

3.1.2 Fixed grid

In a fixed grid treatment of the phase change phenomenon, the interface is assumed as a porous medium (mushy zone) where the phase fraction changes between [0,1]. To calculate the latent heat transfer, enthalpy and temperature changes should be included in the energy equation (Eq. 3) while enthalpy is dependent on the phase fraction and temperature. Including enthalpy as a function of temperature in the energy equation removes the non-linearity that is more convenient for a mathematical model. To do so, there are mainly two methods; including the latent heat source term (L) and enthalpy change (ΔH) as a function of melt fraction (δl) as follows;

$$H = h + \Delta H \tag{4}$$

$$h = h_o + \int_{T_o}^{T} c_p dT \tag{5}$$

$$\Delta H = \delta l \times L \tag{6}$$

In the second method, an apparent heat capacity (c^A) is defined. The apparent heat capacity in conjunction with the temperature gradients accounts for the enthalpy changes in the energy equation.

$$\frac{\partial H}{\partial t} = \frac{dH}{dT}\frac{dT}{dt} \qquad c^A = \frac{dH}{dT} \tag{7}$$

$$c^A = c_p + H\frac{d\delta l}{dT} \tag{8}$$

In this thesis, using the first method (latent heat source term) with a fixed grid, the melt front location is tracked by the temperature–enthalpy distribution. The mushy zone is treated as a porous medium in which the melt fraction in each cell changes between 0 to 1, i.e. porosity in each cell changes from 0 to 1 as the phase changes from solid to liquid. The latent heat transfer changes the total enthalpy during the phase change process. The liquid fraction (δl) which is defined to be equal to 1 for temperatures higher than T_m and equal to 0 for temperatures lower than T_m, is used to calculate the latent heat transfer.

In the momentum equation (eq. 2), a sink term is defined considering zero velocity in the solid region.

$$So = \frac{(1-\delta l)^2}{\delta l^3+\epsilon} A_{mush}\vec{\vartheta} \quad (9)$$

Where ϵ is a small number (0.001) to prevent zero in the denominator and A_{mush} is the mushy zone constant that measures how fast the fluid velocity approaches zero as it solidifies.

Using the enthalpy-porosity [130] method with a fixed grid in FLUENT, the melt front location is tracked by the temperature–enthalpy distribution. In this environment, a model has been set up, using the melting and solidification option and for the validation of this model the benchmark experimental data provided by Jones et al. [40] was used and results are presented in the next sections. The validated model was used for different numerical studies presented in chapters 4, 5, 6 and 7 of this thesis.

The numerical studies presented throughout this thesis start from the two and three dimensional cases with low temperature PCMs and then continue with high temperature PCMs for the CSP applications.

3.2 Model setting and validation

In this section, results and validation of two and three dimensional models for low temperature PCMs are presented. The predicted results are compared with experimental data and discrepancies are discussed.

3.2.1 Two dimensional axisymmetric modelling of inward melting, fixed wall temperature

A numerical study of inward melting of a low temperature PCM in a vertical cylinder was performed, using FLUENT 15, for validation purposes. The predicted results were compared with the experimental data from the literature. The results of this study show that the developed numerical model captures the details of the melting process with buoyancy driven convection for Ra<10^8, i.e. laminar flow, and can be used for further investigation of higher temperature PCMs.

3.2.1.1 PCM system

To validate the numerical study, the benchmark experimental investigation of Jones et al. [40] was selected, for which measured data was provided by the authors for the validation of other numerical models. The authors examined the inward melting process of n-eicosane having a melting temperature of 36.4°C in a cylindrical enclosure with 59.8 mm height and 31.9 mm radius. Three cases were conducted, maintaining the outer surface of the enclosure at three different constant temperatures (45°C, 55°C, 70°C) within a warm water bath. For all three cases, the bottom of the enclosure was kept at constant temperature of 32°C and the top was insulated to achieve an adiabatic boundary condition [40]. For all three cases Ra <10^8, and Ste was 0.3265, 0.1807, 0.0836 for cases I, II, III, respectively. The second case with the outer temperature of 55°C, was selected for the numerical modelling and results were compared to the measured data. Thermo-physical properties of the n-eicosane (Table 3.1) were taken from the same paper as the experimental data provided in [40]. The density of the liquid phase is taken into account as the melting process and natural convection in the liquid phase is investigated. A linear temperature dependency on dynamic viscosity is taken into account (Table 3.2) in the numerical modelling from the polynomial that was provided by the authors.

Table 3.1: Thermophysical properties of n-eicosine [40]

Density, kg/m^3	796
Specific heat, kJ/kg K	2400
Latent heat of fusion, kJ/kg	248
Thermal conductivity, W/m K	0.146
Thermal expansion coefficient	0.0008161
Dynamic viscosity (average), Pa s	0.0032
Melting temperature, ˚C	36.4

Table 3.2: Dynamic viscosity of n-eicosine [40]

Temperature, K	Viscosity Pa s
310	0.004362
312	0.004165
314	0.00398
316	0.003707
318	0.003644
320	0.003491
322	0.003347
324	0.003211
326	0.003084
328	0.002963
330	0.00285

3.2.1.2 Numerical Calculations

Numerical modelling of the melting process with natural convection was performed. The solidification and melting model in FLUENT [35] was implemented with the pressure based coupled algorithm to solve the momentum and continuity equations. The second order upwind scheme for the advection term, the central

differencing for the diffusion term and the second order implicit as discretization scheme for transient term were used. For the transient calculations, PRESTO was implemented as pressure interpolation scheme. For all cases, two-dimensional axisymmetric calculations were performed due to the symmetry of the cylindrical enclosures. The convergence threshold for all calculations were at least 10^{-4} for the continuity equation and 10^{-6} for other equations.

The simplifying assumptions are:

i) density is constant apart from the linear density-temperature relation in the Boussinesq approximation,
ii) same density for the solid and liquid phases,
iii) constant thermophysical properties for PCM and HTF except otherwise where mentioned for a specific case,
iv) the natural convection flow is laminar, incompressible and inviscid flow,
v) internal thermal radiation is negligible as the Boltzmann number >> 1, i.e. ~ 10^3, as suggested by Modest [131].

3.2.1.3 Geometry and grid

The numerical study was the test case of inward melting of n-eicosane in a cylinder with a fixed outer surface temperature of 55°C. The schematic drawing of the numerical model to mimic the experimental setup [40] is shown in Fig.3.1. Thermophysical properties of the PCM, polycarbonate shell and acrylic base were adopted from [40] and boundary conditions were set accordingly. The temperature dependency of dynamic viscosity was considered, and different specific heat capacity and thermal conductivity values were implemented for the solid and liquid phases. For this case the initial temperature was 23°C, $T_h - T_m$=18.6°C, Ra =8.8x10^7 and Ste=0.18, i.e. in the same range as Case II in the reference work [40].
A coarse grid consisting of 150x80 in the axial and radial directions for the PCM domain (59.8x31.9mm), 150x10 for the polycarbonate shell (59.8x2.85mm) and 20x80 for the acrylic base domain (5.97x34.75mm) was used for the calculations with 0.05 seconds as the time step. A fine grid (300x150, 300x15, 30x150 for the PCM, shell and base domain, respectively) was used with three different time steps of 0.01, 0.03 and 0.05 seconds to achieve grid and time step independency. Comparison of the melt fraction calculation from the coarse grid using the 0.05 seconds as time step with the result of the fine grid and different time steps (0.03, 0.05) showed less than 1% difference (Fig. 3.2c). This comparison presented more impact due to the time step compared to the grid resolution, meaning that better agreement with the experimental data might be achieved with a smaller time step. Due to the minor enhancement effect and longer calculation time, the coarse grid (fine enough to capture details within thermal and velocity boundary layers) with 0.05 seconds time step was selected for the numerical analysis and comparison with the experimental data.

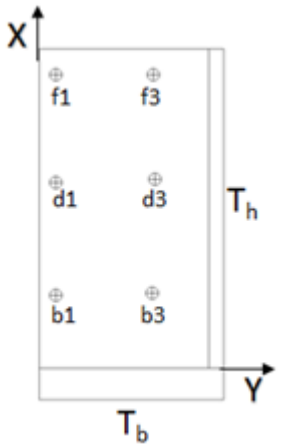


FIGURE 3.1. Schematic drawings of the numerical model with hot wall at the outer surface.

3.2.1.4 Results and discussion

Comparison of the predicted results of the simulation with the measured data [40] are presented in Fig. 3.2, which shows good agreement. Results for the points f3-b3, closer to the hot outer surface, show more deviation from the experimental results compared to the points f1-b1which are located closer to the centre of cylinder, experiencing lower temperature differences and later in time as the melting process proceed. Point f3 and f1 which are at the top of the enclosure experience dramatic temperature changes due to the buoyancy effects driven by convection

mass and heat transfer. However, f1 located closer to the centre of cylinder, results in a longer period of isothermal melting and a clear plateau of latent heat transfer in comparison to the temperature profile of f3, which hardly demonstrates a flat curve. Temperature profiles of b1 and b3, located at a lower level in comparison to d1 and d3, present a longer period of isothermal melting due to the lower temperature difference where the melting front reaches later with less impact of natural convection and lower final temperature. The melt fraction prediction is around 6.5% higher compared to the measured data. For the temperatures and melt fraction locations, a complete data was available in [40], but melt fraction rate data was adopted from the melt fraction graph which is provided in [40]. Hence, a low resolution of the experimental graph of melt fraction might be regarded as a reason of deviation. However, in the early stages of the melting process, a higher melting rate prediction is expected due to the adiabatic boundary condition at the top of the enclosure while in reality about 5% heat transfer through the top of the experimental set up was reported by Jones et al. [40]. The numerical solution shows a higher rate of melting up to the end of the process while at the later stages of the melting process a lower rate is expected compared to the measured data. Air pockets trapped in the solid PCM during the preparation of the experiment was reported by the authors [40]. Due to less material in the experimental phase change process which was not accounted for in the numerical model, a lower melting rate prediction is expected in the later stages of the process. Prediction of the melt front locations are in good agreement with the experimental results, as shown in Fig. 3.2d. In summary, the predictions of the numerical model are in good agreement with the experimental results and the model can be used to examine higher temperature PCMs in the same range of Ra and Ste with lower Pr.

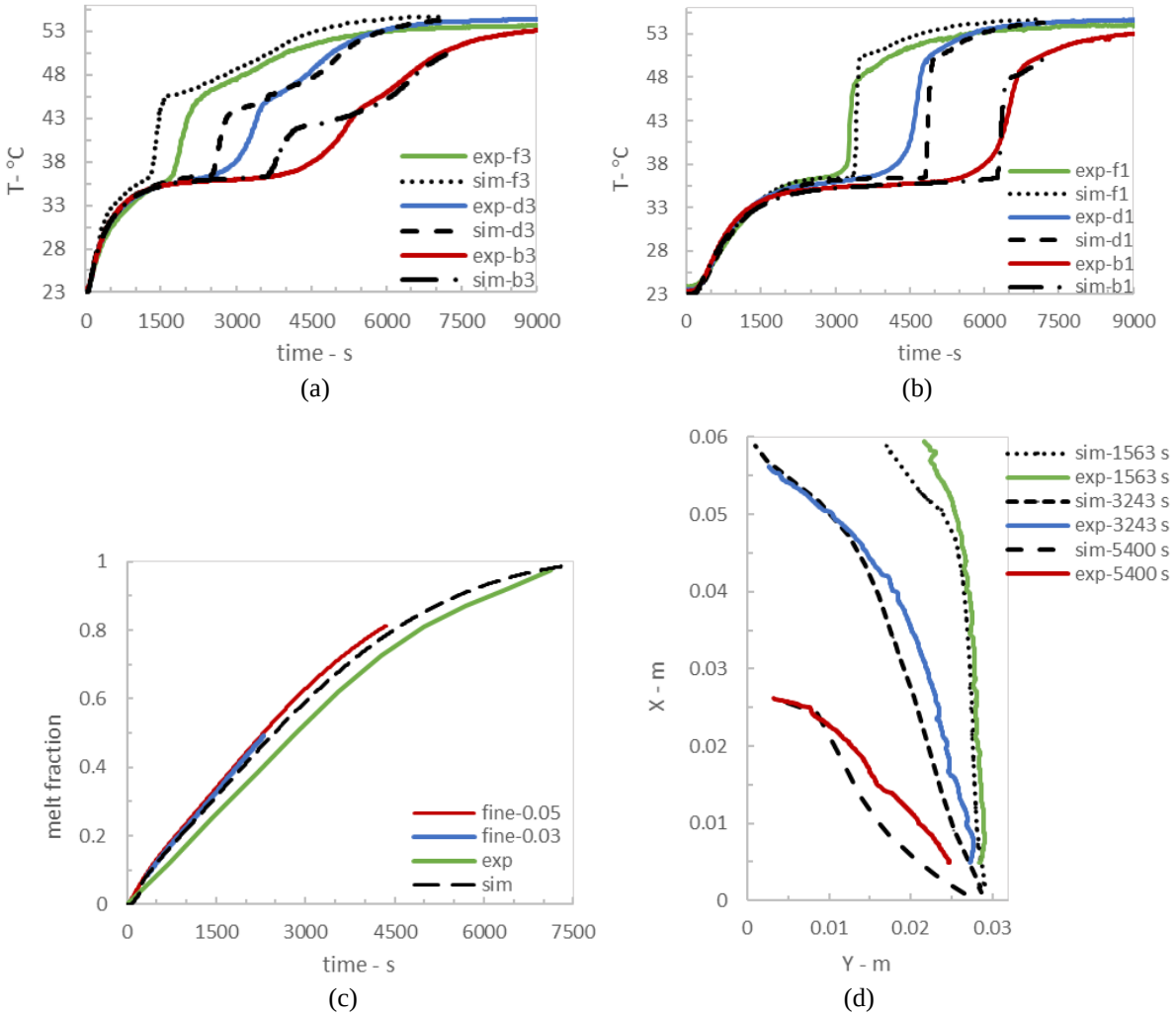


FIGURE 3.2. Temporal evolution of the scalar fields including experimental (exp) and simulated (sim) results: (a) temperature b3-f3, (b) temperature b1-f1, (c) melt fraction including fine grid results for 0.05 and 0.03 seconds time step, (d) melt front locations

3.2.2 Two dimensional axisymmetric modelling of melting in an annulus

A numerical study of outward melting of a low temperature PCM in an annulus was performed, using FLUENT 15, for validation purposes. While a fixed wall temperature was considered in the previous study (3.2.1), a HTF is flowing through the inner tube, which imposes a temperature profile along the tube-PCM interface. The annulus is considered as an element of a parallel flow and represents thermal behaviour of PCM in such a configuration. The predicted results were compared with the experimental data, providing more insight in the accuracy of the developed model. However, the uncertainty of the experimental data and assumptions for the numerical study should be considered in the comparison and assessment of the model.

3.2.2.1 PCM system

To validate the modelling accuracy using two-dimensional axisymmetric model, which includes more of the impact of the three-dimensionality of real cases, a numerical study of ice melting in an annulus replicating an element of a parallel flow in a shell and tube LHTES system is carried out. The experimental setup (Fig. 3.3a) comprises of an annulus where an aqueous based fluid with dissolved ionic solid as HTF flows through the inner tube and water as PCM fills the outer tube. The inner tube is made from stainless steel and the outer shell is made from clear polycarbonate. Five thermocouples were used to record the temperature profile through the PCM. Tay et al. [132] provided the results of the experimental work.

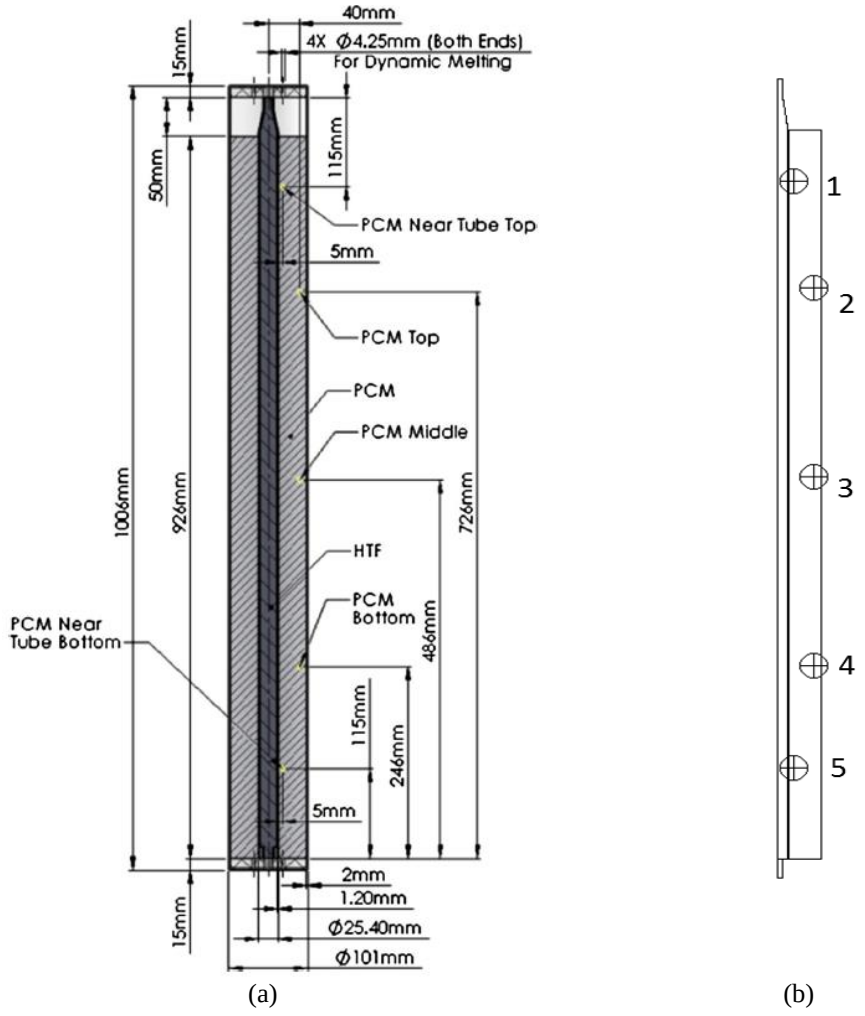


FIGURE 3.3. Schematic drawings of the annulus geometry a) experimental setup [132], b) symmetrical numerical model showing locations of temperature monitoring

3.2.2.2 Numerical calculation

Using the same model setting in Fluent [35] as described in section 3.2.1.2 with the same assumptions, and convergence thresholds, two-dimensional axisymmetric modelling was performed due to the symmetry of the

annulus. The schematic drawing of the experimental set up and the numerical model are shown in Fig.3.3a and 3.3b, respectively.
The thermophysical properties of water as the PCM and those of the heat transfer fluid are given in Tables 3.3 and 3.4, respectively. The boundary conditions were set according to the measurements from the experimental set up. A grid consisting of 78000 cells was used for the calculations with 0.1 seconds as a time step.
For the numerical study, the HTF inlet temperature was set at 10 °C (e.g. an average inlet temperature from the experimental data, resulting in $T_h - T_m$=10 °C), the initial temperature was set to -4°C while it is slightly different at different locations in PCM. The relevant non-dimensional parameters were: Ra =3.62x10^{11} and Ste=0.125.

Table 3.3: Thermophysical properties of water

Density, kg/m^3	1000
Specific heat, kJ/kg K	4178
Latent heat of fusion, kJ/kg	334
Thermal conductivity, W/m K	0.625
Thermal expansion coefficient	0.0004
Dynamic viscosity, Pa s	7.25e-4
Melting temperature, ˚C	0

Table 3.4: Thermophysical properties of HTF [132]

Density, kg/m^3	1345
Specific heat, kJ/kg K	2680
Thermal conductivity, W/m K	0.498
Dynamic viscosity, Pa s	0.0038
Mass flow rate, kg/s	0.021
Velocity in tube, m/s	0.039

3.2.2.3 Results and discussion

Figure. 3.4. shows a comparison of the predicted and measured temperatures at different locations in the PCM and the outlet temperature of the HTF. Predicted and measured temperatures at the outlet of the HTF, and at the thermocouple locations near the tube top (1), middle (3), and at the bottom (4) in the PCM are in better agreement compared with the other two locations at top (2), and near tube bottom (5) which are in fair agreement. The measurement uncertainties during the experiments and simplifying assumptions for the numerical modelling such as the perfect insulation as boundary condition at the outer surface, top and bottom of PCM are the main factors for the deviations as the melting advances faster in the modelling compared to the experiment. Also, the specific heat capacity and thermal conductivity were assumed the same for the solid and liquid states which might be other factors for the discrepancy between the predicted and the measured data.

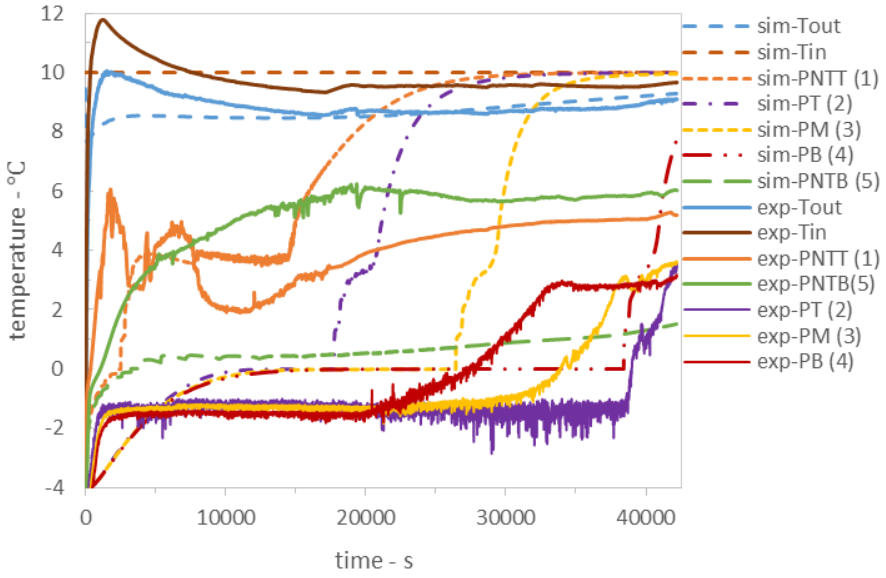


FIGURE 3.4. Comparison of the measured and predicted temperature profile with THTF=10°C and Tini=- 4 °C

One of the more important parameters in the design of a LHTES unit is the heat transfer rate provided by the system during a phase change process. Fig.3.5. shows a comparison between the predicted and measured heat transfer during the charging process. The results show some overestimation of the heat transfer during the convection dominant stage and an underestimation of the heat transfer during the later stages while the phase front moves downward and the solid is shrinking. Considering the uncertainty of the experimental data, ignoring the heat losses and assuming fixed HTF inlet temperature (the HTF inlet temperature changes during experiment) might be the main factors for the deviation.
The magnitude of discrepancy is large, however, an uncertainty study for the experiments and measured data was not available for a more rigorous assessment of the predicted data. The model can be used in the design of a

parallel flow LHTES system, considering an annulus as an element of such a system and scale up to an industrial scale LHTES system.

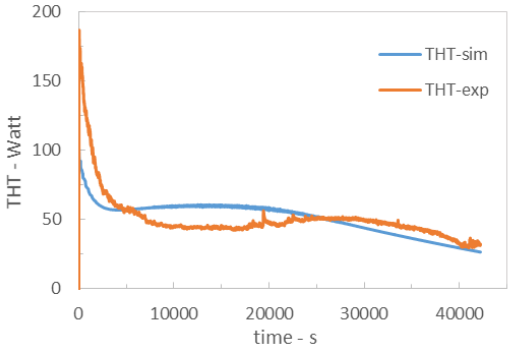


FIGURE 3.5. Comparison of the measured and predicted total heat transfer rate with THTF=10 °C, Tini= - 4 °C

3.2.3 Three dimensional modelling of a U-tube element of a two pass prototype at ECN

Numerical modelling in conjunction with scale analyses provides effective means to examine the performance of different configurations of latent heat storage systems. There has been considerable research effort in the numerical analysis of shell and tube configurations as a LHTES system. In most numerical investigations, an annulus has been selected as the model where HTF passes through the inner tube and PCM is confined in the outer tube. Considering a larger system, an annulus can represent parallel flow in a shell and tube system, and provide some insight in the thermal behaviour of PCM during a phase change process. However, the annulus model might have shortcomings in a system where the temperature profile on the tubes might not be the same, for instance in a counter flow system. Tube surfaces are the interface between the HTF and PCM where the temperature profile plays an important role in the evolution of the phase front.

While two-dimensional axisymmetric models were used in previous sections (3.2.1, 3.2.2), here, a three-dimensional U-tube element of a two-pass laboratory-scale shell and tube LHTES system has been selected to examine its validity to represent the system. The experimental data was acquired from collaboration work at the Energy Centre of the Netherlands (ECN). The author spent one month at ECN, working with the PCM group and collecting measured data from a laboratory-scale two-pass shell and tube system. The main objective of this section is to scale down the two-pass shell and tube experimental set up to a three dimensional model that can represent the thermal behaviour of the system within reasonable computational time. Using ANSYS FLUENT [35], modelling of the melting (charging) and solidification (discharging) processes was carried out and compared with experimental results.

3.2.3.1 PCM system

Rubitherm70 (RT70), an organic PCM (thermophysical properties provided by the manufacturer, Table 3.5) is confined in the shell of a two-pass shell and tube experimental storage system as shown in Fig.1. The experimental setup was built as a LHTES unit to investigate the thermal behaviour of PCMs at the ECN. Specification of the system is as follows: length of the shell = 1 m, the inside shell diameter = 0.39 m, stainless steel (SS316) tube diameter = 0.012 m, tubes were spaced in triangular pitch = 0.036 m.

Water as the heat transfer fluid (Table 3.6) passes through the tubes at either 20 K, or 10K higher than the melting temperature of PCM for the charging processes and 10K lower than the PCM melting temperature for the discharging process. While the experimental setup can be tested in the horizontal and vertical orientations, this study covers the modelling of horizontal cases. Figure 3.6c shows a cross section of the system in the horizontal orientation including the thermocouple locations. Using 1 mm diameter thermocouples, fixing of the thermocouples at the exact locations appeared to be very difficult in practice. Deviations of up to 5 mm in their locations, with consequent significant impact on the measured temperatures needs to be considered in the comparison to the predicted data from the modelling.

Table 3.5: Thermophysical properties of RT70

Density, kg/m^3	770
Specific heat, kJ/kg K	2000
Latent heat of fusion, kJ/kg	260
Thermal conductivity, W/m K	0.2
Thermal expansion coefficient	0.001
Dynamic viscosity, Pa s	0.02
Melting temperature, ˚C	70

Table 3.6: Thermophysical properties of water

Density, kg/m^3	998
Specific heat, kJ/kg K	4182
Thermal conductivity, W/m K	0.6
Dynamic viscosity, Pa s	0.001
Mass flow rate, kg/s	0.0034
Inlet temperature, °C	88.7
Velocity in tube, m/s	0.087

As mentioned before, for PCM systems with the same Ra, differences in the Prandtl number (Pr) do not affect the natural convection phenomenon if $Pr \gg 1$ [127]. Thus, the validated model using RT70 as PCM with Pr=100 can be used to model and design higher temperature PCM (e.g. sodium nitrate with Pr=9 and melting temperature 306.8 ℃) systems for industrial and CSP applications, which are presented in section 3.3 and chapters 4, 5.

3.2.3.2 Numerical calculations

Three dimensional numerical modelling of the charging and discharging processes with natural convection was performed, using ANSYS FLUENT [35]. All of the modelling schemes and thresholds are the same as described in section 3.2.1.2. A three dimensional geometry and grid for the U-tube was generated with ANSYS Design Modeller [37], taking into account the symmetry in geometry with about 860000 cells, fine enough to capture the details of thermal and velocity boundary layers within the domains of PCM, tube and HTF as shown in Fig. 3.6b. This grid facilitates a convenient size in comparison to another symmetric grid that was built from the half of the shell and tube system (Fig. 3.6a) comprising more than 16×10^6 cells. The assigned boundary conditions are symmetrical around the PCM outer surface, adiabatic conditions at the top and bottom of PCM, velocity inlet and outflow at the inlet and outlet of HTF.

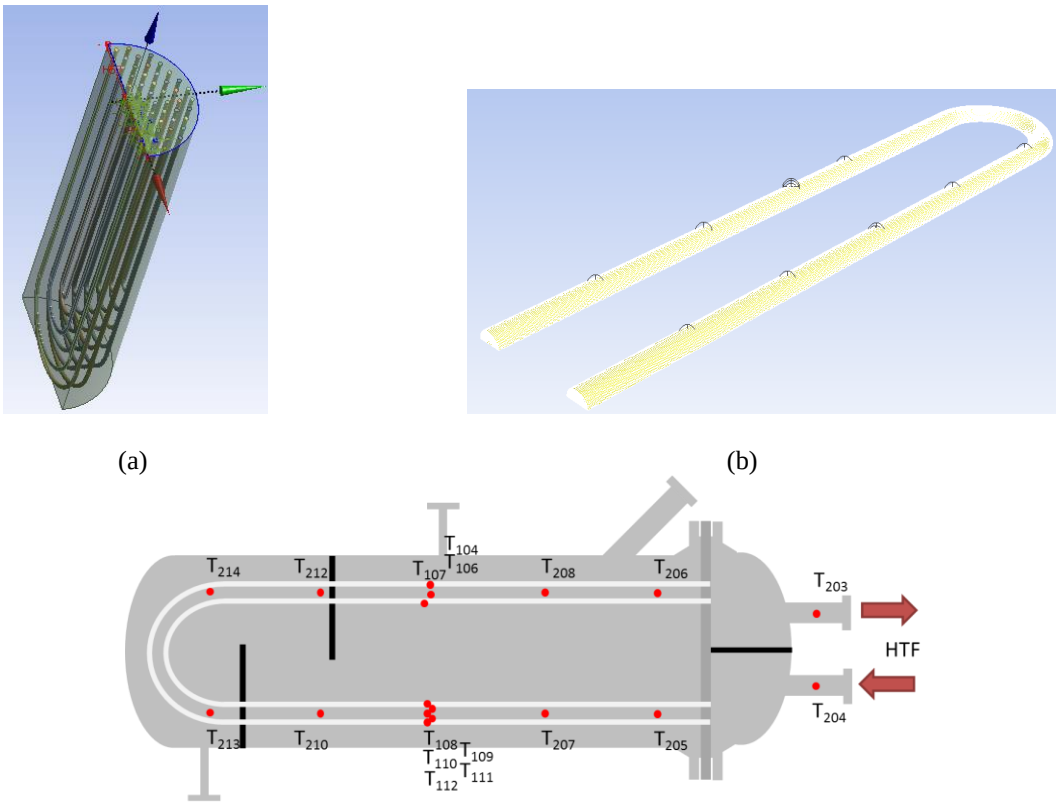


FIGURE 3.6. Schematic drawings:
(a) Three dimensional symmetric geometry of the shell and tube system, (b) Three dimensional symmetric grid of an element of the shell and tube system including the location of temperature monitors (tm), (c) A cross section of the experimental system including the locations of thermocouples (tc).

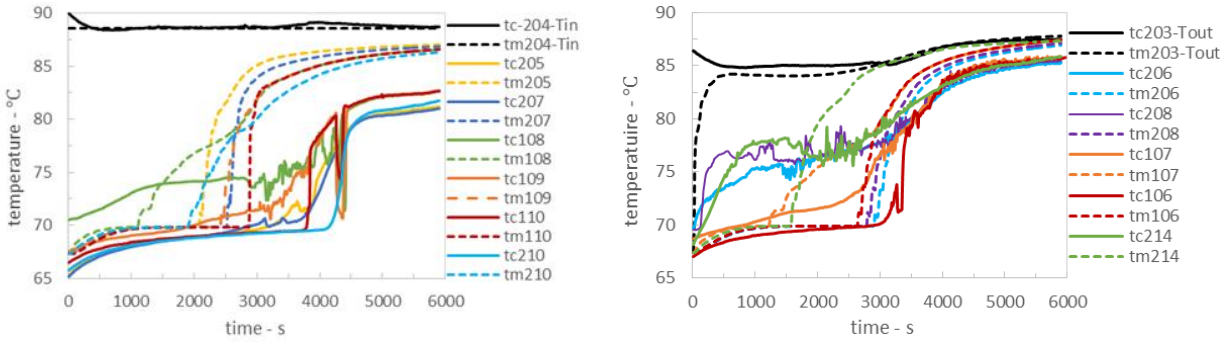
For the melting processes, four cases were studied including the impact of A_{mush} which is included in the sink term (Eq.9) of the momentum equation (Eq.2) and explained in section 3.1.2; the first case where the inlet temperature of HTF is 20 K higher than the melting temperature of PCM (ΔT =20 K) and A_{mush} =10^7. In the second case, ΔT =10 K and A_{mush}=10^7. With the same temperature difference, a third case was performed with A_{mush} =10^5 to investigate the impact of the A_{mush} on the rate of melting. For the fourth case, ΔT =10 K, A_{mush}=10^8 and turbulence calculation was included to investigate the combined impact on the temperature field evolution in PCM and the rate of melting. In the first and second numerical models of the melting process, the average initial temperature from the experimental process (67.35°C and 66.85°C) was used while in the third and fourth numerical calculations different initial temperatures at different locations from the experimental data were used.
For the solidification case, the temperature difference between the inlet temperature of the HTF and the PCM was set at ΔT=10 K. The average measured initial temperature (70.85°C) from the solidification experiments was used for the modelling of the discharging case.
Temperatures were monitored during the charging and discharging processes at the outlet of the HTF and also at 12 other locations (Fig. 3.6b) consistent with the thermocouple locations in the experimental setup (Fig. 3.6c).

3.2.3.3 Results and discussion

3.2.3.3.1 Melting

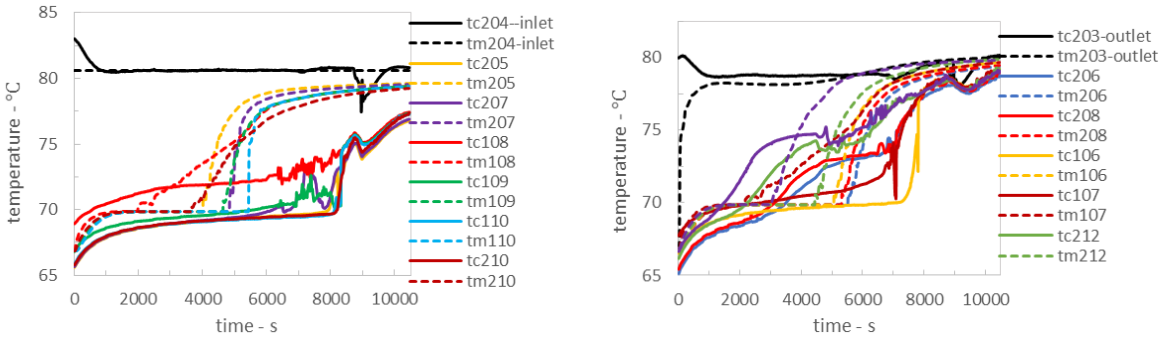
Figures 3.7, and 3.8 show the temperature profile evolutions during the melting processes with temperature differences (ΔT) between the inlet HTF and the melting temperature of the PCM being 20 K and 10K, respectively. Figures. 3.7a and 3.8a show the temperature profiles at the inlet or the lower section of the U-tube (Fig. 3.6c) where temperature differences between the PCM and HTF are higher and Fig. 3.7b and 3.8b show the temperature profiles at the outlet or the upper section of the U-tube with lower temperature differences between HTF and PCM. At the early stages of the melting process in both cases, there is better agreement between predicted and measured temperatures at the inlet section where temperature differences are higher resulting in a higher rate of convection heat transfer. However, at the later stages of the melting process there is better agreement between the

measured and predicted temperatures at the upper section of the system due to the liquid accumulation at the top of the shell resulting in higher rate of natural convection heat transfer.
For the temperature profiles at different locations in the PCM domain, there is a better agreement for the first case with ΔT =20 K compared to the second case with ΔT =10 K. This is to be expected with lower temperature differences as more detail is captured with numerical modelling. However, for the applications in CSP plants, temperature differences of 20 K and higher are expected as higher temperatures are involved. In both cases, the duration of the melting processes is in good agreement with the experimental data.



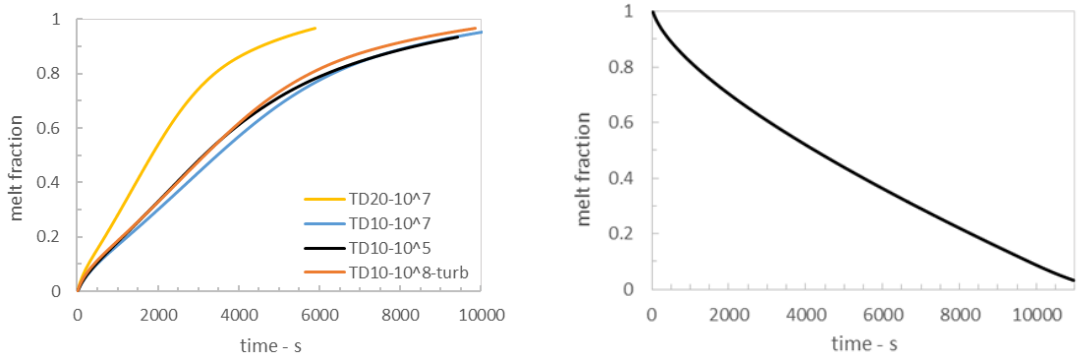
(a) (b)

FIGURE 3.7. Temperature comparison between model temperature (tm) and thermocouple readings (tc) in the PCM during the melting process (first case) with ΔT =20 K: (a) HTF inlet (Tin) and the lower section of the U-tube, (b) HTF outlet (Tout) and the upper section of the U-tube



(a) (b)

FIGURE 3.8. Temperature comparison between model temperature (tm) and thermocouples (tc) in PCM during the melting process (second case) with ΔT =10 K: (a) HTF inlet (Tin) and the lower section of the U-tube, (b) HTF outlet (Tout) and the upper section of the U-tube

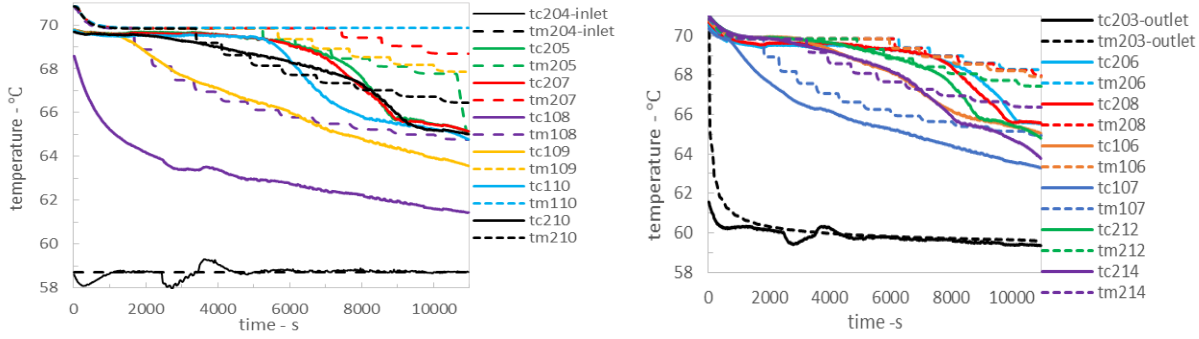


(a) (b)

FIGURE 3.9. Phase fraction in PCM:
(a) melting processes, including four cases with different temperature differences ΔT20, ΔT10, different mushy region constants and fourth case with turbulence modelling, (b) solidification

In general, the predicted melting rates is higher than the measured data due to the simplifying assumptions including adiabatic boundary conditions that ignore the heat loss from the system. Uncertainty in the location of the thermocouples as mentioned in the PCM system section and its impact on the temperature measurements is another factor in the discrepancies between the experimental results and modelling.
To check the impact of the mushy region constant (A_{mush}) on the rate of melting, two additional cases with ΔT =10 K were modelled for which the results are included in Fig. 3.9a. Results show minor differences between the three different cases of A_{mush} =10^5, 10^7, 10^8. In the fourth melting process with A_{mush} =10^8, a turbulence calculation was included to capture more detail. Although the melt fraction rate is higher but compared to the second and third cases with same TD =10 K, the differences are not significant.
Considering the impact of the initial temperature at each thermocouple location, in the third and fourth melting cases with ΔT =10 K, the initial temperature at each point was set the same as the experimental data while for the second case of melting with ΔT =10 K, an average initial temperature (66.85°C) from all the thermocouple locations was used. The results of melt fraction for the three cases are presented in Fig. 3.9a which shows insignificant differences, however, starting from different initial temperature shows higher impact on the temperature profile evolution at each point. For instance, Fig.3.7a shows a higher discrepancy between the measured (tc108) and predicted temperature (tm108) profile at thermocouple 108 for which the initial temperature was 71°C while the initial temperature at tm108 was set to 67.35°C for the first modelling case.

3.2.3.3.2 Solidification
Figures 3.10a and b show a comparison of the temperature evolution in the PCM domain during the discharging process. Figure 3.10a shows the temperature profiles at the inlet or the lower section of the U-tube (Fig. 3.6c) and Fig. 3.10b shows the temperature profiles at the outlet or the upper section of the U-tube. Figure 3.10b shows good agreement between the measured and predicted outlet temperature of the HTF (tc203 and tm203). There is good agreement between the measured and predicted temperature profiles for the locations where the initial temperature of the modelling is the same or close to the measured initial temperature in the experiments. For instance, there is a higher discrepancy for the thermocouple 108 (tc108) as the initial temperature is about 2.26 K cooler than what was assumed in the modelling process, using the average initial temperature of all thermocouples (70.85 °C).
In general, the predicted results are closer to the data captured during solidification experiments compared to the melting processes, mainly due to the conduction being the dominant heat transfer mode in the solidification cases. This results in step-wise temperature profiles as there is no mixing effect while the higher rate of convection in the melting processes results in smooth temperature profiles. Convection being the dominant heat transfer mode in the melting processes makes it more complex to be captured by the numerical calculations. Moreover, the predicted duration of the solidification process agrees with the experimental data. .



(a) (b)

FIGURE 3.10. Temperature comparison between model temperatures (tm) and thermocouples (tc) in PCM during the solidification process with ΔT =10 K: (a) HTF inlet (Tin) and the lower section of the U-tube, (b) HTF outlet (Tout) and the upper section of the U-tube

Overall, the results of this study demonstrate that the selected element of the shell and tube system provides an approximate representation of the system with a smaller scale model and grid for a numerical study compared to a half symmetrical grid (Fig. 3.6a). This geometry and grid validated for a low temperature PCM can be used to explore higher temperature PCM [127] systems within the same shell and tube geometry for concentrated solar thermal applications. In addition to the temperature field in the PCM domain, the evolution of the phase front at the interface between the solid and liquid, mass and heat transfer rates are other predicted results from the modelling which are not included. Results from the modelling provides a full picture of the thermal behaviour of

PCM during the charging and discharging processes which can be used in the design and optimisation of a LHTES system for CSP plants and many other industrial applications.

3.3 Investigation of transport phenomena

3.3.1 Flow and mass transfer

The mass flow rate of liquid PCM and the impact on the phase front and ultimately the heat transfer from/to the HTF is an important aspect of the phase change process. The mass transport or natural convection in the liquid PCM can be the result of density/temperature gradient. Assuming constant density except in the calculation of the buoyancy forces in the momentum equation (Eq. 2), the temperature gradient drives the mass flow in the liquid region of the PCM. The resulting stream functions as a vector field defines the velocity field and mass flow. Therefore, the inclusion of the natural convection in a LHTES system is needed to identify the impact on heat transfer. Time dependent conservation equations of mass, momentum and heat account for the changes of scalar and vector fields and their interaction during a phase change process. Here, to solve the problems involving the transport phenomena, time dependent Navier-Stokes equations are solved numerically.

3.3.1.1 Laminar or turbulent flow

The forced convection flow in the HTF side of a LHTES system is normally turbulent; however, the natural convection in the liquid PCM can be laminar or turbulent. The threshold is defined by the Rayleigh (Ra) number, which is different for the enclosures being heated from the side or from the bottom. The thermal behaviour of fluids in enclosures heated from the side and heated from below has been explored in the literature [133]. In most cases of enclosures heated from the side natural convection is laminar, particularly in low temperature PCMs (e.g. T<50°C) resulting in a process with $Ra < 10^9$. However, in high temperature PCMs (e.g. 300°C<T<850°C) with higher temperature differences between a heat source (e.g., HTF) and melting temperature of PCM ($\Delta T=T_h-T_m$), the flow becomes turbulent for $Ra\sim10^{12}$ as reported by Bejan [134]. Turbulence makes the natural convection more effective in mixing the PCM medium.

In enclosures heated from below when the Ra (based on the height of the horizontal case) increases above 1708, the flow becomes turbulent where Benard convection cells [133] form along the bottom side of the enclosure. The Benard cells are smaller and faster compared to the larger cells, which circulate upwards along the hot side and downwards along the colder side of the vertical enclosures heated from the side.

Due to the impact of mixing on the phase change process and melting front evolution, it is important to investigate the impact of natural convection and turbulence in the melting process of a high temperature PCM by employing numerical investigation.

There are some studies where natural convection was included or ignored, however, limited research has investigated the natural convection impact on the mass transfer, heat transfer area (melt front in a melting process), temperature gradient in space and time for the melting process of a high temperature PCM. Moreover, there is a lack of investigations in the impact of turbulence modelling on the melting process in a LHTES system and the importance of this phenomenon in high temperature PCM systems. Due to the importance of natural convection and turbulence in the charging process of heat storage systems, firstly the effect of including natural convection and secondly the flow nature (laminar or turbulence) in the numerical calculations on the temperature and velocity fields, heat transfer area and rate, and duration of the phase change process are numerically investigated in this study. Apart from the very early stages in the solidification process of PCMs, the dominating mode of heat transfer is conduction. Thus in this study the focus is on melting process of PCMs.

3.3.2 Modes of heat transfer

Heat transfer in the melting and solidification is a conjugate problem, involving conduction and natural convection in the PCM, and at the HTF side, the main mode of heat transfer is forced convection with consequent low thermal resistance. The energy equation (eq. 3) from the transient Navier-Stokes equations accounts for the spatial changes of enthalpy and temperature during a phase change process due to the advection and diffusion of heat.

In the scope of high temperature PCMs (300 °C – 750°C) relevant for CSP plants, conduction and natural convection are considered as the main heat transfer modes. Depending on the thermophysical properties of PCM, structure of the LHTES system, and phase change process being melting or solidification, one mode of heat transfer can be dominant. This is important as the defining parameter of the thermal behaviour of PCM and characteristics of the system. Radiation heat transfer is assumed to be negligible based on the study of radiation combined with conduction and convection by Modest [131]. Two non-dimensional numbers are introduced; N the conduction to radiation parameter and Boltzmann (Bo) number as a convection to radiation parameter, providing a qualitative measure of the relative magnitude of radiative heat fluxes compared with the other modes of heat transfer.

$$N \equiv \frac{k\kappa}{4n^2\sigma T^3} \qquad\qquad Bo \equiv \frac{\rho c_p u}{n^2\sigma T^3}$$

where k is the thermal conductivity, κ is the absorption coefficient of the participating media, and n is the refraction index. In the studies included in this thesis for melting processes with convection as the dominant heat transfer mode, Bo parameter is ~ 100 >>1 which satisfies the assumption of negligible radiation. However, in the solidification cases of molten salts as semi-transparent media where conduction is the dominant mode, the N parameter is smaller than one. The impact is that irradiation from the melt zone can be absorbed in the solid zone which results in a delay of the solidification process. In this thesis, this effect has been ignored due to the complication of the modelling problem. However, comparing to other thermal storage systems such as packed bed thermocline systems where conduction is the dominant mode of heat transfer in charging and discharging processes and radiation impact is important [90, 92], ignoring radiation heat transfer in LHTES is justified as its impact becomes important in discharging when conduction is dominant.

As the thermal conductivity of potential PCMs are generally low (reported in a review study by Kenisarin and Murat [28]), the natural convection role is important to enhance the heat transfer rate.

Using Fluent, numerical modelling was performed to study the impact of modelling natural convection and turbulence on the thermal performance of a high temperature PCM in a melting process with $Ra=10^{12}$. This process is weakly turbulent and adding more models in different cases provides an opportunity to compare the predicted results and the impact of the simplifying assumptions such as neglecting convection or turbulence. Numerical calculations were conducted considering a two-dimensional symmetrical grid of a dual-tube element in a parallel flow shell and tube configuration where the heat transfer fluid passes through the tube and PCM fills the shell. Three melting processes for the PCM were considered; pure conduction (ignoring convection), conduction and laminar natural convection, and finally the latter modelling turbulent natural convection.

3.3.3 PCM system

The LHTES system assumed using sodium nitrate as the PCM and air as the HTF (Table 3.8) in a shell and tube configuration with parallel flow. In such a system, the HTF flows though tubes in parallel and melts/solidifies PCM, which is confined in the shell (Fig. 3.6a). The melting temperature of the PCM, T_m =306.8°C, and all other thermophysical properties were acquired from a study by Lan and Yang [135] as it is shown in Table 3.7. Using this system, three melting processes were studied to compare the impact of convection and turbulence on the thermal behaviour of PCM.

Table 3.7: thermophysical properties of PCM [135]

Density, kg/m^3	2000
Specific heat, kJ/kg K	1730
Latent heat of fusion, kJ/kg	182
Thermal conductivity, W/m K	0.57
Thermal expansion coefficient	0.00066
Dynamic viscosity, Pa s	0.00302
Melting temperature, ˚C	306.8

Table 3.8: thermophysical properties of air

Density, kg/m^3	1.226
Specific heat, kJ/kg K	1006
Thermal conductivity, W/m K	0.0242
Dynamic viscosity, Pa s	1.789e-5
Mass flow rate, kg/s	0.089
Velocity in tube, m/s	8.957

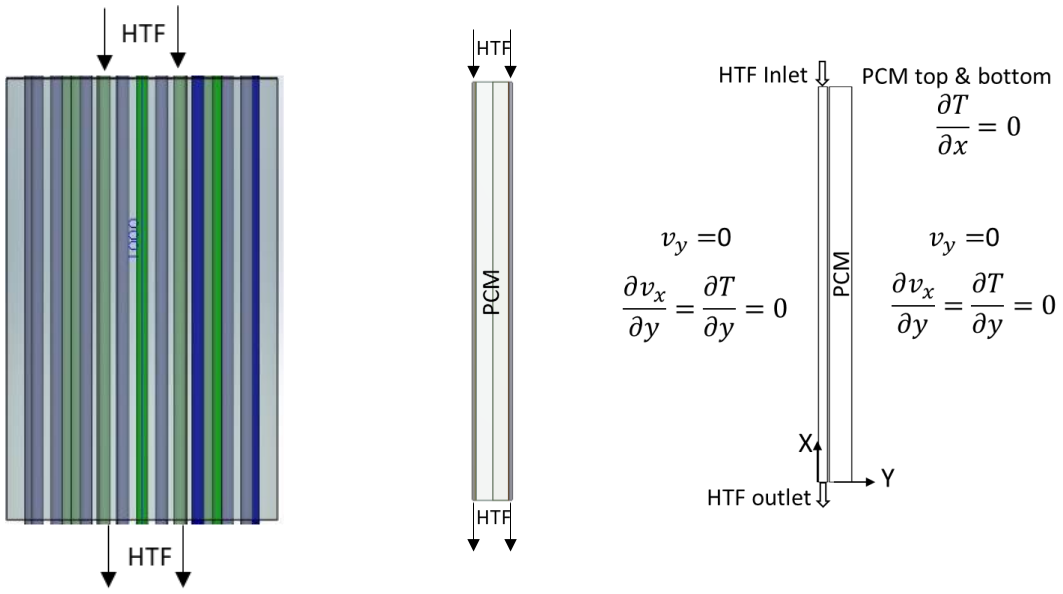
3.3.4 Numerical calculations

The model described and validated in the previous section 3.2, was used for the investigation of convection and turbulence impacts on the temperature and velocity fields, heat flux and melting process duration. The simplifying assumptions are the same as mentioned in section 3.2.1.2 except for the third model, where liquid PCM flow was considered turbulent. The numerical schemes and threshold are the same as defined in section 3.2.1.2 except for the turbulence model where realisable k-ε model with the standard wall functions as the near-wall treatment method was implemented.

Two adjacent tubes of a parallel tube bundle immersed in a shell and tube LHTES system (Fig. 3.11b) were selected to study the thermal behaviour of PCM in a melting process under $Ra\sim10^{12}$ where turbulent natural convection is involved. The specification of this model was acquired from a lab-scale LHTES prototype (Fig. 3.11a), for which more information is provided in chapter 4, section 4.2. The height of the tubes and PCM was 55cm and the width of the geometry (centre to centre of tubes) was 6 cm (Fig. 3.11b). Three domains of HTF, tube thickness and PCM were defined for the symmetrical model (Fig. 3.11c).

The boundary conditions were set as symmetrical at both sides of the geometry, adiabatic conditions at bottom and top of PCM, flow inlet at HTF top and flow outlet at HTF bottom, as shown in Fig. 3.11c. The HTF inlet temperature was set at 456.8°C resulting in $T_h - T_m$=150°C. The initial temperature was set 5°C colder than the PCM melting temperature (T_m=306.8°C) to capture the latent heat transfer after the first stage of sensible heat transfer from the HTF to the PCM.

A two-dimensional symmetrical grid with 33,000 cells was generated from half of the geometry (Fig. 3.6) with a maximum aspect ratio = 2 and orthogonal quality = 1. A fine grid with 78,000 cells was generated to investigate the grid dependency of the results. The results of melting rate for the melting without turbulence with the fine grid



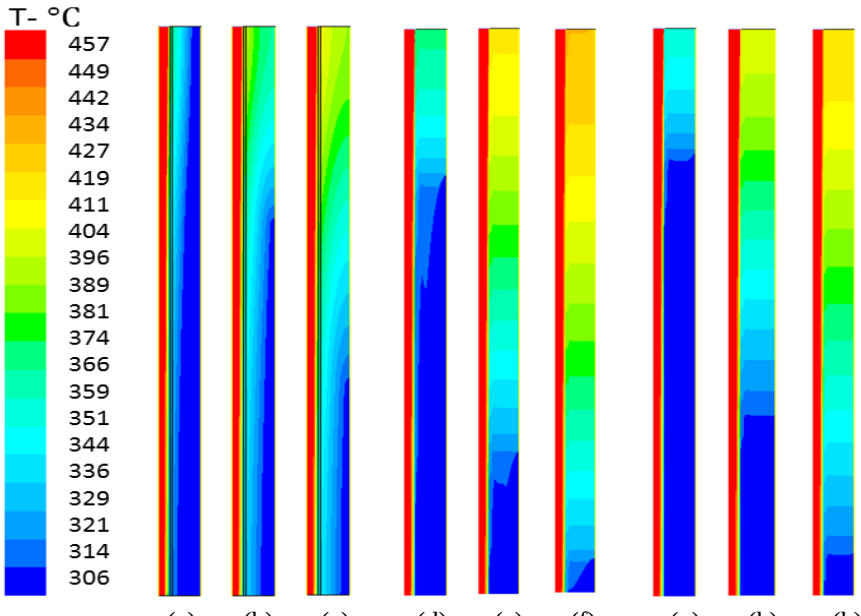
(a) (b) (c)

Figure 3.11. Schematic drawings: (a) tube bundle carrying HTF in a shell filled with PCM, (b) centre to centre of two adjacent tubes, (c) numerical model, symmetrical half of the dual-tube element in parallel flow

(cwt-fg) is included in the Fig. 3.9b and shows minor differences with the results of the coarse grid for the same case. The time step was set to 0.1 seconds to capture details in the temperature and velocity fields in a feasible computation time. Modelling of the three melting processes with the same setting were performed, firstly calculating conduction heat transfer in PCM, then adding laminar convection calculation, and finally including turbulent natural convection in the third melting process.

3.3.5 Results and discussion

3.3.5.1 Temperature field



(a) (b) (c) (d) (e) (f) (g) (h) (k)

Figure 3.12. Evolution of temperature profile during melting: Pure conduction, ignoring convection (a) δl =53.2% at 2300s, (b) δl =87.8% at 4450s, (c) δl =97% at 5600s. Conduction and assuming laminar convection: (d) δl =53.2% at 2250s, (e) δl =87.8% at 4950s, (f) δl =97% at 6500s. Conduction, and turbulent convection modelling: (g) δl = 53.2% at 2000s, (h) δl =87.8% at 4200s, (k) δl =97% at 5600s.

The spatial temperature distribution in three time slots are presented in Fig. 3.12a-k. Figure 3.12a-c present the temperature field of the melting process considering pure conduction heat transfer (ignoring convection) with isotherms being mainly vertical. Compared to Fig. 3.12d-f, the result demonstrates that including natural convection modelling causes horizontal isotherms with higher peak temperatures and temperature gradients. Due to the convection heat transfer at the higher levels of PCM, melting starts earlier during the process. However, adding turbulence (Fig. 3.12g-k) modelling (relaxing the laminar flow assumption) with a higher rate of mixing due to the higher rate of mass transfer, peak temperatures and temperature gradients are lower in comparison to the melting process assuming laminar natural convection (Fig. 3.12d-f). In all melting processes, evolution of isotherms being vertical in pure conduction and horizontal with convection and turbulent modelling is consistent with the melting front evolution, as shown in Fig. 3.13a, b.
Moreover, Fig. 3.12 demonstrates the evolution of temperature profiles and time of same liquid fractions (53.2%, 87.8%, 97%) for different modelling cases. For instance, 53.2% of solid PCM melts after 2300, 2250, and 2000 seconds for modelling conduction only, considering laminar convection (ignoring turbulence) and including turbulence model, respectively.

3.3.5.2 Mass transfer

As expected, the melting process with pure conduction results in no mass transfer in the liquid PCM. The mass transfer rate with the assumption of laminar natural convection and with turbulent natural convection is represented by stream functions in the numerical modelling. For three different melt fractions (δl), maximum and average mass transfer rate in the PCM domain are shown in Table 3.9. In general, including turbulence in the numerical calculations results in a higher rate of mass transfer as the melt fraction increases, shown in Table 3.6. In other words, higher liquid PCM results in more turbulent convection cells with higher velocity to carry and mix the fluid. Without turbulence, the mass transfer rate decreases during the melting process as the main driving force (difference between average temperatures of HTF and PCM) diminishes and slows down convection cells.

Table 3.9: Average (ave) and maximum (max) stream functions:
laminar convection without turbulence model (cwt), turbulent convection (c&t)

δl	cwt- ave-kg/s	cwt-max-kg/s	c&t-ave-kg/s	c&t-max-kg/s
53.2%	0.0398	0.0456	0.044	0.05
70%	0.0357	0.0412	0.05	0.058
87.8%	0.0217	0.0248	0.051	0.057

3.3.5.3 Heat transfer

The heat transfer area being the melt front (Fig. 3.13a, b) and heat flux (Fig. 3.14a) can be compared to evaluate the impact of assuming laminar natural convection and turbulent convection on the predicted melting results.

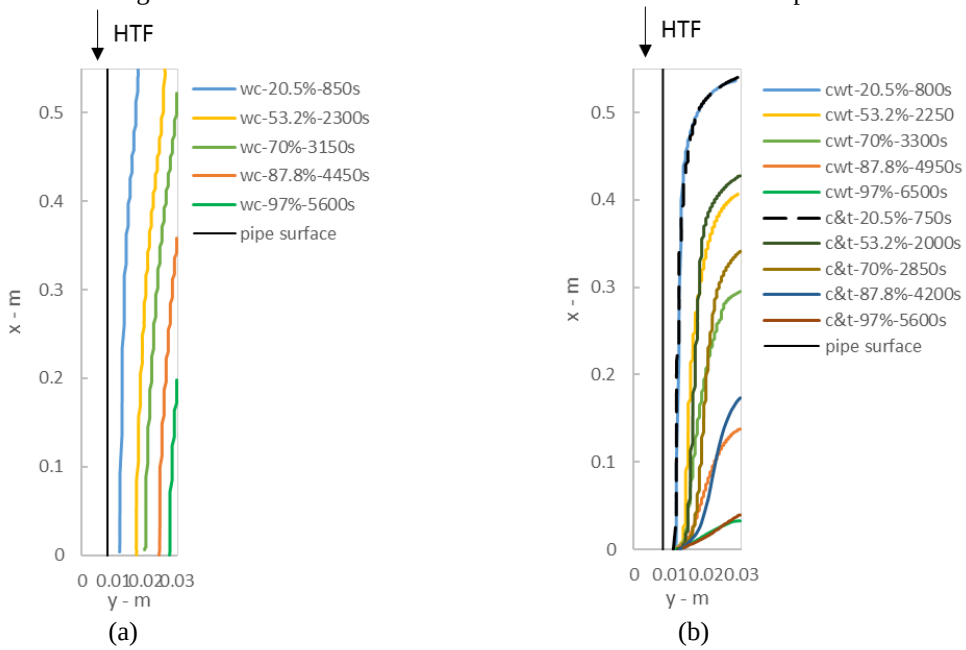
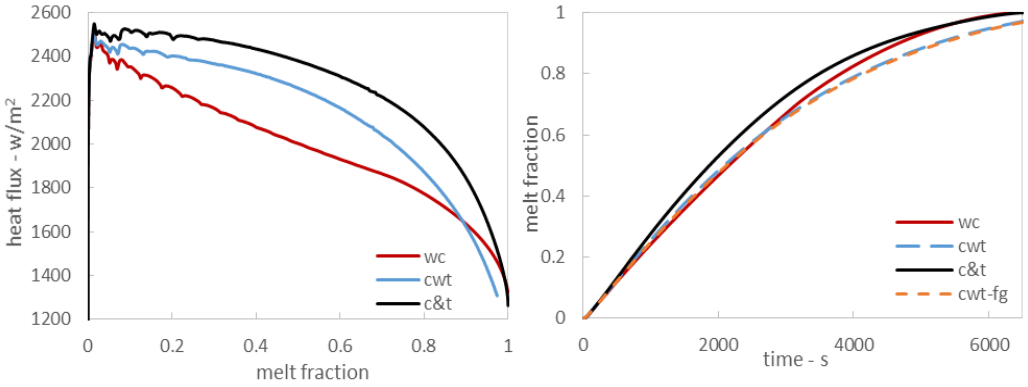


Figure 3.13. Evolution of melt front during the melting process: (a) without convection modelling (wc), (b) including laminar natural convection (cwt), including turbulent natural convection (c&t)



(a) (b)

Figure 3.14. Results comparison: (a) heat flux at the tube surface, without convection modelling (wc), including natural convection (cwt), and turbulent natural convection (c&t), (b) melt fraction, wc, cwt, c&t, and cwt coarse grid result (blue dashed line) versus the fine grid (cwt-fg orange dashed line).

For the case of pure conduction, the melt front is one-dimensional and evolves parallel to the tube until 65% melt fraction is reached. Thereafter it starts to shrink downward. In contrast, melt fronts in the two other cases with laminar and turbulent convection are two dimensional, moving perpendicular to the tube after reaching about 20% melt fraction. The two-dimensional melt front before the 20% melt fraction means higher heat transfer area with modelling laminar convection and turbulent convection. However, for most of the process (after 20% melt fraction) the melt front shrinks downward faster compared to the pure conduction melting case where the melt front holds higher heat transfer area between solid and liquid up to the end of the process.
For pure conduction melting, the heat fluxes are lower and decrease sharply during the process whereas including natural convection modelling presents a more uniform process due to the mixing effect of convection cells that facilitates a higher rate of heat transfer. Comparing turbulent convection with the case of ignoring turbulence (Fig. 3.14a), clearly shows a higher rate of heat flux with a more uniform process; providing a higher rate of heat transfer for a longer period and starts to decrease sharply at the later stages of the process.
At about 90% melt fraction, pure conduction melting shows a higher heat transfer rate compared to the melting with convection due to the lower heat transfer area and lower velocity of convection cells which is the result of the lower temperature gradient as driving force. However, including turbulence compensates for the losses as a higher rate of turbulence (i.e. more convection cells with higher velocity) occurs at higher melt fraction resulting in higher heat transfer in comparison to the pure conduction melting and melting with convection.

3.3.5.4 Melting time

Despite the lower heat flux for the case of pure conduction, the melting time is shorter in comparison to the melting with convection, e.g. 97% of PCM melts after about 5600s and 6500s, respectively. This is due to the higher heat transfer area of the 1-D melting front in pure conduction which is effective at the later stages of process, e.g. after 60% melt fraction (Fig. 3.14b). Comparing the results, it has been found that incorporating turbulence results in a shorter melting time (5600s in comparison to 6500s to melt 97% of PCM) due to the higher rate of convection heat transfer, which increases with a higher rate of melt fraction and compensates for the lower average temperature difference between the heat source (HTF) and sink (PCM).

3.4 Conclusion

In this chapter, four major numerical studies were presented. The first, second and third studies aimed to validate the model setting for two and three dimensional cases while the fourth study aimed to investigate the involved transport phenomena in a PCM during a melting process.
In the first study in section 3.2.1, a numerical study of the inward melting of n-eicosane in a vertical cylindrical enclosure was performed and the results were validated with the experimental data from [40]. The heat source was defined as a fixed temperature at the outer surface of the PCM enclosure with all boundary conditions to replicate the experimental system. The predicted temperature and melt front location comparison with the experimental data were in good agreement. The quantitative and qualitative analysis of the results showed the capability of the model to capture the heat and mass transfer detail of the inward melting process of the PCM.

In the second numerical study presented in section 3.2.2, an annulus was selected as an element of a shell and tube PCM system where HTF passes through the inner tube and PCM fills the outer tube. For this system, experimental data was available for validation purpose. The quantitative and qualitative analysis of the results showed the capability of the model to capture the heat and mass transfer detail of the outward melting of water as the PCM.

As a three dimensional case, numerical modelling of the melting and solidification processes was performed to examine the validity of employing a small-scale model to represent a laboratory-scale shell and tube as a latent heat storage system, in section 3.2.3. Using water as the HTF and Rubitherm70 (RT70) as the PCM, evolution of the temperature profile in the PCM domain, outlet temperature of the HTF and duration of the phase change processes were compared with the experimental data. The discrepancies between the measured and predicted data are mainly due to the uncertainty in the measurements during experiments and simplification assumptions such as adiabatic boundary conditions for the numerical modelling.
For the four melting processes, there is better agreement between the measured and predicted data where the temperature difference between the PCM melting temperature and inlet temperature of the HTF are higher, e.g. $\Delta T = 20$ K compared with $\Delta T = 10$ K. While some discrepancies can be seen in the detail of the temperature field in the PCM, the predicted outlet temperature of the HTF and the predicted duration of the melting processes are in good agreement with the experimental data. While using different mushy region constants ($A_{mush} = 10^5$, 10^7, 10^8) has a minor impact on the results, starting the modelling from the same initial temperature at each thermocouple location can improve the results.
For the solidification process, the predicted temperature profiles show better agreement with the experimental data as conduction is the dominant mode of heat transfer. The outlet temperature of the HTF and duration of the phase change process are in good agreement with the experimental data. Similar to the melting processes, starting the modelling from the same initial temperature at each thermocouple location provides a better agreement with the measured data.
Overall, the three validation studies (two and three dimensional) show that the model used for inward and outward melting of low temperature PCMs can accurately predict the thermal behaviour of a phase change process. Considering the previous literature findings [126, 127], the model validated for a low temperature PCM can be used for high temperature PCMs within the same Ra number and where differences in Pr number are not influential. Thus, the validated model can be used to examine the thermal behaviour of high temperature PCMs in different cases of melting and solidification. Results are presented in chapters 4, 5, 6, 7.

To explore the impact of different heat transfer modes by the validated model, three numerical studies of a turbulent melting process ($Ra=10^{12}$) for a high temperature PCM were presented in section 3.3. The main objective was to compare the predicted results of modelling the system with pure conduction where natural convection is ignored with the two other cases where laminar convection and turbulent convection are included in the modelling. The first study showed a 1-D melt front, evolving parallel to the tube that results in lower peak temperatures and temperature gradients, higher heat transfer area for longer period, however, lower heat transfer rate due to neglecting natural convection. The second study presented a 2-D melt front, which evolves mainly perpendicular to the tube, shrinking downward resulting in loss of heat transfer area and higher peak temperatures and temperature gradient, however higher rate of heat transfer rate was observed due to the creation of convection cells which facilitate mass and heat transfer.
Including turbulent convection modelling led to a higher mixing effect due to higher velocity of convection cells, resulting in a more uniform process with lower peak temperature and temperature gradients and higher heat transfer rate. In a melting process with $Ra>10^{11}$, including convection (laminar or turbulent) modelling provides more realistic data of flow, mass and heat transfer for the purposes of design and optimisation of a high temperature LHTES for CSP applications.

A poster and a conference paper were prepared from the results of the first study for the SolarPACES2015 and the paper was published in the journal of American Institute of Physics (AIP) [136].

From the results of the third study, a poster has been presented in SolarPACES2017 and a full paper has been submitted which is going to be published by AIP.

The result of the fourth study was presented in the 14th International Conference on Simulation and Experiments in Heat Transfer and its Applications (2016) and a paper was published in International Journal of Computational Methods and Experimental Measurements [137].

4 Thermal performance evaluation and comparison of high temperature PCM systems during charging and discharging

For design and optimisation purposes, understanding the performance characteristics of different configurations of PCM systems during charging and discharging processes is crucial, particularly for thermal storage in CSP. Sensible heat storage is an inherent part of the melting and solidification process, contributing to a higher percentage of storage or release of heat for PCMs with higher Ste number. The focus of this study is to provide more insight into the characteristics of the latent heat storage/release process and the impact of different geometries and system arrangements, which ultimately can be used to create a more effective design of a LHTES system.

The main objective in designing a PCM system is to minimise thermal and flow resistance to achieve the highest heat transfer rate in a fixed volume (e.g. highest heat transfer density) and minimum pressure drop in the flow path. Having reviewed the literature in chapter 2, the shell and tube system and different types of plate fin arrangements in rectangular tanks are considered promising for high temperature PCM applications including thermal storage for CSP plants. The shell and tube (sometimes referred to as coil in tank) arrangement represents a potential practical application of PCM energy storage technology for high temperature storage. Specifically, it lends itself for use with gases such as supper critical-CO_2 coupled with the s-Co_2 Brayton power cycle [12, 23, 25], as well as superheated steam [138] for industrial heat and power. An alternative rectangular LHTES system comprising fin plates in vertical orientation is considered to explore the viability of this system in providing higher heat transfer density, resulting in a lower cost of the system. The main advantages of this system is the decoupled location for the PCM in a tank framed by the fin plates from the flow path of the HTF, which is a collective piping system at the bottom of the tank. Decoupled zones for PCM/tubes removes part of the constrains on the material selection to adapt for high working temperature/pressures, which are required for high performance electricity generation cycles. Having a major piping system at the bottom of the alternative fin plate system compared with a more distributed tubes (smaller sizes including more joints and/or bends) in a shell and tube system may reduce pumping electricity consumption. Moreover, the modularity of the fin plate system facilitates the design and optimisation of the system for different applications and scales.

Thus, this study aims to compare four configurations of shell and tube LHTES systems and with the alternative fin plate system. The shell and tube LHTES systems where HTF passes through tubes and PCMs fills the shell are considered in counter flow (two pass shell and tube, Fig. 4.1a) and parallel flow arrangements (one pass, Fig. 4.1b) in vertical and horizontal orientations. The alternative case considered here is comprised of fin plates in a PCM tank where HTF passes through a separate channel at the bottom of the tank. More information about the systems and model scale for numerical studies are provided in sections 4.2, 4.3, and 4.4.

Numerical studies using FLUENT have been performed to explore and compare the characteristics and thermal behaviour of PCM in these configurations. Modelling of melting (charging) and solidification (discharging) processes in different configurations provide detailed profiles of flow, mass and heat transfer in space and time. A thermodynamic analysis of this data clarifies the viability of each system for different applications.

4.1 Thermodynamic analysis, first and second law

From the first law of thermodynamics perspective, the system should provide the highest efficiency in both melting (charging) and solidification (discharging) processes. Adapted from the shell and tube literature, latent heat effectiveness (Eq. 10) can be used to assess the efficiency of a shell and tube LHTES system in the storage of the provided heat or in releasing of the stored heat. Ideally, the highest performance of the system ($\varepsilon = 1$) occurs when the outlet temperature of the HTF equals the melting temperature of the PCM ($T_{out} = T_m$) for both charging and discharging processes.

$$\varepsilon_{ch} = \frac{T_{in} - T_{out}}{T_{in} - T_m} \qquad \varepsilon_{dch} = \frac{T_{out} - T_{in}}{T_m - T_{in}} \tag{10}$$

While Eq. 10 provides a means to evaluate latent heat effectiveness of a shell and tube LHTES system, there is no such equation for systems with fixed temperature/heat flux surfaces as heat source/sink (e.g. a fin plate model). It is possible to evaluate the ratio of the average heat transfer to PCM to the heat input (in a melting process) to the system. In this numerical study, Eq. 10 is used to compare the thermal performance of shell and tube LHTES systems described in section 4.2. To avoid further approximation and comparison of thermal performance on the same basis, the average heat flux (W/m^2) is used for the first law performance comparison of shell and tube systems with an alternative rectangular system with fin plate explained in section 4.3.

In designing a LHTES system, there are limitations such as the available temperature of HTF in a charging process while in a discharging process, it is crucial to provide the required rate of heat transfer at the necessary temperature. For the melting processes, the temperature difference between the HTF and melting front lasts longer, whereas this difference decreases faster during the discharging processes due to a solid layer formation on the heat transfer surfaces such as the tubes [65]. As a result, part of the PCM becomes redundant and incapable to provide the required heat transfer rate to support the demand side in the later stages of the discharge processes [23, 139]. Based on the first law analysis of a LHTES system, an optimum design should decrease or eliminate the redundant PCM to achieve a higher energy storage density in a smaller size system, which is more cost effective.

On the other hand, considering the second law of thermodynamics, an optimum design should minimise entropy generation and recover the highest exergy or the highest available work/power as the ultimate goal of a storage system[38]. The irreversibility due to the heat transfer, mass transport and viscous dissipation may affect the performance of LHTES systems like many other thermal systems. Entropy, a thermodynamic property, quantifies such irreversibility and provides a tool for the second-law analysis of the system, realising the limits and improvement opportunities [110]. Assuming inviscid, laminar flow (assumption (iii), section 3.1), irreversibility generation due to the viscous dissipation is negligible in comparison to the heat transfer [111]. The rate of entropy generation in the PCM domain of a LHTES system can be written as follows:

$$\nabla \dot{s} \ = \frac{q.\ \nabla T}{T^2} \qquad\qquad \dot{s} = \int_{T_m}^{T_h} \frac{q}{T^2}\ dT \tag{11}$$

Where q is the heat flux between the HTF and PCM domains through the heat transfer area (tube/plate thickness). The proportionality of the entropy generation with the temperature gradient (∇T) is obvious, however, proportionality to q and reverse proportionality to T^2 should be considered simultaneously.
Exergy is the available work at any stage of a cycle, and in an exergy analysis, the available work (e.g. input, output) and the lost part of it (e.g. E_{in} -E_{out}) is calculated. However, the ultimate objective in a design optimisation process is entropy generation minimisation (EGM) [109, 110].

$$\dot{W}_{rev} - \dot{W} = T_0 \dot{s} \tag{12}$$

Here the real available rate of output work from a process ($\dot{W}$, J/s) is compared to the ideal rate of output work ($\dot{W}_{rev}$) and the difference is the rate of destroyed available work or exergy.
In this numerical study, entropy generation through the charging and discharging processes in different configurations of LHTES systems (described in sections 4.2, and 4.3) is the basis for the second law comparison.

4.2 Shell and Tube system

The performance of parallel and counter flow (Figs. 4.1a, and b) configurations of a shell and tube heat exchanger used as a latent heat thermal storage system is investigated. The comparative analysis of the melting and solidification processes (charging and discharging) in the vertical and horizontal orientations of counter and parallel flow is included in this study to make the results conclusive for the design purpose of the storage system to be used in a CSP plant. In this analysis, which includes natural convection, numerical calculations were performed using ANSYS Fluent.

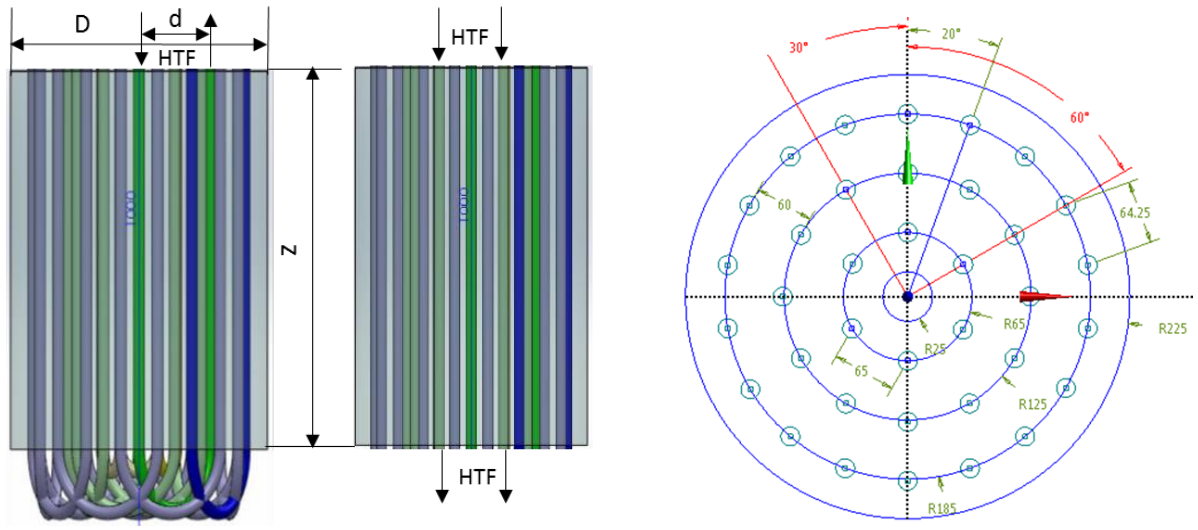
The modelling conducted in this study is a representative of a counter flow prototype currently under investigation at the University of South Australia (UniSA) suited to this application. For practical testing purposes the prototype uses ambient pressure air as the HTF and is designed using the ε-NTU method as outlined in [23]. The ε-NTU method enables a design of the configuration considering the resistance to heat transfer through the PCM, HTF and tube wall assuming one dimensional heat transfer. Dimensions and flow rates were specified to ensuring the

Table 4.1: Thermophysical properties of PCM [135]

Density, kg/m^3	2000
Specific heat, kJ/kg K	1730
Latent heat of fusion, kJ/kg	182
Thermal conductivity, W/m K	0.57
Thermal expansion coefficient	0.00066
Dynamic viscosity, Pa s	0.00302
Melting temperature, ˚C	306.8

Table 4.2: Thermophysical properties of air

Density, kg/m^3	1.226
Specific heat, kJ/kg K	1006
Thermal conductivity, W/m K	0.0242
Dynamic viscosity, Pa s	1.789e-5
Mass flow rate, kg/s	0.005
Velocity in tube, m/s	0.5



(a) (b) (c)

FIGURE 4.1. Schematic drawings of vertical view of the shell and tube systems:
(a) counter flow, (b) parallel flow, (c) horizontal cross section (dimensions are in mm)

thermal resistance in the HTF is sufficiently low as to enable investigation of the heat transfer characteristics through the PCM. The design was based on applying the heat transfer and energy storage requirements for a CSP plant outlined in [23], with a nominal capacity about 4.9 kWh. Fig 4.1c shows a cross section of the prototype with dimensions in mm. The shell radius is 225 mm with 1000 mm height that provides z =550 mm as the height of active PCM (Fig. 4.1a). The tube material is copper with thickness equal to 1.41 mm, outer diameter equal to 19 mm and centre to centre tube distance on average is 60 mm (Fig. 4.1c). Mass flow rate through each tube can be varied between 0.001 to 0.01 kg/s.

To simplify the numerical calculation, an element of the shell and tube arrangement was selected for which specifications were acquired from the system described above. The height of the vertical tube is z =55 cm with a centre to centre distance between tubes equal to d = 6 cm as shown in Fig. 4.2c. Sodium nitrate was considered as the PCM with a melting temperature of 306.8 ºC and atmospheric air as the HTF (Table 4.2) with an inlet temperature of 356.8ºC for the melting case and 256.8 ºC for the solidification case. All thermophysical properties of the PCM were adopted from [135] and is shown in Table 4.1. In this case the temperature difference between the inlet of the HTF and melting temperature of the PCM is 50ºC; $\Delta T=|T_{in}-T_m|=$ 50ºC. Using high temperature PCM in LHTES systems for CSP plants, a high ΔT is expected, leading to a high Ra which is ~ 10^{10} and ~ 10^{7} for the vertical and horizontal cases, respectively. To focus on the phase change process, the initial temperature of the PCM was set to 302 ºC for the melting case and 310 ºC for the solidification case (within 5ºC of the phase change temperature).

To make the heat input to the parallel flow case comparable to the counter flow in 2D modelling, the mass flow rate (ṁ) through each tube in the parallel flow configuration (PF) is half of the mass flow rate in the U- tube of the counter flow configuration (CF). The tube diameter is half for the parallel flow arrangement to keep the velocity of the HTF the same as the CF. As a result, heat transfer area at the tube-PCM interface is the same for all cases in the 2-D analysis. The Ra number was the same for all vertical cases equal to10^{10} and for all horizontal cases equal to10^{7}.

$$\text{(CF side)} \quad \dot{m}C_p(T_{in}-T_{out}) = 2\times\frac{\dot{m}}{2}C_p(T_{in}-T_{out}) \quad \text{(PF side)} \qquad (13)$$

4.3 Plate Fin system

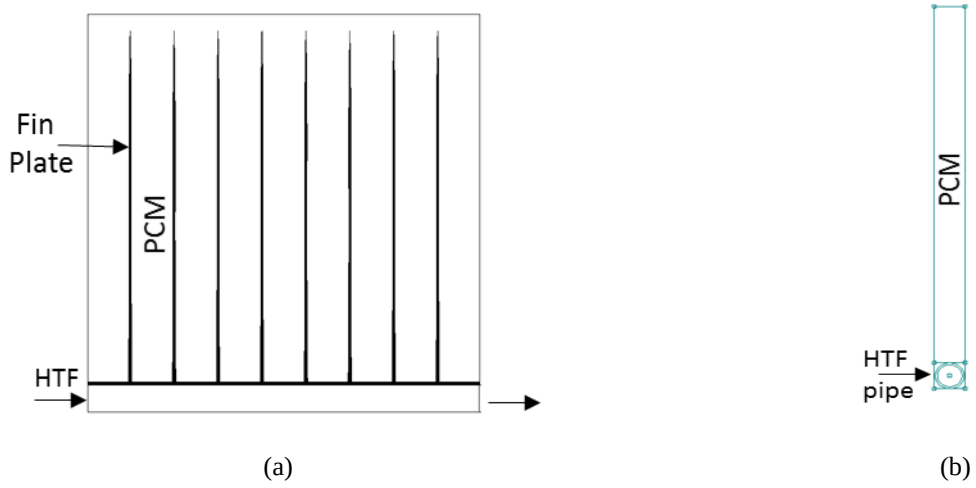
For the purpose of comparison with the shell and tube configurations, the rectangular LHTES concept adapted from Verdier at al. [32] was designed with a rectangular PCM chamber framed by vertical plate fins while the HTF passes through a channel at the base of the PCM (Fig. 4.2a). The HTF transfers heat to the PCM only from the bottom of the rectangular chamber through the plate fins while the two end sides of the PCM system and top are insulated. The HTF channel at the base, and the plate fins in the PCM chamber are made of copper and conduct heat from/to the HTF to/from the PCM where conduction and forced convection heat transfer are involved. The main objective in designing a PCM system is to minimise thermal and flow resistance to achieve the highest heat transfer rate in a fixed volume (e.g. highest heat transfer density) and minimum pressure drop in the flow path.

For the PCM section, the plate aspect ratio (height to distance between the plates), ratio of the height of plate to the height of the enclosure, and plate thickness (e.g. the thinnest robust plate for the highest PCM volume fraction) need to be optimised, leading to the minimum global resistance (flow and thermal) to the conduction and convection heat transfer. This concept was designed according to the constructal law used by Da Silva and Bejan [140]. An approximate optimal solution was developed as a complete application of the constructal approach is beyond the scope of this study. Ultimately, the final optimal solution will deliver less entropy generation than that defined for this study. The optimal thickness of plates, distance between the plates (width of PCM), and the aspect ratio (ratio of height to the width) were calculated using the constructral approach proposed by Naegu and Bejan [121]. The height and distance between plates (z, d) are considered comparable to the shell and tube system, ensuring the same heat transfer area, and amount of PCM. For instance, the optimum distance between plates follows two correlations regarding the thermophysical properties (e.g. *k*, thermal conductivity of plates and PCM), and PCM volume fraction;

$$Conduction: \qquad \tilde{k} = \frac{k_{plate}}{k_{PCM}} = 680, \ \emptyset = 0.95, \quad \Rightarrow \quad \frac{d}{z}\Big)_{opt} = 0.35 \tag{14}$$

$$Covection: \qquad d = 2\delta_T = 2z\, Ra^{-0.25} \tag{15}$$

Here, δ_T is the thickness of the thermal boundary layer of natural convection at the plates. On the other hand, the distance and height of the plates should be consistent with the shell and tube geometry, ensuring the same amount of PCM, resulting in d = 4.2 cm which is close to the optimum for maximising natural convection in the PCM.
For the HTF section, the highest thermal contact between the HTF and the plate structure to get the highest rate of heat transfer and minimum pressure drop are the main objectives. While free convection and conduction are the heat transfer modes in the PCM section, forced convection and conduction are the heat transfer modes through the wall and the HTF. From the two feasible alternatives for the flow architecture of the HTF; using plates (plates forming channels, and one channel being the best as proposed by Bejan and Lorente [54]) or pipes, a single pass pipe formed in the solid structure has been selected. Practically in a 3 -D case, this selection replicates a parallel flow, single row arrangement, Fig. 4.2b. This configuration has been selected, with a circular cross section for the HTF channels delivering a lower pressure drop than that with a rectangular cross section.
The criteria defined by Eq. 14, 15 and comparability with the shell and tube system were considered for a preliminary design of the vertical plate fin LHTES system for a preliminary 2-D numerical study. However, the constraints of being comparable to the specific shell and tube cases are not required as part of the criteria in a practical detail design of the system. The aim of this preliminary design and numerical study was to understand the thermal behaviour and characteristics of such a system. The acquired knowledge from the preliminary numerical study provided information (e.g. boundary conditions) for the model of an element of a rectangular plate fin system (Fig. 4.3a) comparable to the element of the shell and tube systems (Fig. 4.3b-g) for the main numerical study.
For the preliminary two-dimensional numerical study, the same PCM and HTF as for the shell and tube system were used. The results showed that at the quasi steady state phase change process, a constant heat flux from the base of each PCM chamber is a reasonable assumption. The assumption is relevant for the middle chamber (Fig. 2a) as an element of the plate fin LHTES system (Fig. 4.3a) considered for the main two-dimensional numerical study and comparison to the element of the shell and tube configurations (Fig. 4.3b-g).



(a) (b)

FIGURE 4.2. Schematic drawings: (a) vertical flat plate LHTES system, (b) side view of the flat plate system

4.4 Numerical modelling

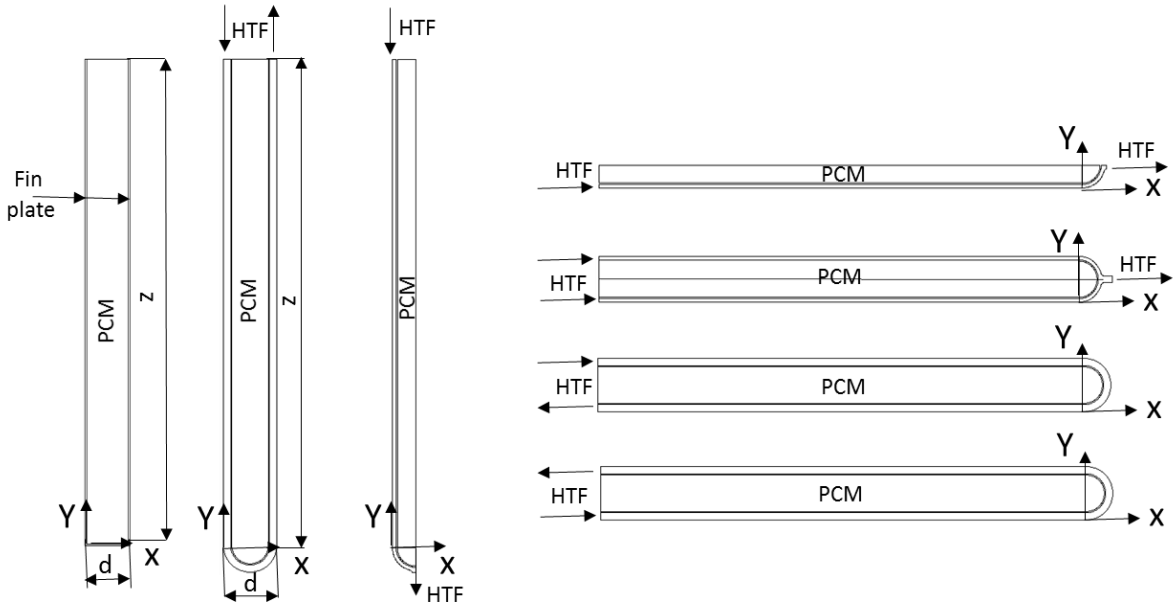
The time dependent Navier-Stokes equations (in section 3.1) were solved including the latent heat transfer and phase change in the mushy zone, and zero velocity in the solid region. The assumptions to simplify the problem were the same as described in section 3.2.1.2. Assuming constant density of PCM (ii) except in the Boussinesq approximation (i) ensures the accuracy of buoyancy forces and natural convection calculation (Eq. 3) in the liquid phase.

4.4.1 Geometry and grid

4.4.1.1 Shell and Tube models

Due to symmetry in the parallel flow vertical (PFV) case, a two-dimensional geometry of half of the element (half HTF in one of the 2 parallel tubes and half surrounding PCM, Fig. 4.3c) was considered with a grid size of 33650 cells, fine enough to capture details within thermal and velocity boundary layers. Considering a grid independency study, using a fine grid with 56000 cells of the parallel symmetry model (Fig. 4.3c) in a melting process demonstrated less than 1% difference in the melt fraction up to 91% and less than 2% difference up to 97% melt fraction as shown in Fig. 4.14a (PFV versus PFV-fine). For the counter flow vertical and horizontal (CFV and CFH) arrangements, a grid of a U-tube element of the tube bundle with the PCM contained between tubes (Figs. 4.3b and 4.3f, and g) was considered with 72000 cells. For the parallel flow horizontal (PFH) melting case due to the creation of the Benard convection cells explained in section 3.3.1.1, a full grid of 72000 cells was considered of a dual-tube (Fig. 4.3e). Using a mapped face meshing method, dominant cell types are quadrilateral with minimum size of 0.75 mm at the tube-PCM interface and smooth increase (bias factor = 1.2) towards the centre of the PCM domain were used. The orthogonal quality of the mesh is equal to 1 (in the range of [0,1], 1 is the highest quality) [37] everywhere throughout the grid apart from the bottom circular part of the mesh for which the minimum orthogonal quality is 0.5. The high orthogonal quality of the mesh excludes the artificial impact on the flow, which is particularly important on the convection flow in the PCM domain.

Two cases of the counter flow horizontal geometry were included in the numerical modelling where HTF enters either from the tube at the top (CFHT, Fig. 4.3f) or from the tube at the bottom (CFHB, Fig. 4.3g). The time step of 0.1 seconds was selected to achieve adequate accuracy within a realistic calculation time [141].



(a) (b) (c) From the top: (d), (e), (f), (g)

FIGURE 4.3. Schematic drawing of the numerical models: (a) fin plate vertical, (b) counter flow vertical, (c) symmetrical parallel flow vertical, (c) symmetrical parallel flow horizontal solidification, (d) parallel flow horizontal melting, (e) counter flow horizontal with HTF entrance from the top, (f) counter flow horizontal with HTF entrance from the bottom

4.4.1.2 Fin Plate model

From the vertical plate fin LHTES concept (Fig. 4.2a) a module in the middle was selected as the geometry (Fig. 4.3a) with dimensions; height z = 55 cm, centre to centre of plates = 4.4 cm, and thickness of each copper plate equal to 2mm. In the 2-D geometry, the height of the fin plates (z) are considered the same as the height of the tubes, and the distance between the plates is determined so that the same surface area of PCM is generated between the plates and between the tubes (0.023 m^2).

A grid with about 52000 cells was considered for the rectangular geometry (Fig. 4.3a) with a comparable resolution to the shell and tube cases.

4.4.2 Numerical calculations

The solidification and melting model in Fluent [35] was implemented with the pressure based coupled algorithm to solve the momentum and continuity equations. The numerical schemes and thresholds are the same as explained in chapter 3, section 3.2.1.2.

4.4.3 Boundary conditions

4.4.3.1 Shell and Tube models

Three domains of HTF, tube thickness and PCM were introduced. In PFV, taking half the tube and half the PCM as the grid, symmetry boundary conditions were used at the HTF and PCM, adiabatic conditions were used at the top and bottom of tube and PCM, and a fixed inlet/outlet at the top/bottom of the HTF. The setting of boundary conditions including the symmetry at the HTF and PCM mimics an element of a tube bundle in a shell and tube arrangement for which the edge effect is experienced only at the top and bottom of the tube and shell. This is justified as the dual-tube size is small compared to the diameter of the shell, i.e. 6 cm << 45 cm. For the cases of CFV, CFH, and PFH a full grid was used (Fig. 4.3b, e, f, and g), and the boundary conditions are: symmetry at the side of HTF, inlet and outlet of HTF, and adiabatic at the top of the PCM, tube, and at the bottom of the HTF.

4.4.3.2 Fin Plate model

For the fin plate vertical model (Fig. 4.3a), three domains were included; copper base, plates (sides) and PCM. The boundary conditions assigned; constant heat flux at the base, symmetry at the sides, and adiabatic at the top of the PCM and plates. The amount of heat flux to/from the PCM, for the melting and solidification cases were determined as 175/192 W, respectively (Eqs. 16, and 17). The values were taken to be equal to the average heat flux to/from the PCM transferred by HTF during the latent heat transfer in the counter flow shell and tube case (Fig. 4.13c) with the relevant temperature differences from the modelling results.

$$For\ melting\ in\ CF: \qquad \dot{m}_{HTF} C_p (T_{in} - T_{out})_{ave} = 0.005\ \frac{kg}{s} \times 1006\ \frac{J}{kg\ K} \times 35\ K = 176\ W \qquad (16)$$

$$For\ solidification\ in\ CF: \qquad \dot{m}_{HTF} C_p (T_{out} - T_{in})_{ave} = 0.005\ \frac{kg}{s} \times 1006\ \frac{J}{kg\ K} \times 38.2\ K = 192.2\ W \qquad (17)$$

4.5 Results and discussion

In this section, results of the numerical studies of the four shell and tube cases (CFV, PFV, CFH, PFH) and fin plate vertical model (FPV) are discussed and compared. The models for the 2-D cases (Fig. 4.3a-g) were determined on the bases of the same heat transfer area, same amount of PCM and same average amount of heat input/output for the melting/solidification cases, which were outlined in section 4.4.1.1 and 4.4.1.2.

As a basic first law analysis of the shell and tube cases, their thermal performance is assessed and compared using Eq.10. The lowest performance system is removed from the detailed analyses in the following sections. Then, the temperature field, temperature gradient and velocity field (stream function as a vector field is the indicator of the flow and velocity field, providing data of mass transfer) for the solidification and melting processes are discussed and compared. It is important to present and compare the mass flow in different cases as it shows the level of natural convection which carries and transfers heat in the PCM domain. The knowledge of temperature and velocity fields provides the fluid dynamic background to understand the transient phase front evolution in the PCM domain. The phase front formation and changes are the outcomes of the temperature gradients and mass transfer in the PCM domain, being the subject of section 4.5.4. As the first law evaluation with the background knowledge, the assessment of heat transfer in different configurations and the reasons behind the differences are discussed in section 4.5.5. Afterwards, the duration of charging and discharging processes is discussed/compared.

Finally, the second law analysis gives a full picture of the performance and characteristics of different systems and plausible applications. The entropy generation in both processes within all cases are compared on the bases of the temperature field and temperature gradients as the entropy generation due to viscous dissipation is assumed to be negligible (assumption iv in section 3.1). The temperature gradient driving a mass flux in the liquid region (density is assumed constant except in the Boussinesq approximation (assumptions i, ii in section 3.1) of the PCM is compared for different cases in section 4.5.2.

4.5.1 Effectiveness

As mentioned in section 4.1, considering the first law assessment/comparison of different shell and tube configurations, the latent heat effectiveness (Eq. 10) is the relevant parameter. Assessment and comparison of the first law performance of the fin plate system with the shell and tube systems is performed based on the average heat transfer to or from PCM during charging and discharging processes. Results are discussed in section 4.5.4.

Figure. 4.4 presents the effectiveness of different configurations of the melting process. Comparing PFV and CFV, again parallel flow provides a higher effectiveness with lower uniformity. The effectiveness starts to decline after 40% melt fraction for both configurations, however a steeper decline is observed in PFV. Comparing the vertical and horizontal orientations, a more uniform process leading to a longer plateau in effectiveness profile is noticeable for the horizontal cases. In between the CF cases, results show the highest effectiveness for CFHB, then CFV, and the lowest for the CFHT. This is consistent with the analytic results that reported lower Nu for the enclosure heated from the top (180 degree inclination) [133].
PFH presents the greatest effectiveness due to the PCM exposure to the HTF inlet temperature from both tubes, and the Benard convection mixing impact in providing a lower temperature gradient and more uniform process. As mentioned previously in section 4.4.1.1, the numerical calculation of the melting process in PFH was performed with a full geometry (Fig. 4.3e). The result of this case shows the same trend as other PF melting processes at early stages but continues at a longer plateau due to the impact of Benard cells formation at the bottom of PCM.
Moreover, the results show a smaller difference between PFV-MC and PF-MWC compared to CFV-MC and CF-MWC, due to the higher rate of natural convection in CF compared to the PF. Hence, including natural convection in the numerical calculation of CF is more important. The results for melting process in counter flow without natural convection (CFV-MWC), shows a more uniform process and longer plateau in effectiveness profile which is related to the melt front, heat transfer area between solid/liquid and temperature gradient across the PCM. Results show that neglecting natural convection results in a one-dimensional phase front evolving parallel to the tube until the final stages in the process, which leads to higher heat transfer area for a longer period (e.g. up to 83% melt fraction). However, in the melting with natural convection (CFV-MC) the melt front is two-dimensional (Fig. 4-11b), and heat transfer area starts to decrease earlier in the process (effectiveness starts steep decrease after 40% melt fraction).

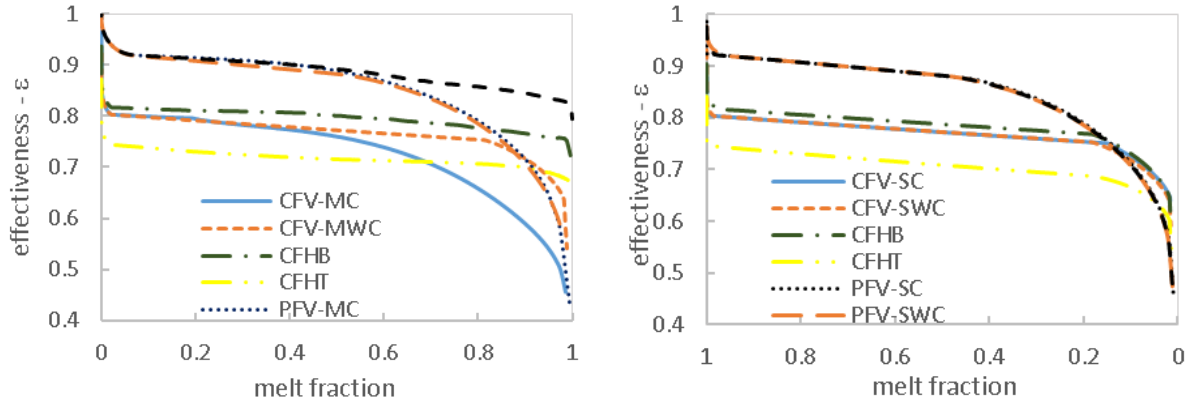


FIGURE 4.4. Temporal evolution of effectiveness: (a) melting, (b) solidification

In solidification, again the main difference is observed between PF and CF, PF providing higher effectiveness which drops after 55% freezing compared to the lower effectiveness provided by CF configuration which starts to decrease after 85% of liquid PCM changed to solid. The less uniform temperature field in space and time for the PF compared to the CF resulted in a decrease in heat transfer area earlier during the process for the PF configurations (Figs. 4.9a, b). Comparing horizontal and vertical orientations, while there is not much difference among the PF cases, CFHB provides on average a 2% higher effectiveness and CFHT presents about 5% lower effectiveness compared to CFV. In the CFHB, cold HTF entering from the bottom and leaving warmer from the top tube, forms a natural thermosiphon loop, creating a low temperature gradient in the liquid phase across the width of PCM. Results of mass flux show that this low temperature gradient (warmer at the upper layers and colder at the lower layers) results in convection cells with higher velocity that increases the heat transfer rate in the CFHB (higher mass flux in CFHB compared with CFHT as shown in Fig. 4.5d, e). Whereas in CFHT, the cold HTF entering from the top and exiting warmer from the bottom tube hinders the thermosiphon loop

formation, resulting in lower mass flux. Therefore, the best performance is provided by CFHB among the CF solidification processes. Results of the solidification process without natural convection (CFV-SWC) show that the effectiveness starts to decrease sharply after 78% of PCM changes to solid. Indeed, the effectiveness starts a steep decrease after 85.8% solidification because of a very low impact of natural convection (CFV-SC). In a numerical modelling of PF solidification, a lower impact from including natural convection is expected.

As explained above, the effectiveness of the horizontal counter flow system where the HTF entrance is from the top tube (CFHT) is the lowest for both charging and discharging processes. Thus, in the next episodes of assessment and comparisons the more effective case of horizontal counter flow is considered where the HTF entrance is from the bottom tube (CFHB).

4.5.2 Temperature field

4.5.2.1 Discharging

Figure. 4.5 presents temperature contours at different time-slots during the discharging process for different configurations. First considering the shell and tube cases and comparing the CFV and PFV (Figs. 4.5d-i), a higher temperature gradient can be observed along the height of the PCM in PFV because of the exposure of PCM to the inlet temperature of HTF from both tubes. However, the temperature profile across the width of PCM is symmetrical in PFV and there exists a higher temperature gradient across the width of CFV. A higher temperature gradient across the width results in a greater rate of natural convection in CFV. This condition results in a more uniform process in CFV, providing a nearly constant effectiveness and heat transfer rate which starts to decrease in the later stages in the process compared to the PFV (Figs. 4.4b, 4.13b).
Due to the minor role of natural convection in the solidification process, minor differences can be seen between vertical and horizontal temperature distributions compared to the melting processes. This is particularly true for the PF cases, however, there is a higher temperature gradient in the horizontal CF case (CFHB) compared to the CFV. It is known that in the later stages of a solidification process a lack of temperature gradient and driving force of free convection results in a reduced heat transfer rate. In this regard, a higher temperature gradient can be considered an advantage of the horizontal CF.

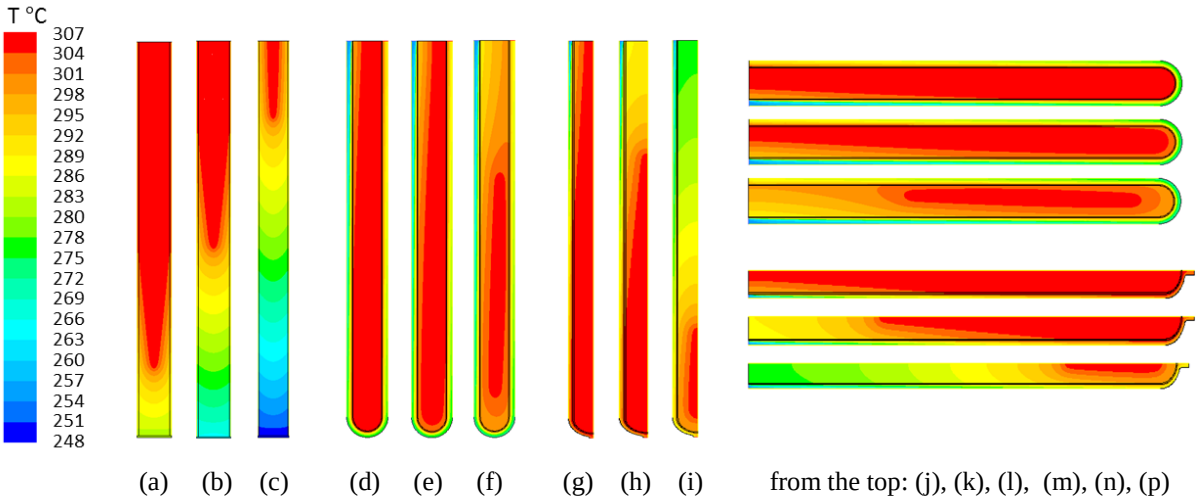
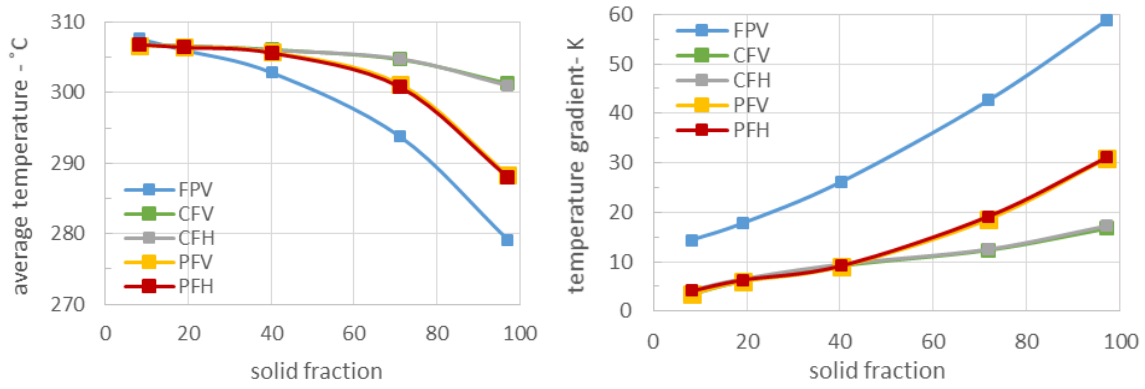


FIGURE 4.5. Temporal evolution of temperature profile during solidification process:
FPV: a) 20900s, δs=40.3%, b) 38750s, δs=71.1%, c) 56650s, δs=97.2%, **CFV**: d) 19600s, δs=40.3%, e) 34350s, δs=71.1%, f) 48400s, δs=97.2%, **PFV**: g) 16200s, δs=40.3%, h) 29500s, δs=71.1%, i) 46150s, δs=97.2%, **CFHB**: j) 19600s, δs=40.3%, k) 34350s, δs=71.1%, l) 48600s, δs=97.2%, **PFH**: m) 16200s, δs=40.3%, n) 29650s, δs=71.1%, p) 46300s, δs=97.2%.

Figure. 4.5a-c shows the temperature field at three stages of different configurations namely fin plate vertical (FPV), where the coolest medium occurs in FPV compared with all other cases, particularly towards the end of the process. Figure. 4.6 provides a comparison of average temperatures and temperature gradients in the PCM during the discharging process for different configurations. Fig. 4.5 and Fig. 4.6 collectively demonstrate that the lowest average temperature but highest temperature gradient up to the end of the process occurs in the FPV system. Regarding the lack of the temperature gradient and driving force for heat transfer at the later stages [65], the FPV configuration provides a higher temperature gradient for a longer period, resulting in higher driving force for heat transfer that continues longer during the discharging process relative to the other configurations. (Fig. 6b).



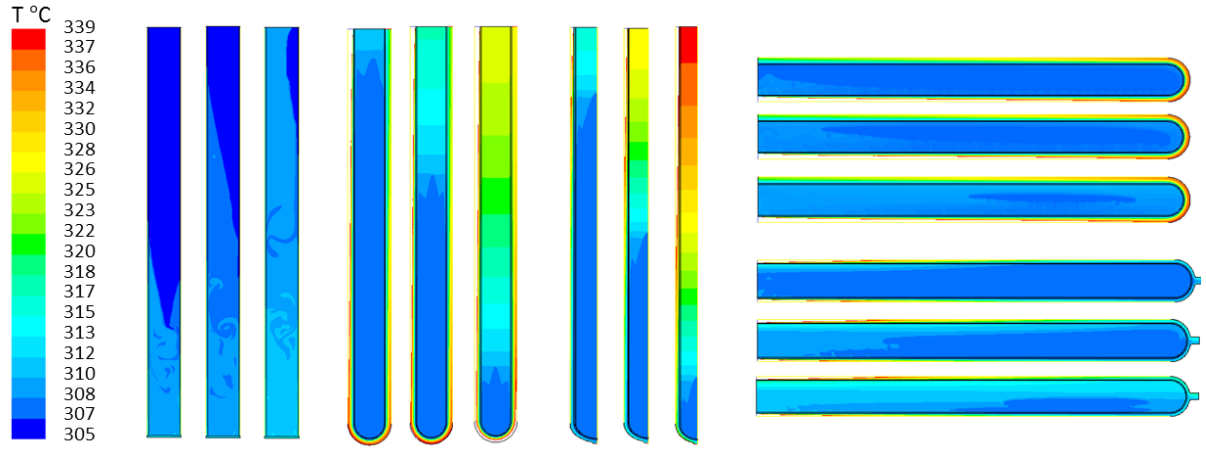
(a) (b)

FIGURE 4.6. Temperature evolution in PCM during discharging processes versus: (a) average temperature, (b) temperature gradient

In general, a higher temperature gradient across the width and lower temperature gradient across the height occur in the CFV. On the other hand, a lower temperature gradient across the width and higher across the height occur in the PFV and FPV. As a result, the average rate of heat transfer for the FPV during the discharge process is shown to be between the PFV and CFV cases (Fig. 4.13b).

4.5.2.2 Charging

Figure. 4.7 provides a comparison of the temperature field during the charging process for all configurations. Temperature profiles demonstrate the same tendency as in the discharging cases, higher temperature gradient across the height and symmetrical temperature profile across the width for the PFV, resulting from the HTF entering into the tubes within the same direction. Comparing the profiles in Figs. 4.7d-i, the temperature gradient is lower across the height of the CFV arrangement and there is a recognisable temperature difference across the width, (i.e., no symmetry). A higher temperature gradient and higher peak temperature in the PFV configuration results in a less uniform process, decreasing effectiveness and heat flux sooner in the process (after 35% melt fraction) compared to the CFV for which heat flux starts to decline after 50% melt fraction (Fig. 4.4a, and 4.13a). Comparing the vertical and horizontal cases, a higher temperature gradient can be seen across the PCM in vertical cases while a more uniform temperature can be observed in the horizontal cases. In the vertical configuration, Ra is higher compared to the horizontal configurations (10^{10}, and 10^{7}) which means a higher rate of natural convection in the vertical cases. However, Benard convection cells [133] distributed along the bottom of the horizontal cases provide a higher rate of mixing due to the distribution of smaller convection cells (Fig. 4.10e-l). Velocity of the smaller cells are higher compared to the fewer larger cells (Fig. 4.10a-d) with lower velocity stretching across the



(a) (b) (c) (d) (e) (f) (g) (h) (i) from the top: (j), (k), (l), (m), (n), (p)

FIGURE 4.7. Temporal evolution of temperature profile during melting process: **FPV**: a) 20050s, δl =36.9%, b) 35000s, δl =68.4%, c) 48000s, δl =94.7%, **CFV**: d) 18650s, 36.9%, e) 34300s, 68.4%, f) 52300s, 94.7%, **PFV**: g) 15600s, δl =36.9%, h) 29800s, δl =68.4%, i) 44950s, δl =94.7%, **CFHB**: j) 18450s, 36.9%, k) 32700s, 68.4%, l) 42500s, 94.7%, **PFH**: m) 15350s, δl =36.9%, n) 27450s, δl =68.4%, p) 38500s, δl =94.7%.

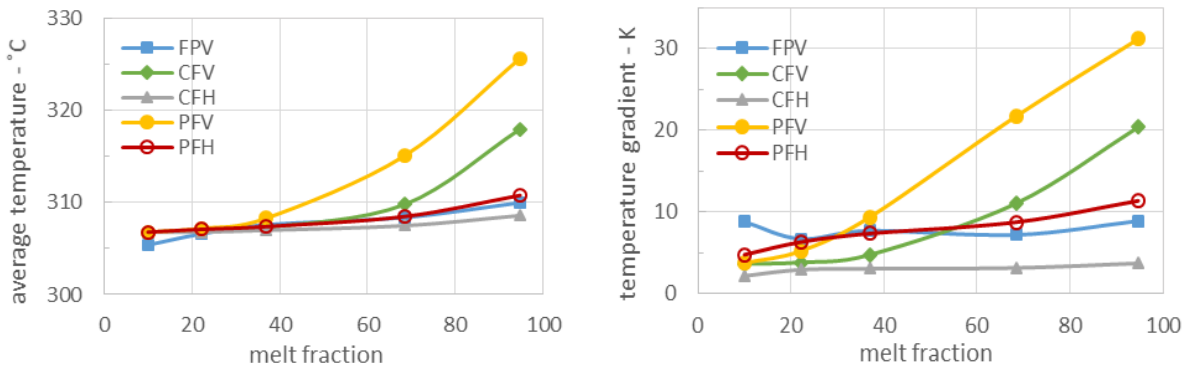


FIGURE 4.8. Temperature evolution in PCM, during charging processes versus:
(a) average temperature, (b) temperature gradient

height of PCM in the vertical orientation, resulting in a lower mixing rate for the vertical cases. Thus, the horizontal configurations provide a more uniform temperature field and lower peak temperatures (Fig. 4.7j-p), leading to a longer plateau in the heat transfer rate (Fig. 4.13a) and effectiveness (Fig. 4.4a) profiles.
Figures. 4.7a-d show lower temperature gradients during the charging process of FPV compared with the vertical cases of counter and parallel flow but almost at the same level compared to the horizontal orientations of counter and parallel flows. This can be clearly seen in the graphs of Fig. 4.8a, which show a lower and more uniform average temperature for FPV, CFH and PFH while there is a steep rise in temperature in the vertical orientation of PF and CF. With a similar trend, Fig. 4.8b reveals a lower and more uniform temperature gradient during the charging process for the FPV compared to the horizontal orientation of CF and PF, however a steep rise of temperature gradient is shown in the vertical cases of CF and PF. This means the thermal behaviour and performance of a FPV system during a charging process is closer to the horizontal orientation of CF and PF.

4.5.3 Mass transfer

Assuming constant density except in the calculations of the buoyancy forces in the momentum equation (transient Navier-Stokes equations including momentum are presented in chapter 3, section 3.1), the temperature gradient drives the flow in the liquid region of the PCM. The resulting stream functions as a vector field define the mass flow and velocity field.

4.5.3.1 Discharging

Figure 4.9 shows a comparison of the stream functions during the solidification process in different configurations. In PFV, HTF entering in both tubes results in a symmetrical temperature profile across the width and lower driving force for natural convection, as it is shown through the stream function. The magnitude of maximum mass flux is higher in the CFV (0.0031 kg/s and 0.0025 kg/s at 8.2% solid fraction, Figs. 4.9a, b) compared to PFV.
Comparing the horizontal and vertical configurations, the results show almost identical mass flux for PF (PFV: 0.0025 kg/s, PFH: 0 .0026 kg/s), however, there is a notable difference in the pattern of stream function for the CF (CFHB: 0.0042 kg/s, CFV: 0.0031 kg/s). Considering the temperature difference between two tubes in CF cases, convection cells are smaller in the horizontal cases compared to the vertical ones. In the PF configuration without temperature difference between tubes, convection cells form the same pattern in both orientations.
On the other hand, the highest rate of mass transfer occurs for the FPV case compared to all other configurations. This is due to the higher temperature gradients across the PCM domain (Fig. 4.6b) which provides a higher driving force for natural convection during the early stages of the process.

4.5.3.2 Charging

Figure. 4.10 demonstrates the mass flux across the PCM during the melting processes. A symmetrical temperature profile across the width means a lower driving force for natural convection in PFV, leading to stream functions showing lower mass flux across the PCM during the melting process. The mass flux at the early stages of the process shows a lower difference in CFV and PFV due to low melt fraction (e.g. at δl =22.1%, the average mass

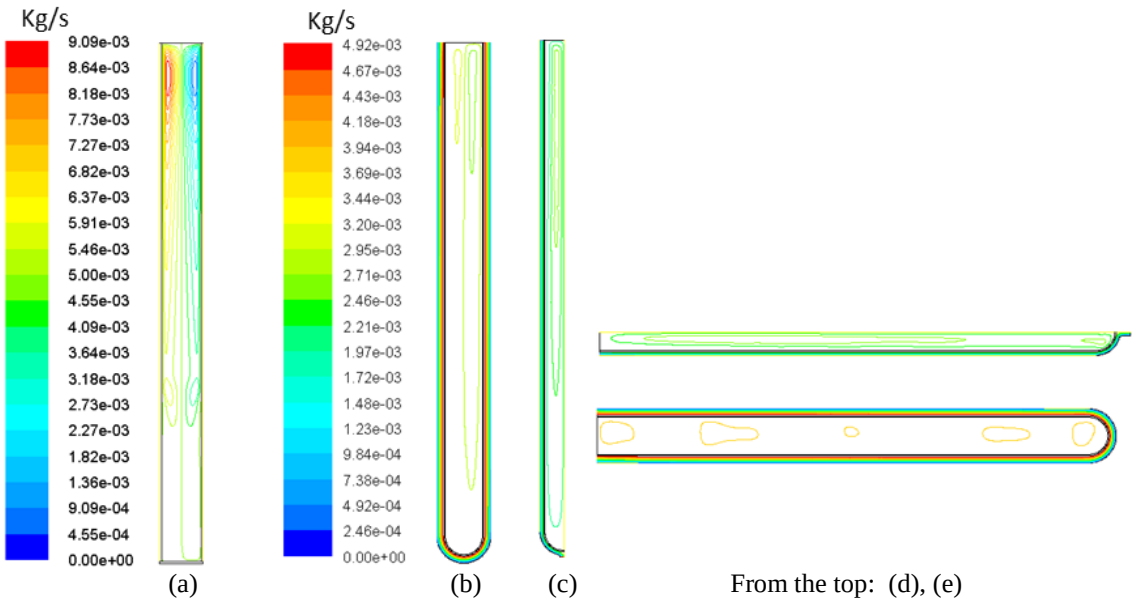
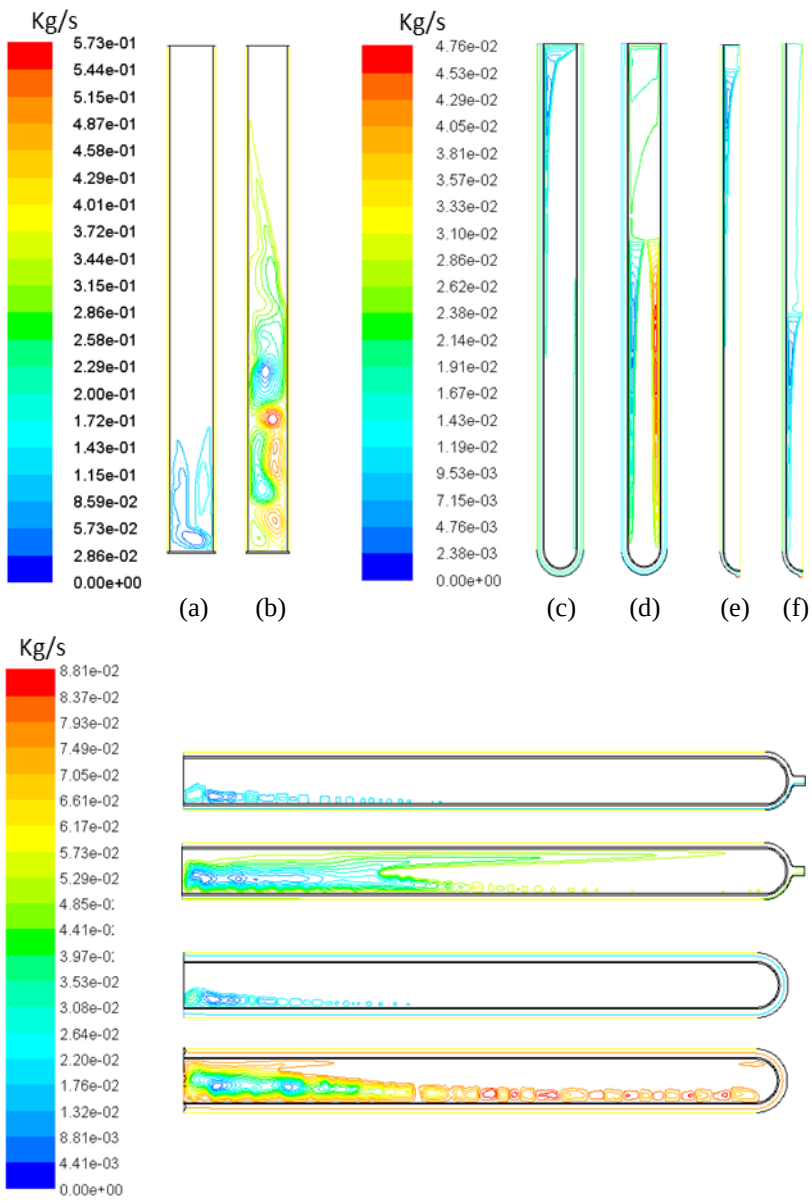


FIGURE 4.9. Temporal evolution of stream function (kg/s) during solidification process at δs =8.2%, (a) FPV, (b) CFV, (c) PFV, (d) PFH, (e) CFHB

flux is 0.018 kg/s in CFV and 0.014 kg/s for PFV, Figs. 4.10c, and e). However, at the later stages with higher rate of melt fraction, mass flux in the CFV is about three time higher as compared with the PFV (e.g., maximum 0.015 kg/s in PF and 0.047 kg/s in CFV at 68.4% melt fraction, Figs. 4.10d, f).

Since natural convection is a major mode of heat transfer in the melting process, a greater impact from the orientation of enclosure on the thermal behaviour of PCM is expected for melting compared to the solidification process. In the horizontal melting process due to the formation of the Benard convection cells [133] in the CFHB (HTF entering from the bottom tube), the maximum mass flux is twice that of the CFV (e.g. 0.088 kg/s compared to 0.0476 kg/s, Figs. 4.10j, and d). To conclude, smaller Benard convection cells distributed along the bottom of the PCM provide faster access to the whole domain, resulting in a higher mixing rate and uniformity across the domain. Whereas in the vertical cases, larger and fewer convection cells with lower velocity take longer to circulate and so their mixing impact on the domain becomes slower and lower.

Furthermore, among the horizontal cases, the observed mass flux is highest for the CFHB compared to the PFH, (maximum 0.088 kg/s, and 0.058 kg/s at 68.4% melt fraction, respectively). In the CFHB, the Benard convection and the temperature difference between tubes result in a higher rate of natural convection and mass flux, while in the PFH, Benard convection is the only driver for natural convection. Furthermore, Benard convection cells form at early stages of the melting process in CFHB and PFH as the bottom surface is hot (HTF entrance).



From the top: (g), (h), (i), (j)

FIGURE 4.10. Temporal evolution of stream function during melting process:
FPV: (a) 12650s, δl =22.1%, (b) 35000s, δl =68.4%, **CFV**: (c) 12150s, δl =22.1%, (d) 35000s, δl =68.4%, **PFV**: (e) 10000s, δl =22.1%, (f) 30550s, δl =68.4%, **PFH**: (g) 10000s, δl =22.1%, (h) 28000s, δl =68.4%, **CFHB**: (i) 12100s, δl =22.1%, (j) 33300s, δl =68.4%.

Tables 4.3, and 4.4 provide a summary of mass transfer during the discharging and charging processes in different configurations. Table 4.3 demonstrates the mass transfer during the discharge processes up to 20% phase change, where the highest rate of mass transfer occurs for the FPV case compared to all other configurations. This is due to the higher temperature gradients across the PCM domain (Fig. 4.6b) which provides a higher driving force for natural convection.

Table 4.3 – Mass transfer (kg/s) during solidification process

δ_s	FPV		CFV		PFV		CFH		PFH	
	max	mean	max	mean	max	mean	max	mean	max	mean
8.2	0.009	0.004	0.0035	0.0031	0.0031	0.0027	0.00316	0.0031	0.0027	0.002
19.1	0.008	0.004	0.0030	0.0030	0.0025	0.0025	0.00309	0.0031	0.0025	0.002

Table 4.4 demonstrates a particular higher mass transfer for the FPV, but in general it is higher for the FPV, CFH and PFH compared with the vertical orientation of CF and PF. This means a higher rate of natural convection and mixing rate in the FPV, CFHB, and PFH leading to a more uniform heat transfer up to the end of the process (Fig. 4.13a). This is consistent to the temperature field analyses in section 4.5.2.2, where a conclusion was that a similar thermal behaviour is expected for the FPV and horizontal orientation of CF and PF.

Table 4.4 – Mass transfer (kg/s) during melting process

δ_l	FPV		CFV		PFV		CFH		PFH	
	max	mean	max	mean	max	mean	max	mean	max	mean
36.9	0.641	0.33	0.0325	0.0286	0.0158	0.0147	0.0571	0.0403	0.053	0.037
68.4	1.07	0.642	0.0477	0.0264	0.0147	0.0133	0.081	0.0585	0.0689	0.0533
94.7	1.757	1.08	0.0285	0.0136	0.0209	0.0116	0.1032	0.0587	0.051	0.0323

4.5.4 Phase front evolution

4.5.4.1 Discharging

Figures. 4.11a-e show the evolution of the phase front in the solidification processes. The phase front is almost vertical or one-dimensional as conduction is the major mode of heat transfer, particularly after 10% of the liquid solidifies. However, the faster rate of discharging in PF is clear as the phase front meets sooner at the mid-width and starts to move downwards in PF compared with the CF. As explained before this is due to exposure of PCM to a lower HTF temperature from both tubes. In comparing horizontal and vertical solidification processes, because of the dominant role of conduction heat transfer, the phase front is one-dimensional for both orientations and moves parallel to the tube during most of the process. However, due to the higher temperature gradient in PFV and PFH, the heat transfer area decreases more rapidly compared to the CF configurations.

More importantly, the main difference between FPV in comparison with all other cases is that even after 40% of liquid changed to solid, both surfaces of the plate fins (left and right) are not completely covered with a solid layer, providing significant heat transfer area in direct contact with the liquid phase. Although the phase front area (heat transfer area between solid and liquid) in each phase fraction is smaller for the FPV case, there is more heat transfer area available between the plates and liquid phase, leading to a higher heat transfer rate compared to the CFV and CFHB. Overall, the FPV achieves a more uniform heat transfer rate up to the end of the process compared to all other cases (Fig. 4.13b).

4.5.4.2 Charging

Figures. 4.12a-e present the melting front evolution in the melting or charging processes. The phase front is two-dimensional due to the natural convection heat transfer and its shape depends on the isotherms and pattern of convection cells (i.e., temperature and velocity fields) in the vertical orientation (Fig. 4.10-f). Again, the main difference between CF and PF is the faster rate of charging in PF. A symmetrical melting front is observed in PF compared with progressive melting front from left to right in CF as HTF flows into the left pipe and exits from the right pipe (Fig. 4.3b). In both charging and discharging cases, the heat transfer area being the phase front remains higher in CF cases compared to the PF. A higher rate of charging and discharging occurs in the PF which means between the two terms of heat transfer area and temperature difference, the impact of the latter is dominant and overrides the impact of lower heat transfer area in the PF cases.

The lower temperature gradient and the mixing effect of Benard cells in the horizontal configurations (Fig. 4.8b and Figs. 4.10g-j) leads to a one-dimensional melt front that is evident in Fig. 4.12d, and e in comparison to the two-dimensional melting front in the vertical cases, Figs. 4.12a-c. This phenomenon results in a lower heat transfer area (decreasing heat flux) earlier during the process in a vertical configuration compared to a horizontal configuration in which the heat transfer area remains the same during most of the process.

The phase front shapes of FPV (Fig. 4.12a) show similarity to the horizontal cases (Fig. 4.12d, e). Comparing to the vertical cases (CF and PF), heating from the bottom in FPV hinders the accumulation and superheat of the liquid in the upper level of the geometry (e.g. two-dimensional melt front at the top of CFV and PFV), leading to lower peak and average temperatures and consequently lower temperature gradients (Fig. 4.8a, b). Despite the lower temperature gradient, the mass transfer is higher in the FPV compared to all other cases (Table 4.4) due to the combined effect of Benard convection [133] as explained in [142] and high Ra number due to the height of the geometry. This results in the generation of a large number of fast and small convection cells with superior mixing effect, similar to the high rate of natural convection in the horizontal orientation of CF and PF.

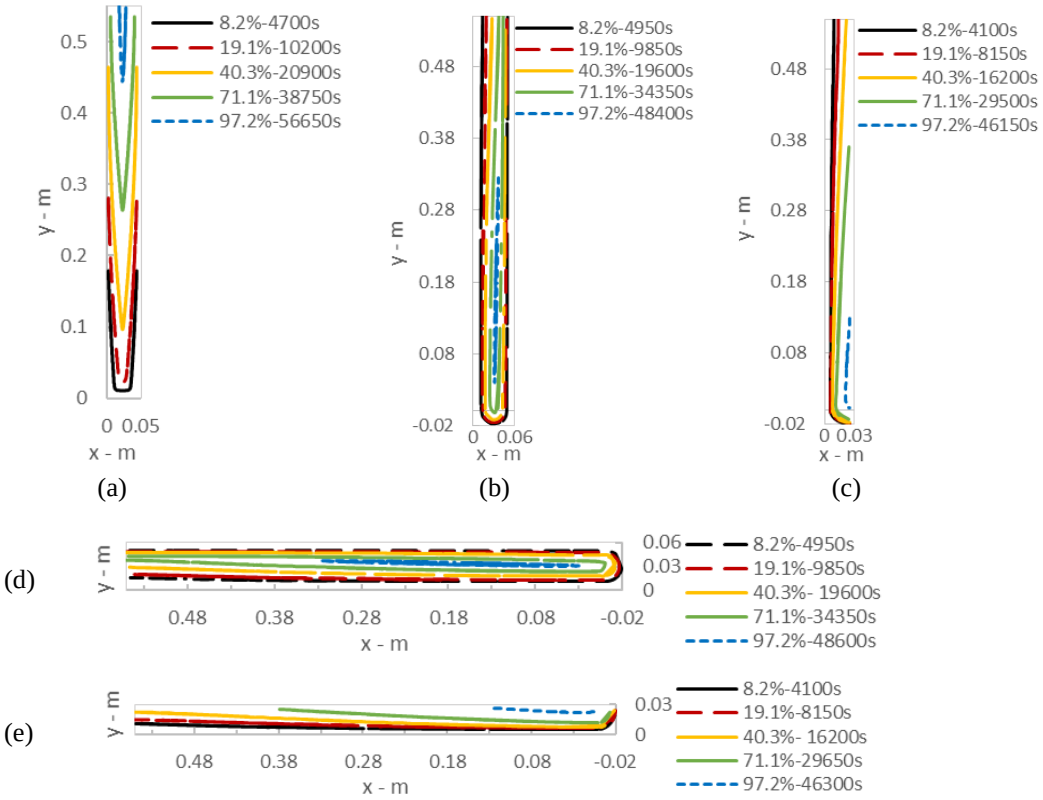


FIGURE 4.11. Temporal evolution of phase front in solidification processes:
(a) FPV b) CFV, c) PFV, d) CFHB, e) PFH

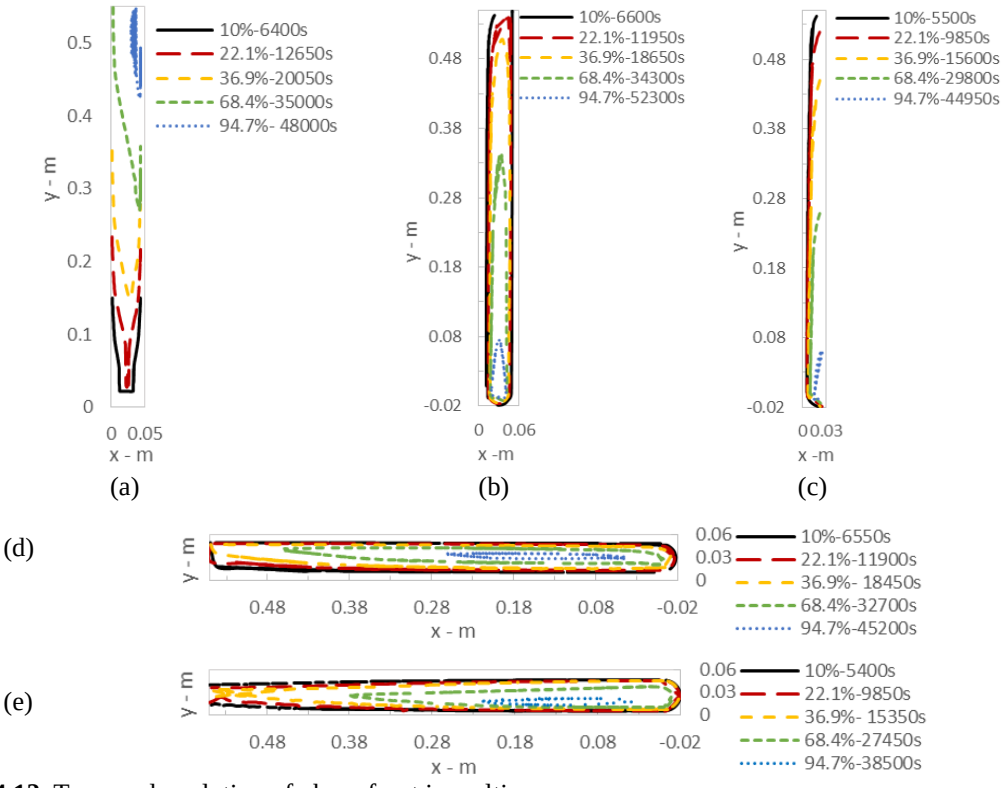


FIGURE 4.12. Temporal evolution of phase front in melting processes:
(a) FPV, b) CFV, c) PFV, d) CFHB, e) PFH

4.5.5 Heat transfer

Figure. 4.13 shows a comparison of heat flux for different flow arrangements for the charging and discharging processes. The first observation from the melting processes is a higher heat flux in the PF compared to the CF as the PCM is exposed to a higher temperature of HTF entering both tubes in PF. The total energy input in both PF and CF are the same as half of HTF enters each tube in PF (equation 13). The difference is the result of distribution of heat source; in CF, a higher mass flow rate ($\dot{m}$) is in contact with the PCM in two passes whereas in the PF, half of the mass flow rate ($\dot{m}/2$) with the higher inlet temperature flows in each single pass.

The second observation is that heat flux experiences a longer plateau before it starts to decrease after 50% melt fraction in CFV compared to the PFV in which the heat flux starts to decrease rapidly from 35% melt fraction. This is the result of a higher rate of natural convection in the CFV compared to the PFV leading to a more uniform temperature field across the height of CFV (explained in section 4.5.2). The more uniform temperature field along the height correlates with a larger heat transfer area at the phase change front for a longer period (Figs. 4.12b, and c) and more uniform heat transfer rate for CFV compared with PFV.

The third observation is that the horizontal orientations provide higher heat flux in both CF and PF due to the impact of Benard convection cells formation along the bottom side of the PCM, which can be clearly seen in Fig. 4.10g-j. The smaller convection cells with higher velocity provides a higher rate of natural convection heat transfer.

Summarising the results for the shell and tube cases, the PF configuration provides the highest heat transfer rate, and the highest temperature gradient and peak temperature for the same amount of energy input and PCM. Whereas CF provides a more uniform process in which the heat flux starts to decrease later in the process compared to the PF, (after 50% and 35% melt fraction in CFV and PFV, and after 97% and 93% melt fraction in

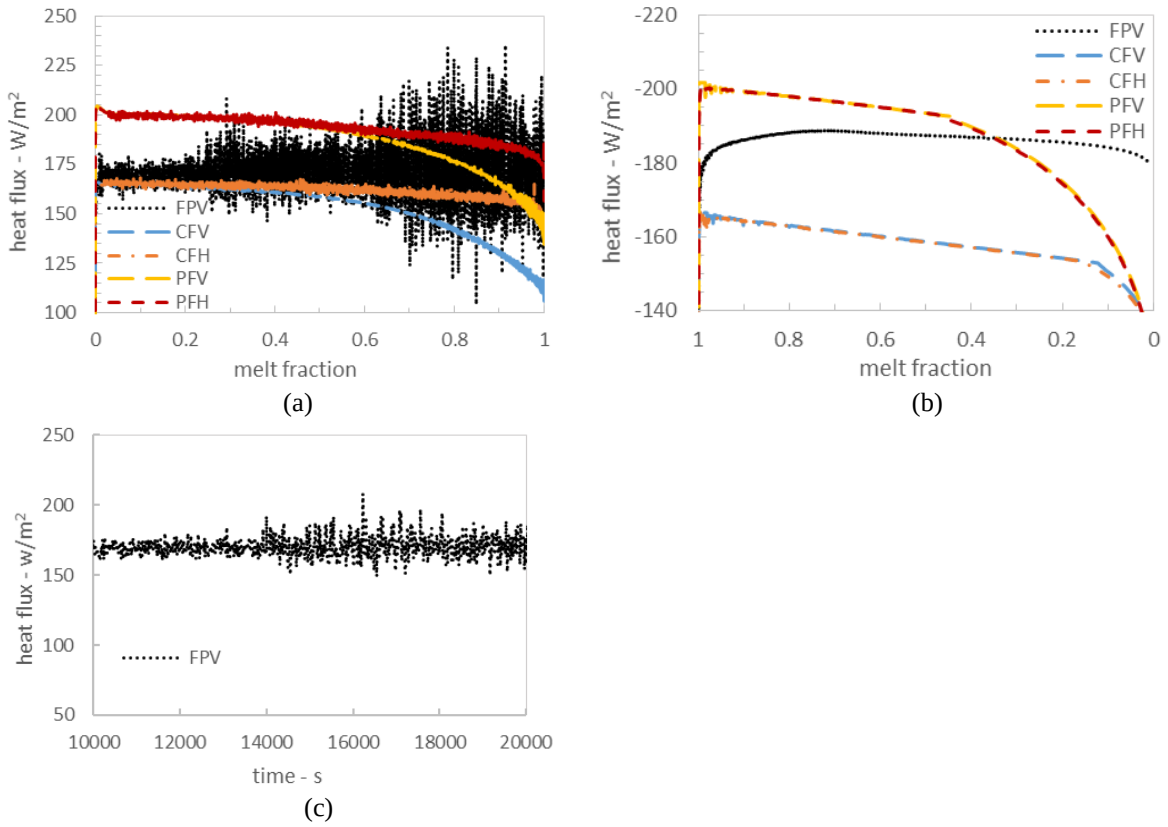


FIGURE 4.13. Temporal evolution of average heat flux: (a) melting, (b) solidification, (c) a time frame enlargement of the melting process in FPV

horizontal CFHB and PFH, respectively). However, the horizontal orientation provides a higher heat transfer rate for a longer period in both CF and PF.

Regarding the FPV case, the average heat flux is higher in comparison to the CFV and CFH. Even after 60% melt fraction, the average heat transfer rate for the FPV is 4.5% higher compared to CFH due to higher Ra number ($10^{10} > 10^{7}$). The rate of natural convection and fluctuations in the heat flux rate are higher for the FPV case compared to the other vertical cases, despite the same Ra = 10^{10} for all vertical cases of CFV and PFV. The reason

is related to the small and fast convection cells, circulating the mass and heat through the enclosure being heated from the bottom. Ra = 10^{10} for the FPV is much higher than the turbulent threshold of Ra>1704 for an enclosure heated from the bottom, and higher than Ra = 10^{7} for the CFHB and PFH cases. As a result, more fluctuations in heat transfer rate is observed for the FPV compared to the CFHB and PFH. Figure 4.13 c captures a time frame between 10000 – 20000 seconds (e.g. between 16.5 – 36.5 % melt fraction). This shows as more solid transforms to liquid, more convection cells and a higher fluctuation of heat transfer takes place.
In the solidification processes, the average heat flux is about 10% higher for PF compared to the CF because of the HTF entering in both tubes. The horizontal and vertical orientations do not have much impact on the heat flux as conduction is the major heat transfer mode, particularly after 10% of liquid phase is changed to solid. Due to a lower temperature gradient in the CF, the heat transfer process is more uniform compared to the PF (Heat flux starts to decrease sharply after 85% and 55% phase change in the CF and PF, respectively) as the same tendency was observed in the melting processes.
Comparing the FPV case with the shell and tube cases, the plateau in the average rate of heat flux lasts longer in the discharging process for the FPV case. This is very important in the discharging process for which the heat transfer rate is uniform even after 70% solid fraction in the FPV case while a sharp decrease occurs in all other cases. This leads to the lowest redundant PCM for the FPV. The average rate of heat flux is higher in the FPV compared to the CFV and CFH due to the higher temperature gradient mentioned in the section 4.5.2.1.

4.5.6 Phase Change Duration

A comparison of the duration of the charging processes is demonstrated in Fig. 4.14a which shows a higher rate of phase change for the horizontal configurations (CFH, PFH), compared to the vertical ones for both CF and PF. This is the result of the impact of Benard convection cells and higher rate of mixing provided in the horizontal orientation. Among CF and PF configurations, a higher rate of phase change is provided by the PF as PCM experiences the temperature of inlet HTF from both tubes. Among the CF configurations, CFHB provides the shortest time followed by CFV taking the longest time. This is also consistent with the explanation of natural convection and the special form of Benard convection that was explained in the previous sections. The uniform thermal performance of FPV as shown in Fig. 4.13a results in a longer period of charging in comparison to the horizontal cases; however, a faster process compared to the CFV case. In the charging processes, 94.7% of PCM melts after 48000, 52300, 44950, 45200 and 38200 seconds for FPV, CFV, PFV, CFHB, and PFH, respectively.

In the solidification cases (Fig. 4.14b), apart from the main difference between the PF and CF due to the HTF entry from both tubes in PF, there is not a major difference between the performance of the system in the horizontal and vertical orientations. Conduction is the main heat transfer mode after 10% of PCM freezing, leaving a very low temperature gradient as the driving force for natural convection. The duration of the discharging process as shown in Fig. 4.14b is the longest for FPV compared to other cases, being 18% longer than the quickest process achieved by the PFH configuration. However, Fig. 4.13b clearly shows a uniform and higher heat transfer rate of the FPV compared to the CF cases, leading to a smaller system, lower amount of redundant PCM, and lower cost.

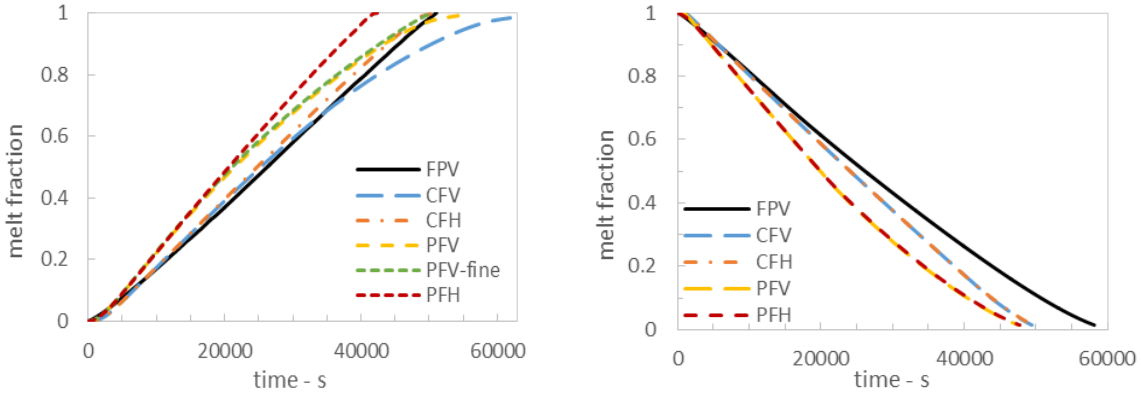


FIGURE 4.14. Temporal evolution of phase fraction: (a) melting, b) solidification

This analysis shows that depending on the application, whether a fast heat storage/release is a priority or a more uniform phase change process being a more cost effective system is acceptable, an optimum configuration can be matched to the specific design requirement.

4.5.7 Entropy Generation

Finally, as the second law assessment of the thermal performance of different configurations, entropy generation during the charging/discharging processes are discussed. Referring to the definition of entropy and exergy provided from the literature and Eqs.11, and 12, in section 4.1, the rate of entropy generation through the PCM domain is numerically calculated in space (PCM domain) and time (phase change duration). The average quantity at different phase fraction is compared for different cases as an indication of destroyed exergy.

Figures. 4.15a and b show the avarage entropy generation in the PCM domain during the discharging process in different configurations. Entropy generation through the discharging processes decreases as the average temperature decreases in all cases. However, for the FPV case, entropy generation decreases faster and to a lower amount due to the higher temperature gradient (Fig. 4.6b), leading to a higher driving force for heat transfer up to the end of the process. The uniform heat transfer rate, particularly after 70% phase change (Fig. 4.13b) means lower entropy generation leading to higher exergy recovery. This result achieves lower redundant PCM [23, 139] leading to a smaller system size and more cost effective storage system.

Figure. 4.16 shows the entropy generation during the charging processes and for different temperature gradients. The entropy generation is lower in the FPV, CFHB and PFH compared with the CFV and PFV due to the lower average temperature and temperature gradients (Figs. 4.8a, b). This leads to a higher and more uniform heat transfer rate for the FPV, CFHB, and PFH compared with the other vertical configurations.

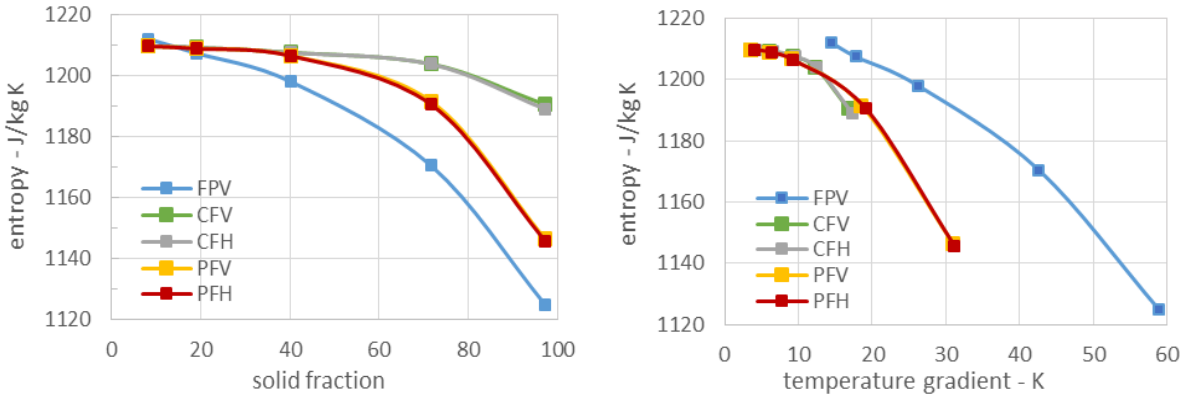


FIGURE 4.15. Entropy generation in PCM during discharging processes versus:
(a) solid fraction, b) temperature gradient

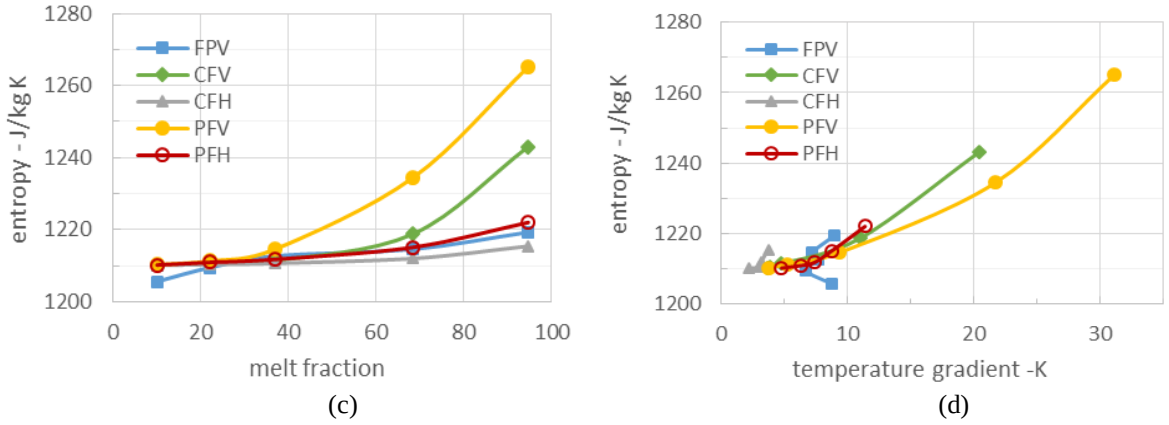


FIGURE 4.16. Entropy generation in PCM during charging processes versus:
(a) melt fraction, b) temperature gradient

4.6 Conclusion

The four shell and tube system configurations have been compared with that of an alternative design using plate fins. Based on the same heat transfer area, amount of PCM and input energy, the thermal performance was determined based on the first law assessment (effectiveness and heat transfer rate) and the second law assessment (entropy generation). While sensible heat storage might be part of the thermal storage process in a LHTES system, the focus of this study was on the performance and characteristics of the latent heat transfer in different configurations.

The following conclusions can be drawn from the comparison of the shell and tube cases:

The parallel flow configuration provides the highest heat transfer rate due to PCM being exposed to a higher temperature difference for both melting and solidification processes. However, due to the higher temperature gradient and higher peak temperature in space and time, the phase change process is less uniform and starts to decline earlier compared to the counter flow case that is reflected in a shorter plateau in the heat flux profile and effectiveness.
For the melting processes in the vertical orientation, a higher rate of natural convection in CF compared to the PF results in more uniformity in the temperature field and a lower peak temperature in space and time. This phenomenon leads to a more uniform heat transfer rate, presenting a longer plateau in heat flux and effectiveness profile during the CF melting process.
In general, horizontal configurations provide higher and more uniform effectiveness which leads to smaller and more cost effective LHTES systems for CSP plants. Due to the Benard convection and smaller convection cells distributed along the bottom side of the horizontal case, a higher rate of mass flux and mixing rate in the horizontal orientation results in a lower temperature gradient and lower peak temperatures in space and time compared to the vertical orientation. Therefore, the horizontal orientation of both configurations (PF and CF) provides a more uniform heat transfer rate resulting in a longer plateau in heat flux profile and effectiveness compared with the vertical configurations.
In the vertical configurations of PF and CF, the temperature gradient and the pattern of natural convection cells correlate with a two-dimensional phase front that starts to decrease early in the melting process. Therefore, a one-dimensional front is more desirable to keep a higher heat transfer area at the phase front for a longer period. The results of this study show that the horizontal configuration provides a nearly one-dimensional phase front that moves parallel to the tube, resulting in a larger heat transfer area and heat transfer rate for a longer period during the melting processes. This is observed as a longer plateau in the heat transfer profile and effectiveness.
For the solidification cases, the results show minor differences between the vertical and horizontal configuration compared to the melting cases due to the minor impact of natural convection. However, the higher effectiveness observed for the CFHB compared with the CFHT provides a guidance that an optimal design is the CFHB.

Moreover, conclusions from the comparison of the fin plate system with the shell and tube configurations are:

A higher heat transfer rate for the fin plate vertical arrangement compared to the counter flow shell and tube configurations, as well as a more uniform heat transfer rate compared to all shell and tube arrangements for both the charging and discharging processes. Overall this study has demonstrated that using equal amounts of PCM and heat transfer surface area, the fin plate vertical, FPV, configuration achieves enhanced thermal performance compared to shell and tube configurations. The proposed design leads to less redundant PCM, as well as a smaller and more cost effective PCM system as a heat storage unit.
Providing the main heat source/sink from the bottom of the system results in a similarity between the thermal performance of FPV and other horizontal cases (counter and parallel flow, CFH, PFH) due to Benard convection phenomenon. A lower temperature gradient in the melting process for the FPV configuration leads to lower entropy generation, and a uniform heat transfer rate compared to the other cases. For the discharging process with the FPV configuration, a higher temperature gradient compared to all other cases results in a higher driving force for heat transfer up to the end of the discharge process. This is leading to lower entropy generation, higher exergy recovery, a more uniform heat release up to the end of the discharge process, and consequently lower redundant PCM and a more cost effective LHTES system for CSP plants. While achieving a more uniform thermal performance in the FPV configuration, the phase change process is longer in both charging (only shorter time compared with the counter flow vertical, CFV) and discharging. Depending on each application of a LHTES, when the shortest time of heat storage/release is not a priority in a specific application, the FPV has been demonstrated to provide the best thermal performance considering the first and second law analyses leading to a cost effective system with smaller size. Overall, the fin plate vertical configuration maximises the useful heat that can be extracted for a given amount of heat and PCM, which has direct applicability to thermal storage solutions for CSP and other applications.

Furthermore, comparing the design/practical aspects of the fin plate system with the shell and tube systems shows that the decoupled PCM location from the path of flow of the heat transfer fluid provides a main practical advantage of the alternative design, reducing the constraints on the materials in the design and optimisation stage. Confining heating/cooling pipes in a channel at the bottom of the PCM enclosure makes it more flexible to match the required working temperatures/pressures, and simplifies the design and material (PCM/plate) selection. This is a significant issue as higher temperatures and pressures are being required for improving the overall solar thermal system performance. In the shell and tube systems, corrosion of tubes in contact with PCM is a major problem and a higher maintenance cost and reduced life cycle of the system can be expected. However, having a

collective piping system at the bottom of the alternative fin plate system compared with more distributed tubes in a shell and tube system, will result in a lower HTF pressure drop and reduced pumping power.
The modular design of the fin plate system also facilitates the selection and optimisation of different parameters for specific applications e.g. as a heat storage for electricity production or as a protection system for a receiver from high thermal stresses in a CSP plant.
The results of this study can be used for the design and optimisation of LHTES for a CSP plant. For instance, if quick heat storage is desired (e.g. fast heat removal to protect a receiver from high temperatures and thermal stresses), a PFH can be beneficial, however, FPV and CFHB provide more uniform heat removal up to the end of the process. Moreover, results of this study provide valuable insight into the thermal performance of the fin plate and shell and tube configurations and can be used to achieve optimum designs for LHTES applications.

From the results of the presented studies in this chapter, two journal papers have been published in Solar Energy [142] and Applied Energy [143].

5 Impact of Periodic Flow Reversal on the Solidification and Melting Processes in a Latent Heat Shell and Tube Storage System

In order to investigate potential methods for improving heat transmission to or from a PCM storage system, a numerical study has been conducted on a shell and tube latent heat storage system whereby the inlet heat transfer fluid direction is periodically reversed during charging and discharging. The impact of varying the boundary condition at the interface of the tubes carrying the heat transfer fluid and phase change material (PCM) on the evolution of the phase change front, heat transfer area and heat transfer rate are evaluated during the charging and discharging processes.

5.1 PCM system

Two adjacent tubes including the PCM between them was selected for this study from a vertical parallel flow shell and tube arrangement. The specifications and boundary conditions for the model are adopted from the prototype system, which was introduced in chapter 4, section 4.2. In the 2-D model, the tube cross section is 8.115 mm, the thickness of tube is 1.41 mm and the thickness of the PCM between tubes is 40.95 mm, resulting in a total width of the geometry (centre to centre of the tubes) equal to 60 mm.

Sodium nitrate was the selected PCM with a melting temperature of 306.8 ºC and air as the HTF with an inlet temperature of 356.8ºC for the melting case and 256.8 ºC for the solidification case. The thermophysical properties of the PCM are included in Table 4.1 and Table 4.2 in chapter 4. For all cases, the velocity of the HTF was set to 8.957 m/sec, and the temperature difference between the inlet of the HTF and melting temperature of the PCM is 50ºC; $\Delta T=T_h-T_m= 50ºC$. When using high temperature PCM in LHTES systems for CSP, a high ΔT is expected, leading to a high Ra ~ 10^{11}. To focus on the phase change process, the initial temperature of the PCM was set to 302 ºC for the melting case and 310 ºC for the solidification case (within 5ºC of the phase change temperature).

5.2 Numerical modelling

The numerical modelling schemes and thresholds are the same as explained in chapter 3, section 3.2.1.2.

5.2.1 Geometry and grid

A grid size of 33650 cells was considered for the two-dimensional geometry, fine enough to capture details within thermal and velocity boundary layers. A grid independence study using a higher resolution grid, about 81400 cells was carried out and produced the result of melt fraction with no recognisable changes as shown in Fig. 5.9a as Fine-FBC. A time step of 0.1 seconds was selected to achieve accuracy and a realistic calculation time [141]. Using 4 processors in parallel, calculations on a machine with 3.2 GHz Intel core i5-4570, on average took two weeks for a simulation.

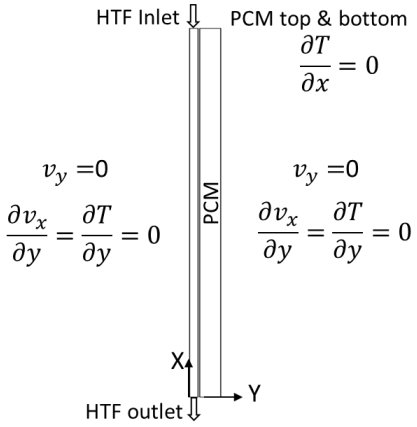


FIGURE 5.1. Schematic drawing of the numerical model

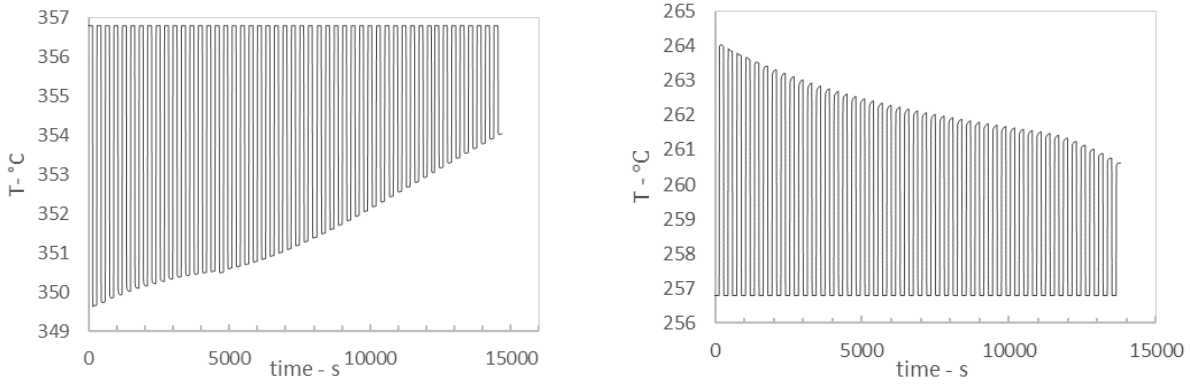
5.2.2 Fixed Boundary Condition - FBC

Three domains of HTF, tube thickness and PCM were introduced. Taking half of the tube and half of the PCM as the grid, the boundary conditions assigned are: symmetry at the sides of HTF and PCM, adiabatic conditions at

the top and bottom of tube and PCM, and a fixed inlet – outlet at the top and bottom of the HTF. The setting of boundary conditions including the symmetry at HTF and PCM mimics an element of a parallel flow shell and tube arrangement for which the edge effect is experienced only at the top and bottom of the tube and shell. This aligns with the focus of the study that aims to investigate the impact of the imposed boundary condition from the tube surface on the evolution of the phase change front and heat transfer area.

5.2.3 Periodic Boundary Condition – PBC

Using the same grid and on the basis of Eq. 19 [100], the inlet and outlet of the HTF were reversed every 150 seconds to resonate the free convection in the liquid PCM. All other conditions were kept the same, to investigate the impact of changes on the phase front evolution, the temperature field and heat transfer rate during the melting and solidification processes. Fig. 5.2 shows the implemented periodic flow reversal boundary condition at the HTF inlet and outlet in the melting and solidification cases.



(a) (b)

FIGURE 5.2. Periodic flow boundary condition at HTF inlet-outlet:
(a) melting, (b) solidification

From the literature review [103, 104], it was concluded that a periodic heat source with a specific amplitude at a moderate frequency, close to the resonance frequency, enhances the time-mean natural convection heat transfer rate. For this study using a fixed heat source (HTF inlet temperature fixed at 356.8°C) while reversing the inlet-outlet of the HTF, results in the implementation of a periodic boundary condition on the tube-PCM interface. This is a practical method for introducing a periodic heat source which can be implemented using a flow control system. While there were two variables in previous studies [103, 104], namely amplitude and frequency, for this study we are investigating the impact of the periodic boundary condition with a frequency close to the resonance frequency. To calculate a frequency close to the resonance frequency, results of scale analysis from [100] proposing an estimation of a critical non-dimensional frequency (*f*) and dimensional period (*w*), was used. The critical non-dimensional frequency corresponds to the resonance of natural convection heat transfer in the steady state periodic regime. Ra ~ 10^{11} is high enough to make convection heat transfer the dominant mode in the melting process to respond to the periodic boundary condition. Eq. 19 provides an estimate for one period, and half of one period was used as the time interval to enable a change in the flow direction.

$$f \sim \frac{1}{4} Ra^{-0.1} \Pr^{-0.5} \qquad \Pr \geq 1 \tag{18}$$

$$w \sim 4 \frac{Z^2}{\alpha} Ra^{-0.4} \qquad \Pr \geq 1 \tag{19}$$

$$w \sim 4 \times \frac{0.55^2}{1.65 \times 10^{-7}} \times (10^{11})^{-0.4} = 292\ s$$

In applying this condition to a LHTES unit with a tube bundle in a shell filled with PCM, reversing the flow of the HTF between the inlet and outlet is possible with a control system and motorized valves.

5.3 Result and discussion

5.3.1 Periodic Boundary Condition at tube-PCM interface

Figure. 5.3 shows the temperature profile at the tube-PCM interface for the time interval between 200-1400 seconds during the melting process. The interval has been chosen from the start of the reversal method for four complete periods as a sample to show the impact of periodically reversing the flow of HTF on the temperature profile at the tube-PCM interface. The figure clearly presents how the temperature profile changes in each period, as indicated by the solid lines and dashed lines in consecutive periods. Consequently, a periodic boundary condition can be achieved at the tube-PCM interface by periodically reversing the flow direction of the HTF.

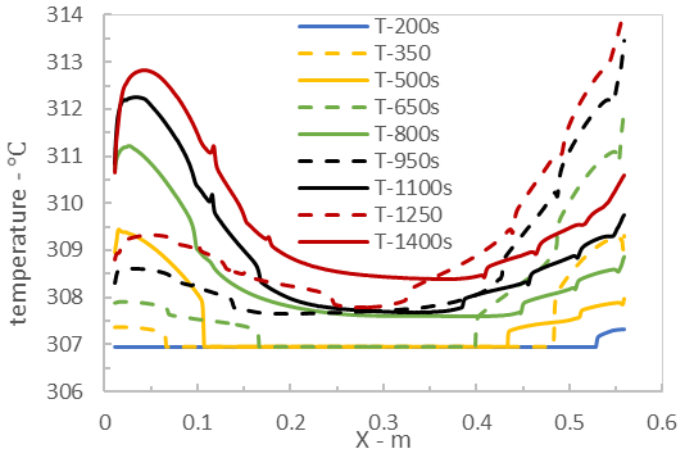


FIGURE 5.3. Temporal evolution of temperature profiles at the tube-PCM interface

5.3.2 Impact on Phase Front

Figure. 5.4a, b show the evolution of the phase change front in the fixed and periodic cases for solidification. While the phase change front is mainly parallel to the tube in all cases, it reaches the symmetry side at 66.6% and 86.2% solid fraction for the cases of fixed and periodic cases, respectively. This means after 66.6% solid fraction, the heat transfer area starts to shrink and moves downwards for the case with a fixed boundary whereas in the periodic boundary case, the phase front continues to move parallel to the tube up to 86.2% solid fraction. The phase front holding on greater heat transfer area leads to a higher heat transfer rate and energy release as demonstrated in Figs. 5.8b and 5.8d. Moreover, Fig. 5.4c clearly shows a significantly higher heat transfer area at 87.2% solid fraction for the PBC compared to the FBC case.

Figures. 5.5a, and b show the evolution of the melt front for the charging processes. The melt front moves parallel to the tube up to 15.5% melt fraction for the fixed case whereas it is parallel to the tube up to 25% melt fraction for the periodic case. In the case of FBC, the melt front reaches the symmetry side at 15.5% melt front and starts to move downwards, leading to the loss of heat transfer area. The periodic melt front touches the symmetry side at 25% melt fraction, leading to a higher heat transfer area up to 25% melt fraction compared to the fixed case. Fig. 5.5c shows almost the same heat transfer area at 88.2% melt fraction for both cases. This result is mainly due to the mixing effect of convection heat transfer at the later stages of the melting process.

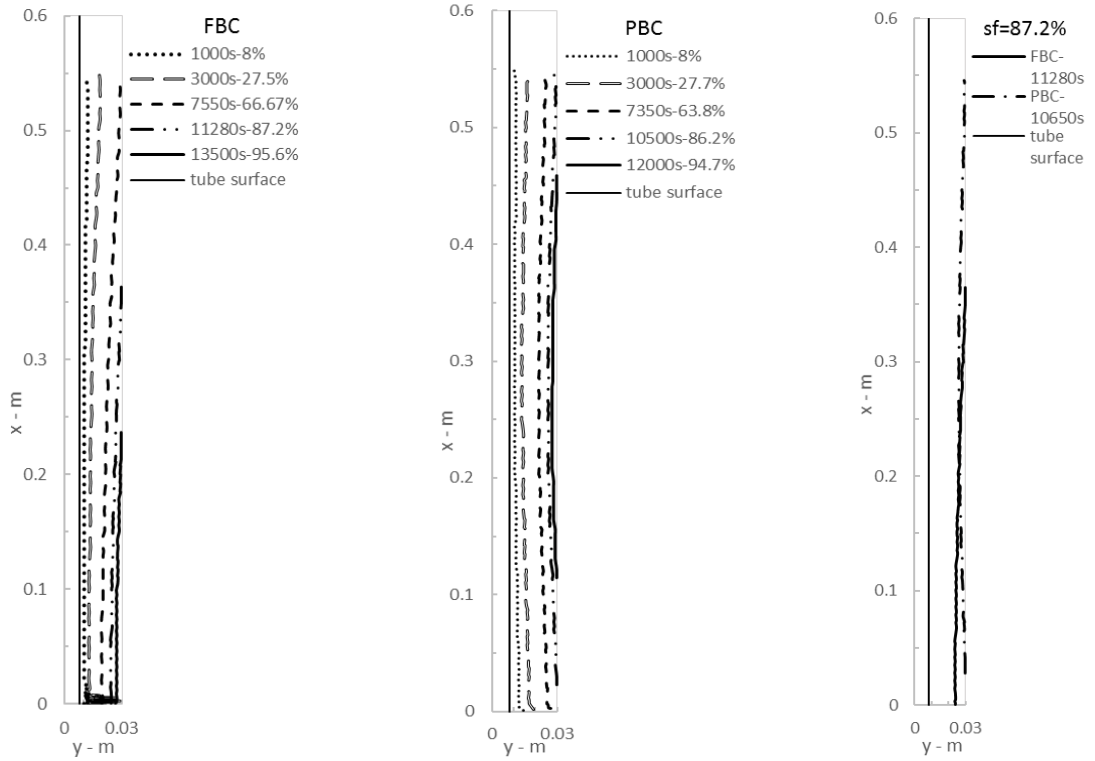


FIGURE 5.4. Temporal evolution of solid front during solidification process:
(a) fixed boundary condition, (b) periodic boundary condition, (c) comparison of the solidification front at 87.2% solid fraction.

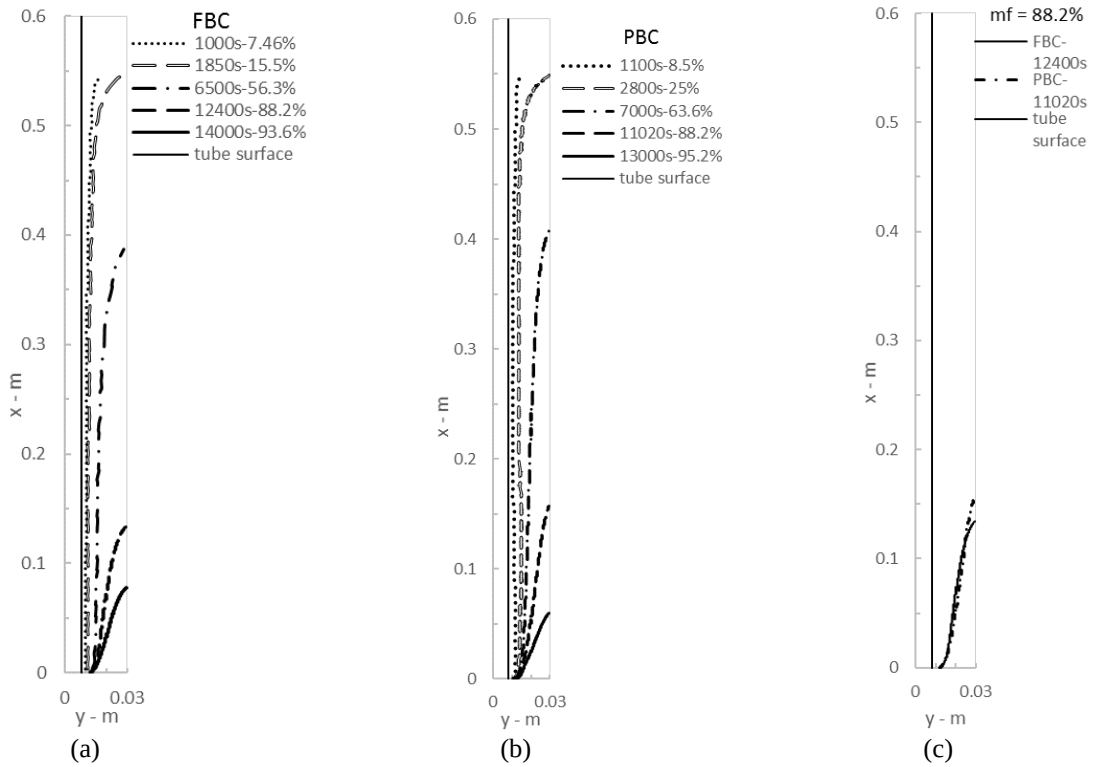


FIGURE 5.5. Temporal evolution of melt front during melting process:
(a) fixed boundary condition, b) periodic boundary condition, c) comparison of the melting front at 88.2% melt fraction.

5.3.3 Impact on Temperature Field

Figures. 5.6 and 5.7 present temperature contours at three different time-slots during the charging and discharging processes using FBC and PBC. Figure.5.6 provides a comparison of temperature contours for the FBC and PBC during the discharging process. This comparison demonstrates a more uniform profile and lower temperature gradient, in the PBC case. The PBC enables a higher rate of heat release at the later stages of the discharging process (after 75% solid fraction which is apparent in Fig. 5.8b) with a more uniform temperature in space and time. This is consistent with the parallel evolution of phase change front as the phase front is an isotherm at the melting temperature of the PCM. Periodic reversal of the HTF inlet, periodically changes the temperature profile at the tube-PCM interface, resulting in a more uniform temperature distribution throughout the PCM during the phase change process compared to the fixed temperature profile at the tube-PCM interface in the case of fixed HTF inlet.

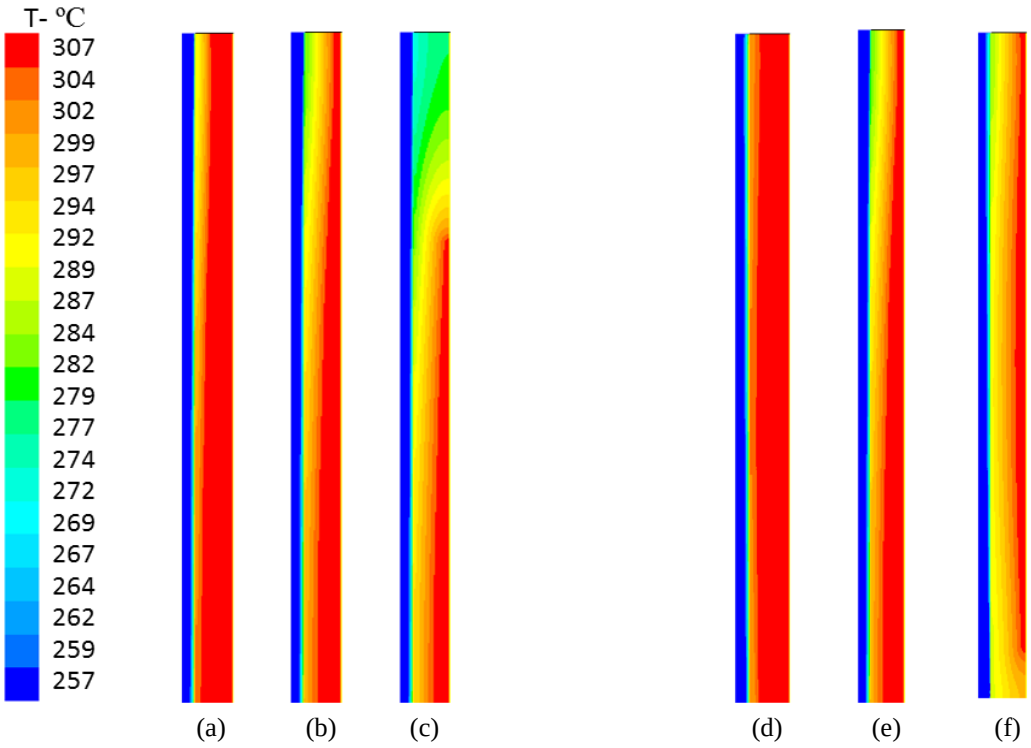


FIGURE 5.6. Temporal evolution of temperature profile during solidification process:
FBC: a) 3000s, δs=28%, b) 7350s, δs=64%, c) 11000s, δs=86%, **PBC**: d) 3000s, δs=28%, (e) 7350s, δs=64%, f) 11000s, δs=90%.

Likewise, Fig. 5.7 provides a comparison of temperature contours for the melting process in the two cases of FBC and PBC. This comparison shows a more uniform profile with a lower temperature gradient, and a lower peak temperature in the case of PBC. Fig. 5.7f clearly demonstrates a lower peak temperature in PBC compared to the FBC case, for example 340 ºC at 92% melt fraction in 12000 seconds, compared to 350 ºC at 86.6% melt fraction. A higher rate of heat storage at the later stages of the melting process occurs in the case of periodic boundary, which is also apparent in Fig. 5.8a. This demonstrates the potential of the periodic boundary condition to deliver a higher rate of heat storage in PCM through a more uniform temperature process with lower peak temperatures. In other words, a lower peak temperature and temperature gradient leads to lower entropy generation and higher exergy or second law efficiency of the system [110]. A low temperature gradient in space and time, and high heat transfer density are the major objectives in designing a heat storage system, leading to a smaller unit with less material [58, 122], and lower cost. This is particularly important in the case of high temperature PCM systems for CSP applications with the potential of high temperature gradient and peak temperatures.

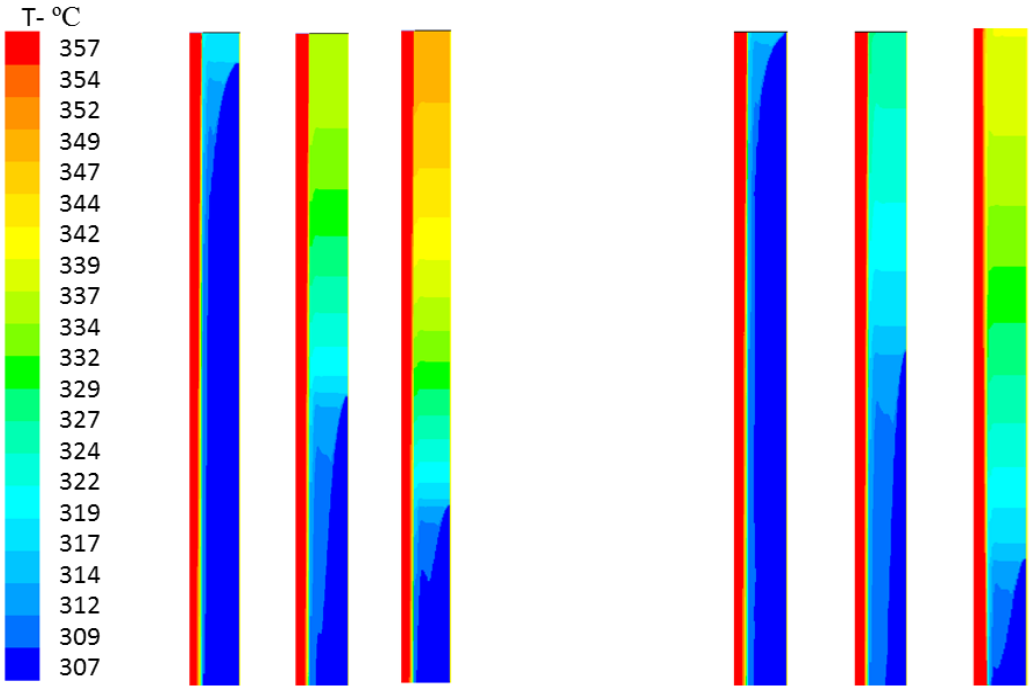


FIGURE 5.7. Temporal evolution of temperature profile during melting process:
FBC: (a) 2800s, δl =25%, (b) 7000s, δl =60%, (c) 12000s, δl =86.6%, **PBC**: (d) 2800s, δl =25%, (e) 7000s, δl =63.6%, (f) 12000s δl =92%.

5.3.4 Impact on Mass Transfer

Table 5.3 shows a comparison of the stream functions during the two melting processes with PBC and FBC. Stream functions with the unit of kg per second represent the convection cells that transfer mass across the PCM. In the case of FBC, the stream function increases due to the higher liquid fraction and decreases towards the end of process as the average temperature difference deceases. In the melting process with PBC, mass flux increases until the end of melting process with a higher rate compared to the melting process with FBC. An increase in stream function demonstrates increase in the number of convection cells, carrying mass and heat through the PCM.

Table 5.3. Comparison of stream function in melting processes:
(a) fixed boundary condition, (b) periodic boundary conditions

time - s	melt fraction - %	a – kg/s	b – kg/s
2800	25	0.02	0.019
7000	60	0.0272	0.0367
12000	86.6	0.0193	0.0769

5.3.5 Impact on Heat Transfer

Figure. 5.8 shows a comparison of heat flux for FBC and PBC for the charging and discharging cases. Heat flux is defined as the heat transfer per square metre of heat transfer surface area between tube and PCM. The discharging results for the PBC show that after the initial transition period at approximately 10% solid fraction, the system evolves to a quasi-steady state regime despite the fluctuations with a small amplitude. A higher heat flux in PBC occurs after 75% solid fraction, and the last 25% PCM solidifies faster compared to the FBC case, providing better performance towards the end of the process. This is consistent with the heat transfer area shrinkage after 66.6% solid fraction in case of the FBC as the phase front reaches to the symmetry side while in the PBC case, the phase front continues to move parallel to the tube leading to a higher heat transfer area until the end of the process. The time-mean heat transfer rate is 5.5% higher for the PBC compared to the mean heat transfer rate in the FBC. Accordingly, Fig. 5.8d presents the improved latent heat energy discharge as MJ per square metre of PCM, which is observed in the later stages of the process from 9500 seconds. This enhancement of heat release, particularly towards the end of the discharging process, is important in reducing the redundant PCM, which can translate to a smaller size LHTES unit. The redundant PCM is the last part of the PCM, which is not capable of providing the desired outlet temperature of HTF.

In the melting case, presented in Fig. 9a steady oscillatory regime and resonance of natural convection heat transfer occurred as was demonstrated in previous studies [100, 103, 104, 106]. Heat flux evolution shows higher heat flux in the PBC case after 40% melt fraction up to the end of the melting process. As an example, the total heat transfer rate to the PCM at 88.2% melt fraction is 20% higher for the PBC compared to the FBC case. Overall, the time-mean heat transfer rate delivered by the PBC is 6.8% higher compared to the FBC. In comparison of PBC to the FBC, a higher heat transfer area occurs between 15.5% and 25% melt fraction while the higher rate of heat storage is delivered after 40% melt fraction until the end of the process. The higher rate of heat transfer is due to amplification of convective heat transfer and the mixing effect, particularly after 40% melt fraction where more fluid becomes available. Fig. 5.8c presents the stored heat in MJ per square metre of PCM, in the time frame of the melting process, that is, it shows higher heat storage after 5000 seconds.
Hence, the periodic flow boundary condition has been demonstrated to enhance heat storage through the resonance of natural convection heat transfer. Moreover, it delivers a higher rate of heat release due to spatial improvement in the heat transfer area at the phase change front and lower the temperature gradient in time and space (resulting in higher exergy recovery) in a conduction dominant process.

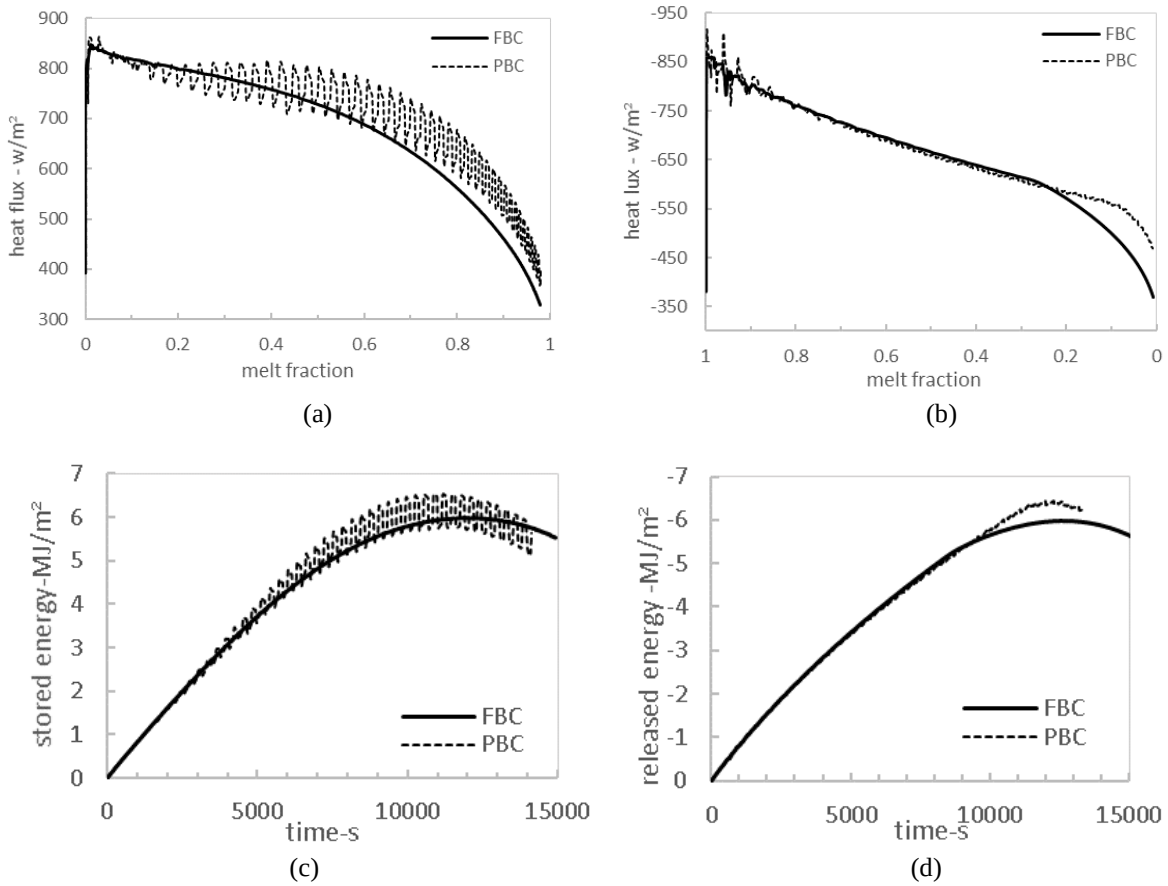


FIGURE 5.8. Temporal evolution of heat flux: (a) melting, (b) solidification
Temporal evolution of energy stored during: (c) charging, (d) discharging

5.3.6 Impact on Phase Change Time

A comparison of the melt fraction for the fixed and periodic cases is demonstrated in Fig. 5.9 which shows a higher rate of melting and solidification for the PBC cases. In the charging processes, 97.93% of PCM melts after 15790 and 14135 seconds for FBC and PBC cases, respectively. In the discharging processes, 99.2% of PCM solidifies after 15190 and 13365 seconds for the FBC and PBC cases, respectively. For the case under consideration, using the periodic boundary condition facilitates 10% faster melting and 12% faster solidification compared to the fixed boundary condition.

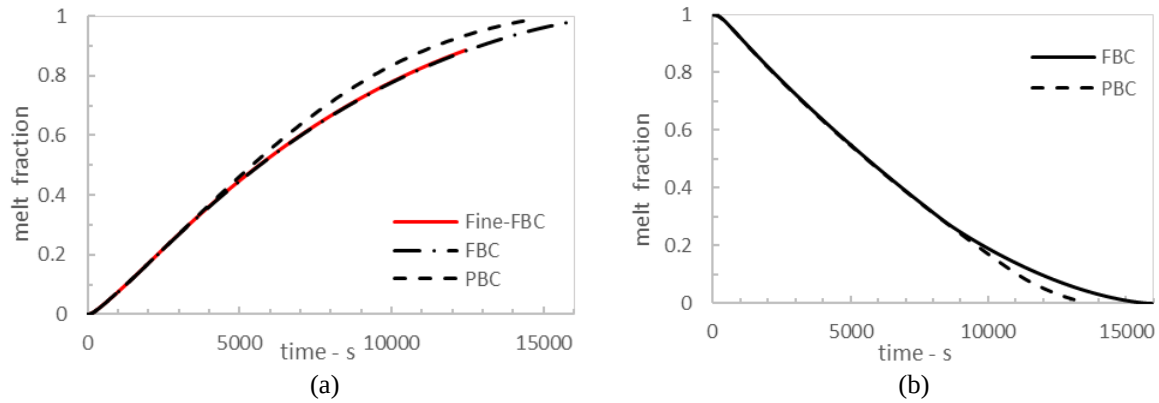


FIGURE 5.9. Temporal evolution of melt fraction:
(a) melting, (b) solidification

5.4 Conclusions

The main objective of the present study was to demonstrate a novel practical method, namely periodic reversal flow to implement a periodic boundary condition without changing the heat source. The method and its impact on the thermal behaviour of high temperature PCM in a shell and tube LHTES unit were examined through a numerical study.

In summary, the most significant outcome of introducing the periodic flow reversal results in a noticeable enhancement of heat transfer during the final 25% of the discharge process which is important in the reduction of the storage system size due to having less redundant PCM. The potential to decrease the temperature gradients and peak temperatures in space and time is also very important for CSP plants where high temperature PCM systems are expected. Moreover, faster charge and discharge processes provide an opportunity in LHTES applications where a higher power density is desired**.** For example, in CSP applications a smaller size auxiliary LHTES unit using the periodic flow reversal technique, alongside a main LHTES unit can assist in providing the peak energy demand while the main LHTES system can be sufficient for most of the off-peak use period. Regarding a latent heat storage system as a protection unit for a receiver from high thermal stresses [32], the method provides a novel opportunity for fast heat removal from the receiver with no requirement to reduce the solar heat absorbed, maximizing solar energy collection.

The introduction of the periodic flow reversal technique was found to enhance natural convection in the melting case. On average, a 6.8% enhancement in heat transfer was found. With higher melt fractions above 40% the heat transfer enhancement was found to increase, due to the resonance of natural convection, with a 20% increase achieved at 88.2% melt fraction. The performance improvement in the solidification case for PBC was due to the impact on the temperature field and phase change front. The temperature gradients were smaller in space and time, and the phase change front was parallel to the tube, sustaining a larger heat transfer area for a longer period before starting to shrink. This sustained heat transfer area directly improved heat transfer near the end of freezing, which reduced the redundant amount of PCM improving its cost effectiveness.

The results have demonstrated that for the case under consideration, the duration of the phase change process has decreased by 10% and 12% for the charge and discharge processes, respectively. The potential of a higher heat transfer rate with higher rate of exergy recovery can be used in cases where higher power density is required such as fast heat release to respond to peak electricity demand or fast heat storage to protect a tubular receiver from high thermal stresses in a CSP plant.

A novel concept is presented in this study, however, the full potential of this concept and its application to other heat exchanger applications warrants further investigation through examining additional case studies and experimental work.

A journal paper has been published from the results of this study in Applied Energy [144].

The result of this study was presented in the Asia-Pacific solar research conference (2016) in Canberra and a peer reviewed paper has been published in the conference proceedings [145].

An international patent has been registered for the novel method found through this study to enhance the heat exchanger performance, for which the number is: PCT/AU2017/000145

6 Two and three dimensional modelling of high temperature PCM

Using two and three-dimensional numerical modelling to explore different configurations and orientations provided a deep understanding of their performance and characteristics as LHTES systems. Also, using different scale models in chapter 3 for low temperature PCMs and comparing the predicted results with the experimental data shed light on the reliability of the models for different cases (applications). Overall, the knowledge gained from previous studies provides a firm background for numerical investigation of specific cases of high temperature PCMs in conjunction with new generation of HTFs like sodium nitrate (Na). This thesis being a part of the ASTRI, the upstream and downstream conditions (such as inlet temperature for melting and solidification) are acquired from the collaborative work with other partners such as CSIRO.
A combination of numerical modelling and scale analysis offers a reliable path towards the design and optimisation of a LHTES system for CSP applications. In this chapter, numerical studies are arranged to provide more specific data for a design and optimisation approach described in chapter 7. The practical upstream and downstream data acquired from the other partners (ASTRI) working on the design and optimisation of the whole cycle (solar field to the power block), shows less flexibility on the inlet temperature of the HTF in the charging process compared to the inlet temperature for the discharging process. This results in lower temperature difference available for charging compared with the discharging process, e.g. $\Delta T=25$, $\Delta T=153$ K, respectively. For this reason, in this chapter being the base for the preliminary design in the next chapter (7), the focus is on the charging process. However, the delivered heat transfer rate, HTF outlet temperature and effectiveness of the discharging process as crucial factors are presented and discussed.

Firstly, the annulus model used for low temperature melting in chapter3, section 3.2.2, is used for high temperature melting in the horizontal orientation considering better performance compared with the vertical case. The predicted temperature distributions and heat fluxes can be used for a preliminary design of a parallel flow LHTES system. Moreover, a three dimensional U-tube model of the prototype at UniSA (introduced in chapter4, section 4.2) provides specific data of the temperature profile and heat flux for a preliminary design of a high temperature counter flow system. Aiming for the specific data necessary for a preliminary design of a parallel flow or counter flow LHTES system, the more relevant results from numerical modelling are presented in this chapter in comparison with the comprehensive analyses and discussion delivered in the previous chapters, 3, 4, and 5.

6.1 Two dimensional axisymmetric modelling of an annulus

Moving forward from the simple two-dimensional geometries (used in chapter3, section 3.3, and chapters 4, and 5) to the more realistic ones, a two-dimensional axisymmetric option is a good approach for analysing cylindrical and spherical geometries. The temperature profile, heat flux and other results of such a study can be used in the design and optimisation of a parallel flow shell and tube system for which a procedure is proposed in chapter 7. Considering the annulus as one which replicates above and below of this model, the symmetry assumption is reasonable. Comparing to the two-dimensional modelling, the two-dimensional axisymmetric approach includes the three-dimensional effect of the tube surface and fluid flow.

6.1.1 PCM system

A two-dimensional axisymmetric geometry of an annulus considering the effective length L= 0.925 m, inner tube radius r = 0.0125 m, and outer tube radius R= 0.048 m was generated to mimic an experimental set up, which was built at UniSA to investigate dynamic melting conducted by Tay et al. [132] and more information is provided in chapter 3, section 3.2.2.1. The geometrical non-dimensional parameters (introduced in chapter2, section 2.5) are; L/d = 37, R/r = 3.84 (Fig. 6.1). This geometry in the vertical orientation was used for modelling the melting process of ice as a low temperature PCM and a type of thermal oil as HTF. Results of that study were verified with the experimental data which is included in chapter 3, section 3.2.2. In this section, the same geometry and grid was used to study an element of a horizontal parallel flow arrangement with a new high temperature PCM (Na_2SO_4-NaCl, 68:32 wt.%) in conjunction with liquid sodium (Na) as the HTF. The new PCM is under investigation in the UniSA material laboratory and the preliminary or assumed thermophysical properties of the PCM are included in Tables 6.1. Average thermophysical properties of HTF, and other variables are included in the Table 6.2.

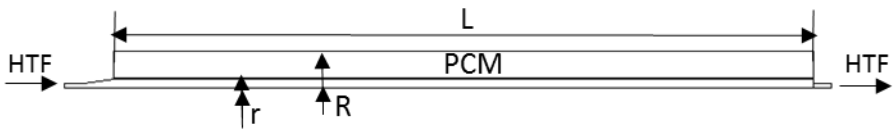


FIGURE 6.1. Geometry of the model scale

Table 6.1: Thermophysical properties of PCM

Density, kg/m^3	2000
Specific heat, kJ/kg K	1730
Latent heat of fusion, kJ/kg	285
Thermal conductivity, W/m K	1
Thermal expansion coefficient	0.0006
Dynamic viscosity, Pa s	0.0032
Melting temperature, ˚C	625

Table 6.2: Thermophysical properties of HTF [146]

Density, kg/m^3	792
Specific heat, kJ/kg K	1251.38
Thermal conductivity, W/m K	53.42
Dynamic viscosity, Pa s	0.0002
Mass flow rate, kg/s	0.01028
Velocity in tube, m/s	0.04

6.1.2 Numerical calculations

All the model setting and thresholds are the same as explained in chapter 3, section 3.2.1.2. The same grid as used in the previous modelling presented in chapter3, section 3.2.2, with 78000 cells and 0.1 seconds as time step is used for this modelling. The boundary conditions are; symmetry at the HTF side, mass flow inlet and outflow at the HTF inlet and outlet, and adiabatic elsewhere.

For the charging process, the HTF inlet temperature was set at 650 °C, resulting in $T_h - T_m$=25 K with the initial temperature setting at 620 °C, 5 K subcooled. For the discharging case, respective figures are 472˚C, $T_m - T_c$ =150 K, and 627 ºC, 3 K superheated. The relevant non-dimensional parameters are: Ra =1.4x10^6 and Ste=0.152.

6.1.3 Results and discussion

6.1.3.1 Charging process

In this section, results of the flow, mass and heat transfer showing the characteristics of the charging process are analysed. Figs. 6.2a shows the temperature profile at 8050 second and 60% melt fraction while Fig. 6.3c provides a temporal evolution of average temperatures at the HTF outlet, at the tube interface between HTF and PCM, and in the PCM domain. Combined together, they provide an insight into temperature distribution; for instance the temperature range in the PCM domain is 624-646.4 °C with an average of 629.2 °C can be used for stress analysis and shell and/or tube material selection. An important figure is the average temperature at the tube interface between PCM and HTF that can be used for the sectional modelling as proposed in chapter 7.

Figure. 6.2b shows the radial velocity range which is between 0.018-0.04 m/s in the PCM domain, where the minus sign shows counter clockwise circulation and white color shows a stagnant region or where the velocity is nearly zero. The higher radial velocity shows faster convection cells to transfer mass and consequently higher convection heat transfer.

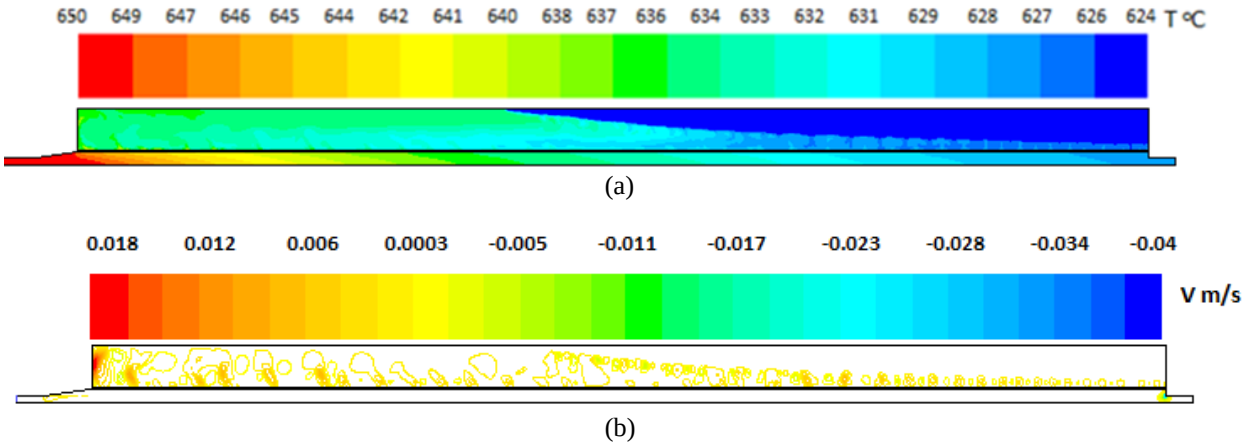


FIGURE 6.2. Profiles of the melting process at 8050 seconds and 60% melt fraction:
(a) temperature, (b) radial velocity

Figure. 6.3a shows the average heat transfer rate during the convection dominant regime, e.g. after 10% melt fraction and up to the end of process is approximately 3800 W/m^2 or 0.28 kWh$_{th}$ per metre of the annulus. Figure. 6.3b reveals the effectiveness being higher than 80% up to 80% melt fraction. Here, the high effectiveness is the result of low velocity of the HTF, however using this result to design a system for a CSP plant, a higher mass flow rate might be necessary to account for optimum number of tubes for a cost effective system.

The melt fraction graph in Fig. 6.3d, provides information about the duration of the melting process which is useful for the preliminary design of a similar LHTES system.

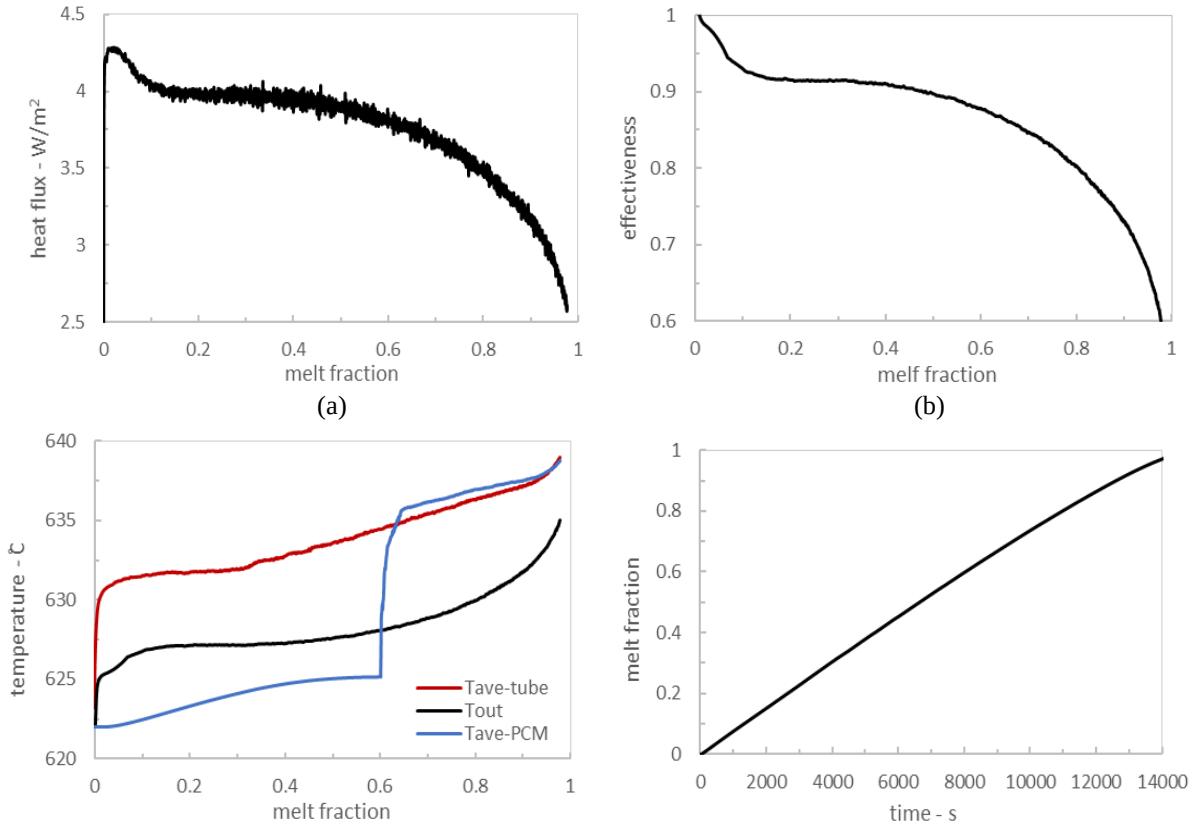


FIGURE 6.3. Temporal evolution of scalar fields during the charging process:
(a) heat flux (b) effectiveness, (c) temperature profiles, (d)melt fraction

6.1.3.2 Discharging process

Figures. 6.4, and 6.5c demonstrate the temperature field in space and time. Fig. 6.4a, the temperature profile at 1350 seconds with 10% of liquid changing to solid shows that almost half of the tube surface (downstream of the HTF) is in direct contact between HTF and liquid. This results in a higher temperature difference and driving force for natural convection and consequently an inclination in the isotherms, which are visible closer to the upstream of the HTF. However, at 1700 seconds with 12.4% of the solid formation (Fig. 6.4b), almost all the tube surface is covered with a solid layer leaving a small temperature difference to drive the conduction heat transfer as the main heat transfer mode. Consequently, the isotherms or the phase front is one-dimensional and moves parallel to the tube up to the end of the process. From this observation, one can expect low convection cell formation from the start of the process to nearly zero number of cells from the 12.4% solid fraction up to the end of the process. Consequently, a radial velocity contour at 1700 seconds shows no profile, and for this reason it is not presented.

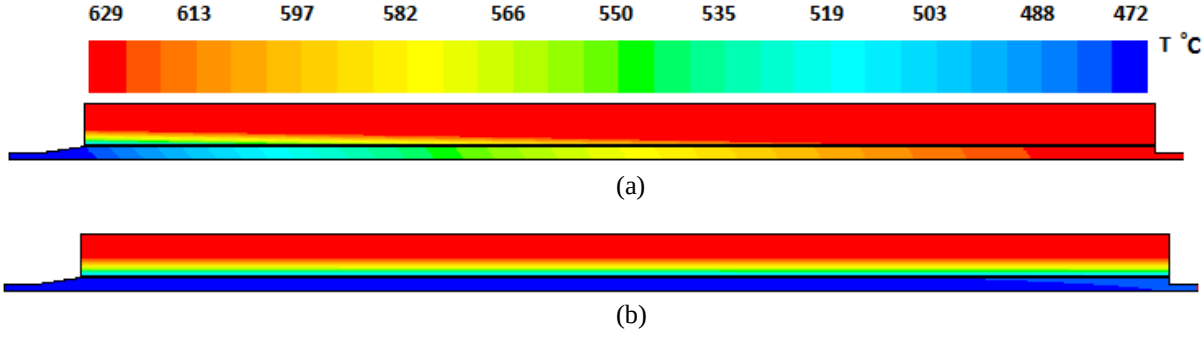


FIGURE 6.4. Temperature profiles of the discharging process:
(a) at 1350 seconds and 10% solid fraction, (b) at 1700 second and 12.4% solid fraction

While the charging process characteristics (e.g. HTF inlet temperature) are deterministic parameters for the design purposes, the heat flux (Fig. 6.5a) and outlet temperature (Fig. 6.5c) available from the discharging process are important factors as the HTF delivers the required amount of thermal energy to the power generation block in a CSP plant. Fig. 6.5c shows the delivery outlet temperature during the discharging process. In case the inlet temperature required for the turbine is in a range of 580-600 ºC, this parallel configuration is capable of providing it up to the 50% solid fraction where the effectiveness of the system is almost 70% (Fig. 6.5b). This is consistent with the results of the comparison study of different configurations presented in chapter 4, section 4.5. In general, parallel configuration provides a quicker phase change process with a high effectiveness at first, which starts to decline earlier and sharper compared with the counter flow and fin plate configurations. However, considering the tube length being one metre, the longer tube can provide a higher effectiveness enabling the system to deliver the required thermal energy for a longer time. The average temperature at the tube/PCM interface shown in Fig. 6.5c can be used for sectional modelling, which is part of the proposed design and optimisation procedure in chapter7.

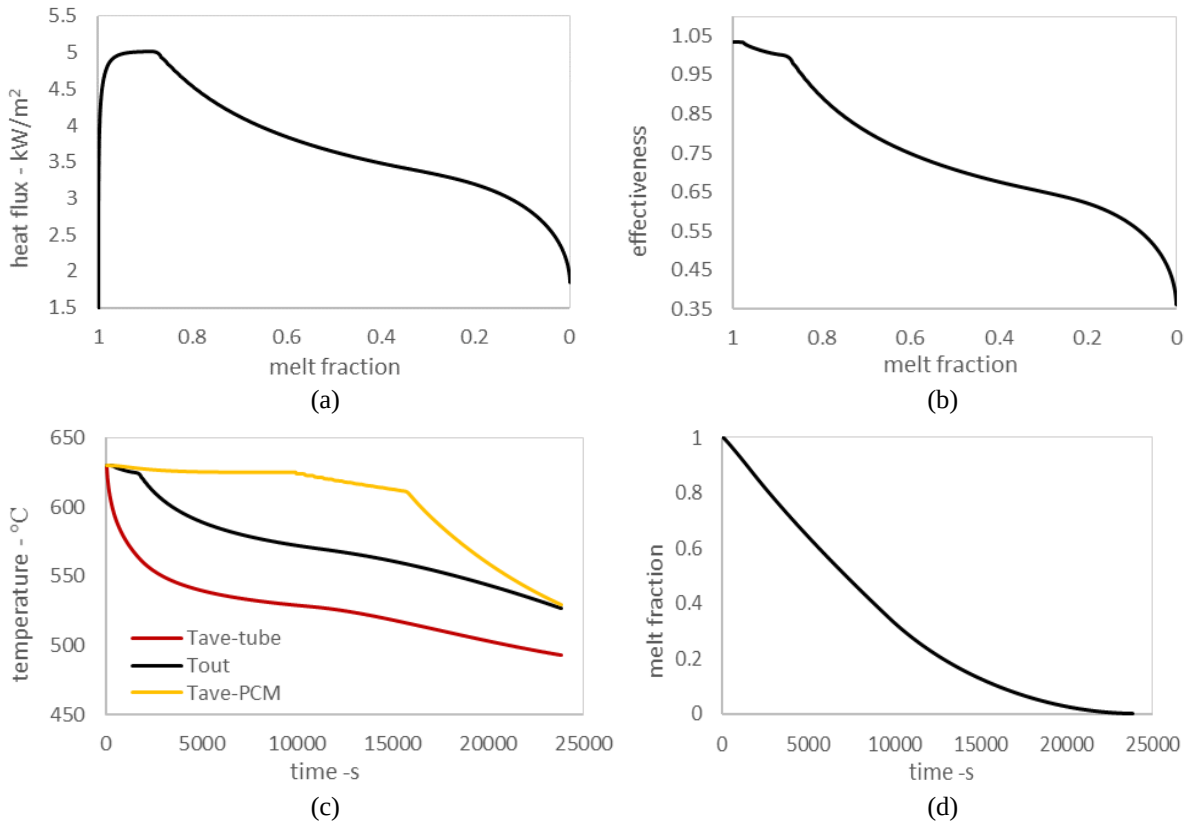


FIGURE 6.5. Temporal evolution of scalar fields during the discharging process:
(a) heat flux (b) effectiveness, (c) temperature profiles, (d)melt fraction

6.2 Three dimensional modelling of a U-tube from the UniSA prototype

From the study in chapter 3, section 3.2.3 it was found that a three-dimensional U-tube model as an element of a two-pass shell and tube system can be selected as a scale down model of the whole system for a numerical study. Here, a different type of three-dimensional U-tube as an element of a counter flow LHTES system was selected (Fig. 6.6). The model specifications are adopted from the prototype shell and tube system built at the University of South Australia as described in chapter 4, section 4.2. As the results of numerical modelling presented in Chapter 4 showed that the horizontal orientation provides a higher effectiveness, the horizontal orientation is used in this analysis.

6.2.1 PCM system

For this study, high temperature PCM (PCM621) was selected with liquid sodium (Na) as the HTF, for which thermophysical properties are shown in Tables 6.1, and 6.2, respectively. Here, charging and discharging processes are investigated with adopted design criteria from a real application in a CSP plant from the ASTRI partners. Due to the upstream limitations of the HTF outlet temperature from the receiver, the inlet temperature to the LHTES during the melting process was set to 650ºC, resulting in $\Delta T=T_{in}-T_m= 25$ K. The velocity and mass

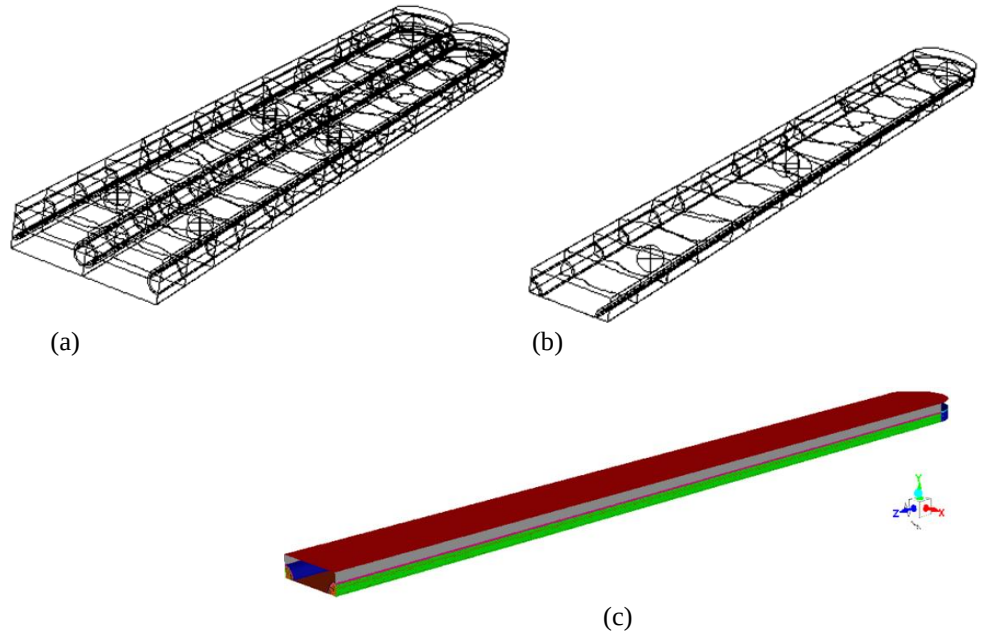
flow rate were set to 0.2 m/s and 0.0082kg/s respectively. This is a matter of trade-off between a lower Reynolds number resulting in lower pressure drop and higher effectiveness, and fewer pipes (heat transfer area between HTF/PCM) resulting in a more cost effective system. The initial temperature was set 5 K lower than the melting temperature of the PCM to capture the onset of the latent heat transfer when the system temperature approaches the melting point.

For the discharging case, due to the outlet temperature from the downstream condenser, the inlet temperature to the PCM system was set to 477ºC, leading to $\Delta T = T_m - T_{in} = 148$ K. To represent a discharging case closer to the real application, a final stage of the charging case as melt fraction = 99.2%, and average temperature in PCM = 614 ˚C were selected as the initial condition for the discharging case. However, due to the higher ΔT, the velocity and mass flow rate of the HTF decreased to 0.04 m/s and 0.0016 kg/s to achieve a higher effectiveness.

6.2.2 Numerical calculation

6.2.2.1 Geometry and grid

The straight length of the tube is 55 cm with a horizontal distance of r = 6 cm between centre to centre of tubes (width of geometry). As mentioned before, details of the shell and tube system are included in chapter4, section 4.2. Considering a complete U-tube including the PCM between the tubes (Fig. 6.9a), a quarter of the U-tube was selected as the numerical model as shown in Fig.6.6b. Fig. 6.6a is included to show an extended view of the counter flow system, clarifying the selection of the quarter of the U-tube and PCM between them. A three-dimensional grid was generated with ANSYS Design Modeller [37], with about 995600 cells, covering three domains of the PCM, tube and HTF as shown in Fig. 6.6c.



(a) (b)

(c)

FIGURE 6.6. Three-dimensional schematic drawings: (a) a complete U-tube geometry, (b) symmetrical geometry of a quarter of the U-tube and PCM (c) symmetrical grid of the quarter of the U-tube

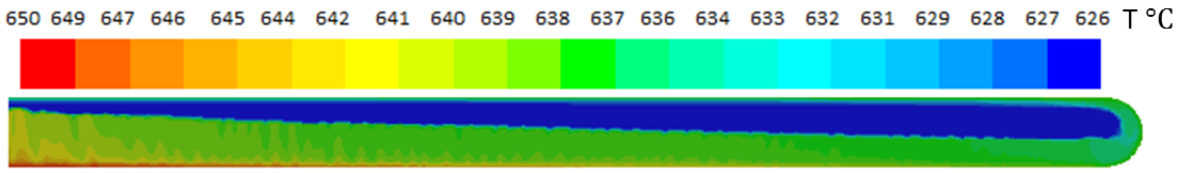
6.2.2.2 Modelling

Three dimensional numerical modelling of the charging and discharging processes with natural convection was performed, using ANSYS FLUENT [35]. All the numerical schemes and threshold are the same as explained in chapter3, section 3.2.1.2. The assigned boundary conditions were; symmetry at different sides of the PCM and the HTF, adiabatic conditions at the top and bottom of PCM and tube, velocity inlet and outflow at the inlet and outlet of HTF.

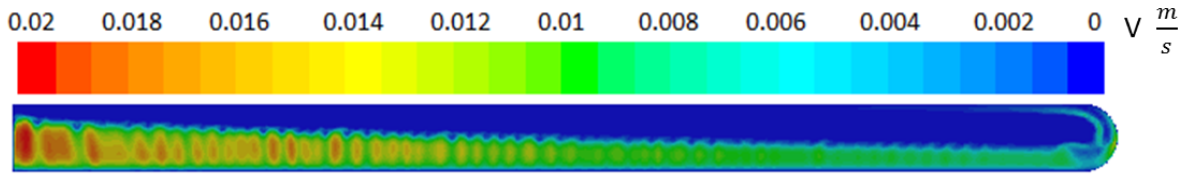
6.2.3 Results and discussion

6.2.3.1 Charging

Results from the model study show the characteristic scales in the PCM domain: velocity range between 0.004-0.023 m/s (Fig. 6.7b), mass transfer between 0-0.65 kg/s (Fig. 6.8e), and average temperature in the PCM domain 636 °C (Fig. 6.8d). Starting from the same initial temperature in all domains, at the early stages in the conduction dominant mode, the heat transfer rate to the PCM is very high (Fig. 6.8a) and the average temperature at the tube

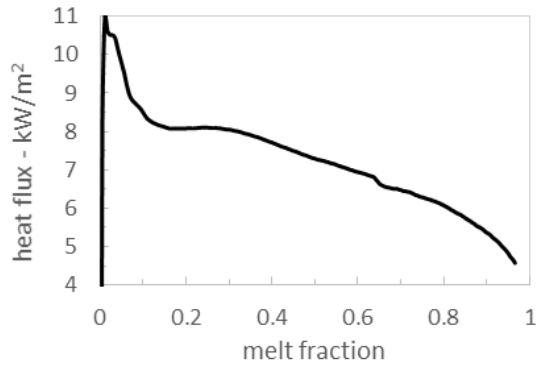


(a)

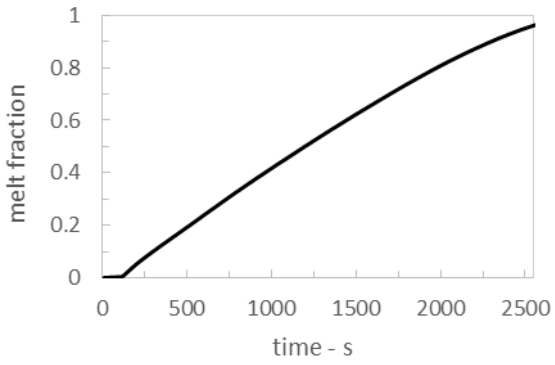


(b)

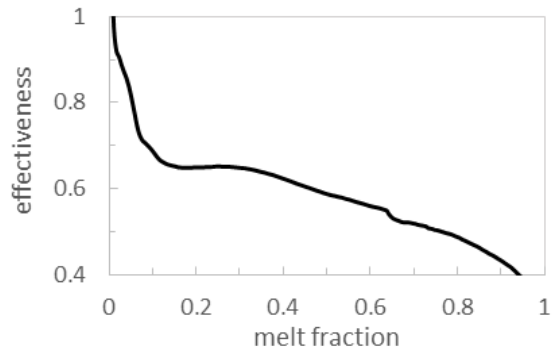
FIGURE 6.7. Profiles at 1500 seconds and 60% melt fraction: (a) temperature, (b) radial velocity



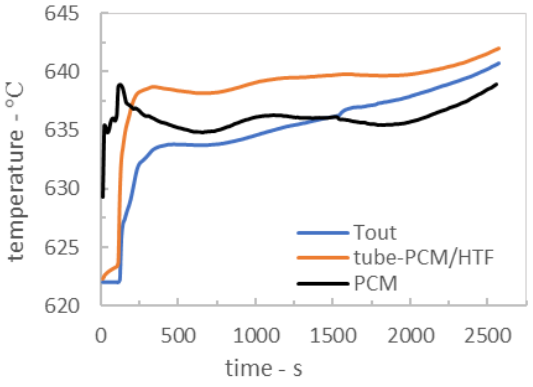
(a)



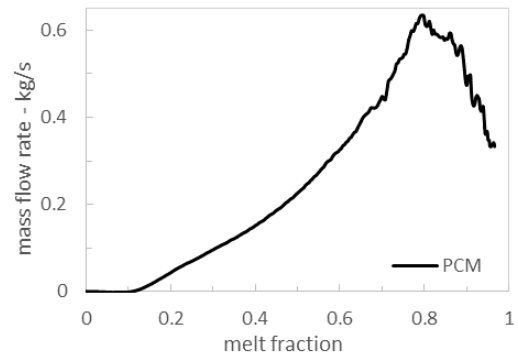
(b)



(c)



(d)



(e)

FIGURE 6.8. Temporal evolution of scalar variables during the charging process: (a) heat flux at tube/PCM interface, (b) melt fraction (c) effectiveness, (d) average temperature profiles, (e) PCM mass flow rate.

surface (the material being stainless steel) are lower than the average temperature in the PCM domain (Fig. 6.8d). After about 100 seconds, with more liquid PCM when the convection heat transfer gets momentum, the average temperature of the tube surface becomes the highest as expected. The average heat transfer rate after 10% melt fraction and up to the end of the convection dominated regime is approximately 6800 W/m^2 (Fig. 6.8a) which equals 136 W for a quarter of the u-tube (the model comprises a quarter of a tube and the PCM in between the u-tubes) with 0.02 m^2 heat transfer area. The average effectiveness of the u-tube element is higher than 60% up to the 50% melt fraction (Fig. 6.8c). Increasing the inlet temperature of the HTF and/or the number of tubes to decrease the mass flow rate improves the effectiveness.

6.2.3.2 Discharging

Results from the model show the characteristic scales in the PCM domain: velocity range between 0-0.023 m/s, mass transfer between 0-0.6 kg/s up to 60% of the liquid changes to solid (Fig. 6.12e), and average temperature in the PCM domain 625 °C (Fig. 6.9d). The average heat transfer after 15% solid fraction and up to the end of process is approximately 7200W/m^2 (Fig. 6.9a) that is equal to 160 W for the quarter of the u-tube (the model comprises a quarter of a tube and the PCM in between the u-tubes) with 0.02 m^2 heat transfer area. Starting the discharging case from the melt fraction = 99.2% and average temperature in PCM = 614 ˚C, which means time starts from 2750 seconds where charging stops. Accordingly, Fig. 6.9b shows the start of solidification process at 2750 second, taking about 4000 seconds for the complete discharging.

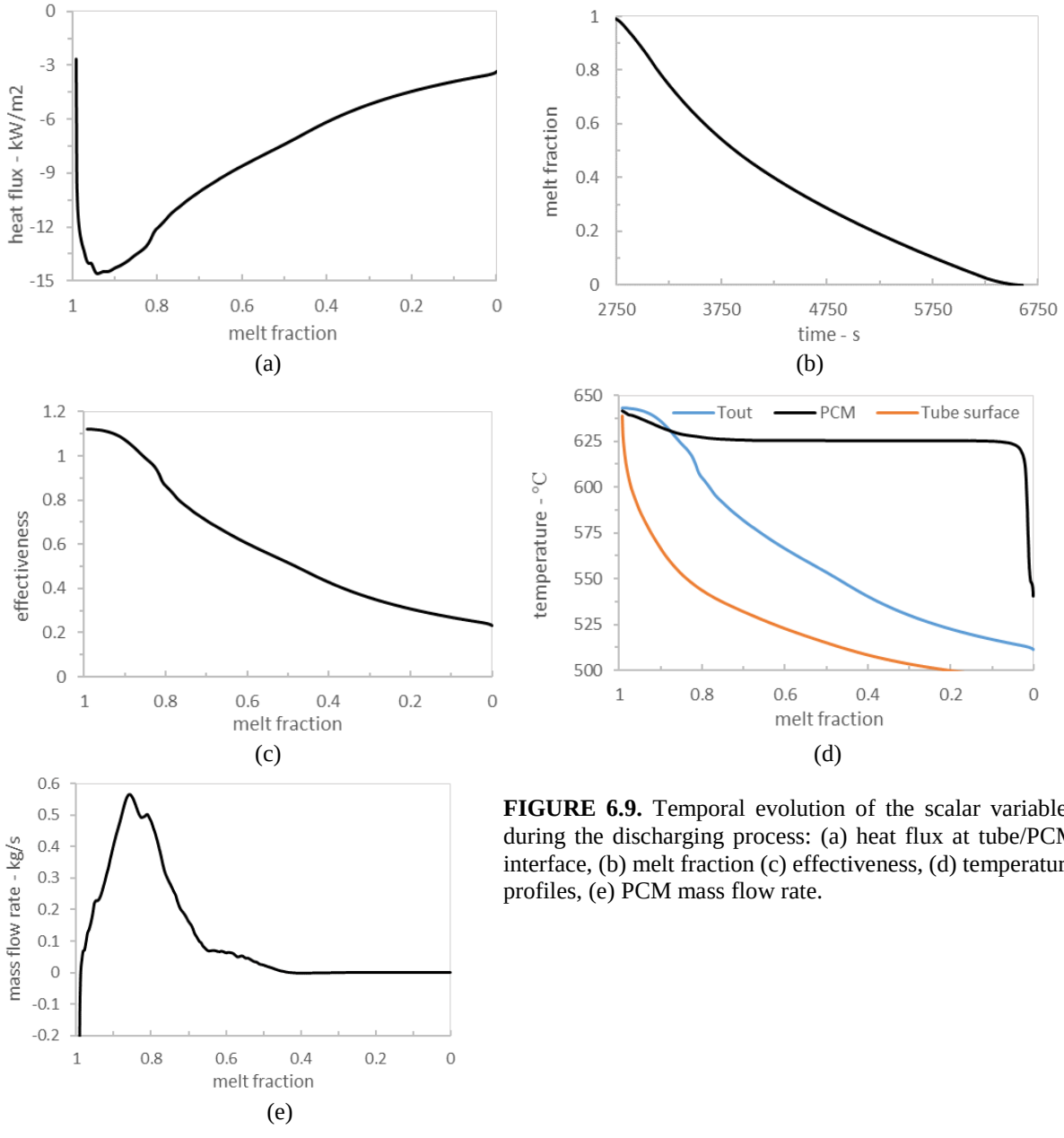


FIGURE 6.9. Temporal evolution of the scalar variables during the discharging process: (a) heat flux at tube/PCM interface, (b) melt fraction (c) effectiveness, (d) temperature profiles, (e) PCM mass flow rate.

Figure 6.9c presenting the effectiveness shows the sensible and latent heat release at the early stages (where the effectiveness is higher than 1) of the discharging process up to 85% solid fraction. After this point, effectiveness shows solely the latent heat transfer effectiveness which on average equals to 64%.
Regarding the mass transfer in the charging process, Fig. 6.8e shows that mass flow rate increases up to the maximum ~0.6 kg/s and decreases afterward due to the reduction of temperature gradients, which is the result of higher mixing effect at higher melt fraction. Whereas, the mass flow rate increases first due to the high melt fraction and starts to decrease earlier due to the diminishing temperature gradient (a flat average temperature in PCM visible in Fig. 6.9d) as a solid layer covers the tube/PCM interface. This results in a declined (two-dimensional) melting front in the charging and a one-dimensional phase front for the most of the discharging process. These are consistent with the results of the previous studies.

6.3 Conclusion

For design purposes, the melting process was considered as the core focus because the upstream data (e.g. inlet temperature of HTF from the receiver and solar field) of the CSP cycle shows less flexibility compared with the downstream data (e.g. outlet temperature of HTF from the storage system which is the inlet temperature to the turbine and the power block). However, the delivered heat flux and outlet temperature of the HTF during the discharging process are also significant parameters.

Results from the first melting process showed the temperature range in the PCM domain is 624-646.4 °C with an average of 629.2 °C, useful for stress analysis and material selection. Average temperature at the tube interface between PCM and HTF ~ 630 ºC can be used for the sectional modelling as it is proposed in chapter 7. Radial velocity range is between 0.018-0.04 m/s in the PCM domain, and the rate of average heat transfer is approximately 3800 W/m^2 or 0.28 kWh$_{th}$ per metre of the annulus. The high effectiveness ~ 80% is the result of the low velocity of the HTF, however, a higher mass flow rate might be necessary to account for the optimum number of tubes for a cost effective system. The melt fraction provides information about the duration of the melting process useful for the preliminary design of a similar LHTES system. The delivery heat transfer rate during the discharging process are ~3500 W/m^2 of the tube/PCM interface at the outlet temperature of 580-600 ºC up to the 50% solid fraction where the effectiveness of the system is almost 70%. Considering the tube length being one metre for the modelling, a longer tube can provide a higher effectiveness enabling the system to deliver the required thermal energy for a longer time. The average temperature ~525 ºC at the tube/PCM interface.

The characteristic scales in the PCM domain during the second melting process are: velocity range between 0.004-0.023 m/s, mass transfer between 0-0.65 kg/s, and average temperature is 636 °C. The average heat transfer rate is approximately 6800 W/m^2, which is equal to 136 W for a quarter of the U-tube with 0.02 m^2 heat transfer area. The average effectiveness of the U-tube element is higher than 60% up to the 50% melt fraction. Increasing the inlet temperature of HTF and/or the number of tubes to decrease the mass flow rate improves the effectiveness.
During the discharging process, the velocity range is 0 - 0.023 m/s, mass transfer between 0 - 0.6 kg/s up to 60% of the liquid changes to solid, and average temperature in the PCM domain is 625 °C. The average heat transfer is approximately 7200W/m^2 equal to 160 W for the quarter of the u-tube. The latent heat transfer effectiveness, on average equals 64%.

The results of the three-dimensional study provided insight into the thermal behaviour of the PCM and the main characteristics of the system. The results of the studies are to pave the path and form the basis for the design and optimisation of a shell and tube system in the next chapter,7.

7 Design and optimisation procedure of geometrical parameters of a PCM storage system

In the process of incorporating a storage system in a real life application, the design criteria demands different priorities for different storage applications due to specific constraints and variables. For instance, targeting 6 hours duration for a charging process in a CSP plant and varying other parameters might lead to an optimal design. On the other hand, in cases where LHTES is used to protect a receiver from overheating [32], or as an auxiliary source of energy during peak energy demand periods in a CSP plant, higher rates of energy release might be necessary. Design criteria for a TES system is defined by the upstream conditions (e.g. HTF inlet temperature from the solar field/receiver in a CSP plant) and the downstream conditions (e.g. outlet temperature to the turbine component of a power block in a CSP plant).

A LHTES system should be capable of storing the required amount of heat during the available time depending on the site upstream design criteria. An optimal design for every application should use the highest volume fraction of PCM for the highest heat storage density during a melting process. In reality this means the smallest unit with a uniform melting process of PCM in space and time without hot-spots [122], leading to a cost-effective thermal storage system. From the discharging standpoint, it is crucial to deliver the required heat release rate during a certain period complying with the downstream conditions. In contrast to the melting processes where the temperature difference between the HTF and melting front lasts longer, temperature differences as the driving force for the heat transfer decreases faster in the discharging processes due to a solid layer formation on the heat transfer surfaces such as the tubes, plates and/or fins [65]. As a result, part of the PCM, namely the redundant PCM loses the capability to provide enough heat transfer rate to support the demand side in the later stages of a discharging process [23, 139]. An optimal design should reduce/eliminate the redundant PCM, leading to a smaller system and minimised system costs.

The first and second law analyses provide a means to optimise the design. From the first law analysis, a system with highest effectiveness is desirable while through the second law analysis one can realise/reduce the imperfections causing irreversibilities and entropy generations. The optimal system is a compromise between two main goals; highest effectiveness and lowest entropy generation leading to the highest exergy recovery or the highest density of storage/delivery of useful work [38].

In a CSP plant, a LHTES system working in the charging and discharging cycles might impose different criteria, depending on the scale and operating temperature/pressure of the cycle, the HTF inlet temperature (outlet from a receiver), and the outlet temperature required for the turbine. PCM is selected mainly according to its melting temperature and latent heat of fusion to work with a specific HTF at available inlet (T_h) temperature from the solar field/receiver and also, from the power block/turbine (T_c) to the LHTES system. The inlet/outlet temperatures as the upstream/downstream of a CSP cycle and the consequent selected HTF/PCM is the result of the first and second law (energy/exergy) analyses of the whole cycle including a PCM system. This analysis is beyond the scope of this thesis, and here, we assume a HTF/PCM combination, which is selected as an outcome of such an analysis. Hence, the HTF inlet (for both charging/discharging), and the required outlet temperature during discharging, the PCM melting temperature plus the thermophysical properties are known as an input for the design and optimisation of the LHTES system.

There are a few alternative eutectic salts as PCM matched to the criteria which is decisive for the temperature differences (e.g. $\Delta T_{ch} = T_h - T_m$ or $\Delta T_{dc} = T_m - T_c$) during the charging and discharging cycles. From the knowledge acquired so far a probable range is ΔT_{ch} (20-50 K) < ΔT_{dc} (100-200 K). The narrow range of upstream temperature difference requires the design and optimisation of a LHTES system based on the melting process through which natural convection is the dominant heat transfer mode. Certainly, this is after the main selection of which the configuration leads to the best performance for both charging and discharging processes according to the knowledge gained from the numerical studies and comparison of different configurations (chapter 4).

Here, implementing all the knowledge gained through the numerical studies and from the previous literature in the scope of design and optimisation, a step by step method is proposed with the assistance of numerical modelling and dimensional analysis. While the method can be used for different applications of a LHTES, the focus in this chapter is on CSP applications.

7.1 Design and optimisation procedure using numerical modelling

To achieve the ultimate goal of the highest density of storage/delivery of useful work, the previous numerical studies described in chapter 4 provide necessary insight into the flow, heat and mass transfer, the impact on the thermal performance in different configurations, and suitability for different applications. Building upon the knowledge gained from the scale model studies presented in chapters 3 to 6, selection of a configuration for a specific purpose is possible. Furthermore, the two main tools of scaling and parametric analyses can assist in using the results from a numerical examination for the design and optimisation of a system at the prototype or

industrial scale. Using these tools, here the following main steps are proposed for the design and optimisation of a LHTES, which are elaborated through the next sections of this chapter.

- Selection of a configuration delivering the best performance for a specific application, based on the results of previous numerical modelling.
- Preliminary design of a LHTES system to match a set of design criteria at the industrial scale (e.g. the required storage capacity), using the results of previous parametric studies (reviewed in chapter 2, section 2.5). This includes looking at parameters such as total mass, volume and PCM volume fraction, height, length and diameter/width, HTF mass flow rate/velocity, tube arrangement, size and spacing.
- Selection of a scale model, lab scale and/or prototype through scaling analysis compared to the real application at the industrial scale.
- Evaluation of the characteristics of the specific configuration of PCM/HTF through a numerical study of the scale model. The main characteristics are; velocity, temperature and temperature gradients, dominant heat transfer mode and heat transfer rates.
- Detailed design of the LHTES system at the prototype/industrial scale. Using information from the modelling of the scale model.
- Numerical study of a part, a section or different sections of the prototype and/or industrial scale LHTES system.
- Optimisation of the system, using the results of sectional numerical study for further parametric analysis/revision to reduce heat transfer area (e.g. highest PCM volume fraction) or total volume, and cost.

7.1.1 Preliminary design of geometric specification

The thermal behaviour of each system depends on the thermosphysical properties of the PCM and HTF, the selected configuration, and temperature differences (e.g. $\Delta T_{ch} = T_h - T_m$ or $\Delta T_{dc} = T_m - T_c$), leading to unique characteristics for each system. It has been shown in previous studies [118] that optimisation of geometrical specifications should be carried out for each combination of HTF/PCM, mainly due to the unique characteristics. For the design and optimisation of a LHTES system, the characteristics of the specified HTF/PCM should be evaluated, e.g. velocity scales, temperature gradients, and heat transfer rates in the charging/discharging processes. Numerical modelling provides a means for this evaluation.

As a first step, a configuration should be selected according to the knowledge gained from previous studies (chapters 4), e.g. a horizontal counter flow shell and tube configuration or a vertical flat plate system, providing a uniform heat storage and heat release with relatively high effectiveness. Selecting a configuration, a preliminary design of the LHTES system at the industrial scale is possible for specific storage/release of heat (e.g. 1 MWh_{th}, deliverable energy/power) including the PCM mass/volume, and the HTF mass flow rate.

$$Q\ (J) = \dot{\mathrm{Q}}\ \left(\frac{J}{s}\right) \times \mathrm{t}\ (s) \quad , \quad V_{pcm}(\mathrm{m}^3) = \frac{Q\ (J)}{\rho\left(\frac{kg}{\mathrm{m}^3}\right) \times h\left(\frac{J}{kg}\right)} \quad , \quad \mathrm{m}_{pcm}(kg) = \rho\ \left(\frac{kg}{m^3}\right) \times V_{pcm}(\mathrm{m}^3) \tag{20}$$

Assuming a volume fraction for the PCM leads to an estimation of the volume fraction of tubes/plates. Consequently, the total volume of the system and an estimation of the heat transfer area follows, depending on the material selection and its properties. The mass flow rate of the HTF needs to be estimated to enable the delivery of the required heat transfer rate during the melting process when designing a LHTES that is based on the charging process.

$$\dot{m}_{HTF} = \frac{\dot{Q}}{C_p(T_{in} - T_m) \times \varepsilon} \tag{21}$$

Moreover, a first estimation of the geometric parameters can be selected using the non-dimensional geometrical parameters (L/d, R/r, S/d). Summarising the relevant results of previous parametric studies reviewed in chapter 2, section 2.5, a preferred framework can be realised for a preliminary selection of different parameters including L, R, d=2r;

- Laminar flow of HTF
- The ratio of R/r should be selected from the range of R/r = [1.3, 5]
- The ratio of L/d should be selected from the range of L/d = [10, 100]

For the optimal spacing between parallel plates (S_{opt}) confined in a fixed volume (fixed L, w, z) while convection heat transfer occurs with a fluid passing through them, Bejan and Lorente [122] and Bejan et al. [123] proposed correlations to achieve the highest heat transfer density, balancing fluid flow resistance and heat flow resistance.

$$\frac{S_{opt}}{z} \cong 2.3\, Ra_z^{-\frac{1}{4}} \tag{22}$$

$$q_{max} \approx 0.45\, k_{fluid}\, (T_w - T_0)\, \frac{L}{z} z^{\frac{1}{2}} \tag{23}$$

T_w and T_0 are the heat transfer surface (tube or plate) and the entering fluid flow temperature, respectively. In a LHTES system, the counterpart temperatures are T_h and T_m, HTF inlet and melting temperature of PCM, respectively. Moreover, the authors of those studies [122, 123] proposed dimensionless groups for the optimal spacing between tubes and the maximum thermal conductance in a horizontal staggered arrangement of pipes confined in a fixed volume (fixed L, W, Z) for the highest heat transfer density to/from the tube bundle in a cross flow.

$$\frac{S_{opt}}{d} \propto \left(\frac{z}{d}\right)^{\frac{1}{3}} Ra_d^{-\frac{1}{4}} \qquad \frac{S_{opt}}{z} \propto \left(\frac{z}{d}\right)^{\frac{1}{12}} Ra_z^{-\frac{1}{4}} \qquad Ra_d = \frac{g\beta\, d^3 (T_w - T_0)}{\alpha\vartheta} \tag{24}$$

$$\tilde{q} = \frac{q}{zWL}\, \frac{d^2}{k(T_w - T_0)} \qquad \tilde{q}_{max} \propto \left[\left(\frac{z}{d}\right)^{\frac{1}{3}} Ra_d^{-\frac{1}{4}}\right]^{-1.6} \tag{25}$$

Considering the forced convection cooling of a stack of parallel plates generating heat, Bejan and Lorente [122] proposed another dimensionless group as follows:

$$\frac{d_{opt}}{L} \propto Be^{-\frac{1}{4}} \qquad Be = \frac{\Delta P\, L^2}{\mu\alpha} \tag{26}$$

Equations were proposed valid for the range of the study; Ra_d [350-10^4], Pr=0.7, z/d [6,20], S/d [0.5,3] as follows:

$$\frac{S_{opt}}{d} = 2.72 \left(\frac{z}{d}\right)^{\frac{1}{3}} Ra_d^{-\frac{1}{4}} + 0.263 \tag{27}$$

$$\tilde{q}_{max} = 0.448 \left(\left(\frac{z}{d}\right)^{\frac{1}{3}} Ra_d^{-\frac{1}{4}}\right)^{-1.6} \tag{28}$$

$$\frac{S_{opt}}{z} \cong 2.72 \left(\frac{z}{d}\right)^{\frac{1}{12}} Ra_z^{-\frac{1}{4}} + 0.263 \left(\frac{d}{z}\right) \tag{29}$$

$$\frac{d_{opt}}{L} \cong 2.7\, Be^{-\frac{1}{4}} \tag{30}$$

Two Ra numbers can be accounted for, Ra_z as the global order of natural convection while Ra_d presents the impact of tube diameter on the local boundary layer which is important in a horizontal orientation of the tubes. $\tilde{q}$ represents the dimensionless heat transfer volumetric density.
Where Be (Bejan number) is the Ra counterpart in a forced convection fluid flow and ΔP is the pressure drop. To introduce a correlation from the above proportionality, a coefficient should be found through a set of numerical parametric study.
The total number of tubes in the staggered tube arrangement can be derived from the following equation [123] at the preliminary design stage.

$$n = \frac{zw}{(S+d)^2 \cos 30^\circ} \tag{31}$$

As the next step, a decision can be made for the scale of a research prototype, e.g. with a 1/10 capacity 100 kWh_{th}.

7.1.2 Numerical modelling of a scale model

7.1.2.1 Scale analysis

The quality and quantity of storage/release of heat in a phase change process depends on the thermal and geometrical parameters of the system. The scale analysis provides valuable means to narrow down all the parameters to a few correlations governing the transport phenomena regardless of the scale. The range of those correlations might cover special cases in specified ranges of the thermal and geometrical parameters. However, those correlations are helpful for a preliminary design of a system or scale down model from an industrial size application to a lab scale prototype for experimental study or to a scale model for numerical study.

The relevant non-dimensional groups can be driven from dimensional analysis [147] or from the normalisation of the Navier-Stokes equations. In the field of phase change process, the non-dimensional groups are known from the literature; namely Rayleigh number (Ra =Gr PR), Prandtl number (Pr), Fourier number (Fo), and Stephan number (Ste). Through these groups, the role and importance of the viscous and buoyancy forces (natural convection), thermal diffusion (conduction) and the ratio of the sensible heat to latent heat can be identified depending on the thermophysical properties of the PCM, and the geometry and arrangement of the LHTES system. For the HTF side in a LHTES system, Reynolds number (Re) representing the ratio of convection, and viscous forces is relevant due to the forced convection and flow resistance phenomena. Nusselt number (Nu) as the ratio of convection to conduction, is another relevant number in both sides; forced convection (HTF) and natural convection (PCM). Considering the geometry and arrangement of a LHTES system, there are other geometrical dimensionless groups that are proposed in the literature [118-120, 122, 123], (Eqs. 21-30).
As mentioned at the start of this chapter, from the thermal and geometrical design parameters of a LHTES system for a CSP plant, the type of HTF/PCM and the inlet/outlet/melting temperatures are the output of the first/second law analyses of the whole cycle including receiver and turbine. Here, we assume thermal parameters are the input to our study to find/optimise the geometrical parameters. This assumption relaxes the consideration of Ste and Pr from the main non-dimensional groups when the PCM and temperatures are fixed. The two other groups remaining for consideration are Ra and Fo number, regarding transient convection and conduction heat transfer.
However, characteristic length and geometrical parameters need to be identified in conjunction with the system configuration. Here, a counter flow shell and tube system in the horizontal orientation is the selected configuration for a case study. In this case, tube length (L), diameter/radius (d/r), spacing (S), the PCM radius (R) and the shell diameter (H) are the geometrical parameters. Reducing the number of parameters, they can be combined in non-dimensional groups for which Eqs. 23-29 might provide guidance. Main characteristic lengths are the tube diameter (d=2r), PCM radius (R) and the tube length (L) while tube spacing (S) and PCM radius (R) are related as 2R= S+d. Selecting d, S, and L and in compliance with previous literature, we consider three dimensionless geometrical group, namely S/d, H/d and L/d. Hence, a combination of thermal and geometrical dimensionless groups for a horizontal shell and tube configuration can be considered as follows:

PCM side: $$Ra_d = \frac{g\beta d^3(T_h - T_m)}{\alpha\vartheta} \qquad Ra_z = \frac{g\beta z^3(T_h - T_m)}{\alpha\vartheta} \tag{32}$$

$$Fo_d = \frac{\alpha t}{d^2} \qquad \tilde{s} = \frac{S}{d} \qquad \tilde{L} = \frac{L}{d} \qquad \tilde{Z} = \frac{z}{d} \tag{33}$$

HTF side: $$Re = \frac{\rho V d}{\mu\alpha} \tag{34}$$

As mentioned before, for a horizontal orientation Ra_d is more significant, showing the impact of tube diameter on the local boundary layer, particularly for the purpose of scale down to a model from the preliminary design of prototype/industrial scale. Using the same argument, H/d can be disregarded at this stage. The remaining relevant dimensionless groups are; Ra_d, Fo_d, $\tilde{s}$, $\tilde{L}$, and Re.

7.1.2.2 Scaling down to a model

The scale down method and the size of a model for the numerical studies depend on the computational resources. To scale down for a three dimensional scale model, the relevant dimensionless groups should be kept equal between the model and the prototype/industrial scale. However, for a minimum computation time and cost, a two dimensional geometry of an element of the system is preferable, depending on the complexity of the selected configuration. A two dimensional scale model can be provided as a view/section (e.g. top or side view or symmetrical section) of a three dimensional scale model. While for a rectangular system scaling down/up from a two dimensional simplified model and the real scale by the dimensionless groups is easier. On the other hand, for a shell and tube system more caution and engineering judgement are necessary.
For a repetitive configuration such as a shell and tube, the preferred geometry through the literature was an annulus where HTF flows through the inner tube and PCM is confined in the outer tube. Considering large-scale systems, an annulus can represent parallel flow in a shell and tube system, and provide insight in the thermal behaviour of PCM during a phase change process. However, the annulus model might have shortcomings in a system where the temperature profile on the tubes might not be the same for instance in a counter flow system. Tube surfaces are the interface between the HTF and PCM where the temperature profile plays an important role in the evolution of the phase front in the PCM and thermal characteristics of the system.
In the numerical studies demonstrated through chapter 4, a two dimensional geometry of a u-tube was selected to represent a counter flow and the two closest parallel tubes were selected for a parallel flow configuration to study the transport phenomena between two adjacent tubes (with different or same temperature profiles) in the horizontal and vertical orientations. Furthermore, a two dimensional axisymmetric model of an annulus, and a three

dimensional geometry of a U-tube were selected to represent parallel and counter flow, respectively. Using different scale models depends on the complexity of the system and available computational resources. Numerical studies for these cases are presented in Chapter 6, to provide insight in the three dimensional geometry impact on the predicted thermal behaviour of PCM.

7.1.2.3 Scale up from the model

For the scale up from a three dimensional model to the prototype or industrial scale, the characteristic lengths, velocity, and temperature can be scaled as long as the non-dimensional groups remain constant. However, if the thermal parameters were fixed (e.g. defined from the energy/exergy analysis of the CSP cycle), here lengths such as d, L, S and velocity of HTF can be changed while Ra_d, Fo_d, $\tilde{s}$, $\tilde{L}$, and Re remain the same. In case of a two dimensional model more caution/engineering judgement is required.

Moreover, one of the main characteristic features to be found from the model study is the heat flux or heat transfer per square metre of the heat transfer area in the specific PCM/HTF combination and configuration. Using the results, a detail design from the preliminary design can accommodate the required heat transfer area, delivering the required heat storage/release capacity. For instance, using the results of the model study (one element including tube/PCM), the total number of tubes can be calculated.

7.1.3 Parametric numerical modelling

The numerical study of a model provides information about the thermal performance of a particular configuration of PCM/HTF including the impact of materials/properties and temperatures in a specific geometry. As a final step in fine-tuning the geometry design for the specific problem in hand, another numerical study, e.g. modelling of one or more cross section of the prototype and/or industrial scale system might assist in decreasing the heat transfer area and/or the total volume of the PCM system and the cost. For this purpose, Eqs. 23, 24 provide some guidance. They represent the maximum heat transfer density ($\tilde{q}_{max}$) and optimal distribution of heat transfer surfaces in single phase natural convection for a staggered tube arrangement. Adapting the proposed groups to the melting process involving natural convection, the following groups can be introduced:

$$\frac{S_{opt}}{d} \propto \left(\frac{z}{d}\right)^{\frac{1}{3}} Ra_d^{-\frac{1}{4}} \qquad \frac{S_{opt}}{z} \propto \left(\frac{z}{d}\right)^{\frac{1}{12}} Ra_z^{-\frac{1}{4}}$$

$$\tilde{q} = \frac{q}{\pi\left(\frac{z}{2}\right)^2 L} \frac{d^2}{k(T_h - T_m)} \qquad \tilde{q}_{max} \propto \left[\left(\frac{z}{d}\right)^{\frac{1}{3}} Ra_d^{-\frac{1}{4}}\right]^{-1.6}$$

$$\frac{d_{opt}}{L} \propto Be^{-\frac{1}{4}}$$

To find correlations for the phase change process with natural convection, more parametric /numerical studies are required. For this purpose, different sectional modelling assists. Examples of the sectional modelling are presented in the following sample study in section 7.2.

7.1.4 Design review

Using the results of sectional modelling to find the optimal geometry, the detailed design from previous sections can be revised for example d, S, and L can be finalised. Using parametric analysis to optimise the preliminary design, the main objective is to minimise the total resistance; the fluid flow resistance (e.g. in the natural convection flow in PCM and forced convection flow in HTF) and thermal resistance, particularly at the PCM side. In practice, simultaneous minimisation of both resistances is not possible/practical and a trade-off between the two should be found which might be unique for each case. Overall, there is a narrow range for S/d and H/d ratio that provides the highest heat storage density in a fixed volume of PCM system based on the melting process.

7.2 Geometrical design and optimisation process case study

7.2.1 Preliminary design

The preliminary thermal parameters of the LHTES system as the output from the first/second law analysis of the CSP cycle has been provided by the ASTRI partners as the input to this study for the geometrical design procedure. Liquid sodium (Na) was selected as the HTF with inlet temperature of 650 °C and a PCM has been selected with a melting temperature T_m = 625 °C. The relevant thermophysical properties of the HTF and PCM are included in the Table 7.1. Tubes material is taken as stainless steel Sch. 40S.

Table 7.1- Thermophysical properties of PCM and HTF

	ρ (kg/m^3)	C_p (J/kg K)	k (W/m K)	h (kJ/kg)	μ (Pa s)	T_m (°C)
HTF (Na)	796	1253	58.2	-	0.0002	-
PCM (Na_2SO_4-NaCl)	2000	1700	1	285	0.003	625

The required capacity for the prototype is 100 kWh_{th} for which a horizontal counter flow configuration is selected. Using the thermophysical properties of the PCM, the required volume can be calculated as follows;

$$Q = 100000\ \frac{J}{s} \times 3600\ s = 36 \times 10^7 J \qquad V_{pcm} = \frac{Q}{\rho h} = \frac{36 \times 10^7 J}{2000\ \frac{kg}{m^3} \times 285 \times 10^3\ \frac{J}{kg}} = 0.631\ m^3$$

From the results of the previous numerical studies presented in chapter 4, section 4.1, it was found that the average effectiveness of this configuration is about ε = 0.8 in the charging process and less than ε = 0.7 in discharging heat after 80% solid fraction. For the system being able to deliver the demand of 100 kWh_{th} heat for one hour, ε = 0.65 is a first assumption as the system effectiveness. Assuming 0.95 as the PCM volume fraction, the total volume of the system (shell and tube LHTES system) can be calculated.

$$V_{pcm} = \frac{Q}{\rho h} \times \frac{1}{\varepsilon} = \frac{0.631}{0.65} m^3 = 0.971\ m^3$$

The length of the system is taken to be 3 meters which results in 0.67 m as the internal diameter of the shell.
To calculate the mass flow rate of Na as the HTF, the effectiveness of the melting process has been selected (average ε = 0.8) while for the PCM mass calculation the effectiveness closer to the discharging process has been selected (0.65 < average ε = 0.7) due to the redundancy problem during the later stages of the discharging process. Moreover, selection of the HTF mass flow rate based on the melting process is relevant due to a lower ΔT (e.g. <50 K) expectation while for the solidification process a higher ΔT (e.g. >100 K) is plausible.

$$\dot{m} = \frac{\dot{Q}}{C_p(T_{in} - T_m) \times \varepsilon} = \frac{100000}{1253\ \times (25) \times 0.8} = 4\ \frac{kg}{s} \quad where\ \ \varepsilon = \frac{T_{in} - T_{out}}{T_{in} - T_m}$$

With L=3 m, d = 0.0334 m (tube thickness = 0.00338 m), L/d = 90, R/r =3, R = 0.0501 m, this results in 61 pipes in a shell with diameter = 0.65 m and the tube material volume Vt = 0.065 m^3.
With L=3 m, d = 0.0267 m (tube thickness = 0.00287 m), L/d = 112, R/r =3, R = 0.040 m, this results in 97 pipes in a shell with diameter = 0.65 m and tube material volume Vt = 0.07 m^3.

While the volume of the tube materials estimated for two pipe sizes, the total volume of the tubes (e.g. with HTF) should be calculated for the estimation of the total volume of the LHTES system:

d = 0.0334 m, L= 3m, n = 61 → V_p = 0.16 m^3 → V_{LHTES} = 0.16 + 0.971 = 1.13 m^3

Considering about 7% margin, the total volume of the system equals 1.2 m^3, for which the PCM volume fraction is 81% and the volume fraction of tube materials is equal to 5.3%.

Taking the smaller pipe, estimation of the system is:
d = 0.0267 m, L= 3m, n = 97 → V_p = 0.163 m^3 → V_{LHTES} = 0.163 + 0.971 = 1.134 m^3
With the same margin as 7%, the total volume of the system is 1.2 m^3, for which the PCM volume fraction is 81% and the volume fraction of tube materials is equal to 6.25%.

7.2.2 Scale model study

Considering fixed thermal parameters (e.g. defined from the energy/exergy analysis of the CSP cycle), here lengths such as d, S, L, and velocity of HTF can be changed while Ra_d, Fo_d, $\tilde{s}$, $\tilde{L}$, and Re remain the same.
To scale down the prototype LHTES, a three dimensional geometry of a u-tube considering a quarter of a u-tube and the relevant PCM between the tubes is selected. The straight length of tube L= 0.55 m, r = 0.00811 m (inside radius of the tube), and R= 0.03 m (R/r = 3.7) is selected for the numerical study. This model has been selected according to the existing prototype for which detailed specification are provided in chapter 4, section 4.2. Using the same size of tube, and spacing, the specified u-tube model has the same Ra_d, Fo_d, and $\tilde{s}$ for the PCM side.
With this model the only difference between the model and real case is $\tilde{L}$, and Re, both relating to the HTF side. The length of the u-tube is one-sixth of the length of the real case (1m / 6m). With the model study, the flow velocity of sodium HTF is set at 0.2 m/s, which results in mass flow rate of 0.032 kg/s, resulting in Re ≈ 13000. This setting was selected to deliver reasonable effectiveness in conjunction with 25 K temperature difference (T_h-T_m=25K). While this velocity results in turbulent flow in the u-tube model (expected for the real case), in actual case with about 4 kg/s total mass flow rate of HTF, a higher velocity and Re are expected. This might affect the heat transfer rate from the HTF to the PCM, however, a higher mass flow rate in a longer tube length compared with the model study might compensate the lower mass flow rate in a shorter tube and result in the same effectiveness and heat transfer rate.

Results from the model study presented in chapter 6, section 6.2, show the characteristic figures in the PCM domain: velocity between 0.004-0.023 m/s, mass transfer between 0.3-0.65 kg/s, with an average temperature in the PCM domain equal to 636 °C. The average heat transfer rate during the convection dominated regime after 10% melt fraction and up to the end of process is approximately 6800 W/m^2 which equals 136 W for a quarter of the u-tube (the model comprises a quarter of a tube and the PCM in between the u- tubes) with 0.02 m^2 heat transfer area. The average effectiveness of the u-tube element is 0.56. This is lower than the assumed ε = 0.65 for the PCM mass calculations. This is the result of the length of U-tube in the model being a sixth (2x0.55 vs 2x3) of the prototype (100kWh$_{th}$). In the real scale, HTF passing through longer tube results in a higher temperature difference (T_h-T_m) and a higher ε.

7.2.3 Detailed design, scaling up the model to the prototype scale

Scaling up the results of the model study to the prototype scale (100 kWh$_{th}$), calculations are as follows:

$$Average\ heat\ transfer\ rate = 6800 = \frac{136}{0.02}\ W/m^2 \qquad \frac{100000}{6800} \cong 14.7\ m^2$$
$$with\ D = 20\ mm\ tube\ schedule\ 40 \quad \rightarrow tube\ thickness = 2.87\ mm\ and \quad D_o = 0.0267\ m$$

$$outer\ \frac{surface}{m} = \pi\ \times\ 0.0267\ \times 1 = 0.08388\ m^2 \qquad \frac{14.7}{0.08388} = 351.7\ m \qquad \frac{351.7}{3} = 117.23\ \cong 118$$

In a shell with ~ 3 metre length, the calculation shows that 118 tubes will be needed. However, using the correction factor (0.8) proposed by Tehrani et al. [119] for the number of tubes:

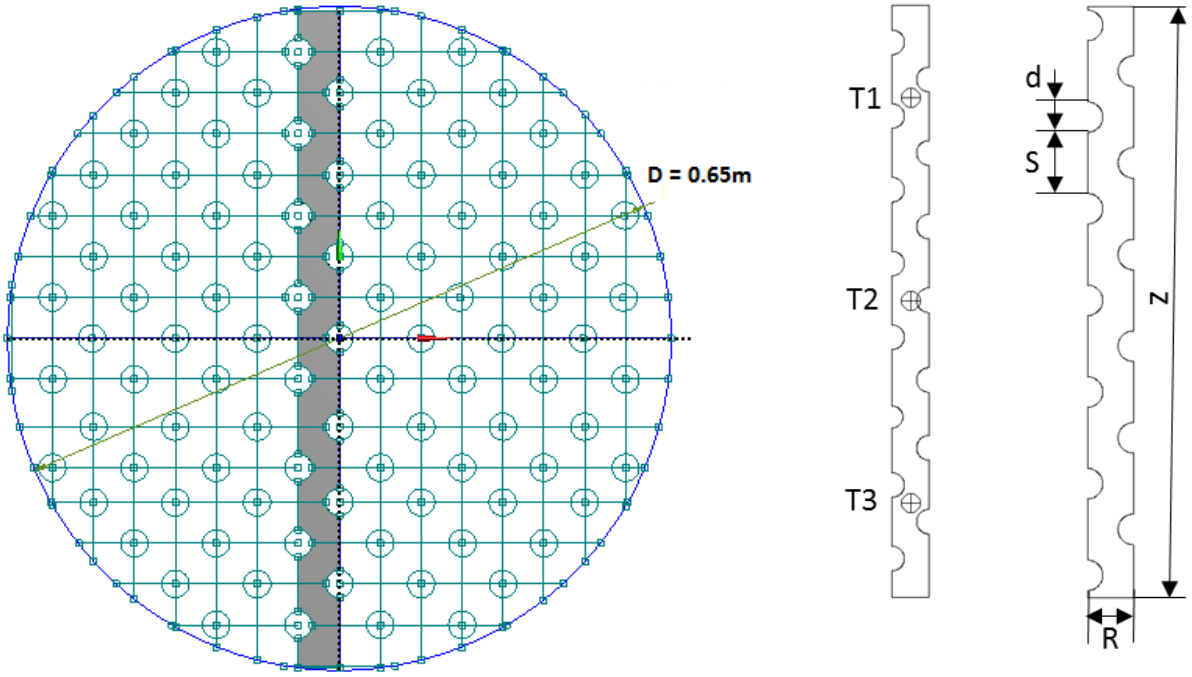
$$118\ \times 0.8 = 94.4\ \cong 95$$

Fig. 7.1a shows an arrangement of 98 tubes (49 U-tubes) in a shell with 65 cm diameter with the above parameters.

7.2.4 Sectional numerical modelling

7.2.4.1 Geometry and grid

A further two dimensional modelling of a cross section of the prototype can assist in the assessment of the impact of the tube size and spacing on the performance of the system. While the modelling study of the U-tube model scale provided information at the tube scale, a sectional modelling provides more information at the shell scale. More sectional modelling can be arranged to test the impact of z and L, finding the best shell length and diameter combination. Here, a cross section of the system at the middle of the shell and tube system is selected where temperatures can be assumed as the average temperatures of the HTF at each side of the U-tube. The temperatures acquired from the results of the numerical study of the scale model that was discussed in the previous chapter, section, 6.2.3.1.
In this cross-sectional modelling, the impact of the tube diameter, spacing, and the height of the shell can be verified. In a horizontal orientation, the height of the shell defines the Ra_z and global natural convection effect while Ra_d defines the impact of the tube diameter and local convection impact on the evolution of boundary layers and phase front. For the first and second case, an outer diameter of tubes 26.7 mm with spacing equal to 53.4 mm are considered and for the second case the respective parameters are 33.4 mm and 66.8 mm. Fixed temperatures are considered as the boundary conditions at the tube surfaces equal to the average



(a) (b) (c)

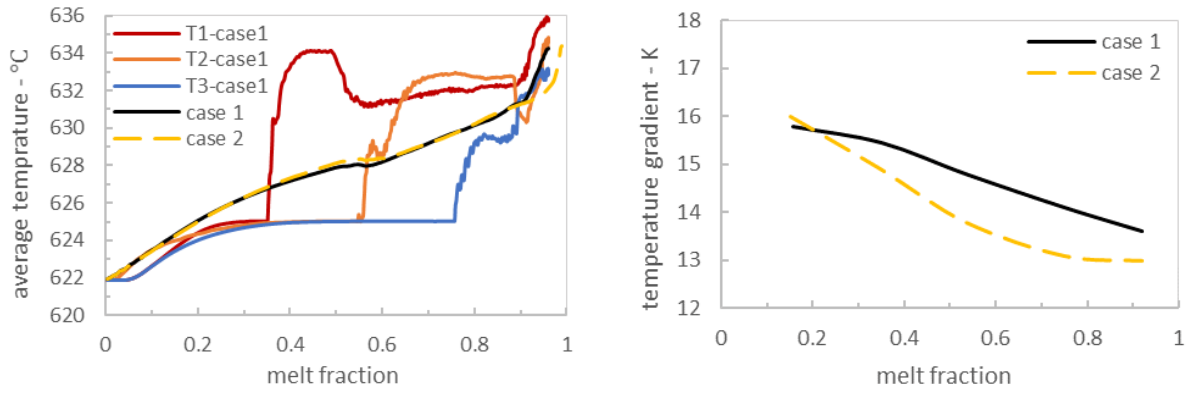
FIGURE 7.1. Schematic drawings: (a) cross section of shell and tube, (b) symmetrical model for **case 1,** (c) symmetrical model for **case 2**
Case 1: d_o = 26.7 mm, R= 40.05 mm, S= 53.4 mm, heat transfer interface = 0.633 m, PCM= 0.0216 m^2
Case 2: d_o = 33.4 mm, R= 50.1 mm, S= 66.8 mm, heat transfer interface = 0.682 m, PCM=0.0267 m^2

temperatures at each side of the U-tube with the no slip condition (velocity at tube surface equals zero). For the melting processes of the PCM with melting temperature of 625°C, temperatures are set at 638°C and 631°C at the left and right sides of both cases, and for the solidification processes, the respective temperatures are set at 502 °C and 532 °C. The initial temperatures were set 5 K higher or lower than the melting temperature of the PCM for the charging and discharging processes, respectively.

7.2.4.2 Results and discussion

7.2.4.2.1 Temperature field

Figures. 7.2 and 7.3 show the average temperature, gradients and temperature profiles in the two cases during the melting process. In general, temperature gradients are lower in the second case due to the higher rate of natural convection and its mixing effect. This is the result of higher tube spacing, providing more room for natural convection. Fig. 7.2a, showing the comparison of the average temperature in the PCM, reveals higher temperature for the second case at the early stages while temperatures are lower when most of the solid changes to liquid.



(a) (b)

FIGURE 7.2. Temperature profile comparison during the melting process:
(a) temperature profile at different locations in case one and average temperature profiles for two

cases, (b) temperature gradients for the two cases.

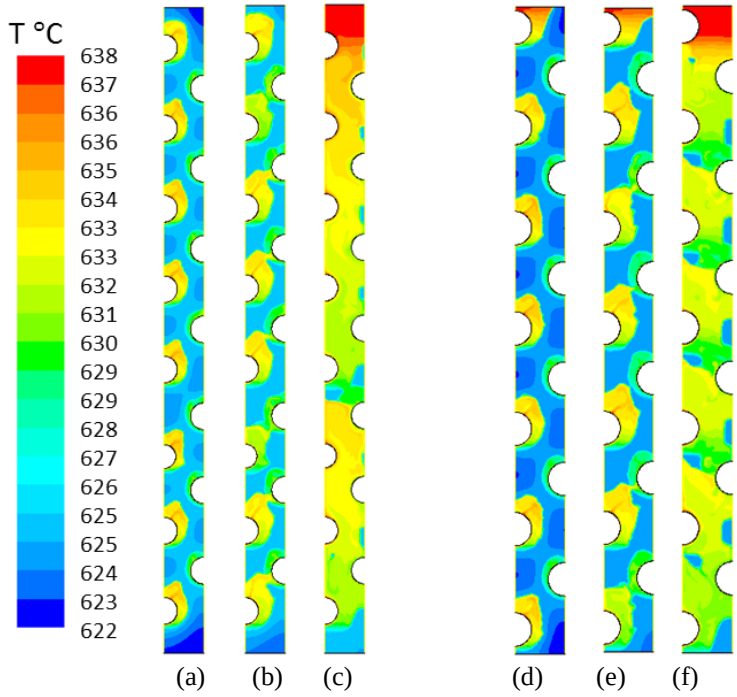


FIGURE 7.3. Temporal evolution of temperature field during melting process:
case 1: (a) 1450s, δl=35%, (b) 2200s, δl=53.5%, (c) 4250s, δl=92%,
case 2: (d) 1750s, δl=35%, (e) 2750s, δl=53.5%, (f) 5400s, δl=92%.

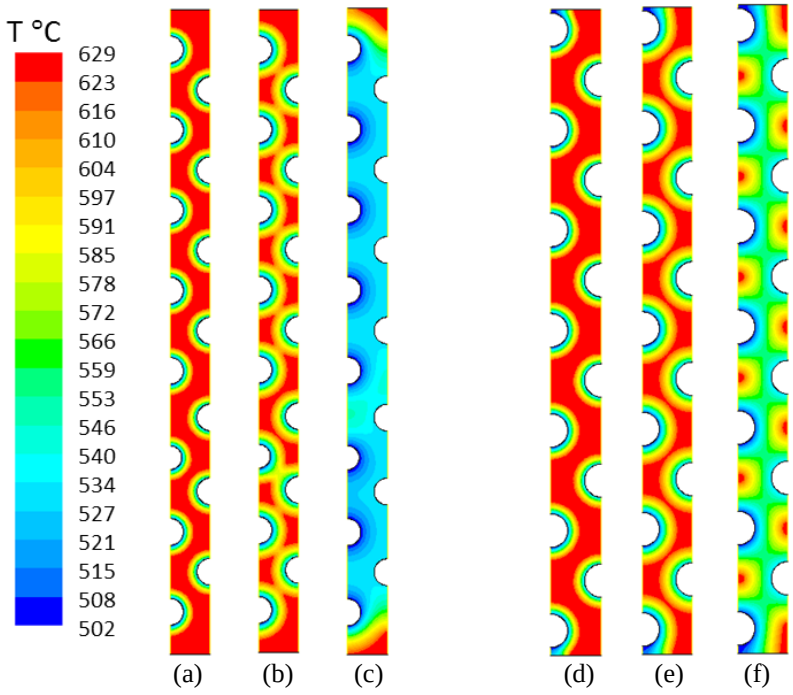
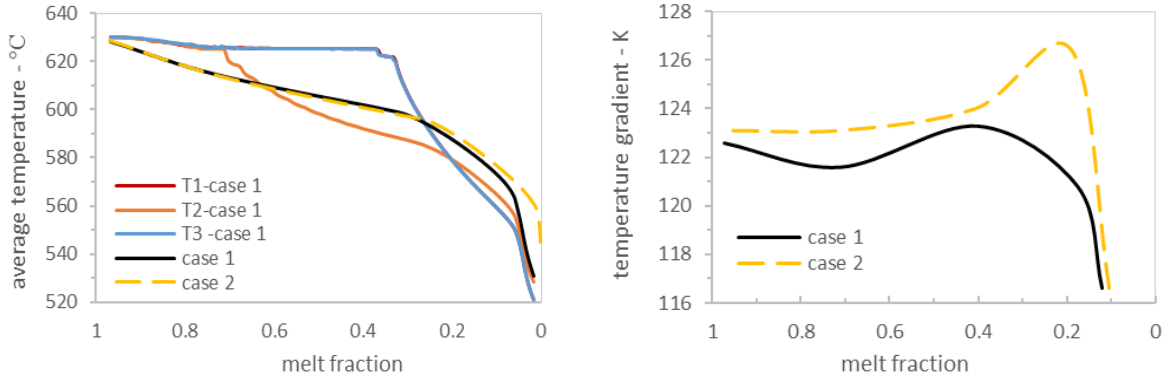


FIGURE 7.4. Temporal evolution of temperature field during solidification process:
case 1: (a) 400s, δs=40.1%, (b) 1000s, δs=71.1%, (c) 3200s, δs=97.3%,
case 2: (d) 550s, δs=40.6%, (e) 1350s, δs=70.7%, (f) 2900s, δs=97.3%.

Figures 7.4 and 7.5 show the temperature field, average temperature and gradients during the discharging process. Higher average temperatures and temperature gradient are shown for the second case with larger tubes while R/r is the same for both cases. This is the result of a higher convection and mass flux that is the highest at about 20% solid fraction (Fig. 7.7) and the consequence on the temperature gradient is seen in Fig. 7.5b.



(a) (b)

FIGURE 7.5. Temperature profile comparison during solidification process:
(a) temperature profile at different locations in case one and average temperature profiles for two cases, (b) temperature gradients for two cases.

7.2.4.2.2 Mass flow

Figure 7.6 shows the comparison of the mass flux during the melting processes of the two cases in three time slots. In the second case with more space between the tubes, more room is available for natural convection and the mass flux becomes higher in the second case as more solid changes to liquid. This leads to more uniform phase change process for the second case compared to the first case with a higher rate of melting (Fig. 7.8b).
In the solidification (discharging) processes, the role of natural convection is more recognisable up to 20% of the liquid solidification (Fig. 7.7), after which the mass flux becomes low with lower impact on the phase change process. In contrast to the melting processes, a higher rate of natural convection results in higher temperature gradients at the early stages of the second case as shown in Fig. 7.5b. The minor impact of natural convection on the temperature gradient (e.g. providing a driving force for heat transfer) lasts up to the end of process as observed in Fig. 7.5b.

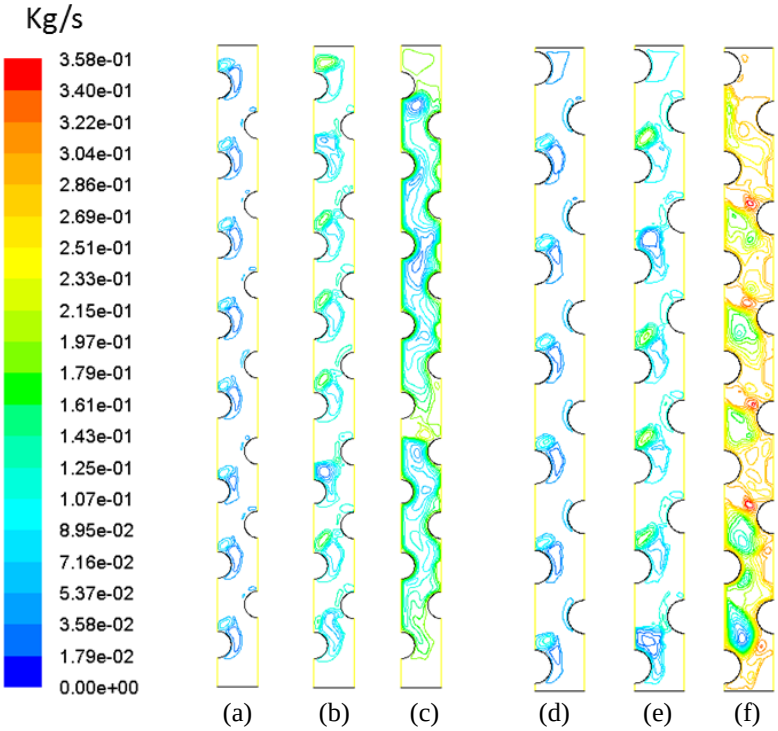


FIGURE 7.6. Temporal evolution of stream function during melting process:
case 1: (a) 1450s, δl=35%, (b) 2200s, δl=53.5%, (c) 4250s, δl=92%,
case 2: (d) 1750s, δl=35%, (e) 2750s, δl=53.5%, (f) 5400s, δl=92%.

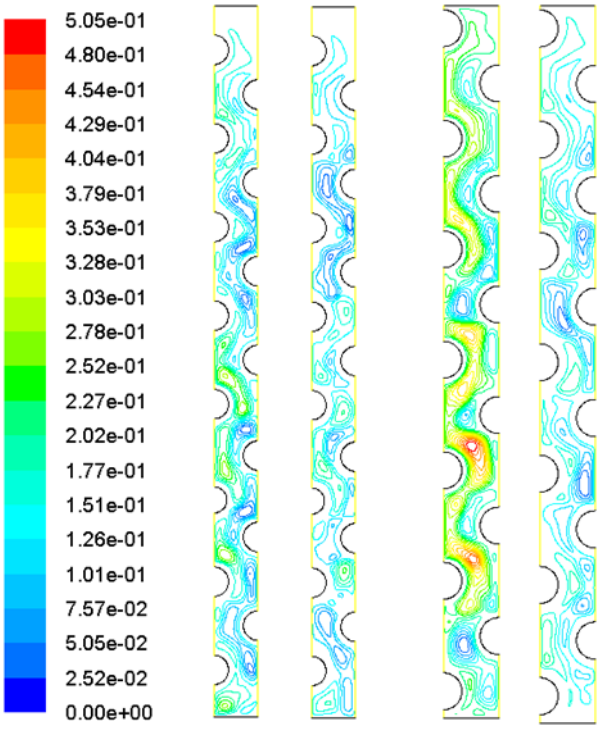


FIGURE 7.7. Temporal evolution of stream function during solidification process:
case 1: (a) 50s, δs=12%, (b) 100s, δs=17.5%,
case 2: (c) 50s, δs=10.5%, (d) 150s, δs=19%.

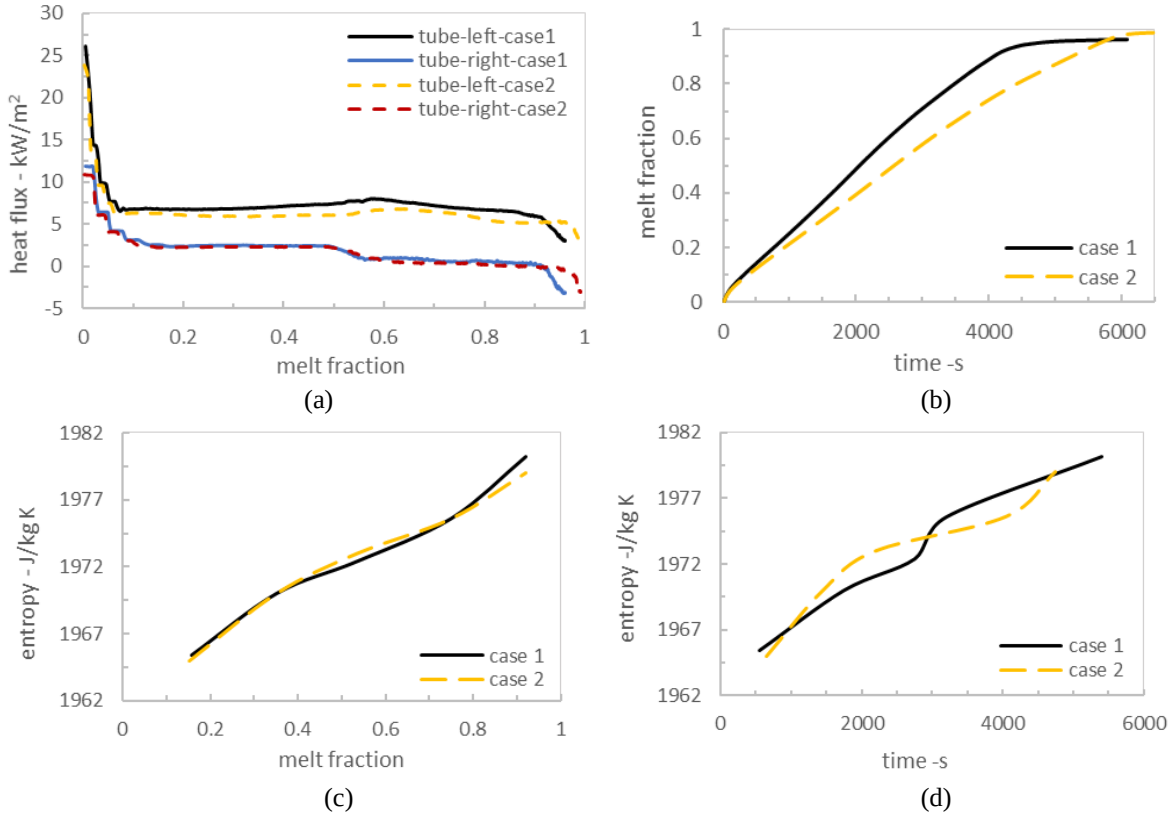


Figure 7.8. Temporal evolution of scalar fields during melting process: (a) heat flux at tube/PCM interface, (b) melt fraction (c) entropy generation vs temperature gradient, (d) entropy generation vs time

7.2.4.2.3 Heat transfer

Figure 7.8a shows a higher heat transfer rate for the first case with the smaller tube size (d_o =26.7 mm) while the heat transfer interface (the outer circumference of the tubes) is higher for the second case (0.629 < 0.682 m). This is to be expected as more PCM is in contact with high temperature HTF for the smaller size tubes compared with fewer larger diameter tubes. However, the second case provides more room for the convection heat transfer as the results show higher rates of mass transfer after 50% melt fraction.

Similar to the melting processes, the heat transfer rate to both sides of the tube surfaces are lower in the second case as less PCM encounters the cooler temperature surfaces. Using smaller tubes provides better distribution of the low temperature surfaces in the PCM resulting in a higher rate of heat transfer.

7.2.4.2.4 Phase change rate

Figure. 7.8b shows the higher rate of melting for the first case while it is slower and more uniform for the second case due to the higher rate of natural convection and its mixing effect for which a higher rate of mass flux are visible in Figs. 7.6d-f compared with the Figs. 7.6a-c as for the first case.

With a similar trend to the melting process, Fig. 7.9b shows a higher rate of solidification (discharging) for the first case (Fig. 7.1b) because of the more PCM being in contact with the cooler temperature surfaces. This result is consistent with the previous studies of the parallel and counter flow arrangements where smaller tubes in parallel flow delivered a higher rate of phase change compared to a counter flow case with a larger tube size (Chapter 4).

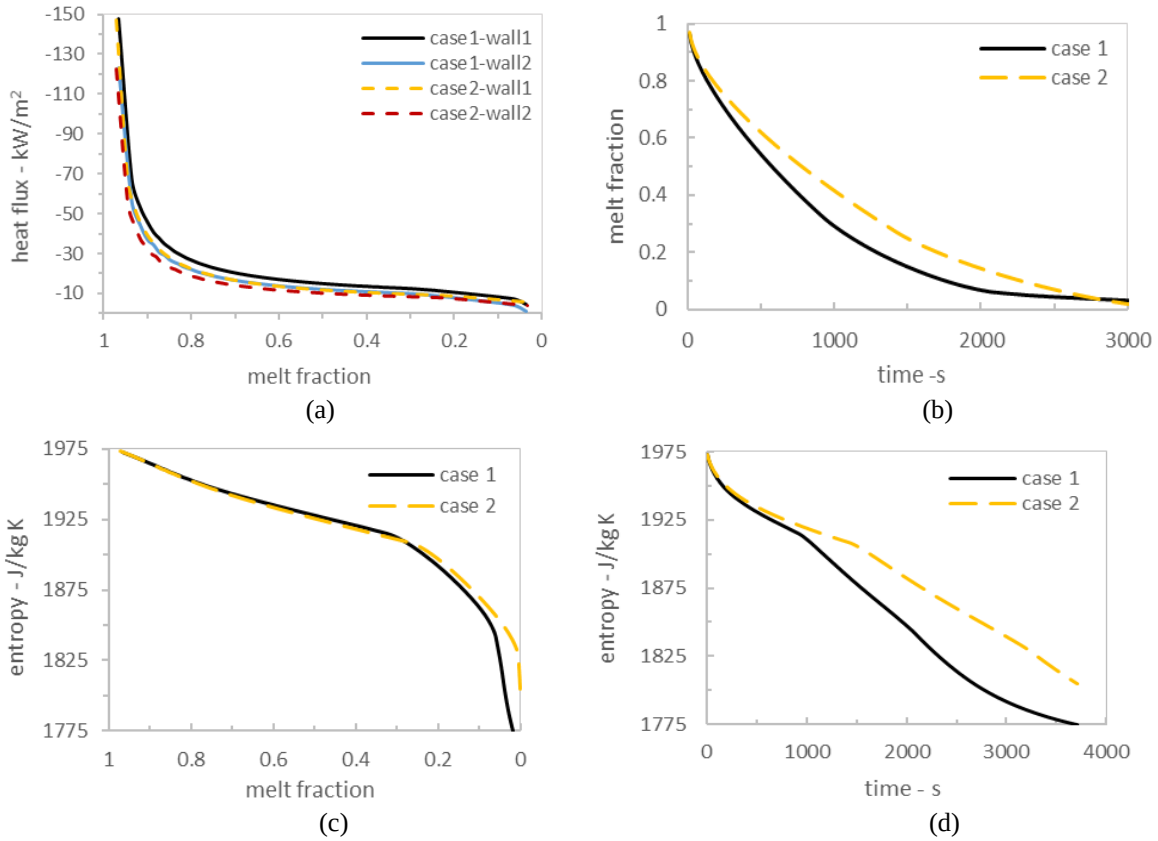


Figure 7.9. Temporal evolution of scalar fields during the solidification process:
(a) heat flux at tube/PCM interface, (b) melt fraction (c) entropy generation vs melt fraction,
(d) entropy generation vs time.

7.2.4.2.6 Entropy generation

Figures. 7.8c and 7.8d show a comparison of entropy generation in the PCM for the two melting cases. Fig. 7.8c shows that entropy generation is lower in the second case in relation to the temperature gradient in the PCM. Temperature gradients are lower for the second case as shown in Fig. 7.2b, because of the higher rate of natural convection and its mixing effect in the second case. However, Fig. 7.8d shows that entropy generation is higher for the second case during some times in the process and becomes lower at the later stages. This is due to the combined effect of average temperature and temperature gradient; the proportionality of entropy generation to temperature gradient (∇T) and reverse proportionality to the T^2 (Ch. 4, Eq. 11).

In the solidification processes, the entropy generation is higher for the second case during the whole process as shown in the Figs. 7.9c, d. This is consistent with the higher temperatures and temperature gradients for the second case compared with the first case (Fig. 7.4, and Fig. 7.5).
Comparing the entropy generation during the changing and discharging processes, the mixing effect of the convection compensates for the imperfection of the distribution of the heat transfer surfaces for the second case during the melting process and entropy generations are lower. However, in the discharging process, entropy generation is lower for the first case. A better distribution of heat transfer surfaces provides a better coverage that lessens imperfections [122], overlapping the thermal boundary layers for higher rate of heat transfer. For the second case of discharging, the higher rate of natural convection compensates for the imperfection of less uniform distribution of heat transfer areas only at the early stages and later, the entropy generation is higher.

7.2.5 Detailed design review

While results from the scaled down model provided information to design the prototype scale, the results from the sectional numerical study can assist in a further fine tuning of the parameters such as d, S, z, L. Here, considering the two cases, the numerical study of the cross-sectional grid shows higher rates of heat transfer for the first case with a smaller tube size during the charging and discharging processes. However, entropy generation is higher during the melting process for the first case.
Depending on the priority of the design criteria, where a higher rate of heat transfer is required the first case should be selected. The first design with smaller pipe size results in a higher volume fraction of pipe material (6.25% >5.3%, section 7.2.1) and higher cost. If a more uniform process in a longer period of phase change is acceptable, the second design with less volume fraction of tube material and lower cost is the better choice.
After making a decision about the diameter of the pipe, regarding L, Re and pressure drop, more sectional numerical modelling can assist to optimise the shell dimensions and aspect ratio; a longer shell with a smaller diameter or shorter shell with larger diameter.
This approach to the optimisation of the LHTES system inherently involves the cost as a main factor and progresses toward minimising the size of the system and materials, particularly, the more expensive ones such as steel being used for tubes and shell in comparison to the molten salt as PCM. However, a more rigorous techno-economic analysis is required after the design steps proposed in this chapter.

7.3 Conclusion

Narrowing down all the learnings from the previous literature and numerical studies through chapters 3-6, a design and optimisation process is proposed in this chapter. Here, the aim was to shed light on the role of numerical modelling in such a process, taking advantage of a virtual laboratory examining different cases in a shorter time and with a lower cost compared with experimental studies. From the thermal and geometrical design parameters of a LHTES system for a CSP plant, the type of HTF/PCM and the inlet/outlet/melting temperatures are the output of the first/second law analyses of the whole cycle including solar field and power generation block. Assuming thermal parameters as the input, this study focused on to find/optimise the geometrical parameters. Moreover, depending on the type of PCM, sensible heat storage/release can be part of the process in a LHTES system. The aim of this study was to find the optimal geometrical parameters and maximise the latent heat energy density.

The main dimensionless parameters for the shell and tube LHTES system introduced and how they provide a means to scale down/up to/from the scale model/prototype or industrial scale. A group of dimensionless geometrical groups, which were introduced earlier can assist in the optimisation process. The optimisation process aimed to find the highest volume fraction of PCM for a higher energy storage density (e.g. highest cost effectiveness) and a compromise between the highest effectiveness and lowest entropy generation for optimal useful work storage/delivery. Obviously, this compromise depends on the application and the priorities in the design criteria. The proposed method for the optimisation of the LHTES system takes into account the lowest cost of the system by minimising the size of the system, however a more rigorous techno-economic analysis is required to finalise the system design.
Sectional numerical modelling is proposed to assist the optimisation process. The proposed design and optimisation process applied to a prototype case requiring 100 kWh_{th}, for which a horizontal counter flow shell and tube configuration is proposed. Sectional modelling to find the optimal diameter and spacing is performed and results were analysed. A selection between two systems is proposed depending on the priority in design criteria and cost. For larger systems such as the recently announce system for South Australia, a modular storage system comprising a number of the optimised components using the procedure developed in this chapter is likely to provide a practical solution. While this study provided a step forward in using numerical modelling in the design and optimisation of a LHTES system, an extension work from this study is providing correlations for optimal tube diameter, spacing and also a shell diameter and length to design a shell and tube LHTES system for which more sectional numerical studies are necessary.

8 Conclusion and future research

In the context of a complex and transitioning energy market in Australia and around the world, two streams are competing; the supporters of conventional systems based on fossil fuels and believers in the reality of climate change and the constructive role of renewable energy technologies. Among the latter group are business people who just see the future opportunities and inevitable transition to the renewable era.

One of the major sectors in energy consumption and emission production is electricity generation. As a result, substitution of fossil fuels with renewables such as solar thermal in electricity generation can be a major mitigation solution. Two main challenges in this transition are the dispatchability of renewable energy including solar thermal and reducing the end-user price. Solutions for the dispatchability problem have been already recognised including different types of thermal and electricity storage, followed by better and smarter management of the supply and demand. However, developing these systems to the level that can deliver sufficient and cost effective storage to comply with demand regardless of time and location is still a big challenge. While the electricity storage systems such as batteries provide a flexible solution at the smaller scale installations like photovoltaic systems where electricity is the output of the solar cells, thermal energy storage including sensible and latent heat is the preferred solution for large scale electricity generation including CSP where the thermal energy is the output of the solar field. This preference should be appreciated in the context of the costs as well as the growing concern about the management of batteries' hazardous waste at the end of life.

8.1 Conclusion

CSP plants generating electricity in large-scale from solar thermal energy is a promising solution if it is accompanied by solar thermal energy storage. Compared to sensible heat storage, LHTES proved to provide higher density storage leading to a smaller size and cost savings. To achieve higher performances in CSP plants, higher temperature systems including heat storage are required. This work aimed to investigate the thermal behaviour of PCMs in different configurations of high temperature LHTES system. Building upon the knowledge available from the literature including available experimental data, this study aimed to develop and validate numerical models on the ANSYS FLUENT platform. Using the validated models, different types of high temperature LHTES systems were studied and innovative enhancement method and configurations have been proposed. Moreover, from the results of the modelling studies, different configurations for different applications, design criteria and priorities in CSP plant have been suggested.

The major outcomes from the numerical studies are summarised as follows:

Through scale down investigations, different elements from LHTES configurations have been examined to find out how to determine and analyse a scale model which best represents a real application in order to dramatically reduce the grid cells and computational time and effort. Two and three dimensional elements from the real prototypes were examined, and results showed that two dimensional cases of a U-tube as an element of a counter flow and a pair of parallel adjacent tubes as an element of parallel flow can represent a shell and tube storage system. A two dimensional axisymmetric grid can be used to model an annulus as an element of a parallel flow shell and tube, involving three dimensional aspects of the real system. While an annulus is the best model for a vertical case, this might be less accurate in the horizontal orientation due to the Benard convection. As a result, a pair of parallel closest tubes is a more representative model for horizontal parallel flow. A three dimensional U-tube or a pair of closest parallel tubes for the case of a shell and tube LHTES system, can provide a more realistic prediction but with a larger grid and higher computational time. As for three dimensional models, there are more choices depending on the details of a particular configuration.

The validated model was used for two dimensional investigations of the transport phenomena and their role in defining the flow and thermal characteristics of PCM in each configuration. The study focused on the role of natural convection, both laminar and turbulent for a case where Ra is higher than 10^{12}, which is the threshold for transition to turbulence in vertical cases. Results of the study showed the importance of the mixing effect of convection and the intensified mixing effect with turbulence. In comparison of three different cases, one just with conduction heat transfer, the second including laminar natural convection and third involving turbulence, the model was capable of capturing the details and providing good insight into the differences in heat and mass transfer.

One of the main objectives of this work was to understand different transport phenomena, the interaction between them and the impact on the temperature distribution, phase front transformation, mass and heat transfer. Understanding the nature of the system enables us to exploit its potential for the best outcome, e.g. the optimal case examined against the first and second laws of thermodynamics. As the thermal conductivity of the alternative

molten salt and the eutectic mixture PCMs are low, most of the research effort has been focused on extending the heat transfer area, which reduces the PCM volume fraction (reducing the storage density), adding complexity and cost of the LHTES system. This work has focused on finding means to enhance the natural phenomena occurring in a system, e.g. which configuration or orientation exploits the natural convection to achieve the best outcome, or how to resonate natural convection. The following summary of the numerical studies demonstrates some of the outcomes:

Starting with the conventional shell and tube configuration, through a comparative numerical study, thermal performance of PCM in counter flow and parallel flow in two orientations was investigated. Convection heat transfer is more effective in counter flow as the temperature difference between two tubes and the mixing effect are higher leading to a lower temperature gradient and hot spots. In the horizontal cases, the mixing effect is dominant due to the creation of small fast convection cells (Benard convection) resulting is less variance between different cases. Consequently, a one dimensional melting front evolves during the process compared to a two dimensional one in the vertical cases. The effectiveness of parallel cases were higher due to more PCM being in contact with high temperature HTF (HTF enters in both tubes as parallel flow while enters in one and exits from the other in U-tubes as counter flow). However, the effectiveness keeps steady for a longer period in counter flow compared with parallel flow, which starts to decrease earlier. In general, a more uniform and longer plateau is found in counter flow compared with parallel flow and for horizontal cases compared with vertical cases in the melting processes.

On the other hand, during the solidification processes, less difference has been observed due to the minor impact of convection heat transfer. Similar to the melting cases, the effectiveness is higher for parallel flow, which starts to decrease earlier, however, in all cases the phase front is one dimensional.

In searching for alternative design configurations adjustable for higher temperature and pressures, a fin plate rectangular configuration has been proposed. In this arrangement, PCM is confined in compartments framed by fin plates and HTF passes through channels/tubes at the bottom. Heat transfer occurs between the HTF, fins and PCM, which provides flexibility in the selection of materials for PCM/fins/HTF due to the separation of PCM and HTF zones.

The modularity of this arrangement is another useful feature for facilitating scaling up. Thermal performance comparison of this system with the four cases of shell and tube configurations showed similarity with the horizontal cases while still providing a higher effectiveness compared to all four cases. The most important difference was in the solidification case where the fin plates were not completely covered with a solid layer up to 70% solid fraction, maintaining direct contact between the fins and the liquid PCM for a longer period resulting in a higher rate of heat transfer and less redundant PCM, reducing the size and improving cost effectiveness.

In pursuing other means for performance enhancement, a numerical investigation of periodically reversing the flow direction of HTF in a specific time interval (e.g. close to the natural frequency of the system) in a parallel flow arrangement proved to be effective, both in charging and discharging processes. Implementing the method, a periodic boundary condition appears at the interface between the tube and PCM, which has a mixing effect on the PCM, reducing the amount of liquid accumulation at the top of the PCM enclosure. Results of the study showed improvement of convection heat transfer in the melting process due to the resonance of convection heat transfer. In the discharging process, enhancement of heat transfer occurred after 75% of the liquid transformed to solid due to a higher heat transfer area between solid and liquid. The enhancement of solidification process is particularly important due to the reduction of redundant PCM, and consequently the size and the cost of the LHTES system. Duration of the melting and solidification became shorter by about 12% and 10%, respectively, providing a solution when quick storage or release of heat is a priority in the design criteria.

Building upon all the learnings from the literature and through this work, a step by step PCM storage system design and optimisation procedure was proposed. The innovative step in this procedure is employing numerical modelling at various design and optimisation stages as well as using previous parametric analyses. A lack of realisation of the potential role of numerical modelling in detailed design has been found in the literature review. Moreover, previous parametric studies mainly considered a one dimensional phase change front (e.g. convection heat transfer was ignored) or convection heat transfer included without a phase change process. This study attempted to fill those gaps, using numerical modelling results to select a configuration, then using a scaled down model to investigate characteristics of a specific combination of PCM/HTF for detailed design. At the later stage, sectional modelling was proposed to assist in fine tuning the detailed design by parametric investigation. The procedure uses the numerical modelling in different stages while convection heat transfer (including turbulence) and phase change processes are involved.

The case study in design of a LHTES system of a 100 kWh_{th} showed the implementation of each step for a prototype application. The modelling for the detailed design showed how the characteristic temperature, velocity, mass and heat transfer rate can assist in detailed design. Furthermore, the sectional modelling of the shell and tube system showed the more uniform and effective thermal performance for larger tubes and tube spacing, resulting

in reduced heat transfer area, higher volume fraction of PCM, leading to higher storage density and least cost of the system. However, the charging and discharging processes take longer to complete compared to the other alternative with smaller size tubes and smaller spacing providing higher rate of heat transfer. Therefore, depending on the priority of the design criteria if faster heat storage/release are required the latter system should be selected with a higher cost.

8.2 Future work

Numerical modelling is a powerful tool to explore new combinations of PCM/HTF in different configurations to assist in the design and optimisation of LHTES systems or finding new innovative methods and configurations. The bottleneck of this virtual lab, however, is the computation time, which even becomes longer for more complicated cases for three dimensional models. Using the numerical modelling as a research tool, research for reducing the numerical calculation time is an interesting task by itself. There has been research effort in the literature to introduce correlations for different calculations from the results of numerical calculations, e.g. heat transfer correlations.

In the specific scope of this work and considering the comprehensive studies of convection heat transfer and its impact in different configurations through this thesis, developing correlations and/or equations to account for the convection heat transfer is the next step. Such correlations can be used to account for the convection heat transfer in new numerical modelling studies without including iterative calculation. This will reduce dramatically the computational time particularly in more complicated cases and assist in the use of the proposed design and optimisation procedures.

As higher temperature PCMs are in demand to achieve a higher efficiency in CSP plants, the impact of radiation heat transfer needs to be investigated, particularly in the solidification processes where conduction is considered as the major heat transfer mode.

Regarding the design and optimisation process proposed in Ch.7, the next step is providing correlations for optimal tube diameter, spacing and also a shell diameter and length to design a shell and tube LHTES system. This step requires more sectional modelling to take into account different combination of the parameters.

While the proposed method provides a path for the scale up from a model scale to prototypes or real industrial cases, design and optimisation of large storage systems backing commercial CSPs (.>100 MW) for several hours, require further steps. Modular design that was suggested through this thesis provide a potential solution for the large scale applications. However, the size of modules, total capacity and spare systems (e.g. in total four systems each providing 33% capacity or five systems with 25% capacity) needs to be designed and optimised. In the proposed method, the technical optimisation; maximising effectiveness, minimising entropy generation (leading to size and cost reduction) was the core focus, whereas in the further steps towards large scale implementation, economic analyses from the capital cost and the operation and maintenance costs become the core. Thus, progressing from the component level design and optimisation to a latent heat thermal energy storage system at the commercial cycle level is recommended for future research work.

Furthermore, regarding the need for an optimal thermal energy storage to supply heat on demand including the base and peak loads on time for the power generation in a CSP plant, the more sophisticated systems such as cascade PCMs and hybrid systems of sensible-latent heat storage might be considered in the future investigations.

References

[1] Core Writing Team RKPaLAMe. *Climate Chnage 2014: Synthesis Report. Contribution of working Groups I, II and III to the fifth Assessment Report of the Intergovernmental Panel o Climate Change.* IPCC, Geneva, Switzerland, 151 pp, in IPCC AR5 Sythesis Report website. 2014.
[2] Elliston B, MacGill I, Diesendorf M. Comparing least cost scenarios for 100% renewable electricity with low emission fossil fuel scenarios in the Australian National Electricity Market. Renewable Energy. 2014;66:196-204.
[3] IEA. Energy Technology Perspectives, 2017. IEA 2017.
[4] IEA. Renewables information, statistics. IEA. 2017.
[5] Winslow KM, Laux SJ, Townsend TG. A review on the growing concern and potential management strategies of waste lithium-ion batteries. Resources, Conservation and Recycling. 2018;129:263-77.
[6] Wolfram P, Wiedmann T, Diesendorf M. Carbon footprint scenarios for renewable electricity in Australia. Journal of Cleaner Production. 2016;124:236-45.
[7] operator Aem. AEMO annula report. Australian energy market operator. 2017.
[8] Riesz J, Elliston D, Vithayasrichareon D, MacGill A. 100% Renewables in Australia. Research Summary. 2016.
[9] Jacobson MZ, Delucchi MA, Cameron MA, Frew BA. Low-cost solution to the grid reliability problem with 100% penetration of intermittent wind, water, and solar for all purposes. Proceedings of the National Academy of Sciences. 2015;112:15060-5.
[10] Caldés N, Lechón Y. 5 - Socio-economic and environmental assessment of concentrating solar power (CSP) systems. In: Lovegrove K, Stein W, editors. Concentrating Solar Power Technology: Woodhead Publishing; 2012. p. 120-50.
[11] Garcia P, Olcese M, Rougé S. Experimental and numerical investigation of a pilot scale latent heat thermal energy storage for CSP power plant. Energy Procedia. 2015;69:842-9.
[12] Turchi CS, Ma Z, Neises TW, Wagner MJ. Thermodynamic Study of Advanced Supercritical Carbon Dioxide Power Cycles for Concentrating Solar Power Systems. Journal of Solar Energy Engineering. 2013;135:041007--7.
[13] Segal A. Thermodynamic approach to the optimization of central solar energy systems. NATO ASI SERIES 3 HIGH TECHNOLOGY. 1999;69:323-34.
[14] Kuravi S, Trahan J, Goswami D, Rahman M, Stefanakos E. Thermal energy storage technologies and systems for concentrating solar power plants. Progress in Energy and Combustion Science. 2013;39:285-319.
[15] Khare S, Dell'Amico M, Knight C, McGarry S. Selection of materials for high temperature sensible energy storage. Solar Energy Materials and Solar Cells. 2013;115:114-22.
[16] Wang S, Faghri A, Bergman TL. A Comparison Study of Sensible and Latent Thermal Energy Storage Systems for Concentrating Solar Power Applications. Numerical Heat Transfer, Part A: Applications. 2012;61:860-71.
[17] Belusko M, Halawa E, Bruno F. Characterising PCM thermal storage systems using the effectiveness-NTU approach. International Journal of Heat and Mass Transfer. 2012;55:3359-65.
[18] Halawa E, Saman W. Thermal performance analysis of a phase change thermal storage unit for space heating. Renewable Energy. 2011;36:259-64.
[19] Liu M, Saman W, Bruno F. Development of a novel refrigeration system for refrigerated trucks incorporating phase change material. Applied Energy. 2012;92:336-42.
[20] Vakilaltojjar SM, Saman W. Analysis and modelling of a phase change storage system for air conditioning applications. Applied Thermal Engineering. 2001;21:249-63.
[21] Fan Z, Infante Ferreira CA, Mosaffa AH. Numerical modelling of high temperature latent heat thermal storage for solar application combining with double-effect H2O/LiBr absorption refrigeration system. Solar Energy. 2014;110:398-409.
[22] Campos-Celador A, Diarce G, González-Pino I, Sala JM. Development and comparative analysis of the modeling of an innovative finned-plate latent heat thermal energy storage system. Energy. 2013.
[23] Belusko M, Tay NHS, Liu M, Bruno F. Effective tube-in-tank PCM thermal storage for CSP applications, Part 1: Impact of tube configuration on discharging effectiveness. Solar Energy. 2015.
[24] Belusko M, Tay NHS, Liu M, Bruno F. Effective tube-in-tank PCM thermal storage for CSP applications, Part 2: Parametric assessment and impact of latent fraction. Solar Energy. 2015.
[25] Liu M, Tay NHS, Belusko M, Bruno F. Investigation of Cascaded Shell and Tube Latent Heat Storage Systems for Solar Tower Power Plants. Energy Procedia. 2015;69:913-24.
[26] Le M, Initiative S. Solar Energy Techonologies Office. US Department of Energy. 2015:1-121.
[27] Ho CK, Iverson BD. Review of high-temperature central receiver designs for concentrating solar power. Renewable and Sustainable Energy Reviews. 2014;29:835-46.

[28] Kenisarin MM. High-temperature phase change materials for thermal energy storage. Renewable and Sustainable Energy Reviews. 2010;14:955-70.
[29] Calvet N, Py X, Olivès R, Bédécarrats J-P, Dumas J-P, Jay F. Enhanced performances of macro-encapsulated phase change materials (PCMs) by intensification of the internal effective thermal conductivity. Energy. 2013;55:956-64.
[30] Elmozughi AF, Solomon L, Oztekin A, Neti S. Encapsulated phase change material for high temperature thermal energy storage – Heat transfer analysis. International Journal of Heat and Mass Transfer. 2014;78:1135-44.
[31] Rathod MK, Banerjee J. Thermal performance enhancement of shell and tube Latent Heat Storage Unit using longitudinal fins. Applied Thermal Engineering. 2015;75:1084-92.
[32] Verdier D, Ferrière A, Falcoz Q, Siros F, Couturier R. Experimentation of a High Temperature Thermal Energy Storage Prototype Using Phase Change Materials for the Thermal Protection of a Pressurized Air Solar Receiver. Energy Procedia. 2013;49:1044-53.
[33] Klein S. TRANSYS, a transient system simulation program, Rep. JR-12 Engineering Experiment Station, University of Wisconsin-Madison. 1988.
[34] Ho CK. Software and codes for analysis of concentrating solar power technologies. Sandia National Laboratories; 2008.
[35] ANSYS Fluent Users Guide, Release 15.0. ANSYS; 2015.
[36] COMSOL Multiphysics, Release 5.0. 2014.
[37] DesignModeler Users Guide, Release 15.0. ANSYS; 2015.
[38] Bejan A. TWO THERMODYNAMIC OPTIMA IN THE DESIGN OF SENSIBLE HEAT UNITS FOR ENERGY STORAGE. J Heat Transfer Trans ASME. 1978;100:708-12.
[39] De Lucia M, Bejan A. Thermodynamics of phase-change energy storage: the effects of liquid superheating during melting, and irreversibility during solidification. Journal of solar energy engineering. 1991;113:2-10.
[40] Jones BJ, Sun D, Krishnan S, Garimella SV. Experimental and numerical study of melting in a cylinder. International Journal of Heat and Mass Transfer. 2006;49:2724-38.
[41] Wang S, Faghri A, Bergman T. Melting in Cylindrical Enclosures: Numerical Modeling and Heat Transfer Correlations. Numerical Heat Transfer, Part A: Applications. 2012;61:837-59.
[42] Jany P, Bejan A. Scaling theory of melting with natural convection in an enclosure. International Journal of Heat and Mass Transfer. 1988;31:1221-35.
[43] Sharifi N, Robak CW, Bergman TL, Faghri A. Three-dimensional PCM melting in a vertical cylindrical enclosure including the effects of tilting. International Journal of Heat and Mass Transfer. 2013;65:798-806.
[44] Amin NAM, Bruno F, Belusko M. Effective thermal conductivity for melting in PCM encapsulated in a sphere. Applied Energy. 2014;122:280-7.
[45] Basal B, Ünal A. Numerical evaluation of a triple concentric-tube latent heat thermal energy storage. Solar Energy. 2013;92:196.
[46] Assis E, Katsman L, Ziskind G, Letan R. Numerical and experimental study of melting in a spherical shell. International Journal of Heat and Mass Transfer. 2007;50:1790-804.
[47] Assis E, Ziskind G, Letan R. Numerical and experimental study of solidification in a spherical shell. Journal of Heat Transfer. 2009;131:024502.
[48] Shmueli H, Ziskind G, Letan R. Melting in a vertical cylindrical tube: Numerical investigation and comparison with experiments. International Journal of Heat and Mass Transfer. 2010;53:4082-91.
[49] Fornarelli F, Camporeale SM, Fortunato B, Torresi M, Oresta P, Magliocchetti L, et al. CFD analysis of melting process in a shell-and-tube latent heat storage for concentrated solar power plants. Applied Energy. 2016;164:711-22.
[50] Wang S, Faghri A, Bergman T. Numerical Modeling of Alternate Melting and Solidification. Numerical Heat Transfer, Part B: Fundamentals. 2010;58:393-418.
[51] Markatos NC, Pericleous KA. Laminar and turbulent natural convection in an enclosed cavity. International Journal of Heat and Mass Transfer. 1984;27:755-72.
[52] Lakeh RB, Lavine A, Kavehpour HP, Wirz R. Study of Turbulent Natural Convection in Vertical Storage Tubes for Supercritical Thermal Energy Storage. Numerical Heat Transfer, Part A: Applications. 2014;67:119-39.
[53] Lorente S, Bejan A, Niu JL. Phase change heat storage in an enclosure with vertical pipe in the center. International Journal of Heat and Mass Transfer. 2014;72:329-35.
[54] Bejan A, Lorente S. Multiobjective Configurations. Design with Constructal Theory: John Wiley & Sons, Inc.; 2008. p. 249-328.
[55] Bejan A, Lorente S. Multiscale Configurations. Design with Constructal Theory: John Wiley & Sons, Inc.; 2008. p. 215-47.
[56] Cao Y, Faghri A. A numerical analysis of phase-change problems including natural convection. Journal of heat transfer. 1990;112:812-6.

[57] Kurnia JC, Sasmito AP, Jangam SV, Mujumdar AS. Improved design for heat transfer performance of a novel phase change material (PCM) thermal energy storage (TES). Applied Thermal Engineering. 2013;50:896-907.
[58] Lorente S, Bejan A, Niu JL. Constructal design of latent thermal energy storage with vertical spiral heaters. International Journal of Heat and Mass Transfer. 2015;81:283-8.
[59] Longeon M, Soupart A, Fourmigué J-F, Bruch A, Marty P. Experimental and numerical study of annular PCM storage in the presence of natural convection. Applied Energy. 2013;112:175-84.
[60] Laing D, Bauer T, Breidenbach N, Hachmann B, Johnson M. Development of high temperature phase-change-material storages. Applied Energy. 2013;109:497-504.
[61] Pirasaci T, Goswami DY. Influence of design on performance of a latent heat storage system for a direct steam generation power plant. Applied Energy. 2016;162:644-52.
[62] Amin NAM, Belusko M, Bruno F, Liu M. Optimising PCM thermal storage systems for maximum energy storage effectiveness. Solar Energy. 2012;86:2263-72.
[63] de Gracia A, David D, Castell A, Cabeza LF, Virgone J. A correlation of the convective heat transfer coefficient between an air flow and a phase change material plate. Applied Thermal Engineering. 2013;51:1245-54.
[64] Johnson M, Fiss M, Klemm T, Eck M. Test and Analysis of a Flat Plate Latent Heat Storage Design. Energy Procedia. 2014;57:662-71.
[65] Julian Vogel MJ, Markus Eck, Dorte Laing Numerical analysis of natural convection in a latent heat thermal energy storage system containing rectangular enclosures Eurotherm Seminar, Advances in Thermal Energy Storage. 2013.
[66] Soares N, Gaspar AR, Santos P, Costa JJ. Experimental study of the heat transfer through a vertical stack of rectangular cavities filled with phase change materials. Applied Energy. 2015;142:192-205.
[67] Shatikian V, Ziskind G, Letan R. Numerical investigation of a PCM-based heat sink with internal fins. International Journal of Heat and Mass Transfer. 2005;48:3689-706.
[68] Shatikian V, Ziskind G, Letan R. Numerical investigation of a PCM-based heat sink with internal fins: Constant heat flux. International Journal of Heat and Mass Transfer. 2008;51:1488-93.
[69] Saha SK, Dutta P. Heat transfer correlations for PCM-based heat sinks with plate fins. Applied Thermal Engineering. 2010;30:2485-91.
[70] Hosseinizadeh SF, Tan FL, Moosania SM. Experimental and numerical studies on performance of PCM-based heat sink with different configurations of internal fins. Applied Thermal Engineering. 2011;31:3827-38.
[71] Wei J, Kawaguchi Y, Hirano S, Takeuchi H. Study on a PCM heat storage system for rapid heat supply. Applied Thermal Engineering. 2005;25:2903-20.
[72] Medrano M, Yilmaz MO, Nogués M, Martorell I, Roca J, Cabeza LF. Experimental evaluation of commercial heat exchangers for use as PCM thermal storage systems. Applied Energy. 2009;86:2047-55.
[73] Liu M, Saman W, Bruno F. Review on storage materials and thermal performance enhancement techniques for high temperature phase change thermal storage systems. Renewable and Sustainable Energy Reviews. 2012;16:2118-32.
[74] Liu M, Steven Tay NH, Bell S, Belusko M, Jacob R, Will G, et al. Review on concentrating solar power plants and new developments in high temperature thermal energy storage technologies. Renewable and Sustainable Energy Reviews. 2016;53:1411-32.
[75] Liu Z, Yao Y, Wu H. Numerical modeling for solid–liquid phase change phenomena in porous media: Shell-and-tube type latent heat thermal energy storage. Applied Energy. 2013;112:1222-32.
[76] Zhao D, Tan G. Numerical analysis of a shell-and-tube latent heat storage unit with fins for air-conditioning application. Applied Energy. 2014;138:381-92.
[77] Guo C, Zhang W. Numerical simulation and parametric study on new type of high temperature latent heat thermal energy storage system. Energy Conversion and Management. 2008;49:919-27.
[78] Zheng Y, Barton JL, Tuzla K, Chen JC, Neti S, Oztekin A, et al. Experimental and computational study of thermal energy storage with encapsulated NaNO3 for high temperature applications. Solar Energy. 2015;115:180-94.
[79] Ettouney H, El-dessouky H, Al-ali A. Heat Transfer During Phase Change of Paraffin Wax Stored in Spherical Shells. Journal of Solar Energy Engineering. 2005;127:357.
[80] Jacob R, Trout N, Raud R, Clarke S, Steinberg TA, Saman W, et al. Geopolymer encapsulation of a chloride salt phase change material for high temperature thermal energy storage. AIP Conference Proceedings. 2016;1734:050021.
[81] Ho CJ, Gao JY. An experimental study on melting heat transfer of paraffin dispersed with Al2O3 nanoparticles in a vertical enclosure. International Journal of Heat and Mass Transfer. 2013;62:2-8.
[82] Sciacovelli A, Gagliardi F, Verda V. Maximization of performance of a PCM latent heat storage system with innovative fins. Applied Energy. 2015;137:707-15.

[83] Tay N, Bruno F, Belusko M. Comparison of pinned and finned tubes in a phase change thermal energy storage system using CFD. Applied energy. 2013;104:79-86.
[84] Languri EM, Aigbotsua CO, Alvarado JL. Latent thermal energy storage system using phase change material in corrugated enclosures. Applied Thermal Engineering. 2013;50:1008-14.
[85] Li YQ, He YL, Song HJ, Xu C, Wang WW. Numerical analysis and parameters optimization of shell-and-tube heat storage unit using three phase change materials. Renewable Energy. 2013;59:92-9.
[86] Wang P, Wang X, Huang Y, Li C, Peng Z, Ding Y. Thermal energy charging behaviour of a heat exchange device with a zigzag plate configuration containing multi-phase-change-materials (m-PCMs). Applied Energy. 2015;142:328-36.
[87] Li Y-Q, He Y-L, Wang Z-F, Xu C, Wang W. Exergy analysis of two phase change materials storage system for solar thermal power with finite-time thermodynamics. Renewable Energy. 2012;39:447-54.
[88] Xu Y, He Y-L, Li Y-Q, Song H-J. Exergy analysis and optimization of charging–discharging processes of latent heat thermal energy storage system with three phase change materials. Solar Energy. 2016;123:206-16.
[89] Hänchen M, Brückner S, Steinfeld A. High-temperature thermal storage using a packed bed of rocks – Heat transfer analysis and experimental validation. Applied Thermal Engineering. 2011;31:1798-806.
[90] Zanganeh G, Pedretti A, Haselbacher A, Steinfeld A. Design of packed bed thermal energy storage systems for high-temperature industrial process heat. Applied Energy. 2015;137:812-22.
[91] Anderson R, Shiri S, Bindra H, Morris JF. Experimental results and modeling of energy storage and recovery in a packed bed of alumina particles. Applied Energy. 2014;119:521-9.
[92] Zanganeh G, Khanna R, Walser C, Pedretti A, Haselbacher A, Steinfeld A. Experimental and numerical investigation of combined sensible–latent heat for thermal energy storage at 575°C and above. Solar Energy. 2015;114:77-90.
[93] Zauner C, Hengstberger F, Mörzinger B, Hofmann R, Walter H. Experimental characterization and simulation of a hybrid sensible-latent heat storage. Applied Energy. 2017;189:506-19.
[94] Nithyanandam K, Pitchumani R. Thermal energy storage with heat transfer augmentation using thermosyphons. International Journal of Heat and Mass Transfer. 2013;67:281-94.
[95] Malan D, Dobson R, Dinter F. Solar thermal energy storage in power generation using phase change material with heat pipes and fins to enhance heat transfer. Energy Procedia. 2015;69:925-36.
[96] Almsater S, Saman W, Bruno F. Performance enhancement of high temperature latent heat thermal storage systems using heat pipes with and without fins for concentrating solar thermal power plants. Renewable Energy. 2016;89:36-50.
[97] Shabgard H, Bergman TL, Sharifi N, Faghri A. High temperature latent heat thermal energy storage using heat pipes. International Journal of Heat and Mass Transfer. 2010;53:2979-88.
[98] Naghavi MS, Ong KS, Mehrali M, Badruddin IA, Metselaar HSC. A state-of-the-art review on hybrid heat pipe latent heat storage systems. Energy Conversion and Management. 2015;105:1178-204.
[99] Tay NHS, Belusko M, Liu M, Bruno F. Investigation of the effect of dynamic melting in a tube-in-tank PCM system using a CFD model. Applied Energy. 2014;137:738-47.
[100] Lage JL, Bejan A. The resonance of natural convection in an enclosure heated periodically from the side. International Journal of Heat and Mass Transfer. 1993;36:2027-38.
[101] Antohe BV, Lage JL. Amplitude effect on convection induced by time-periodic horizontal heating. International Journal of Heat and Mass Transfer. 1996;39:1121-33.
[102] Antohe BV, Lage JL. The Prandtl number effect on the optimum heating frequency of an enclosure filled with fluid or with a saturated porous medium. International Journal of Heat and Mass Transfer. 1997;40:1313-23.
[103] Antohe BV, Lage JL. Experimental Investigation on Pulsating Horizontal Heating of a Water-Filled Enclosure. Journal of Heat Transfer. 1996;118:889-96.
[104] Kwak HS, Kuwahara K, Hyun JM. Resonant enhancement of natural convection heat transfer in a square enclosure. International Journal of Heat and Mass Transfer. 1998;41:2837-46.
[105] Roslan R, Saleh H, Hashim I, Bataineh AS. Natural convection in an enclosure containing a sinusoidally heated cylindrical source. International Journal of Heat and Mass Transfer. 2014;70:119-27.
[106] Ho CJ, Chu CH. Periodic melting within a square enclosure with an oscillatory surface temperature. International Journal of Heat and Mass Transfer. 1993;36:725-33.
[107] Ho CJ, Chu CH. The melting process of ice from a vertical wall with time-periodic temperature perturbation inside a rectangular enclosure. International Journal of Heat and Mass Transfer. 1993;36:3171-86.
[108] Krishnan S, Murthy JY, Garimella SV. Analysis of Solid–Liquid Phase Change Under Pulsed Heating. Journal of Heat Transfer. 2006;129:395-400.
[109] Bejan A. Entropy generation minimization: The new thermodynamics of finite-size devices and finite-time processes. Journal of Applied Physics. 1996;79:1191-218.
[110] Bejan A. Fundamentals of exergy analysis, entropy generation minimization, and the generation of flow architecture. International Journal of Energy Research. 2002;26:0-43.

[111] Guelpa E, Sciacovelli A, Verda V. Entropy generation analysis for the design improvement of a latent heat storage system. Energy. 2013;53:128-38.
[112] Jegadheeswaran S, Pohekar SD, Kousksou T. Exergy based performance evaluation of latent heat thermal storage system: A review. Renewable and Sustainable Energy Reviews. 2010;14:2580-95.
[113] Shabgard H, Bergman TL, Faghri A. Exergy analysis of latent heat thermal energy storage for solar power generation accounting for constraints imposed by long-term operation and the solar day. Energy. 2013;60:474-84.
[114] De Lucia M, Bejan A. Thermodynamics of energy storage by melting due to conduction or natural convection. Journal of Solar Energy Engineering. 1990;112:110-6.
[115] Bjurström H, Carlsson B. An exergy analysis of sensible and latent heat storage. Journal of Heat Recovery Systems. 1985;5:233-50.
[116] Rezaie B, Reddy BV, Rosen MA. Exergy analysis of thermal energy storage in a district energy application. Renewable Energy. 2015;74:848-54.
[117] Mahfuz MH, Kamyar A, Afshar O, Sarraf M, Anisur MR, Kibria MA, et al. Exergetic analysis of a solar thermal power system with PCM storage. Energy Conversion and Management. 2014;78:486-92.
[118] Esen M, Durmuş A, Durmuş A. Geometric design of solar-aided latent heat store depending on various parameters and phase change materials. Solar Energy. 1998;62:19-28.
[119] Tehrani SSM, Taylor RA, Saberi P, Diarce G. Design and feasibility of high temperature shell and tube latent heat thermal energy storage system for solar thermal power plants. Renewable Energy. 2016;96:120-36.
[120] Wang W-W, Wang L-B, He Y-L. The energy efficiency ratio of heat storage in one shell-and-one tube phase change thermal energy storage unit. Applied Energy. 2015;138:169-82.
[121] Neagu M, Bejan A. Constructal Placement of High-Conductivity Inserts in a Slab: Optimal Design of "Roughness". Journal of Heat Transfer. 2001;123:1184-9.
[122] Bejan A, Lorente S. Design with Constructal Theory2008.
[123] Bejan A, Fowler AJ, Stanescu G. The optimal spacing between horizontal cylinders in a fixed volume cooled by natural convection. International Journal of Heat and Mass Transfer. 1995;38:2047-55.
[124] Esapour M, Hosseini M, Ranjbar A, Bahrampoury R. Numerical study on geometrical specifications and operational parameters of multi-tube heat storage systems. Applied Thermal Engineering. 2016;109:351-63.
[125] Esapour M, Hosseini M, Ranjbar A, Pahamli Y, Bahrampoury R. Phase change in multi-tube heat exchangers. Renewable Energy. 2016;85:1017-25.
[126] Sparrow E, Patankar S, Ramadhyani S. Analysis of melting in the presence of natural convection in the melt region. Journal of Heat Transfer. 1977;99:520-6.
[127] Wang S, Faghri A, Bergman TL. A comprehensive numerical model for melting with natural convection. International Journal of Heat and Mass Transfer. 2010;53:1986-2000.
[128] J. C. Free and Moving Boundary problems, Clarendon Press, Oxford, 1984, x+ 426 ページ, 24× 16.5 cm, 19,800 円. 日本物理學會誌. 1986;41:84-5.
[129] Voller V, Swaminathan C, Thomas B. Fixed grid techniques for phase change problems: a review. International Journal for Numerical Methods in Engineering. 1990;30:875-98.
[130] Voller VR, Brent A, Prakash C. The modelling of heat, mass and solute transport in solidification systems. International Journal of Heat and Mass Transfer. 1989;32:1719-31.
[131] Modest MF. Chapter 22 - Radiation Combined with Conduction and Convection. Radiative Heat Transfer (Third Edition). Boston: Academic Press; 2013. p. 724-78.
[132] Tay NHS, Bruno F, Belusko M. Experimental investigation of dynamic melting in a tube-in-tank PCM system. Applied Energy. 2012;104:137-48.
[133] Bejan A. Internal Natural Convection. Convection Heat Transfer: John Wiley & Sons, Inc.; 2013. p. 233-94.
[134] Bejan A. Transition to Turbulence. Convection Heat Transfer: John Wiley & Sons, Inc.; 2013. p. 295-319.
[135] Lan CW, Yang DT. Dynamic simulation of the vertical zone-melting crystal growth. International Journal of Heat and Mass Transfer. 1998;41:4351-73.
[136] Riahi S, Saman WY, Bruno F, Tay NHS. Numerical modeling of inward and outward melting of high temperature PCM in a vertical cylinder. AIP Conference Proceedings. 2016;1734:050039.
[137] RIAHI S, SAMAN W, BRUNO F, TAY N. Numerical Study Of Melting Process Of A High-temperature Phase Change Material Including Natural Convection And Turbulence. International Journal of Computational Methods and Experimental Measurements. 2017;5:723-32.
[138] Tamme R, Bauer T, Buschle J, Laing D, Müller-Steinhagen H, Steinmann W-D. Latent heat storage above 120°C for applications in the industrial process heat sector and solar power generation. International Journal of Energy Research. 2008;32:264-71.
[139] El-Dessouky HaA-J. Effectiveness of a thermal energy storage system using phase-change materials Energy Convers. Mgmt 1997.
[140] Da Silva AK, Bejan A. Constructal multi-scale structure for maximal heat transfer density in natural convection. International Journal of Heat and Fluid Flow. 2005;26:34-44.

[141] Ferziger JH, Perić M, SpringerLink. Computational Methods for Fluid Dynamics. 0th ed. Berlin, Heidelberg: Springer Berlin Heidelberg : Imprint: Springer; 2002.
[142] Riahi S, Saman WY, Bruno F, Belusko M, Tay NHS. Comparative study of melting and solidification processes in different configurations of shell and tube high temperature latent heat storage system. Solar Energy. 2017;150:363-74.
[143] Riahi S, Saman WY, Bruno F, Belusko M, Tay NHS. Performance comparison of latent heat storage systems comprising plate fins with different shell and tube configurations. Applied Energy. 2018;212:1095-106.
[144] Riahi S, Saman WY, Bruno F, Belusko M, Tay NHS. Impact of periodic flow reversal of heat transfer fluid on the melting and solidification processes in a latent heat shell and tube storage system. Applied Energy. 2017;191:276-86.
[145] Riahi S, Saman W, Bruno F, Belusko M. Thermal Behaviour of High Temperature PCMs under a Periodic Heat Transfer Fluid Flow Reversal. 2016.
[146] Boerema N, Morrison G, Taylor R, Rosengarten G. Liquid sodium versus Hitec as a heat transfer fluid in solar thermal central receiver systems. Solar Energy. 2012;86:2293.
[147] Gibbings JC. Dimensional analysis: Springer Science & Business Media; 2011.